Multi-scale Dynamics of Organic Light-Emitting Devices

A dissertation submitted to the faculty of the graduate school of the University of Minnesota

Kyle William Hershey

In partial fulfillment of the requirements for the degree of Doctor of Philosophy

Russell J. Holmes, Advisor

July 2018

Acknowledgements

I would like to thank my research advisor Russell J. Holmes for all of his guidance and advice. The Holmes research group members have also provided endless support and discussion.

I would like to thank my parents for all of their support and for constantly pushing me to excel.

I would like to thank my wife for constantly being at my side, and always there to support.

I would like to thank John Bangsund for significant discussion and assistance on our collaborative work. I would also like to thank Professor Thomas Hoye, as well as his student Dr. Feng Xu for their work and discussion on our collaborative work.

This work was financially supported by The Dow Chemical Company, and I would like to thank all of the advisors there that have provided a unique perspective and constructive feedback.

Dedication

I would like to dedicate this work to my wife, Mary Beth.

Abstract

Over the last decade, organic light-emitting devices (OLEDs) have grown to receive tremendous attention for application in commercial displays and in lighting. In display applications, OLEDs offer a wide and tunable color gamut, high peak efficiency, high contrast, and compatibility with novel form factors. For white-lighting, OLEDs can achieve broadband emission and are compatible with flexible substrates, allowing conformal lighting as well as potential for roll-to-roll, low cost processing. OLED technology is ubiquitous for small format mobile displays, and is emerging in the large display and white lighting market. This lag in commercial uptake is partially due to a lack of understanding of the underlying device operation.

This thesis seeks to refine the understanding of device electrical and optical operation. The fundamental kinetics of charge carrier and light precursors (excitons) are investigated in a unified model for the transient and steady-state regimes of operation. Through modeling, a quantification and understanding of performance metrics is developed, aiding in the characterization of OLEDs. Optical modeling techniques were implemented to assist in the understanding of overall device behavior.

Operational stability is investigated through the development of a technique which separates the contributions of loss mechanisms during operation. This is investigated in several systems, and enables a unique understanding of the interplay between distinct degradation mechanisms. Molecular design was also considered via degradation of a molecular family within devices and in isolation.

Contents

List of Figures

List of Tables

Common Acronyms and Terms

EL	Electroluminescence
Pl	Photoluminescence
EQE, η_{EQE}	External Quantum Efficiency
η_{PL}	Photoluminescence Efficiency
η_{EF} ,γ	Exciton Formation Efficiency, Charge Balance
χ	Radiative spin fraction
RZ	Recombination Zone
EML	Emissive Layer
ETL	Electron Transport Layer
HTL	Hole Transport Layer
EIL	Electron Injection Layer
HIL	Hole Injection Layer
EBL	Electron Blocking Layer
HBL	Hole Blocking Layer
LUMO	Lowest Unoccupied Molecular Orbital
HOMO	Highest Occupied Molecular Orbital
OPV	Organic Photovoltaic
OLED	Organic Light-Emitting Device
OFET	Organic Field-Effect Transistor
M-EML	Mixed Emissive Layer
G-EML	Gradient Emissive Layer
S-EML	Single Emissive Layer
D-EML	Double Emissive Layer

Molecules

3TPYMB	Tris(2,4,6-triMethyl-3-(pyridin-3-yl)phenyl)borane
4CzIPN	(4s,6s)-2,4,5,6-tetra(9H-carbazol-9-yl)isophthalonitrile
Ag	Silver
Al	Aluminum
Alq3	Tris(8-hydroxyquinoline)aluminum
Anthracene	Anthracene
Au	Gold
B3PYMPM	bis-4,6-(3,5-di-3-pyridylphenyl)-2-methylpyrimidine
BCBP	b"2,2'-Bis(4-(carbazol-9-yl)phenyl)-biphenyl"
BCP	Bathocuproine
BP2T	5,5u-[Di(1,1u-biphenyl)-4-yl]-2,2u-bithiophene
BP4mPy	3,5,3A,5A-tetra(m-pyrid-3-yl)phenyl[1,1A]-biphenyl
Bphen	Bathophenanthroline
C_{60}	Fullerene
C70	[5,6]-Fullerene
CBP	4,4-Bis(N-carbazolyl)-1,1-biphenyl
CDBP	b"4,4'-Bis(9-carbazolyl)-2,2'-dimethylbiphenyl
ClAlPc	Aluminum phthalocyanine chloride
CuPc	Copper(II) phthalocyanine
CzSi	9-(4-tert-butylphenyl)-3,6-bis(triphenylsilyl)-9H-carbazole
CzTRZ	9-[4-(4,6-diphenyl-1,3,5-triazin-2-yl)phenyl]-9H-carbazole
FIrpic	Bis[2-(4,6-difluorophenyl)pyridinato-C2,N](picolinato)iridium(III)
H_2Pc	29H,31H-Phthalocyanine
HATCN	1,4,5,8,9,11-Hexaazatriphenylenehexacarbonitrile
$Ir(mphq)_3$	Tris[2-phenyl-4-methylquinoline)]iridium(III)
$Ir(ppy)_3$	Tris[2-phenylpyridinato-C2,N]iridium(III)
ITO	Indium Tin Oxide
LiF	Lithium Fluoride
LiQ	8-Quinolinolato lithium (Liq)
MADN	2-Methyl-9,10-bis(naphthalen-2-yl)anthracene
mCBP	b"3,3'-Bis(N-carbazolyl)-1,1'-biphenyl"

mCP	1,3-Bis(N-carbazolyl)benzene
MgPc	Magnesium phthalocyanine
MoO_x	Molybdenum(VI) oxide
NPD	N,N-Di(1-naphthyl)-N,N-diphenyl-(1,1-biphenyl)-4,4-diamine
NTCDA	1,4,5,8-Naphthalenetetracarboxylic dianhydride
P3HT	Poly(3-hexylthiophene-2,5-diyl)
PbPc	Lead(II) phthalocyanine
Pedot	Poly(3,4-ethylenedioxythiophene)-poly(styrenesulfonate)
Pentacene	Pentacene
PPT	2,8-Bis(diphenylphosphoryl)dibenzo[b,d]thiophene
PQIr	(2,4-Pentanedionato)bis[2-(2-quinolinyl)phenyl]iridium(III)
PTCBI	3,4,9,10-Perylenetetracarboxylic Bisbenzimidazole
PTCDA	Perylene-3,4,9,10-tetracarboxylic dianhydride
PTCDI	N,N-Dioctyl-3,4,9,10-perylenedicarboximide
PtOEP	Platinum octaethylporphyrin
PtTPTBP	Platinum(II) tetraphenyltetrabenzoporphyrin
Rubrene	5,6,11,12-Tetraphenylnaphthacene
$SnNcCl_2$	Tin(IV) 2,3-naphthalocyanine dichloride
SubNc	Boron sub-2,3-naphthalocyanine chloride
SubPc	Boron subphthalocyanine chloride
T2T	2,4,6-tris(biphenyl-3-yl)-1,3,5-triazine
TAPC	4,4-Cyclohexylidenebis[N,N-bis(4-methylphenyl)benzenamine]
TAZ	3-(Biphenyl-4-yl)-5-(4-tert-butylphenyl)-4-phenyl-4H-1,2,4-triazole
TCTA	Tris(4-carbazoyl-9-ylphenyl)amine
Tetracene	Benz[b]anthracene
TPBi	2,2,2"-(1,3,5-Benzinetriyl)-tris(1-phenyl-1-H-benzimidazole)
TPD	N,N-Bis(3-methylphenyl)-N,N-diphenylbenzidine
UGH2	1,4-Bis(triphenylsilyl)benzene
ZnPc	Zinc phthalocyanine

Chapter 1

Commercial Scope

Organic electronics is an exciting technology that is rising in commercial popularity.[1–3] These devices exhibit a number of unique features that allow them to compete with traditional semiconductors, as well as occupy new technological space. This has been leveraged in various technologies, including organic light-emitting devices (OLEDs), photovoltaics (OPVs), and field effect transistors (OFETs).[4–6] This chapter seeks to provide an overview of applications as well as outline the focus of this work.

1.1 Organic Devices

Many of the advantages of organic electronics exist across all devices. Since the molecules are semiconductors on their own and do not rely on crystallinity, organic electronics are Van Der Waals bonded and are applied as thin films so do not have to be planar and rigid. This allows compatibility with flexible substrates and has been demonstrated for a variety of flexible devices.[7–9] Additionally, curved and form fitting devices already exist in commercial devices.[10,11]

Compatibility with flexible substrates and a variety of processing techniques also unlocks the possibility of roll-to-roll and web processing.[12] Currently, commercial organic electronics primarily utilize vacuum deposition and batch processing, leading to relatively high cost devices.[13,14] As manufacturing techniques transition to roll-to-roll methods, mass production will offer a great reduction in device cost and will significantly alter the economics of organic electronics. Roll-to-roll compatible device manufacturing methods so far have not demonstrated the highest efficiency devices and requires further development, though some commercial products do use solution processing.[15–17]

Most organic electronics utilize thin films, with total device thicknesses less than 500 nm of active

material. This makes them compatible with extremely thin form factor devices, which are essential for mobile devices and small form factor electronics. As wearable electronics become increasingly important, organic electronics being thin and flexible offer an obvious solution.

Organic molecules consist primarily of earth abundant materials such as carbon and nitrogen. Molecular structures of these materials can be easily modified, allowing for easy tuning of the molecular properties, such as emission and absorption.

1.1.1 Organic Light-Emitting Devices (OLEDs)

OLEDs are becoming a highly commercialized technology and have had the most success of organic electronic applications.[2,3,11,18] OLEDs offer improved contrast and viewing angle with similar power consumption when compared with LCD LED technology, which utilizes a white backlight in combination with color filtering layers to produce the image.[19] These advantages in combination with the thin form factor and compatibility with curved and flexible substrates has made OLEDs excel in the small display market, including wearables and smartphones. Flagship phones from all major manufacturer within the U.S. are utilizing OLEDs, including Samsung, Google, Apple and LG, and are shown in Figure 1.1.[20,21] Several devices feature curved displays, offering a unique customer experience.

Large format displays are also commercially available for televisions.[20,21] Again these displays advertise superior contrast and viewing angle. A flexible large display is seen in Figure 1.1, demonstrated by LG, though not available for purchase.[22] While large format displays offer significant advantage in viewer experience over LED technology, cost has prohibited commercialization.[22] With a significant increase in

Figure 1.1: (a) Commercial OLED white lighting from OLEDworks. (b) Commercial OLED TVs from LG. (c) Flexible OLED TV demo from LG. (d) Smartphones from Apple, Google and Samsung.

cost compared to similar LCD LED devices, OLED TVs require a price reduction to see an improved market share above the current 1.1%.[23]

Commercial white lighting is also available featuring OLED technology. However, OLEDs suffer from significant drawbacks in this space, limiting the scope of their application.[22] OLED panels show shorter lifespan due to degradation (gradual luminance loss) as well as catastrophic failure (dark segment formation) making OLEDs significantly more expensive over their lifetime. This could be reduced by device cost, but OLED fixtures are still more expensive than their LED counterparts. Due to these drawbacks, OLEDs in white lighting are mostly used for architectural applications taking advantage of their thin form factor and flexibility.[24,25] An example of this is shown in Figure 1.1, demonstrating both of these properties.[22] OLED technology for white lighting could become competitive as the manufacturing technology and lifetime of devices improve. Additionally, OLEDs currently suffer from a small market share, and cannot take advantage of the cost savings of large scale manufacturing.

1.1.2 Organic Photovoltaics (OPVs)

OPVs share all of the same form factor benefits of OLEDs. Because of this, OPVs are successful in a few novel implementations that are inaccessible for silicon panels.[1,6,26–28]

Crystalline silicon solar cell panels suffer from their large and heavy form. Due to their thin form factor, OPVs are a good option for areas where traditional panels cannot be installed.[29,30] Figure 1.2a shows a canopy made of OPVs, utilizing an area inaccessible to traditional panels. This is further extended by the ability to have flexible solar cells, shown in Figure 1.2b.[31]

Due to the wide range of absorption bands available to OPVs, it is possible to form transparent solar cells. Though these cells let through all visible light and thus suffer from low efficiency, they capitalize on areas where transparency is needed that could not facilitate opaque panels. The transparent cells, shown in Figure 1.2c, are designed for window cells, where a traditional window can be replaced by a solar unit..[32,33] This

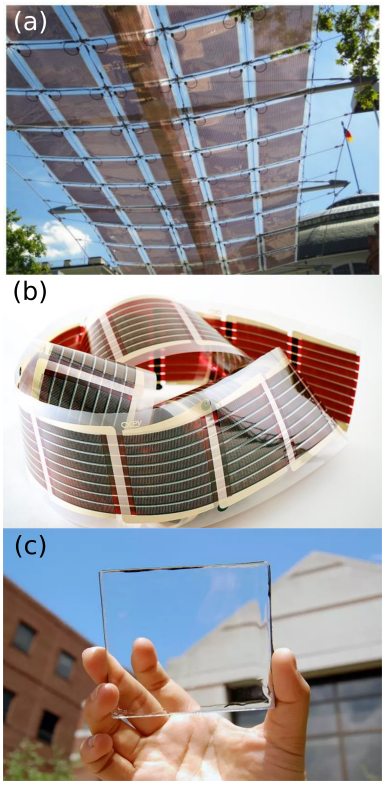

Figure 1.2: (a) Belectric solar cells. (b) Transparent solar cell from Michigan State University. (c) Flexible solar cell from InfinityPV.

is extremely promising in urban environments and high rise
buildings, where horizontal surfaces are at a premium, but windows are in abundance.

1.1.3 Organic Field-Effect Transistors (OFETs)

Organic Field-effect transistors (OFETs) are an essential counterpart to the other devices we have discussed here. On their own, OFETs can take advantage of their low cost and flexible form factor for use in cheap, low complexity electronics. This can include Radio frequency ID (RFID) and single use medical devices.[4,34–37] Additionally, OFETs are an essential part of OLED displays utilizing flexible behavior.

1.2 Scope of This Thesis

This thesis focuses on the understanding and improvement of OLEDs. In particular, a fundamental understanding of the kinetic processes undergone during device operation is sought. This kinetic understanding approach is desired to help in the optimization of device efficiency and lifetime through a better understanding and quantization of device behavior. In addition to this kinetic understanding, lifetime is sought to be improved through the development of blue emitters, which are known to be limiting for device lifetime.

Chapter 2

Overview of Organic Semiconductors

2.1 Organic Semiconductors

Organic molecules are broadly classified as molecules primarily composed of carbon.[38]. These molecules can range dramatically in size, and are often split into small molecule (m_w < 1 kg/-mol) and polymers. For organic electronics, both categories can be used, but this thesis will focus on small molecules, as that is the primary interest of commercial devices.

To exhibit semiconducting behavior, electrons must be delocalized within the system.[40] For organic molecules, this is achieved through overlapping p orbitals from carbon. Through alternating single and double bonded carbon, hybridized 2p and 2s orbitals form three sp^2 orbitals and leave one unhybridized p_z orbital. The remaining p_z orbitals can interact, forming a π-bond and delocalizing of the electron cloud, known as *conjugation*. An example of this is shown for benzene, in Figure 2.1.

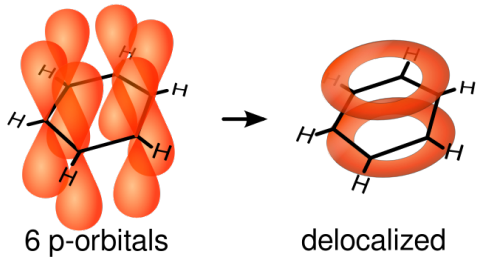

Figure 2.1: Molecular orbitals of benzene. The left figure shows the 6 out of plain p_z orbitals, and the right image shows the delocalized π-bond.[39]

When this conjugation and blending of molecular orbitals occurs, discrete energetic states mix, resulting in multiple energetic states.[41,42] The formed energetic states can be grouped into bands of allowed energies. In order to exhibit semiconducting behavior, the resulting bands should have a set of states filled with electrons separated by a gap from a band of unoccupied states. For the organic small molecules of interest to this study, delocalization occurs on individual molecules,

resulting in less delocalization and thus much narrower bands than would be observed in a typical semiconductor, such as silicon or germanium, but the concept remains the same. In organic molecular semiconductors, the highest occupied molecular orbital (HOMO) and lowest unoccupied molecular orbital (LUMO) are analogous to the valence and conduction bands of inorganic semiconductors in terms of their roles for electrons and holes, though their operation is vastly different. The HOMO is filled with electrons and the LUMO is empty in the ground state. When excited, electrons can be transported through the LUMO levels. This will result in an electron vacancy in the HOMO, known as a *hole*

Films are held together by intermolecular dipole-dipole interactions, known as van der Waals forces. These forces can involve both permanent and induced dipoles. This weak binding with the molecules displaying semiconductor properties as individual molecules allow these films to be flexible. Traditional crystalline semiconductors rely on the periodicity of the lattice to exhibit energy bands. This is a huge advantage of organic semiconductor devices, allowing for a variety of unique applications.

2.2 Charge Transport

Charge transport in organic semiconductors can take on a variety of behaviors, depending on material and morphology.[38,43] Two regimes of operation are typically expected, being band transport and hopping transport. As disorder increases, a shift from band to hopping transport is expected.

2.2.1 Band Transport

Band transport is expected in most atomic crystals, and is thus extensively characterized for inorganic semiconductors.[44] In a crystal, a periodic energy structure is maintained throughout the entire structure. This creates a delocalization of the electron wavefunction across the crystal and electrons have a mean free path that extends for multiple molecular spacings. Because of this freedom of charge movement, charges can be directly accelerated through the crystal by an electric field, $\vec{E}$. This creates a current density of

$$\vec{J} = qn\mu\vec{E}, \tag{2.1}$$

where q is the unit charge, n is the charge carrier density, and μ is the charge mobility. Typically in these materials, the mobility decreases with temperature as vibrations in the crystal lead to more

scattering of the electrons.

2.2.2 Hopping Transport

In less ordered materials, there is substantially less symmetry and periodic potentials and electron distributions are much more confined . In this case, each molecule serves as an individual energetic well, and for transport, charges are forced to conduct individual hops to neighboring molecules. This dramatically reduces the mobility compared to band transport. With temperature, mobility follows an Arrhenius dependence that can be split into a field dependent and field independent term as

$$\mu \propto \exp\left(-\frac{E_a}{k_B T}\right) \exp\left(\frac{\beta\sqrt{E}}{k_B T}\right) \tag{2.2}$$

with E_a being the hopping activation energy and k_B being the Boltsmann constant. β is a constant and E is the electric field.

These two transport mechanisms account for very different physics. Organic semiconductors can operate in either regime. Temperature dependent current measurements can be conducted to illuminate mechanism, and often morphology can be a good predictor. In amorphous organics, a hopping mechanism can typically be assumed.

2.3 Excitons

In organic semiconductors, a critical component of light formation or absorption is the formation of a bound excited state, called an *exciton*, shown schematically in Figure 2.2. An exciton consists of a hole in the HOMO bound to an electron in the LUMO. Due to the low dielectric constant ($\epsilon_R \approx 3$), excitons in organic materials are highly localized and have large binding energies, >100 meV.[45–48] These excitons can be relatively long lived at room temperature, with characteristic lifetimes, τ ranging from 0.5 ns - 1 ms.[49–56] Because of these long lifetimes, the dynamics of excitons, both in their interaction as well as decay into light or heat, are important to the understand of organic semiconductor behavior. Excitons that reside on a single molecule are known as "Frenkel" excitons, while an exciton spanning neighboring molecules is known as a "charge-transfer" exciton. Excitons spanning larger spatial extents are not seen in amorphous

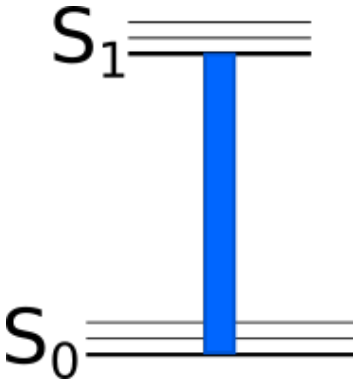

Figure 2.2: Schematic view of an exciton. S_0 and S_1 are the ground and first singlet excited state, respectively.

organic semiconductors.

2.3.1 Singlets and Triplets

Electrons and holes have a spin of $S = \pm 1/2$. These spins can combine into four possible spin combinations, shown in Figure 2.3 Three of these states have spin $S = 1$ and are called *triplets* due to the degeneracy. The remaining state is called the *singlet*, with $S = 0$. Electrically, excitons are formed from loose electrons and holes, and from simple statistics, form 75% triplets and 25% singlets.[57–59] Optically, due to spin conservation from an $S = 0$ photon, only singlet excitons are initially formed.

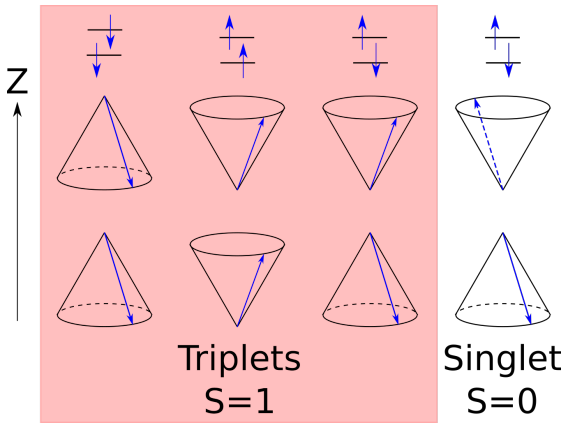

Figure 2.3: Spin vectors for the possible spin state combinations of an electron and a hole. The orientation of the cone represents spin up or down, while the cone indicates the relative phase of the precession in angular momentum. Triplets all yield a total spin of S=1 while the single has $S = 0$.

2.3.2 Electronic Transitions

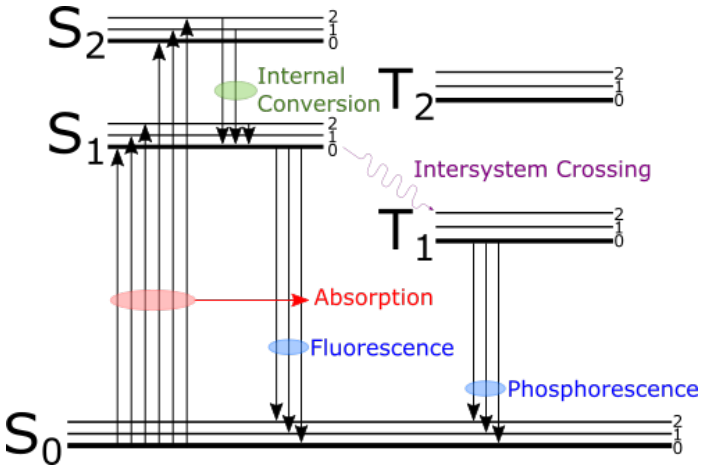

Figure 2.4: Jablonski diagram for an organic semiconductor. Fluorescence and Phosphorescence are both depicted, though in some systems, phosphorescence is not observed.

Figure 2.4 shows the energy landscape available to excitons in an organic semiconductor. The singlet manifold is shown on the left, with the first three electronic energy levels shown as S_0, S_1, and S_2. The vibronic levels of these states are labeled as $0, 1, 2$. The ground state is depicted as S_0. Absorbed photons create excitons in the S_1 and S_2 manifolds. When making electronic transitions,

electrons are assumed to start from the lowest vibronic state, by Kasha's rule.

Once created, excitons rapidly convert from higher energy states back to S_1, losing addition energy to phonons through internal conversion. From S_1, excitons can decay back to the ground state either by non-radiative or radiative means, known as fluorescence. The balance of radiative (k_r) and non-radiative (k_{nr}) rates determines the photoluminescence efficiency by the equation

$$\eta_{\text{PL}} = \frac{k_r}{k_r + k_{nr}}. \tag{2.3}$$

Typically, k_r is on the order of 10^8 s^{-1} for singlet excitons, resulting in lifetimes on the order of 10 ns.[45,60]

Since triplet excitons have an electron and a hole that share the same spin state, they are subject to the exchange interaction, increasing the separation and reducing repulsion, resulting in a lower energy state. In order for a singlet exciton to transition into a triplet, a flip in spin is needed. This transition is promoted in systems exhibiting spin-orbit coupling. Spin-orbit coupling involves coupling of the electron spin with the angular momentum of the orbit, allowing the spin to be reversed. This is much more common as the atomic number increases, and is commonly seen in heavy metal atoms. As spin-orbit coupling becomes more prominent, excitons are allowed to freely transition between the singlet and triplet state, and can become mixed.

In coordinated molecules involving ligands off of a heavy-metal core, it is possible to form Metal-Ligand Charge Transfer states (MLCT). The high energy d-states of the metal atom promote spin-orbit coupling. Molecules exhibiting MLCT states have excited states that reside partially on the metal atom, allowing spin flipping to occur, and promoting singlet-triplet mixing. An archetypical MLCT exhibiting molecule, Tris[2-phenylpyridinato-C^2,N]iridium(III) ($Ir(ppy)_3$) is shown in Figure 2.5.

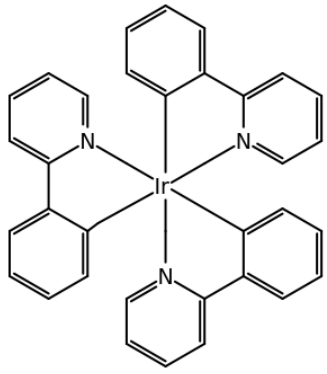

Figure 2.5: $Ir(ppy)_3$, a commonly used OLED molecule with an excited state which exhibits MLCT.

The triplet state is considered a "forbidden state" for emission, and is quantum mechanically disallowed in first order approximations due to the conservation of spin between the triplet ($S = 1$) and the ground state ($S = 0$). However, these spin transitions can occur, especially with significant spin-orbit coupling. Since an additional spin flip is required, the radiative rate of emission from the triplet state is usually $k_r = 10^6$ s^{-1} or longer, dependent on the ability of the molecule to undergo a spin transition. This slower rate of radiative emission when

compared with the singlet state makes phosphorescence much more competitive with non-radiative loss pathways. Because of this, without molecules that promote spin-orbit coupling, triplet emission is extremely inefficient and is not visible at room temperature. However, at low temperature (10K)[45,61–64] or with non-radiative pathways reduced,[65] the triplet emission can be observed. This can be exploited for the measurement of the triplet state energy, as discussed in Appendix B.

The transition from a triplet back into a singlet is also possible, and is known as *reverse intersystem crossing*.[57–59,66–72] Though this is energetically unfavorable in most molecules, due to the energy difference of the singlet and triplet, an exciting area of emitter research is in Thermally Activated Delayed Fluorescence (TADF). In TADF molecules, the singlet-triplet energy difference (ΔE_{ST}) is below the thermal energy at room temperature, and allows promotion back into the singlet state. Efficient transition between the singlet and triplet is observed in TADF systems despite the lack of spin-orbit coupling introduced by MLCT states. This is because the mixing coefficient between the singled and triplet can be expressed as[73]

$$\lambda = \frac{H_{SO}}{\Delta E_{ST}} \tag{2.4}$$

where H_{SO} is the spin-orbit interaction. In TADF molecules, since ΔE_{ST} is small, significant transfer can still be observed. These materials are advantageous in OLEDs because they allow electrically formed triplets to convert to a singlet for emission without using expensive rare-earth metals.

2.3.3 Exciton Transport

As excitons are charge neutral and not subject to drift in an electric field, their transport relies upon a diffusive process in organic materials. Diffusion relies on being able to transfer excitons from a *Donor* molecule which has the initial excitation onto an *Acceptor*. Three mechanisms are common to facilitate this transfer: cascade energy transfer, Dexter transfer and Förster transfer. All three of these mechanisms can contribute to exciton transport, but typically one is dominant for a given material.

2.3.3.1 Cascade Energy Transfer

Cascade energy transfer consists of exciton emission in the form of a photon being reabsorbed by another molecule.[45] The efficiency of this transfer depends on the photoluminescence efficiency of the donor molecule to form a photon, as well as absorption of the acceptor molecule at the photon

energy. Of the three mechanisms, this is the longest range and can allow transport for 10-100 nm, though relies on propagation of the photon through the surrounding media.

2.3.3.2 Dexter Transfer

Dexter transfer is the shortest range process and describes direct physical transfer of the excited state from the donor to the acceptor. The rate of Dexter transfer can be written as[45]

$$k_D = Ke^{-2R_{DA}/R_0} \int E_D(E)A_A(E)dE \tag{2.5}$$

where K is dependent on the specific orbital interactions, R_{DA} is the separation of the donor and acceptor, R_0 is the characteristic length scale for orbital overlap, normalizing the rate to other energy loss pathways, E_D is the donor emission spectrum, A_A is the acceptor absorption spectrum, and E is the energy. As can be seen from the exponential dependence, Dexter transfer requires spatial overlap of the electron density of the two molecules, limiting Dexter transfer to nearest neighbors, typically.

Because Dexter transfer involves the direct exchange of charges, the spin state of the electron and hole are preserved. Additionally, since no intermediate photonic state is required, excitons with $S \neq 0$ (triplets) can be transferred. Dexter transfer is typically the dominant mechanism of transport for triplet excitons.

2.3.3.3 Förster Transfer

Förster resonance energy transfer (FRET) describes transfer of an exciton via an overlap in the dipole field of the donor with the acceptor molecule. In this process, the dipole interaction can be thought of as a transmission and receiver antennae. The exciton on the donor causes an oscillation in the dipole field which excites an electron in the acceptor to become excited. This excitation on the acceptor relaxes the donor to the ground state.

The rate of Förster transfer can be expressed as[60,74,75]

$$k_F(d) = \frac{1}{\tau d^6} \frac{9\eta_{PL}\kappa^2}{128\pi^5 n^4} \int \lambda^4 E_D(\lambda)A_A(\lambda)d\lambda = \frac{1}{\tau}\left(\frac{R_0}{d}\right)^6 \tag{2.6}$$

where τ is the exciton lifetime, d is the distance between the donor and acceptor, η_{PL} is the photoluminescence efficiency, κ is a factor depending on the dipole orientation, n i s the index of refraction, λ is the wavelength, E_D is the donor emission, and A_A is the acceptor absorption. The integral expression in Equation 2.6 is an expression of Fermi's golden rule and requires that the

initial and final spin states be the same. Therefore, Förster transfer is typically restricted to singlet excitons. Because of this field transfer of singlet excitons, FRET is often described as a transfer of a "virtual photon".[38,45]

Förster transfer typically transfers excitons up to 10 nm apart, though is a strong function of distance.[60,76] The radius at which the rate of FRET is equal to other loss pathways is called the Förster radius (R_0).

2.3.4 Excitonic Interactions and Quenching Processes

Excitons are subject to a variety of bimolecular processes and loss pathways. This section seeks to outline these processes.

2.3.4.1 Exciton-Exciton Annihilation

Exciton-exciton annihilation involves the transfer of energy of one exciton onto an already excited molecule. This forms a single exciton with twice the energy, promoting the exciton into the second excited state. This exciton quickly relaxes back into the first excited state, releasing the excess energy as heat.

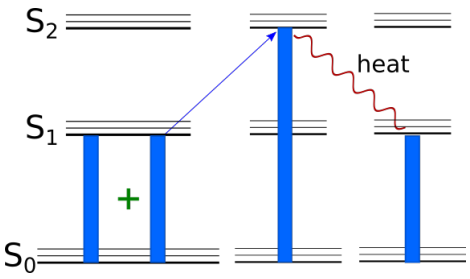

Figure 2.6: Exciton-exciton annihilation process. The energy of two excitons is transferred all onto a single molecule, forming a single exciton. This exciton then relaxes, emitting heat.

Exciton-exciton annihilation is a bimolecular process and has a rate dependent on the exciton density squared of $K = k_{EE}N_{ex}^2$.[46] In this expression, k_{EE} is the material dependent rate constant. Exciton-exciton annihilation can affect both singlet and triplet excitons, though is typically more prominent in phosphorescent systems due to the longer exciton lifetime.

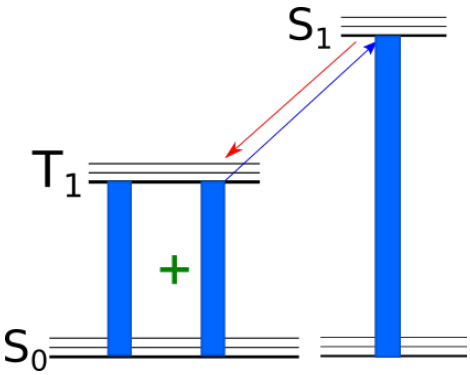

Figure 2.7: (blue arrow) Triplet fusion. Two excitons combine energy, forming a single exciton. (red arrow) Singlet Fission into two triplet excitons.

2.3.4.2 Triplet Fusion and Singlet Fission

Triplet fusion is a related process to exciton-exciton annihilation. In the same process, two excitons combine their energy to form a single exciton, as shown in Figure 2.7. In triplet fusion, these two initial excitons are triplets and the excess energy provided allows the transition into the singlet state. This is beneficial

in materials where emission out of the triplet state is prohibited, as it recovers some excitons lost to the non-radiative triplet. For this mechanism to be possible, the singlet energy can be no more than twice the energy of the triplet state. Emission from upconverted triplets via fusion is known as delayed fluorescence.

In a system with triplet fusion, the rate equation for triplets is[51]

$$\frac{dT}{dt} = G_T - \frac{T}{\tau_T} - \gamma T^2 \tag{2.7}$$

where T is the triplet density, G_T is the triplet generation rate and τ_T is the triplet lifetime.

The corresponding singlet rate equation is then

$$\frac{dS}{dt} = G_S - \frac{S}{\tau_S} + \frac{1}{2}\gamma T^2 \tag{2.8}$$

where S is the singlet density, G_S is the singlet generation rate, and τ_S is the singlet lifetime. In most systems, τ_S is on the order of nanoseconds and τ_T is much longer. To exhibit significant delayed fluorescence, γT^2 must be competitive with T/τ_T. If a significant triplet population is excited, $S/\tau_S \gg \gamma T^2$ and the observed lifetime is governed by triplet fusion.

The inverse process, singlet fission is the division of one singlet exciton into two triplet excitons.[77–79] For this to be possible, the singlet energy must be more than twice the triplet energy. Singlet fusion is important for solar cells because it allows for harvesting of use of excess energy above the band gap which would typically lost to thermal energy. This also allows for quantum efficiencies greater than one. Often, singlet fission and triplet fusion are present in the same system, the most famous of which being pentacene.[51]

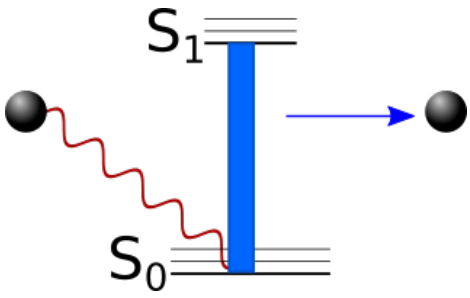

Figure 2.8: Exciton-polaron quenching process. A polaron non-radiatively couples with an exciton, leaving a loose polaron.

2.3.4.3 Exciton-Polaron Quenching

Exciton-polaron quenching occurs when a free polaron interacts with an exciton, as shown in Figure 2.8. An excited charge relaxes to the ground state on a surrounding molecule non-radiatively. This process has an end product of a free electron or hole and quenches the exciton. Exciton-polaron annihilation depends on both the polaron and exciton population as $K = k_{EP} N_{ex} N_{pol}$. Both exciton-exciton annihilation and exciton-polaron quenching are very important for both efficiency and operational lifetime, and are discussed further in Chapters 4 and 5.

2.3.4.4 Field Dissociation

Excitons have a binding energy on the order of 100 meV.[45] This requires careful design in organic photovoltaics to engineer dissociation of excitons. However, in OLEDs with an applied field, the exciton can be dissociated due to the field, as shown in Figure 2.9.[53,80–82] Typically this can occur for local fields larger than $10^6 V/cm$.[46] Due to the distribution of charge within the device being hard to characterize, it is often hard to measure this quantitatively. However, Reineke et al. [46] have shown that for fields observed in typical device operation, the transient photoluminescence is independent of applied field, indicating minimal field dissociation.

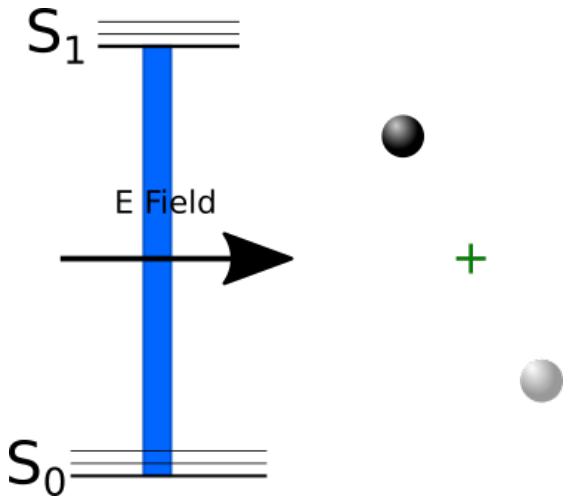

Figure 2.9: Field dissociation of an exciton.

2.4 Conclusion

Excitons are a key component to the operation of OLEDs. Much of device operation can be directly contributed to excitonic processes, including aspects of the device efficiency and operational lifetime.[46,83,84] Connecting these physical processes to device operation in the steady-state and transient regimes is discussed in Chapter 4. Aspects of degradation due to excitonic processes are discussed in Chapters 5 and 6. In general, for both device efficiency and lifetime, utilization of all excitonic states and minimization of energy loss to bimolecular processes is desired. This requires careful consideration of the excitonic processes, and will be a continuing theme throughout this thesis.

Chapter 3

Organic Light-Emitting Devices

3.1 Architecture and Basic Operation

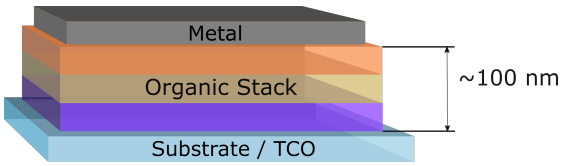

Figure 3.1: Basic layer diagram for OLED devices. TCO is a transparent conducting oxide.

Organic Light-Emitting Devices (OLEDs) consist of an organic layer stack sandwiched between two electrodes. For light to escape, one of the electrodes is transparent, and in most lab scale devices, this is the bottom contact, and is reversed for most commercial devices. This is often accomplished by using glass coated with Indium Tin Oxide (ITO) as a transparent conducting material. The opposing contact is typically a metal, and in most cases Aluminum. An example of this type of structure is shown in Figure 3.1. The organic layer stack typically has an overall thickness of >80 nm and consists of multiple layers. For most materials, deposition at room temperature from the vapor phase at rates of 1 Å/s does not provide the time or energy needed to rearrange into a crystal, and thus yields amorphous films, showing minimal short and medium range order.[85–91] However, most materials will crystallize rapidly with annealing,[92] or slowly over time.[93]

Detailed device operation will be expanded upon in Chapter 4, but the goal of the layer stack is to efficiently form and recombine excitons. When voltage is applied, electrons are injected from the metal contact into the electron transport layer (ETL) and holes are injected from the ITO into the hole transport layer (HTL). Carriers transport through these layers to a region where exciton formation is designed to occur. This can be done in a variety of ways and is discussed in detail in Section 3.4, but most modern devices use a structure with a dedicated emissive layer (EML),

as shown in Figure 3.2. In this type of device, the emitter molecule or guest, is doped at low concentration within a host matrix.[94] This composite film structure is used because most emissive molecules show a reduction in η_{PL} with increasing concentration.[45] The host molecule is used to help transport charge to the emissive molecule and separate the guest molecules. The host molecule is designed to have a wider energy gap, making it energetically favorable for excitons to form on the guest molecule.

Most devices are designed to confine excitons within the EML. However, excitons are not typically formed uniformly throughout this layer. The spatial density profile of excitons is termed the *recombination zone*, and is an important device parameter. The role of recombination zone (RZ) will be discussed throughout this work, and characterization is discussed in Section 3.6.

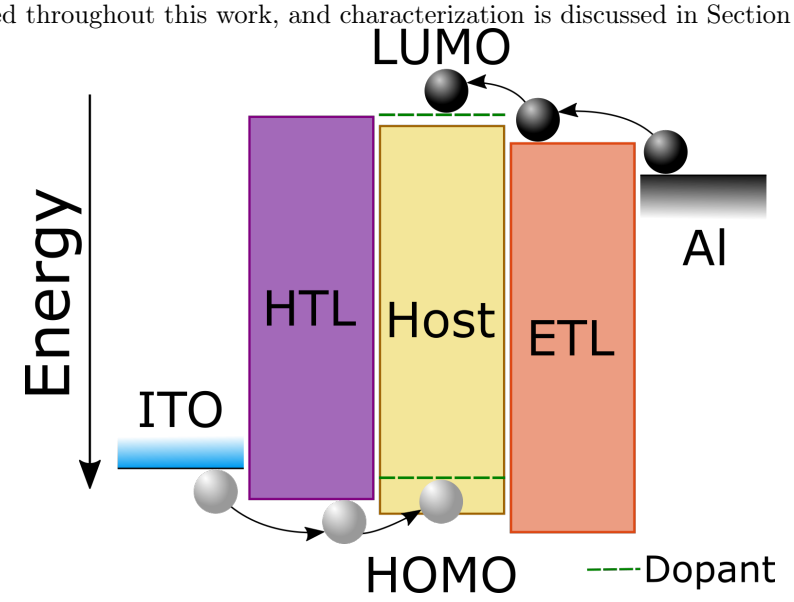

Figure 3.2: Energy level diagram of an OLED. Energy is shown in reference to the vacuum level. Electrons are shown in black spheres, holes shown in white.

The structure shown in Figure 3.2 is greatly simplified from most devices. Injection layers (HIL/EIL) are often used to aid in charge injection into the device between the electrode and transport materials. These materials will sit energetically between the electrode and the transport layer. To confine charges within the EML, blocking layers (HBL/EBL) are often used between the EML and the opposing transport layer. For example, a hole blocking layer would sit between the EML and the ETL and would have an energy level similar to the ETL, so electron transport would not be disrupted, but would have a high HOMO energy or a low hole mobility. These types of layers are often added as needed based on the energetic levels of the other materials in use.

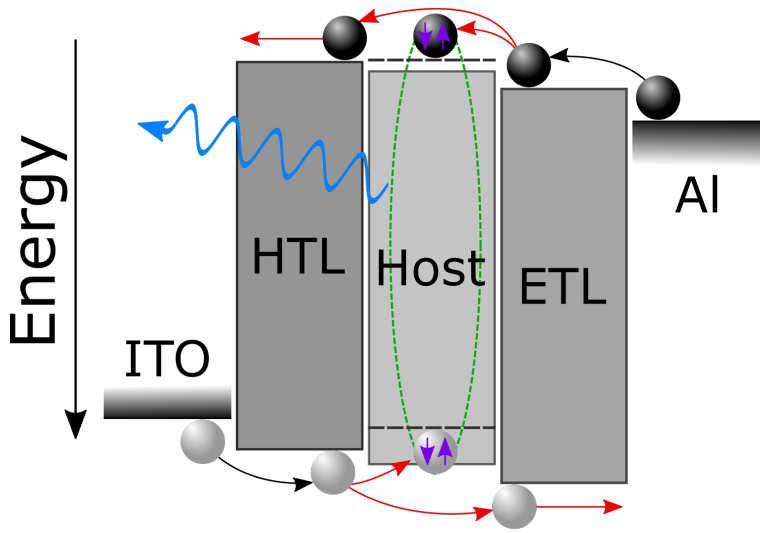

Figure 3.3: External Quantum Efficiency on energy level diagram. η_{OC} represented in blue, η_{PL} in green, χ in purple, and η_{EF} in red.

3.1.1 Efficiency Components

The external quantum efficiency η_{EQE} of a device is the ratio of forward emitted photons per electron injected. Device efficiency is often thought of as a four component process as:[95]

$$\eta_{\mathrm{EQE}} = \chi \eta_{\mathrm{PL}} \ \eta_{\mathrm{EF}} \ \eta_{\mathrm{OC}} \tag{3.1}$$

The efficiency with which injected charges form excitons is the exciton formation efficiency, η_{EF} (also refered to as the charge balance factor,γ). This process competes with charge leakage through the device and is shown in red in Figure 3.3. In efficient devices, η_{EF} can approach 100% at the maximum efficiency point. Electrically, excitons are formed in a 3:1 triplet:singlet ratio, as discussed in Chapter 2.3. The radiative spin fraction, χ, captures the fraction of these formed excitons that are permitted to emit light. For fluorescent materials, $\chi = 1/4$ and for phosphorescent materials, $\chi = 1$. The photoluminescence efficiency, η_{PL} is the efficiency of photon generation from the radiatively allowed excitons and can reach 100% The out-coupling efficiency, η_{OC} , is the fraction of photons that escape the device in the forward viewing direction, and competes with wave-guided modes and surface plasmons.[54,96] For most devices η_{OC} limits efficiency, and typically is limited to 20-30% in bottom emitting devices, but can be aided by enhancing films or layers. A further look at out-coupling is discussed in Chapter E.

3.2 Device Fabrication

Substrates consist of glass pre-coated with indium-tin oxide (ITO). Prior to deposition, substrates are cleaned using 5 minutes each of sonicated Tergitol, water, and two cycles of acetone, followed by two cycles of boiling isopropanol. This is followed by a UV-ozone treatment for 10 minutes. Large area devices on patterned ITO are spin coated with a solution processed hole conducting planarizing layer. In the last 5 years, fabrication in our lab has transitioned from using PEDOT-PSS to the more commercially used Plexcore AQ-1200. PEDOT-PSS is water based and seemed more susceptible to treatment conditions prior to deposition, such as freezing. AQ-1200 has been a more reliable material. AQ-1200 has been replaced with AQ-1250, which appears to be the same formula, but with tighter control over consistency. For all solution processed layers, spin coating is done for 30 seconds at 3000 rpm, followed by a 30 minute bake at 150 °C.

Depostion of organic active layers is carried out by thermal evaporation at base pressures $<10^{-7}$ Torr. This is done in a vacuum deposition chamber from tungsten boat sources for organic materials. Material deposition rates are measured using quartz crystal monitors (QCMs) during deposition. The absolute rate of material deposition is calibrated by ellipsometry on films to determine thickness. Co-deposition of materials allows for the creation of doped layers, which can even be varied with time to create graded composition profiles. For most devices, cathodes consist of 1 nm of lithium fluoride and 100 nm of Aluminum.

For unpatterned devices, the whole substrate is coated in ITO, and device pixels are formed using a metal mask that defines the device area. A hard metal probe is used to contact the ITO by poking through the organic stack. In order to contact the metal, a 100μ gold wire is used to gently contact the metal surface.

Patterned devices, which are necessary for hermetic packaging, consist of a patterned ITO substrate with a corresponding patterned metal mask, where the intersection forms the device area. To ease contacting, an ITO pad is typically placed below the metal at the contact point outside of the organic deposition region as demonstrated in Figure 3.4. This method allows for contacting the device off of the device active area, and does not suffer from the difficulty of contacting and is essential for devices to be encapsulated. In this case, it is important to consider lateral transport within the HIL. A sharp edge on the ITO pattern can result in a discontinuity of the organic stack at the device edges and can frequently short the device with metal directly in contact with the ITO. To prevent this, a planarizing layer is used which minimizes the effects of ITO roughness and the discontinuity of the step edge. While this is effective, planarizing layers are designed to have high

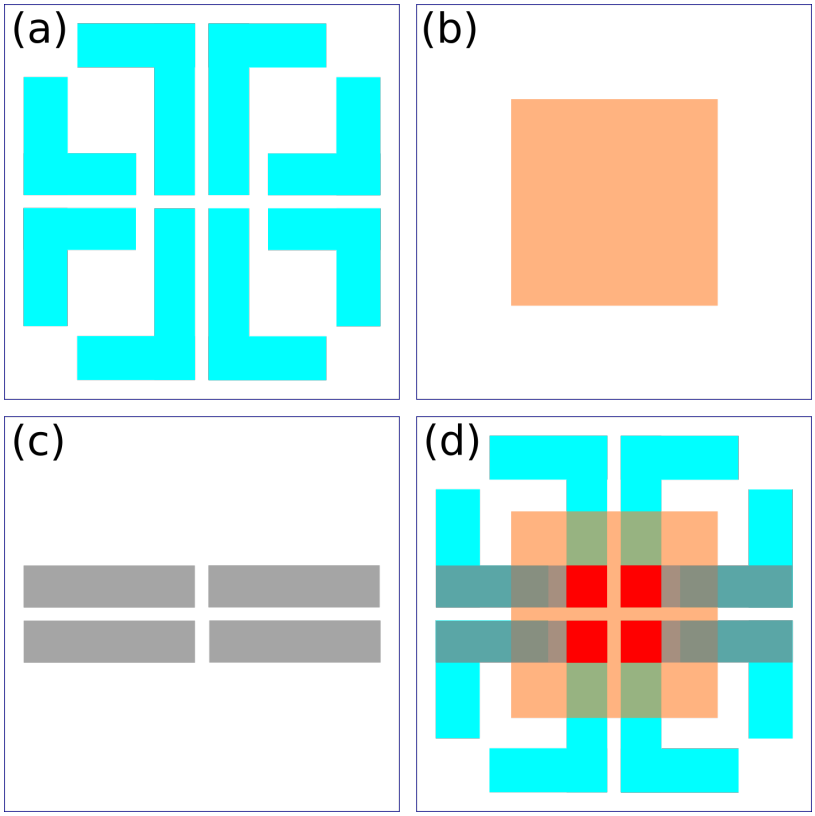

Figure 3.4: (a) ITO Pattern (b) Organic Mask (c) Metal Mask (d) Mask Overlays. Device area shown in red.

mobility and lateral conduction could become important as it may lead to shorting between the anode and cathode ITO pads. To prevent this, the planarizing layer is disturbed between the two pads in order to disrupt lateral transport.

Patterned devices are encapsulated to prevent water and oxygen exposure using a UV cured epoxy seal and a glass microscope slide cover slip. The epoxy is cured with 3 minutes of exposure to a UV lamp. For longer lived devices or higher shelf life, a desiccant can be used, but this is not common in our lab due to the relatively short lifetimes that we are studying.

3.3 Characterization

Though numerous characterizations exist to analyze OLEDs, the standard metrics of performance consist of current-voltage, luminance, and efficiency. Luminance is typically calculated in candelas per meter squared (cd/m^2). There are three common efficiency metrics for devices, including the external quantum efficiency (%), the wall-plug efficiency (W/W) and the luminous power efficiency (lm/W). Though dependent on field of study, for academic OLED interests, the most commonly

explored metric is the external quantum efficiency (η_{EQE}).

3.3.1 Current Voltage and Luminance

The current-voltage behavior of most OLEDs follows a diode-like current-voltage dependence. This is characterized by a weak dependence of current on voltage below some threshold, followed by a strong dependence at high voltage, as shown in Figure 3.5. In terms of device operation, at low voltage below turn-on (Region I), carriers do not have enough energy to make the transitions between molecular orbital energy levels and cannot be injected into the device. The observed current is due charge leakage in through these non-ideal barriers. Soon after turn on, carriers are overcoming the injection barriers of the material stack and in an ideal device, forming a strong recombination current for light emission (Region II). In this region, the current is limited by carrier injection and follows an exponential dependence as carriers overcome the injection barrier potential.[38] At high voltage, injection barriers have been overcome and there is a charge buildup in the device which limits the current. This region is known as the space-charge limit and the current-voltage characteristic shows a power law dependence.[38,43,97] In a well formed device, luminance should closely follow current, as most current should be consumed by exciton recombination.

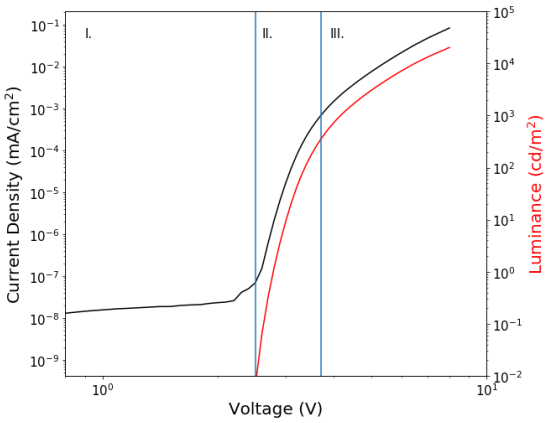

Figure 3.5: a. Device current voltage and luminance voltage behavior

For device brightness characterization, either optical power or luminance can be used. Optical power is simply a characterization of the total photon power exiting a device. This is typically calculated by measuring the total device light output using a large area photodiode. For optical power or optical power density measurements, it is important to know the measured light producing region being measured. This can either be done by ensuring the total device area and all light output is measured, in which case the area of interest is the device area, or by measuring a known subsection of the device. The current output by the detector can be related to the incident optical power by the responsivity function of the detector, reported as a function of wavelength as W/A. A typical responsivity for a silicon detector is shown in Figure 3.6a.

Luminance is reported in candelas per meter squared (cd/m^2), sometimes called a 'nit'. The candela is a measure of perceived light intensity per solid angle and is equivalent to 1 candle power. To

measure luminance, the light output must be normalized to the wavelength dependent response of the human eye, known as the photopic response, shown in Figure 3.6b. This is typically done in one of two ways. The first method (employed by our group) is to use a spectrometer to measure the output light spectrum in Watts per nanometer. Then the spectrally averaged photopic response can be found for the light source of interest. Then, the output optical power can be measured by a simple photodiode and calibrated using the average photopic response. Alternatively, three wavelength selective diodes can be used that mimick three types of cones in the eye can be used to calculate the X,Y,Z coordinates in a CIE color space (discussed in Section 3.3.3, and the corresponding photopic response can be looked up.

In this case, the photodiode would directly output the luminance. Both methods are standardly used in research groups.[68,84,98]

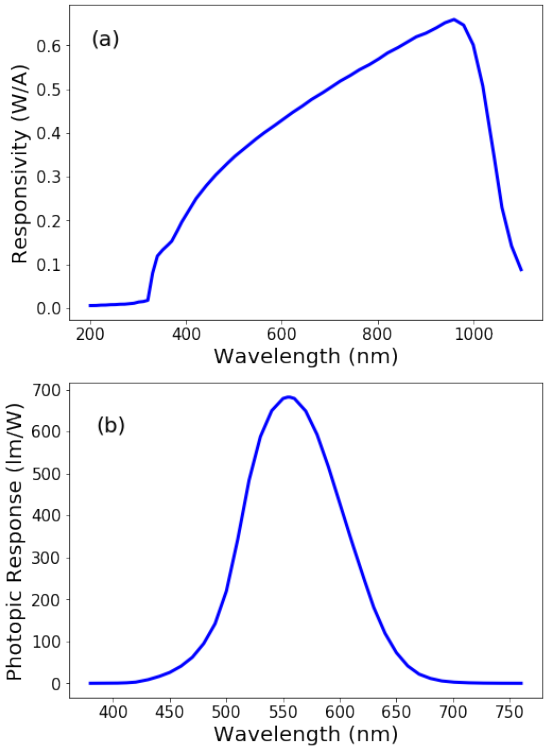

Figure 3.6: (a) Silicon detector responsivity (b) Photopic response

3.3.2 Efficiency

As mentioned previously, there are three common measures of device efficiency. The first is power efficiency, measured in W/W. This is straightforward to calculate given the previous discussion of measuring optical power. The luminance efficiency lm/w is related to the luminance output. The lumen is a measure of total light output and is related to the candela by 1 lm = π candelas. A keen eye would note that the candela is normalized per solid angle and a factor of 4π may be expected, but OLEDs are only able to emit in the forward direction and have a lambertion emission shape, resulting in this reduction.

The external quantum efficiency (η_{EQE}) is a measure of photons exiting the device per electron injected. The photon flux out of the device can be calculated from the optical power by dividing by the average photon power, hf_{avg}, where f_{avg} can be calculated from the measured spectrum. The injected electron flux is simply I/q where I is the device current. The mathematical details of this

model are discussed in detail by Forrest et al. [98].

3.3.3 Chromaticity

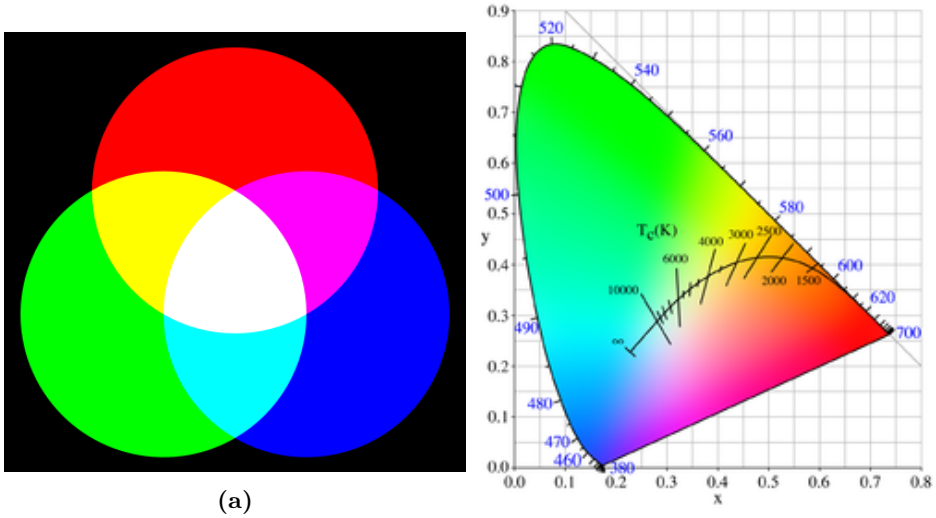

Figure 3.7: (a) Simple color addition diagram. (b) 1931 CIE xyY color space.

In addition to the efficiency and brightness characterization, the quality of light can also be assessed, known as chromaticity. This is very important for both displays and lighting applications. This characterization is standardly done using the CIE chromaticity diagram and xyY color space.[99–101]

The chromaticity of an emitter is defined to reflect the sensitivity of the human eye. In the eye, there are two color sensing cones, roughly corresponding to red, green, and blue. The wavelength sensitivity of these cones for red, green, and blue are defined as $\bar{x}(\lambda)$,$\bar{y}(\lambda)$, and $\bar{z}(\lambda)$, respectively. A three dimensional color-space is then defined to define any color using

$$A = \int_{\lambda} L_{e,\Omega,\lambda}(\lambda)\bar{a}(\lambda)d\lambda \tag{3.2}$$

where A and $\bar{a}$ are X, Y, Z and $\bar{x}, \bar{y}, \bar{z}$. These three dimensional coordinates are able to accurately describe the light, but are not very useful for visualizing the color-space. Therefore, the brightness is normalized out, leaving us with two color coordinates and a brightness value. Since our eye is most sensitive to green stimulus, the Y coordinate is taken to represent the brightness. The color coordinates can be normalized by

$$a = \frac{A}{X + Y + Z} \tag{3.3}$$

where a and A are x, y, z and X, Y, Z. Note that x is a new color coordinate, not the standard observer sensitivity, $\bar{x}$. This remapping still has three coordinates, but here, $z = 1-x-y$. Therefore, the color can be represented using just x, y. This can be seen in Figure 3.7b, where the perimeter is defined by mapping single wavelength light through these coordinate transformations. All possible visible colors are defined within the locus, and x, y coordinates are shown on the axes. For white light, the color temperature is calculated in reference to a black-body emission and is also shown in Figure 3.7b. While sophisticated in calculation, it is important to note that this concept of color-space is simply an extension of the color addition shown in Figure 3.7a. For displays, CIE color coordinates are the standard for evaluating colors, but in white lighting applications, the color rendering index (CRI) is used. The CRI is a calculation of the ability of a light source to reproduce the observed color of an object when compared with natural light.

3.3.3.1 RGB

For display applications, a single red, green and blue emitter are used, each of which will have x, y coordinates which can be expressed on the CIE diagram. Using this method, only colors within the enclosed triangle can be expressed, making it critical for a vibrant display to maximize the area of this triangle. Various phone displays are shown in Figure 3.8, with the pure color components being generated using a RGB color picker application. Interestingly, the iPhone SE, the only phone not using an OLED display, shows the worst response in the green, a clear advantage of OLED color representation. The scatter points in this figure represent individual pixels measured in the course of this thesis.

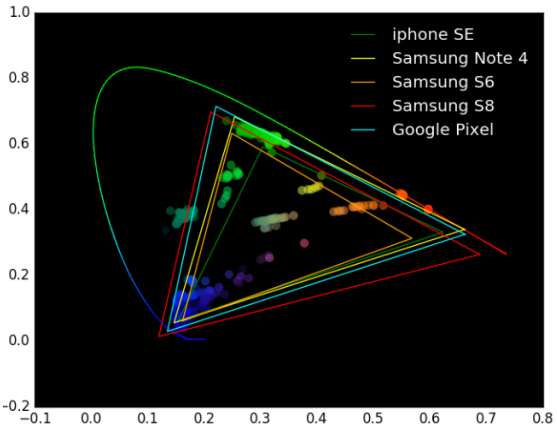

Figure 3.8: Various phone display limits shown on CIE coordinates. Each point shown is the CIE coordinates of devices grown during this thesis work.

One limit of RGB color representation is that it is not consistent across displays. For example, the RGB coordinate (0,1,0) looks different on the Google Pixel versus the iPhone SE due to their different CIE coordinates. To account for this, display RGB values can be calibrated to accurately represent the CIE coordinates. However, in doing so, the color space available to the display is shrunk and the full color range of the display cannot be used. This is an important issue in commercial devices where consumer demands must be carefully considered with respect to the trade off between accurate and vibrant colors. This trade off was clearly seen in the release of the Google Pixel 2,

where consumers complained about dull colors because the manufacturers used a calibrated color space.[102]

3.4 Historical Development

3.4.1 The First OLEDs

Early interest in organic materials was generated based on use for pigments and organic laser dyes with demonstrated high fluorescence efficiency.[104–106] Early attempts at producing electroluminescent devices involved the use of thick organic crystals, but required extremely high voltages to produce any light.[107,108] The first successful OLED was demonstrated by Tang and VanSlyke [103] in 1987, one of the first to utilize vacuum deposition for thin films. This was a bilayer device, with the structure shown in Figure 3.9, using 4,4'-Cyclohexylidenebis[N,N-bis(4-methylphenyl)benzenamine] (TAPC) at 75 nm thick and Tris(8-hydroxyquinolinato)aluminum (Alq_3) 60 nm, responsible for the emission of the device, centered at a wavelength of 550 nm. These devices achieved η_{EQE} ≈1% and showed rapid degradation.

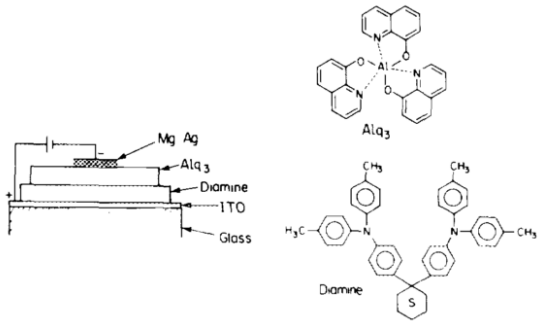

Figure 3.9: Structure of the first OLED cell from Tang and VanSlyke [103]. Diamine is commonly referred to now as TAPC.

In fluorescent cells, $\chi = 0.25$ and without out-coupling enhancement $\eta_{\mathrm{OC}} \approx 0.20$, leaving a maximum η_{EQE} of just 5%, as discussed in Sectio 3.3.2. Doped films were investigated soon after these initial findings in order to capitalize on the improved η_{PL} at low concentration.[109] This host with emissive guest system is utilized by almost all devices.

3.4.2 Phosphorescence

OLEDs saw a massive improvement in efficiency in 1998 with the introduction of phosphorescent dyes.[95] These dyes use a heavy metal atom to create a metal-ligand charge transfer state, which allows mixing of the singlet and triplet states, as well as a coupling between the triplet and the singlet ground state, and thus emission from the triplet exciton. With all excitons able to emit, including the triplet state, the internal quantum efficiency (η_{IQE}) can be increased to 100%. Initial demonstrations utilized the red phosphor PtOEP. This work comments on quenching at high current of the phosphor,

a continuing problem which will be discussed further in Section 3.5.[46,84] Pure red and green emission devices utilizing only a phosphorescent dopant were developed soon after, along with the development of the ubiquitous green emitter, Tris[2-phenylpyridinato-C^2,N]iridium(III) ($Ir(ppy)_3$).Many of these molecules, including $Ir(ppy)_3$ had been well known for almost two decades,[110,111] but had yet to be incorporated into devices.

Since the realization of the phosphorescent OLED, internal quantum efficiencies nearing 100% for green, red, blue, and white devices have been demonstrated.[112,113] With high efficiency achieved, attention has shifted to maximizing operational lifetimes.[114] Despite the high efficiency of blue phosphorescent devices, lifetimes still remain limiting and blue fluorescent materials are still used in commercial technologies.

3.4.3 Thermally Activated Delayed Fluorescence

While phosphorescent devices have been able to demonstrate the high efficiency necessary for commercialization, this has come at a cost. Namely, in the use of expensive and rare heavy metal atoms, such as Ir(III), Pt(III), and Os(II).[115] In order to utilize the triplet excitons without mixing the singlet and triplet states as is done for MLCT molecules, reverse intersystem crossing is utilized. Chapter 2.3 and Figure 2.4 discuss intersystem crossing as an energetically favorable process as the triplet is lower energy than the singlet. However, if molecules are designed where the singlet and triplet energies difference (ΔE_{ST}) is small ($< 1eV$), thermal energy can make the reverse intersystem crossing competitive with intersystem crossing ($k_{RISC} \approx k_{ISC}$). This allows for Thermally Activated Delayed Fluorescence (TADF), shown in Figure 3.10.[57,73,116] TADF materials are a rapidly developing technology that has shown many benefits for efficiency, and rules are being established for molecular design.[57,68–73,75,116–125] These materials are also being investigated for benefits to device lifetime.[59,126]

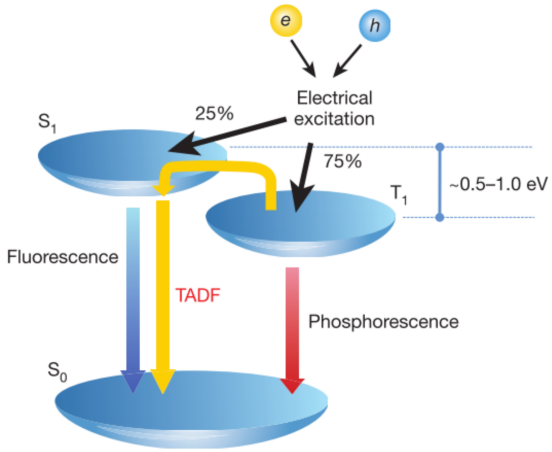

Figure 3.10: Reverse intersystem crossing for TADF materials. Figure taken from Uoyama et al. [73].

3.5 Efficiency Roll-Off

In high efficiency OLEDs, it is almost universally observed that efficiency reduces at high brightness and current density, a phenomenon known as the efficiency roll-off,demonstrated in Figure 3.11.[46,49,53,58,84,120,127–138] This has been extensively studied and largely attributed to the bimolecular quenching processes discussed in Chapter 2.3, though exciton formation efficiency (η_{EF}) is also known to contribute.[84] This is detrimental to commercialization as high brightness is a necessity for display and lighting applications. The bimolecular quenching at high brightness is also detrimental to device lifetime because quenching processes produce hot excited states that release excess energy into the device, which is thought to be a key factor in molecular degradation.[83,139,140] Development of electrically pumped organic lasers has proved unsuccessful because the exciton densities required frustrates the realization of population inversion.[55,95,141–144]

Section 3.1 discussed the characterization of quantum efficiency using a four component efficiency model. This model fails to reproduce the roll-off behavior as it does not account for quenching. Modeling the efficiency roll-off has been the study of numerous works and is the motivation for Chapter 4.[46,53,84,129] These models center around a differential equations for exciton dynamics, such as:

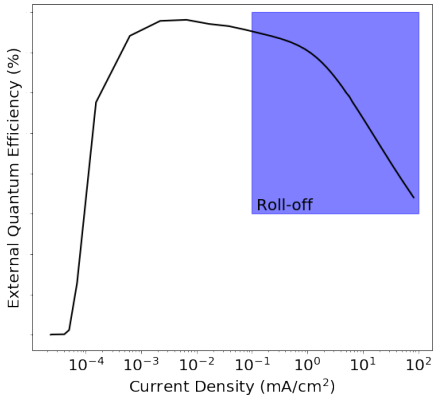

Figure 3.11: Efficiency as a function of current density, with significant roll-off shown above 10^{-1}mA/cm^2, highlighted in blue.

$$\frac{dN_{ex}}{dt} = -\frac{N_{ex}}{\tau} - \frac{1}{2}k_{\text{TT}}\ N_{ex}^2 - k_{\text{TP}}\ N_{pol}N_{ex} + G_{ex} \quad (3.4)$$

where N_{ex} is the exciton population density, τ is the exciton lifetime, k_{TT} is the triplet-triplet annihilation rate constant, k_{TP} is the triplet-polaron quenching rate constant, N_{pol} is the charge density, and G_{ex} is the exciton generation rate. Here we can see that the natural lifetime is competitive with the bimolecular quenching rates, and at high exciton and charge density, the second order dependence of the quenching terms allows them to dominate. This reduces the relative number of excitons that are decaying via the radiative rate, thus decreasing the efficiency. These models have been successful in characterizing the rate constants and describing the roll-off behavior. For further details, see Chapter 4.

Devices are often designed to reduce the roll-off, often through the broadening of the exciton recombination zone.[68,112,117,145–150] These devices have successfully reduced the exciton density and

hence the roll-off, shifting the onset of roll-off to higher brightness.

3.6 Recombination Zone Characterization

Both degradation and bimolecular quenching can be highly dependent on the exciton density and location, known as the exciton recombination zone (RZ).[46,83,84,130,151–154] Therefore, it is important to be able to characterize the spatial profile of excitons. Frequently this measurement is carried out using thin doping layers of a sensitizer molecule.[138,139,148,153–155]

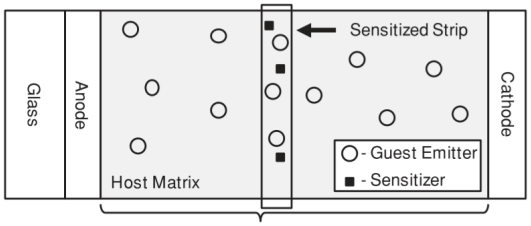

Figure 3.12: Device architecture for the measurement of the exciton recombination zone. The curly brace indicates the device stack. Figure taken from Erickson and Holmes [138]

In these experiments, a dopant is used to efficiently siphon excitons from the emitter molecule. In order to do this, Förster transfer to the sensitizer must be efficient, requiring significant overlap of the emitter emission and the sensitizer absorption, but must also be spatially confined. Sensitized layers are used to locally perturb the exciton density present on the emitter. Translating the sensitized strip across the device as shown in Figure 3.12 allows for comparison of the relative density change and thus determination of the relative magnitude of the recombination zone. The Förster radius defines the spatial resolution that can be obtained using this technique.

Two types of sensitizers are frequently used: quenching and emissive. A quenching (non-radiative) or emissive (radiative) sensitizer can be used for these experiments. With a quenching sensitizer, if the recombination zone overlaps with the sensitizer position, emission is lost and the efficiency is reduced. The reduction in EL intensity can be quantified by the EL ratio of the sensitized intensity compared to the unsensitized intensity, β. β is directly proportional to the unquenched excitons, therefore $1 - \beta$ gives the ratio of quenched excitons.

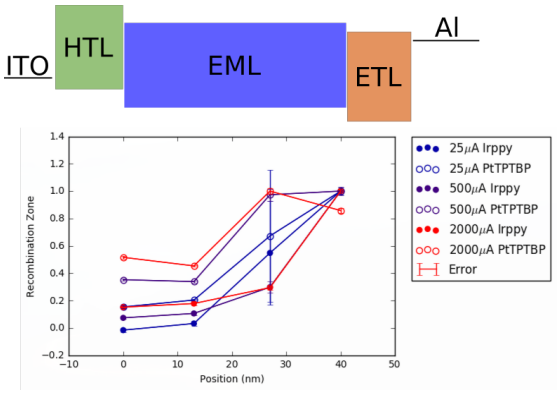

Figure 3.13: (Top) Device Architecture. (Bottom) Recombination zone comparison for an emissive sensitizer analyzed using the quenched ratio (Irppy) and the emitted ratio (PtTPTBP) as a function of current density.

For emissive sensitizers, given the requirement of emission-absorption overlap, red sensitizers are used. For simplicity, the sensitizer should show spectral separation of the emission from the emitter.

The intensity of the sensitizer emission is a direct measure of the local exciton density. However, since the out-coupling is so strongly dependent on emitter position in the EML, it is essential to correct the intensity using a calculation of η_{OC} , discussed in Chapter E. Emissive sensitizers often rely on the use of Pt(II) complexes, such as PtOEP or PtTPTBP.[153,155] Compared with Ir(III) complexes, Pt(II) shows a much longer exciton lifetime, and is therefore far more susceptible to bimolecular quenching.[135] If the sensitizer is in a regime of bimolecular quenching during the measurement, a compressed version of the recombination zone will be measured. This can be difficult to avoid at high current densities that may be of interest for measurement.

An advantage of the emissive sensitizer is that the data generated can be analyzed either using the quenched ratio or using the emitted intensity. This can be helpful for quantifying error in the method, and is demonstrated in Figure 3.13. Here, we see the spatial dependence of the recombination zone for an architecture peaked at the ETL interface. Notice that the emissive sensitizer, PtTPTBP shows a less exaggerated RZ for all current densities. This is likely due to bimolecular quenching on the sensitizer, which is stronger at the higher exciton densities present at the ETL interface.

When constructing these sensitizer layers, there are two common methods. First, the EML can be reproduced exactly with the addition of a light doping of the sensitizer. This creates a strip that matches the composition of the EML, but increases the difficulty of the growth, requiring one more material in a co-deposition. An alternative is to use an extremely thin deposition of the sensitizer molecule in isolation, known as delta doping. A deposition of 1 Å is used, which is in reality, a discontinuous layer. When the EML is continued on top of this discontinuous layer, this is equivalent to an extremely narrow strip of a mixed layer. This is advantageous because it make the deposition much easier and creates a very narrow strip. However, it can be difficult to control the dopant dose as it is difficult to accurately measure films this thin. No quantification of error on these types of doping have been reported.

In order to accurately compare the recombination zone intensity, it is essential to ensure that no differences in the transport and injection properties occur with the introduction of the sensitizer. Since the sensitizer molecules will likely result in a trap state, it is essential to keep doping concentrations low, on the order of 1%. Evidence of minimal interference on the electrical properties by the sensitizer is provided by the current-voltage behavior. If the current-voltage characteristic is within error between all of the sensitizer devices, it is often assumed that the device is representative of the control.[138]

3.7 Single-Carrier Type Devices

When investigating device behavior, it is often important to isolate the behavior of a single charge carrier type.[46,156,157] To do this, devices are created that allow passage of only one carrier type. This can be accomplished by establishing energetic barriers for the opposing charge, prohibiting injection, or mobility imbalance. Examples of hole and electron only devices are shown in Figures

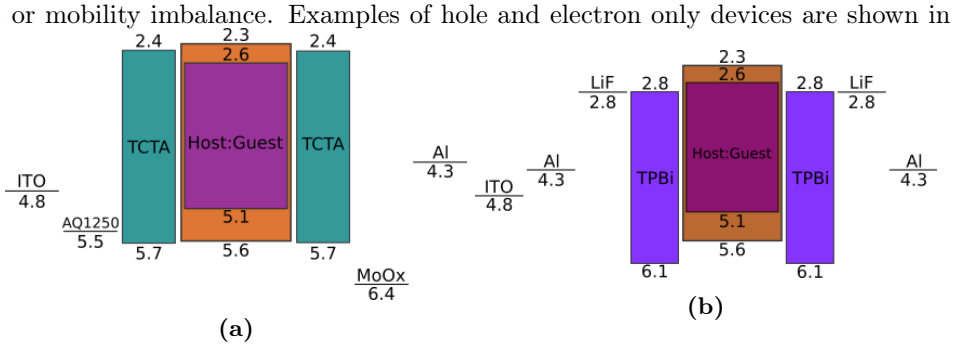

Figure 3.14: Energy level diagrams for: (a) Hole only device. (b) Electron only device.

3.14a and 3.14b. In Figure 3.14a, MoO_x provides a deep energy barrier for electron injection. Additionally, TCTA is used, which has a high hole mobility and lower electron mobility, along with well aligned HOMO levels, encouraging hole injection and transport. In this device, positive bias is applied to the ITO contact, for no particular reason other than tradition and that it works well. An alternative method for producing hole only devices uses a Au cathode instead of MoO_x, and provides a similar barrier for electrons. However, it can be difficult to achieve a uniform Au layer, and host shown more reliable to use MoO_x. In Figure 3.14b, the ITO contact does not facilitate electron injection. Therefore, A thin layer of aluminum is doped on top of the ITO, along with LiF, which adjusts the interface energy to more align with electrons and block holes. TPBi is used to provide a transport barrier for holes and facilitate electrons. The same LiF-Al contact is used to promote electron injection. In this device, improved current-voltage characteristics are seen with positive bias applied to the ITO, in my experience. This may be due to the properties of LiF at the ITO side interface, since in the experiments using this structure, a vacuum break occurred at that interface with LiF exposed. We have not investigated the differences in manufacturing techniques to explore this further.

Single carrier devices have been heavily investigated and modeled for their polaron and current-voltage behavior.[38,43,97] This can be used to help in analyzing these devices for dynamics and comparison to full device behavior, discussed further in Chapters 4 and 6.

3.8 Operational Lifetime

In typical lifetime characterization, devices are degraded while held at constant current density, recording the resulting luminance loss and voltage gain as a function of time. The lifetime is then reported as the time to reach some arbitrary fraction of the initial luminance.

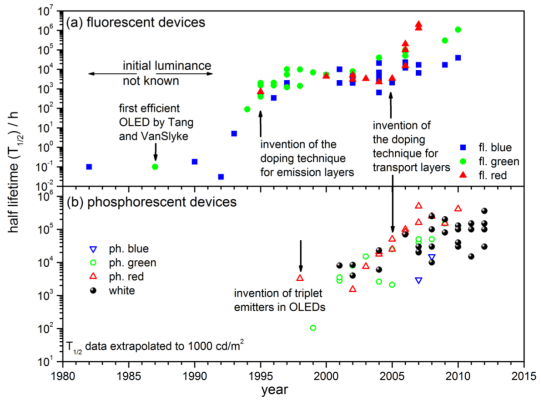

Figure 3.15: Peak reported lifetimes for fluorescent and phosphorescent devices as a function of color and time. Figure reproduced from Scholz et al. [93].

3.8.1 Degradation Mechanisms

Degradation is an ongoing area of research and is not fully understood. However, this section seeks to outline the dominant mechanisms observed in typical devices. In the most empirical case, the degradation of an OLED can be considered wholistically as a stretched exponential curve.[93,158]

$$\frac{L(t)}{L_0} = \exp(t/\tau)^{\beta} \tag{3.5}$$

This approach is able to reproduce the decay behavior relatively well and the scaling with luminance, describing the decay by attributing behavior to emissive centers.

To delve deeper, individual degradation pathways must be investigated. These are typically separated into external and internal mechanisms.[93] External mechanisms are due to influences outside of the active materials impacting the device behavior, and are typically easy to identify, though mitigating is still a challenge, especially in long lived and large area commercial devices.[159] Internal or intrinsic degradation mechanisms are due to physical and chemical processes within the device. These processes can be significantly more difficult to investigate and various analytical techniques are often used to observe this behavior, as discussed in Section 3.8.3. Scholz et al. [93] goes into extensive discussion of observed degradation methods. For the purposes of this discussion, physical degradation pathways, rather than chemical degradation mechanisms will be discussed. This type of analysis identifies sensitivity within the device to various influences and can potentially identify the rate limiting molecules, but does not show the degradation chemistry. The following sections seek to identify the most widely observed degradation mechanisms.

3.8.1.1 External: Dark Spots and Delamination

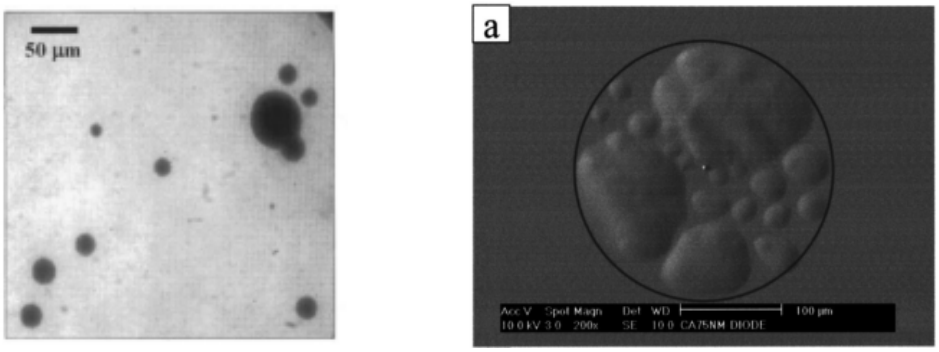

(a) **(b)**

Figure 3.16: (a) Dark spots in photoluminescence on an active device area, taken from Kolosov et al. [160]. (b) Cathode bubbling where delamination has occurred under SEM, as shown in Wang et al. [161]

One of the most widely observed and characterized degradation phenomena is the formation of dark spots.[162–165] This has been long attributed to delamination of the cathode, assisted by water and oxygen contamination or pinholes in the cathode.[160,161,165–167] Around an impurity under the cathode, a hot spot, or a cathode pinhole, the metal starts to delaminate from the underlying organic stack, forming a bubble.[167–169] The field distribution around these dark spots creates high current around the edges, creating local high brightness regions. This causes the dark spot to grow at an accelerated rate, further accelerating degradation.[168–170]

Despite the long history and understood mechanism, dark spots continue to be a major problem in manufacturing of large area lighting panels.[159] The methods for preventing dark spots are largely understood, though control can be difficult. It has been found that carefully controlling vacuum levels along with oxygen and moisture exposure during manufacture helps to prevent dark spot formation from oxygen and moisture under the cathode. After manufacturing, oxygen and moisture can still get into the device through pinholes in the cathode, but this can be mitigated by careful packaging under a nitrogen environment. For long lived devices, the addition of a moisture desiccant within the packaging further decreases dark spot formation.[171]

3.8.1.2 Exciton and Polaron Density

Most degradation mechanisms within a device are facilitated by the exciton and polaron population.[83,93,152,154,172,173] These excited particles within the device provide the excess energy that is responsible for breaking bonds and facilitating the chemical processes that cause molecular degradation. Reducing the exciton density by expanding the exciton recombination zone has been shown to extend lifetime.[154,171,174–182] Despite this knowledge, high exciton densities are still often needed

due to the high brightness of devices, which can not be fully counteracted by continuing to extend the recombination zone. In addition, it is often suggested that current is not uniform and typically confined to narrow pathways through the device.[183] This causes locally high exciton and polaron densities, even with well designed injection and transport for a wide RZ.

3.8.1.3 Interfaces

Some devices have shown sensitivity to charges and excitons at material interfaces within devices.[52,84] Through single carrier device investigation, some materials have been shown to be sensitive to conduction of one type of carrier.[184] In other cases, a buildup of charge or exciton density can occur at an interface, greatly increasing the local degradation rate.[185,186] This type of degradation can result in the formation of Non-Radiative Recombination Centers (NRRCs).[185,187–189] NRRCs are sites, typically of degraded molecules, that are able to recombine electrons and holes through a non-radiative dark state. The higher density of trapped charge at an interface can lead to formation of exciplex and transport layer excitons at the interface.[52] Transport layer excitons can be detrimental to device behavior due to their UV energies, especially when combined with polarons, leading to bimolecular quenching and hot excitons that can be more damaging than the presence of excitons or polarons on their own.[140]

Interfacial degradation is also an exciton and polaron driven process, but bares the critical distinction of sensitivity to location. In materials with known interface and single carrier sensitivity, it is important to engineer the exciton profile away from these interfaces to extend lifetime, as shown in my work, Hershey and Holmes [84], discussed in Chapter 6. This is contrary to the typical thought that only a broad recombination zone is important, discussed in the previous section. Some devices even show sensitivity to both exciton density and recombination zone position, again, discussed in Chapter 6.

3.8.2 Luminance Scaling

For commercially relevant devices, where the time to reach 50% of the initial luminance, t_{50} can be tens of thousands of hours, it is impractical to test devices under their intended operating conditions. Instead, lifetime testing can be done at an increased luminance from the true operating condition.[93] This can dramatically reduce the testing time of devices. The lifetime at other luminances can then be found using the scaling relation

$$L_0^n t_x = C \tag{3.6}$$

where L_0 is the initial luminance, n is a scaling factor characteristic to the device, and C is a constant. To utilize this relation, several lifetimes are obtained at luminances above the operating condition in order to experimentally obtain a value for n. Subsequently, the lifetime of interest can then be extrapolated.

While widely used and observed, caution should be observed in the application of this relation. A variety of degradation mechanisms have been attributed to OLED behavior, as discussed in Section 3.8.1. All of these mechanisms are subject to different temporal dependences and have a variety of degrees of understanding to their functional dependence on time and luminance. At different luminances, different mechanisms may be dominant. For example, first order excitonic processes may dominate at low luminance, but may be overtaken by a bimolecular process at high luminance. The fact that OLEDs are frequently subject to several degradation mechanisms throughout the decay only further complicates the issue. The very idea of a scaling law for all devices and at all current densities is unsound, and should be treated as a loose prediction. Over and underestimates of lifetimes using this relation are observed when trying to predict actual lifetimes.[190,191]

3.8.3 Analysis Techniques

To expand on the luminance as a function of time, various analytical techniques are used to illuminate the degradation mechanisms. These can largely be divided into chemical analysis, modeling, and spectral characterization. These techniques offer valuable and unique insight, and are often used in combination for degradation analysis.

3.8.3.1 Chemical Analysis

Perhaps the most obvious approach is to look directly at the chemical composition of degradation products and use this to inform on which molecules are degrading. A standard approach for doing this is Laser desorption/ionization time-of-flight mass spectroscopy (LDI-TOF-MS).[192–194] With this technique, a laser is used to ionize the sample material, and time-of-flight is used to characterize the molecular weight to charge ratio. An example of this data can be seen in Figure 3.17, taken from Seifert et al. [192]. Here, unaged and aged samples are compared and peaks from known source material are identified. Differences that are seen are attributed to degradation, and can be compared to the expected spectra of proposed degradation products. In this case, a BPhen and FIr6

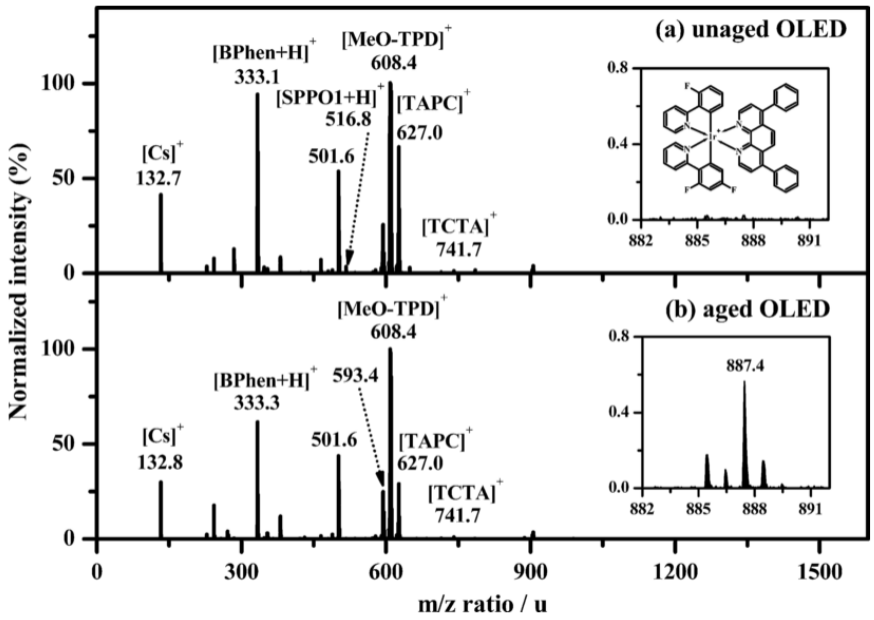

Figure 3.17: Mass spectroscopy data taken from Seifert et al. [192]

molecule have combined to form a new molecule. It is important to note that despite degradation to 15% of the initial luminance, the molecular signatures of degradation products are extremely weak, as seen by the scale on the inset in Figure 3.17. This is a common problem for chemical techniques. In devices, the active material stack is only a few monolayers thick and small amounts of degradation product can have a large impact. Given the extremely low concentration and limited sample material, it can be difficult to do chemical analysis. Even at heavy degradation, if several degradation products are present, none may be in high enough concentration to be observed. Despite this drawback, observed degradation products can usually be attributed to an individual molecule.

High performance liquid chromatography (HPLC) can also be used to view degradation products.[189,195] In HPLC, sample products are dissolved in a solution and filtered through a distillation column. Components can be categorized based on their transit time through the column. This technique offers similar results, but suffers from several drawbacks, namely that it can be difficult to dissolve all of the materials in a devices, and that identification of compounds requires a pure sample of the degradation product to serve as a calibration for the column.

Despite the direct interpretation of results, chemical techniques do have several drawbacks. First of all, these processes can be expensive and time consuming to perform, making it difficult to apply to large scale optimization of devices. In addition, it does not provide any temporal resolution on a single device, since this is an entirely destructive technique. This makes it difficult to understand any kinetics.

3.8.3.2 Modeling

Modeling efforts have been used to try to understand the functional dependence of exciton density dependence and attribute this to a material dependent rate constant.[83,139,155,196] All of these works model the exciton population as a function of time using the equation:

$$\frac{dN_{ex}(x,t,t')}{dt} = \gamma n(x,t,t')p(x,t,t') - \frac{N_{ex}(x.t.t')}{\tau} - K_{DR}Q(x,t')N(x,t,t') \tag{3.7}$$

where N_{ex} is the exciton density, n, p are the electron,hole densities, γ is the Langevin recombination rate, τ is the exciton lifetime, K_{DR} is the defect quenching rate, and Q is the defect concentration. In this model, t is the short term dynamics, while t' represents the degradation scale evolution of parameters. The electron and hole populations are fixed to form a predetermined recombination zone shape. The generated defects serve as first order quenchers to the exciton population, as well as trap states that modify the recombination zone along with charge densities.

$$\frac{dQ(x,t')}{dt'} = \begin{cases} K_X n(x,t'), & K_X p(x,t') \\ K_X N(x,t') & \\ K_X N^2(x,t') & \\ K_X N(x,t')n(x,t'), & K_X N(x,t')p(x,t') \end{cases} \tag{3.8}$$

Applying this model for each of these mechanisms independently, then comparing the fitted results should indicate the dominant defect generation process. Giebink et al. [83] find for their device that exciton-polaron processes are dominant, though this is likely system dependent. This model allows fitting of luminance and voltage behavior as a function of time and luminance, which are shown to be consistent. However, this model has a large number of rate constants that cannot be measured independently, and is largely over-parameterized. Caution must be taken with these results as they do not suggest a unique explanation of the physics happening in the device.

3.8.3.3 Spectral Characterization

The electroluminescence spectra can also provide a large amount of information about the degradation state.[93] This is typically done in two methods: intentional emission and observation of weakly emissive states. Weakly emissive states and host emission have been used to characterize aggregation within the host and guest molecules.[172,197–199] Within these studies, emission from the phosphorescent guest is characterized as a function of time, but careful inspection reveals weak emission from the host, as seen in Figure 3.18.[172] In this figure, the weak CBP emission can be seen in the shoulder

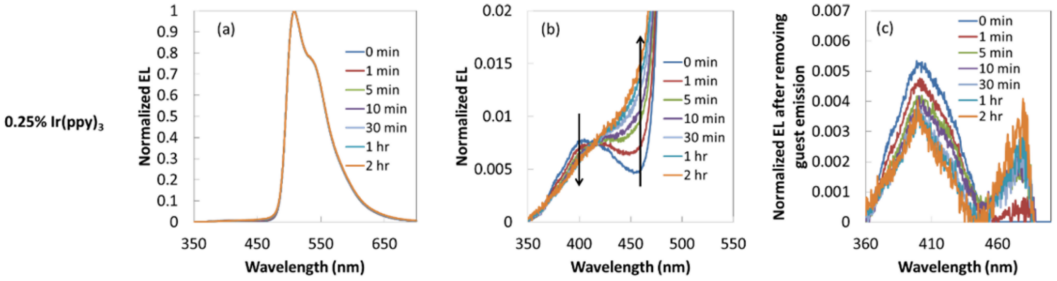

Figure 3.18: Emission from $Ir(ppy)_3$ and CBP, as reported by Zhang and Aziz [172] (a) All emission, (b) Emission shoulder, showing CBP emission, (c) CBP emission with $Ir(ppy)_3$ background subtracted.

of the guest emission, and the losses during degradation characterized. This study finds that host molecules are aggregating due to exciton and positive polaron interactions, accelerating degradation.

Another use of this technique is to track changes in the exciton recombination zone. This has been used in simplified bilayer devices where changes in relative peak intensities between two emissive species can indicate a shift of the RZ from one side of the device to the other.[199,200] This type of spectral characterization provides the temporal behavior of degradation that chemical analysis is lacking, but does not relate to physical processes within the device quantitatively, at least directly. In fact, the understanding of physical mechanisms from the spectral changes can be far from straight forward.

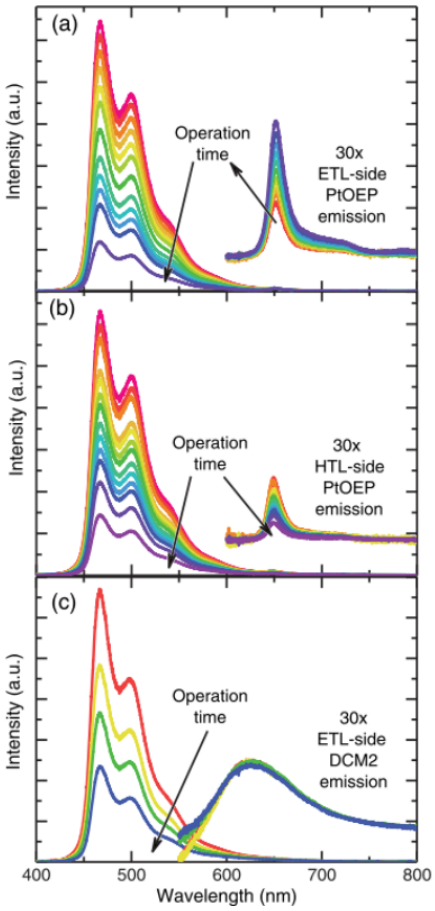

Figure 3.19: Device emission spectra containing (a) PtOEP sensitizer on the ETL side of the device, (b) PtOEP sensitizer on the HTL side of the device, (c) DCM2 sensitizer on the ETL side of the device. Reproduced from Coburn and Forrest [139]

Spectral characterization has been used recently as an extension of a modeling approach by Coburn and Forrest [139]. In this study, characterization of the exciton confinement within the emissive layer is desired. To study this, sensitizer doping layers are used outside of the emissive layer to probe for exciton leakage, using the red phosphor PtOEP, with emission shown in Figure 3.19. Using PtOEP, weak emission is seen in both cases, but is shown to increase in magnitude on the ETL side during degra-

dation. This could indicate a decrease in exciton confinement, but would also be the case if holes were more efficiently leaking through the device. To rule out hole leakage, a fluorescent dopant is used, which would not be able to receive diffusing triplet excitons. Using DCM2, a fluorescent dopant, no increase in emission is seen, indicating that exciton confinement, not hole leakage, is responsible for this behavior. This approach of using modeling in combination with a spectral technique is very promising at providing both more information to aid in modeling, and a more physical understanding to the spectral techniques.

3.9 Conclusion

In this chapter, the state of the field of OLEDs has been discussed with regards to device fabrication and design, as well as evaluation of performance and characterization of degradation. Efforts are still needed in improving the understanding of the efficiency roll-off discussed in Section 3.5, as well as operational lifetime degradation, discussed in Section 3.8.1.2.

In this thesis, these topics will be further explored. Chapter 4 works on using dynamics modeling in the transient and steady-state to better understand and quantify charge and exciton kinetics. Chapters 5 and 6 explore a technique to further dissect the operational lifetime.

Chapter 4

Transient and Steady-State Dynamics of Charges and Excitons in OLEDs

This section is an extension of published work entitled "*Unified analysis of transient and steady-state electrophosphorescence using exciton and polaron dynamics modeling*".[84]

4.1 Motivation

As discussed in Chapter 3, modern OLEDs typically use phosphorescent emitters in order to realize 100% internal efficiencies.[94,95,201,202] However, these phosphorescent emitters, while allowing emission out of the triplet excitonic state, also suffer from the drawback of a longer exciton lifetime, typically on the order of 10^{-6}-10^{-3} s.[61,95] An increased lifetime leads to a larger steady-state triplet exciton density compared to a fluorescent device operating at the same luminance. This becomes problematic at the high current densities associated with high brightness due to well documented quenching events.[46,53,131,134,135,148,203] These quenching events lead to a reduced quantum efficiency at high-current, and termed the "Efficiency roll-off", discussed in Chapter 3.5.

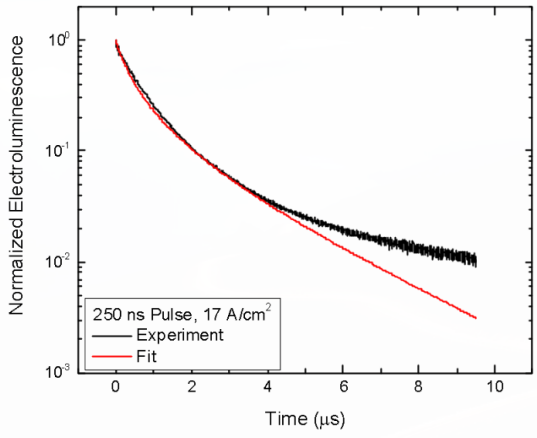

Figure 4.1: Fitting the transient electroluminescence decay without polaron dynamics.

Efficiency roll-off is well attributed to quenching and is ubiquitous to phosphorescent OLED behavior.[46,53,129,130] While previous works have attributed the roll-off to quenching, they have failed to provide a complete picture of the exciton and charge dynamics within the device. All of these works have utilized a differential equations model for the exciton dynamics, solved in the steady state. This becomes apparent when investigating the transient electroluminescence (EL), where a transient voltage pulse, on the order of 500 ns is applied to the device and the resulting luminance is recorded as a function of time. Figure 4.1 is an attempt to fit the transient luminance decay using the model presented by Reineke *et al.*[46] which reproduces the efficiency roll-off. Indeed, this is a well known problem with existing models, and previous attempts to model the transient EL have utilized an empirical biexponential function to quantify the decay.[53,130,136,204] In addition to failing to replicate the luminance decay, no known previous efforts have been made in trying to replicate the experimental transient EL luminance rise. Another problem with this model is that it only replicates the normalized efficiency roll-off, rather than the absolute magnitude of efficiency.

In addition to the problems with the transient EL, the interpretation of the existing model without a full dynamics picture can lead to false predictions. Figure 4.2a shows what a quenching model predicts for the roll-off as a function of increasing recombination zone width.[53] However, even in the most idealized case of a gradient emissive layer device, where no additional interfaces come into play, the predictive model fails to replicate the behavior, as shown in Figure 4.2b. While this device is of little interest for further investigation due to the extreme thickness, the point stands that this model is incomplete for guiding device design.

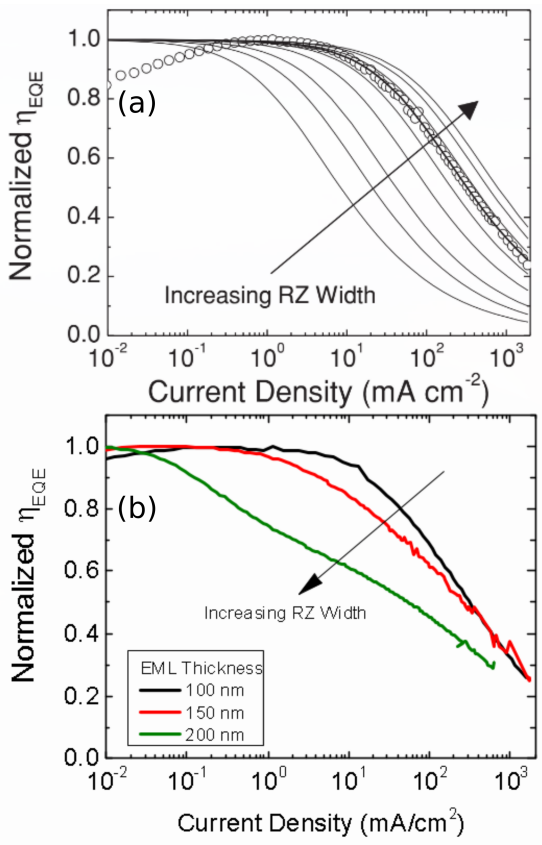

Figure 4.2: (a) Efficiency roll-off predicted by Erickson *et al.* 2014 as a function of recombination zone width.[53] (b) Observed efficiency roll-off for gradient EML devices.

Both the transient EL and the recombination zone dependence issues arise due to an incomplete picture of the device physics, most specifically in the area of polaron dynamics. The work described in this chapter sought to address these issues by including polaron dynamics. Since the steady-state solution of existing mod-

els is able to accurately replicate steady-state performance, the transient EL is utilized as well as the steady-state solution to ensure that the underlying physics are accurately captured. A valid solution should be able to accurately fit both regimes using the same model parameter values. In order to leverage previous work, the archetypical green-emitter tris[2-phenylpyridinato-c_2,N]Iridium(III) ($Ir(ppy)_3$) is used for the extensively characterized photophysics.[94,136,205–208]

4.2 Theory

4.2.1 Exciton Dynamics

The dominant processes that influence the exciton population, first formalized in Baldo et al. [136], have been identified as natural exciton decay, via radiative and non-radiative processes, triplet-triplet annihilation, triplet-polaron quenching, and exciton generation.[53,131] In triplet-triplet annihilation, two triplets are able to interact, and one exciton transfers its energy to the other, resulting in one molecule relaxing to the ground state and the other forming a hot excited state. This hot state releases this additional energy to heat and typically relaxes back to the T_1 state. Triplet-polaron quenching is the interaction of a polaron with a nearby triplet exciton. Here, one of the charges of the exciton non-radiatively recombines with the polaron of the opposite charge, leaving a remaining loose charge. Excitons are also subject to field dissociation, but this mechanism is ignored in this work. Field dissociation is typically observed for fields larger than 2.5×10^6 V/cm.[46] This is near the maximum field used for this study, and would be important to consider for higher voltage characterization.

In agreement with previous models, singlet-triplet exciton intersystem crossing and host-guest exciton energy transfer are assumed to be fast compared to exciton decay.[45,46,136] Since these mechanisms are much faster, they will not be rate-limiting processes and can thus be omitted from the differential equations model without sacrificing accuracy. Within an operational device, electron and hole populations are indistinguishable. Therefore, the electron (n_e) and hole (n_h) densities are treated as a single generalized polaron population, $n_{pol} = n_e + n_h$. For simplicity, the model developed here treats the exciton and polaron populations as spatially uniform and confined to the exciton recombination zone. An spatial inhomogeneity in exciton and polaron density as well as their overlap is absorbed into the bimolecular rate constants. It is important to note that due to this assumption, rate constants are a property of the device stack, and not just a material property. With these assumptions, the dynamic processes determining exciton density (n_{ex}) can be summarized in

the following one-dimensional rate equation:

$$\frac{dn_{ex}}{dt} = -\frac{n_{ex}}{\tau} - \frac{1}{2}k_{\text{TT}}\ n_{ex}^2 - k_{\text{TP}}\ n_{pol}n_{ex} + G_{ex} \tag{4.1}$$

where τ is the natural exciton lifetime, determined by the radiative (k_r) and non-radiative (k_{nr}) decay rates by $\tau = 1/(k_r + k_{nr})$, k_{TT} is the rate constant for triplet-triplet annihilation, k_{TP} is the rate constant for triplet-polaron quenching, and G_{ex} is the exciton generation rate. As this is a one-dimensional model, G_{ex} is a spatially uniform generation rate, a simplifying assumption. Many studies have modeled the exciton recombination zone profile, relying on material energy levels, as well as mobilities.[209–213] While these models are more accurate and explicit, in the way that they capture the physics, they also increase the dimensionality of our model, as well as increasing the parameterization; requiring separate electron and hole rate equations, mobilities and energy levels for every material.[133] Even with this increased accuracy of the physical processes, identifying if the predicted exciton recombination zone is accurate requires significant additional measurements. Since the goal of this work is to provide a functional model to accurately predict the transient and steady-state device behavior, spatially uniform dynamics are assumed. Here, exciton formation is treated using a Langevin recombination formalism based on the polaron density.[212,214,215]

$$G_{ex} = \frac{k_{\text{F}}}{4}n_{pol}^2 \tag{4.2}$$

where k_{F} is the rate constant for exciton formation. The factor of four accounts for the diversity of the polaron population and assumes that electrons and holes are in equal proportion. The accuracy of this pre-factor is reduced for imbalanced charge, and is investigated in Section 4.7.2. For n_e:n_h ratios 2:1 or better, less than 20% error is found in this term.

4.3 Polaron Dynamics

Previous models for efficiency roll-off have ignored polaron dynamics and assumed that all polarons readily form excitons. The steady-state polaron density is then modeled using a space charge limited model.[38] To attribute physics to this process, a simple picture of polaron dynamics is assumed, consisting of charge injection and transport, exciton formation, and polaron loss. In order to preserve our one-dimensionality, polarons must be uniformly distributed. Without competing losses in the transport layers, all injected polarons must eventually reach the emissive layer. We further assume that polarons easily enter that emissive layer and that the majority of polaron build up occurs within

the emissive layer, rather than the transport layers. Therefore, the charges injected from the current density, J, are uniformly generated in the emissive layer by $G_{pol} = 2J/ew$. Here, e is the electron charge, and the factor of two arises from an assumption of equal charge injection. In a well balanced device, the measured current forms holes on one side of the device and electrons on the other, and are both injected into the device. This is discussed extensively in Section 4.7.1 Polaron losses to exciton formation mirror the exciton formation rate presented in Equation 4.2, though at twice the rate due to two polarons forming one exciton.

The introduction of polaron loss from the emissive layer through the device without forming excitons is essential to address the limitations of previous models. Without this term, peak internal quantum efficiency of all devices is assumed to be 100% and the roll-up of efficiency at low current can not be explained. In order to capture polaron loss, a first order approximation is made for loss in that only the majority charge carrier can be lost and leaks through the device with a characteristic time, τ_l. With these mechanisms, the full polaron dynamics can be expressed as:

$$\frac{dn_{pol}}{dt} = \frac{-k_{\text{F}}}{2} n_{pol}^2 - \frac{n_{pol}}{\tau_l} + G_{pol}. \tag{4.3}$$

4.3.1 Transient Electroluminescence

In this work, given a full model for polaron dynamics, the model is easiest to solve starting from the application of the current pulse, rather than at peak luminance. Under pulsed electrical excitation, Equations 4.1 and 4.3 can be solved at the beginning of the pulse with the initial conditions $n_{ex} = n_{pol} = 0$. Upon the application of a voltage pulse, there is a time delay before polarons reach the emissive layer, as evidenced by the delay in luminance turn on. This has been previously attributed to charge injection and transport in the emissive layer.[216] The injection time varies with device area due to the device capacitance and accounts for the majority of the delay time for large devices. Transport is dependent on the mobility, as well as the field, which is a function of time due to the device capacitance. These times can be well predicted using the following equations:[216]

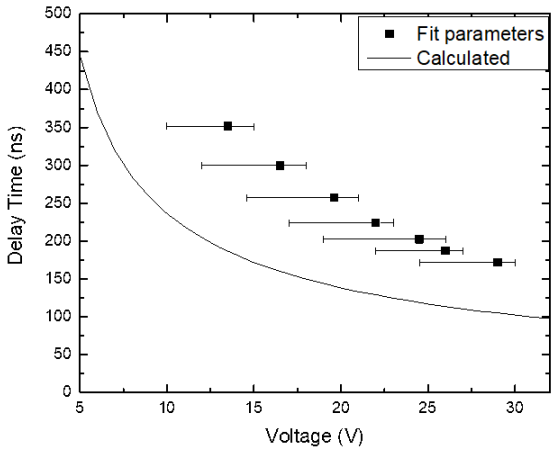

Figure 4.3: Extracted polaron injection time is shown as a function of voltage along with a fit from the model.

$$t_{inj} = \tau \log\left(1 - \frac{V_{th}}{V_0}\right) \tag{4.4}$$

$$d = \int_0^{t_{trans}} \mu_0 E_0 \exp\left(\sqrt{\mu_E E_0 \left[1 - \left(1 - \frac{V_{th}}{V_0}\right) e^{-t/\tau}\right]}\right) \left[1 - \left(1 - \frac{V_{th}}{V_0}\right) e^{-t/\tau}\right] dt \tag{4.5}$$

where τ is the RC time constant of the device, V_{th} is the voltage injection threshold, t_{inj} is the injection time, t_{trans} is the transport time, d is the transport layer thickness, μ_0 is the base mobility, μ_E is the field dependent mobility term, E_0 is the field and V_0 is the voltage. A prediction of the delay time as well as experimental values are shown in Figure 4.3. Interestingly, the functional dependence of the model accurately reproduces the extracted data. The mismatch in absolute value is due to the use of the geometric capacitance in the model, and requires a scaling factor of 2.5 of the geometric capacitance for the calculated and fit delay times to agree. This factor is similar to that predicted by Liu et al. [217] for similar structures. This suggests that the effective charge distribution in our devices is about twice as wide as the emissive layer.

After this delay, constant current polaron generation is assumed for the remainder of the voltage pulse to calculate polaron generation. When the voltage pulse is removed, G_{pol} goes to 0 and the decay can be solved using Equations 4.1 and 4.3. This model does allow polarons to continue to form excitons after the voltage has been removed. In the transient regime, if the pulse width is shorter than τ_l, polarons are not able to traverse the emissive layer during the voltage pulse. Once the voltage is removed, there is no longer a driving force for polaron leakage via drift. Under this assumption, the leakage term in Equation 4.3 can be ignored. After the full device behavior is fit, the validity of this assumption can be assessed based on the fit values for τ_l.

4.3.2 Efficiency Analysis

As discussed in Chapter 3.3.2, the maximum external quantum efficiency of an OLED is often expressed as[95,218]

$$\eta_{\mathrm{EQE}} = \eta_{\mathrm{OC}}\ \eta_{\mathrm{PL}}\ \chi\eta_{\mathrm{EF}} \tag{4.6}$$

Since this equation is intended for the maximum efficiency, further modification would have to be done to account for quenching, as is done in Chapter 5. The exciton formation efficiency, η_{EF} is typically referred to as the charge balance and is used as a correction factor to account for differences

between the observed η_{EQE} and the other calculated factors in Equation 4.6. It is widely hinted at that charge balance relates to the carrier balance, but no formalism is ever given, so it cannot be calculated. Given our full dynamics model, we are able to be explicit in both of these areas in a meaningful way. The internal quantum efficiency of a device is simply the ratio of the radiative exciton rate to the rate of electron injection, and we can therefore recast Equation 4.6 as

$$\eta_{\mathrm{EQE}} = \eta_{\mathrm{OC}} \frac{n_{ex} k_r}{G_{pol}/2}. \tag{4.7}$$

Note that in this equation, exciton quenching is accounted for in the n_{ex} term because in the steady-state, n_{ex} is reduced according to this quenching, which is competitive with k_r. Dynamically, the exciton formation efficiency is the fraction of injected polarons contributing in exciton formation. This can be viewed as the efficiency of Equation 4.3 to form excitons. Exciton formation efficiency can then be calculated as

$$\eta_{\mathrm{EF}} = \gamma = \frac{\frac{1}{2} k_{\mathrm{F}}\ n_{pol}}{G_{pol}} = \frac{\frac{1}{2} k_{\mathrm{F}}\ n_{pol}}{\frac{1}{2} k_{\mathrm{F}}\ n_{pol} + \frac{1}{\tau_l}} \tag{4.8}$$

Equations 4.7 and 4.2 allow us to rigorously tie η_{EQE} and η_{EF} to dynamic processes within the device in a quantitative manner.

4.4 Experimental Details

Devices used for measurements of transient and steady-state EL had the following structure: ITO (150 nm)/poly(3,4-ethylenedioxythiophene)-poly(styr- enesulfonate) (PEDOT-PSS) (40 nm)/tris(4-carbazoyl-9- ylphenyl)amine (TCTA) (30 nm)/10% tris[2-phenylpyridi- nato-C2,N]Iridium(III) ($Ir(ppy)_3$) doped in 4,40-Bis(N- carbazolyl)–1,10-biphenyl (CBP) (10 nm)/bathophenanthro- line (Bphen) (30 nm)/LiF (1 nm)/Al (100 nm). Transient photoluminescence (PL) decays were measured using 60-nm-thick films of CBP doped with 10% $Ir(ppy)_3$ deposited on quartz slides. The hole-only device structure used for steady-state PL quenching measurements had the following structure: ITO (150 nm)/PEDOT-PSS (40 nm)/10% $Ir(ppy)_3$ in CBP (60 nm)/Au (50 nm). The gold cathode was used to prevent electron injection. Transient EL measurements were conducted using a voltage pulse generator (HP 8114a) with pulse amplitudes ranging from 5–40V and pulse widths ranging from 250 ns–500 ns with a period 500 ls. Luminescence was recorded using a set of collection lenses focused onto a fast photodiode (Thorlabs DET36A). Pulsed η_{EQE} measurements were conducted using the HP 8114a pulse generator until the device reached steady state current and luminance, which were

recorded. Overlapping points with the steady state η_{EQE} measurement were used to calibrate the luminance-current ratio to the η_{EQE} . The photodiode signal was recorded using an oscilloscope (Tektronix TDS5104b). Transient PL measurements were collected using a pulsed nitrogen laser (Optical Building Blocks) with a pulse length of approximately 1 ns and emission wavelength of λ= 337 nm at a repetition rate of 6 Hz. Laser light was focused on the sample using a series of lenses, with collection carried out using the same techniques already described for transient EL. Incident laser power was measured using a Coherent EnergyMax 10MB-HE detector. Film thicknesses and optical constants used for modeling the out-coupling efficiency in Equation 4.7 were obtained using a J. A. Woollam variable angle spectroscopic ellipsometer (VASE) using a Cauchy dispersion model.

4.5 Exciton Quenching in PL

PL measurements have been previously used to extract the rate constants for triplet-triplet annihilation and triplet-polaron quenching.[46,53] This is important because it allows an independent confirmation of the extracted rate constants extracted during the EL fitting. The transient PL exposes the natural exciton lifetime, τ and at high incident flux, the triplet-triplet annihilation rate constant, k_{TT} . This measurement involves an incident laser pulse, in this case, from a 337 nm nitrogen laser, which is able to excite a large exciton population. The pulse width of the nitrogen laser is 1ns and is much faster than τ or k_{TT} , allowing us to use Equation 4.1 with the initial boundary condition $n_{ex} = A(E_{\mathrm{pulse}}/hfV)$ where A is the absorbed fraction of photons, E_{pulse} is the pulse energy, hf is the photon energy and V is the film volume. Since this is optical excitation, the other boundary condition is $n_{pol} = 0$ and we can ignore Equation 4.3.[46,53,136] For CBP films doped with $\mathrm{Ir(ppy)_3}$, good agreement with the

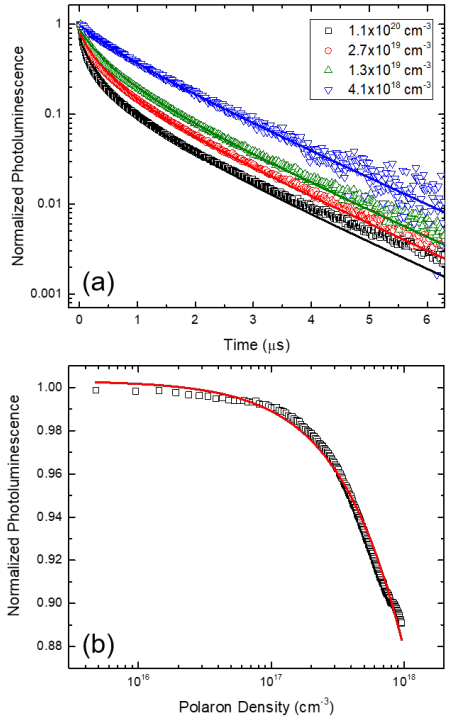

Figure 4.4: (a) Transient PL decays for several initial exciton densities with fits shown as solid lines using Equation 4.2. Fit parameters are discussed in SECTION. Exciton densities are calculated using measured incident power and beam size in combination with Beer's Law. (b) Steady-state PL quenching as a function of polaron density and the resulting fit from Equation 4.11 shown as the solid line.

model is observed across a range on initial exciton densities, as shown in Figure 4.4(a). The exciton lifetime, τ was found to be mostly independent of exciton density and was globally fit to 1.5±0.2 μs. The triplet-triplet annihilation rate constant appears to be a function of intensity and ranges from $k_{\text{TT}} = 2.4 \times 10^{-13}$ cm^3/s at $n_{ex_0} = 4.1 \times 10^{18}$ cm^{-3} to $k_{\text{TT}} = 6.9 \times 10^{-14}$ cm^3/s at $n_{ex_0} = 1.1 \times 10^{20}$ cm^{-3}. The extracted values and trend with intensity are in good agreement with previous reports.[46,53,219] It is important to note, that the exciton environment is very important for these values. Previous studies have shown that the presence of a metal cathode on top of the film can significantly reduce the exciton lifetime by allowing additional non-radiative recombination via surface plasmon coupling.[49] This becomes important in the comparison of these parameters with those obtained under EL within a device. While not performed at the time, a more representative experiment would have involved a full device stack with cathode, rather than just a film.

Measurements of the triplet-polaron quenching rate constant were made in single carrier type devices as a function of polaron density. It is largely uninvestigated as to the differences between electrons and holes, but in previous works, hole only currents are used, a precedent that is followed in this work.[46,53] A steady-state exciton population is generated optically, in this case, using a 405 nm laser. In a single carrier type device, a space charge limited current model featuring an exponential trap distribution is often used.[38,97,152] This model is employed largely because it fits the obtained current-voltage behavior most closely. In reality, a single trap state would be expected, as that is what is introduced by Ir(ppy)$_3$ in a doped film. These models are frequently employed largely for simplicity. A more accurate determination of polaron density is discussed in Chapter D. However, in a space charge limited model with an exponential trap distribution, the current density voltage relationship can be modeled using[38]

$$V = \left[\frac{J}{e\mu N_C} d^{2l+} \left(\frac{eN_0 k_B T_t}{\epsilon} \right)^l \right]^{\frac{1}{l+1}} = C J^{\frac{1}{l+1}}, \tag{4.9}$$

where N_C is the density of states at the transport level, ϵ is the permittivity, μ is the mobility, L is the device thickness and $l = T_t/T$ with T_t being an experimentally determined characteristic temperature of the trap distribution. The Polarons density is then given by[38]

$$n_{pol} = eN_c \left(\frac{\epsilon V}{ed^2 N_0 k T_t} \right)^l. \tag{4.10}$$

Combining Equation 4.10 with Equation 4.1, the ratio of the steady-state PL intensity (L) to the PL intensity in the absence of polarons (L$_0$) can be written as[46]

$$\frac{L(n_{pol}}{L_0} = \frac{1}{1 + \tau k_{\text{TP}}\ n_{pol}} \tag{4.11}$$

After fitting the current density-voltage characteristics of the device are fit using Equation 4.9, Equations 4.10 and 4.11 can be used to extract the triplet-polaron rate constant for a given value of τ. In this case, the value of τ is extracted from transient PL measurements. The fit obtained for a 5% CBP:Ir(ppy)$_3$ hole only device is shown in Figure 4.4b. This devices utilizes a gold cathode to prevent electron injection and shows minimal exciton formation. The organic stack is the same as the emissive layer of the investigated device. In fitting the current density-voltage characteristics using Equation 4.9, a value of $l = (2.4 \pm 0.2)$ was found. The extracted triplet-polaron quenching rate constant from fitting Equation 4.11 was $k_{\text{TP}} = (2.8 \pm 0.2) \times 10^{-13}$ cm^3/s and is agreement with previous measurements.[46,53]

4.6 Application to Devices

In order to fit both the steady-state and transient regimes, decisions need to be made as to a methodology for extracting parameters. The obvious choice may seem to be to try to produce a global fit by fitting both regimes simultaneously. The major draw back of this approach is the value of τ_l, which is a function of the applied field. Additionally, the steady-state provides little insight into the actual quantities of τ, k_{TT} , k_{TP} , and k_{F} , and only the ratio of radiative and non-radiative processes is needed for a quality fit of the efficiency roll-off. Additionally, within this model, only n_{ex} is experimentally available to fit, and the fit parameters are not independent. The most obvious example of this is the values of k_{TT} and k_{TP} , which have similar impact on the exciton population and similar formulation. This makes it near impossible to distinguish a dominant mechanism between these two, and results for exact values of quenching constants need to be considered with caution. This methodology only gives a net effect of the two quenching mechanisms in total, rather than a true separate measurement of both quantities as is obtained in the PL quenching measurements, discussed in Section 4.5.

With these limitations addressed, the method used for this discussion to fit all of the device physics has been carefully considered to achieve the highest parameter sensitivity. The bimolecular quenching constants are most sensitive to the efficiency roll-off since small changes in the quenching constants make a large impact on the roll-off behavior. However, the lifetime and exciton formation can only be determined to within a fixed ratio. In contrast, the exact values of lifetime and exciton

formation rate are critical to the behavior of the transient EL while the bimolecular quenching constants are difficult to probe in the current regime investigated. In order to use these sensitivities, a quenching only model (ignoring τ_l) to fit the normalized efficiency roll-off, such has been previously reported, is used to determine the bimolecular quenching rates, k_{TT} and k_{TP} . Quenching only models can only fit the normalized η_{EQE} roll-off because without a polaron loss term, η_{EF} is assumed to be 100% and the exact magnitude of efficiency cannot be reproduced. Initial values for all parameters, except k_F which is previously unmeasured, are determined by the PL measurement values. With these quenching rates fixed, the transient EL is fit using Equations 4.1 and 4.3 in order to determine τ and k_F . Remember that in the transient regime for short pulses, we can assume that $\tau_l = \infty$ and can be ignored.

With these critical rate constants determined, we will revisit the efficiency as a function of current density. In the first pass, we ignored the exact value of efficiency and only fit the normalized roll-off. Now, since we know the other parameters, we can revisit η_{EQE} , now matching the exact profile for all currents, by conducting a point-by-point fit for k_F. This fit for k_F can then be used to calculate η_{EF} and can be compared to a drift model, to assess its validity.

4.6.1 Quenching Only Steady-State Fit

To measure transient and steady-state EL, devices were constructed using the architecture discussed in Section 4.4. These devices had an η_{EQE} of (9.7±0.1)%. Equations 4.1 and 4.3 were used to fit the peak normalized steady-state efficiency roll-off with $\tau_l = \infty$. Again, omitting a polaron loss term, this model assumes that all roll-off behavior comes from quenching. Parameters were initialized using the values obtained from PL quenching measurements, described in Section 4.5. An experimental fit is shown in Figure 4.5 and shows good agreement, except at very high currents associated with pulsed η_{EQE} measurements. Parameters are summarized in Table 4.1 and are in good agreement with those previously reported.[46,136]

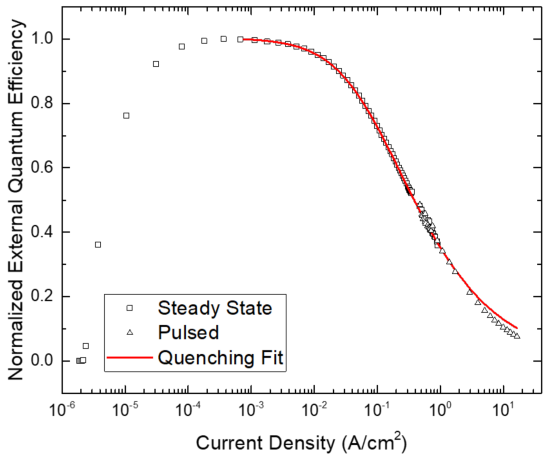

Figure 4.5: Normalized experimental η_{EQE} as a function of current density. Solid line is a fit to the data using Equation 4.1 and 4.3 in the absence of polaron loss. Pulsed EQE measurements are conducted using 50 ms pulses with duty cycles <10% to steady-state luminance to reduce Joule heating in device.

	Transient EL	Efficiency Roll-off
τ (s)	$6.9 \pm 0.1 \times 10^{-7}$	6.1×10^{-7}
k_{TT} (cm^3/s)	7.1×10^{-12}	7.1×10^{-12}
k_{TP} (cm^3/s)	3.3×10^{-13}	3.3×10^{-13}
k_{F} (cm^3/s)	$7.7 \pm 3.5 \times 10^{-12}$	1.6×10^{-11}

Table 4.1: Fit parameters extracted from transient and steady-state EL. Transient EL fit parameters averaged over all measured current densities. η_{EQE} roll-off parameters averaged over several measured devices. Triplet-triplet annihilation and triplet-polaron quenching rates are fixed to those obtained from fitting the normalized efficiency roll-off.

4.6.2 Transient Modeling

Transient EL measurements were conducted on the same devices used for the efficiency measurements described in Section 4.6.1. Pulse widths ranging between 250–500 ns with a period of 500 μs were used with current densities ranging between 0.5–50 $\mathrm{A/cm}^2$. Fast Fourier Transform (FFT) filtering is used to remove experimental noise from the measured signal to increase fit accuracy. The bimolecular quenching rate constants are fixed to the values determined from the fitting of the steady-state efficiency roll-off (Table 4.1). The exciton lifetime and exciton formation rate constant are allowed to vary to fit the transient EL and are summarized in Table 4.1. The value of τ is shorter than that obtained under transient PL, likely due to the cathode present for EL transient studies.[49] Fits using this model are shown in Figure 4.6 and show excellent agreement above the detection limit. The initial turn on is well replicated by the luminance delay model discussed in Section 4.3.1

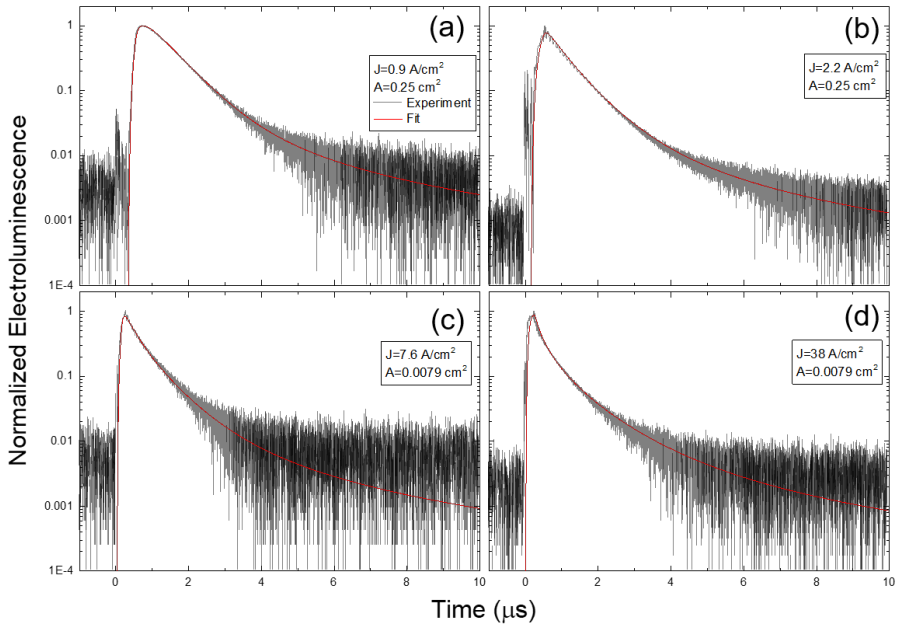

Figure 4.6: Transient EL for four different current densities (J) and device areas (A). (a) 0.25 cm^2 device at a current density during the pulse of J = 0.9 A/cm^2 (b) 0.25 cm^2 device at J = 2.2 A/cm^2 (c) 0.0079 cm^2 device at J = 7.6 A/cm^2 (d) 0.0079 cm^2 device at J = 38 A/cm^2

4.6.3 Transient Term Efficiency

Utilizing the understanding of dynamics developed here, the efficiency of each component in Equation 4.1 for the transient EL can be analyzed. This is shown for representative high and low current density behavior in Figure 4.7. At the application of the voltage pulse, exciton generation is the dominating feature, resulting in a steep rise in luminescence. As the exciton and polaron populations peak, the resulting dependence is seen on the bimolecular quenching terms, leading to the curvature seen before and after the removal of the injected current. During the decay, the exciton and polaron populations rapidly decrease due to quenching, resulting in the natural exciton lifetime becoming the dominant behavior. As the exciton population further diminishes, formation of excitons from the residual polaron population is observed, resulting in the slow decay seen at long times. Figure 4.7a shows the decoupled EL transient behavior at a low current density where exciton formation and the natural lifetime are always competitive processes, resulting in the slow rollover in the experimental behavior of Figure 4.6a. Slightly higher current densities do not show the bimolecular terms rise to prominence, resulting in the linear decay after the pulse seen in Figure 4.6b. Bimolecular quenching terms show increasing importance with current density, especially at times soon after the removal of voltage. We see this behavior in Figures 4.6c and 4.6d with the decoupled high current density behavior of Figure 4.6d demonstrated in Figure 4.7. Here, we are able to see that bimolecular quenching events dominate when the exciton density is peaked after the removal of voltage.

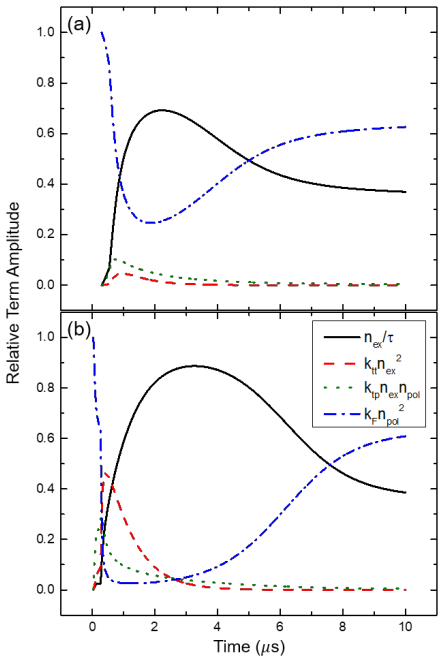

Figure 4.7: Term efficiency for each dynamical process influencing the exciton population for (a) 0.25 cm^2 device operated at 0.9 A/cm^2 for 500 ns and (b) 0.785 mm^2 device operated at a current density of 38 A/cm^2 for 250 ns. Relative term amplitude is calculated as the magnitude of each term in Equation 4.1 divided by the sum of absolute values of each term.

4.6.4 Extracting Exciton Formation Efficiency

Thus far in the fitting, the introduced model has successfully fit the transient EL and steady-state efficiency roll-off using Equations 4.1,4.2, and 4.3 by including polaron dynamics in the absence of

charge leakage. However, only the efficiency roll-off and the normalized reduction in magnitude have been modeled. By including the polaron transit time in the analysis, the exact magnitude can be fit for both the rise and fall of efficiency. Starting with the experimental η_{EQE} as a function of current density, Equation 4.7 can be used to find the exciton density, n_{ex}, as a function of current density, which in turn allows Equations 4.1 and 4.3 to be solved in the steady-state for τ_l. The out-coupling efficiency, η_{OC} , is separately determined using optical modeling and found to be $\eta_{\text{OC}} = 17.7\%$.[54,96] The details of this calculation are discussed in Chapter E. The radiative rate in Equation 4.7 can be extracted from measurements of τ and η_{PL} as $\eta_{\text{PL}} = \tau k_r$. Once the exciton population is known, Equation 4.1 can be solved for the polaron population, n_{pol} using the fit values from the transient EL. With n_{pol} and G_{pol} known, Equation 4.3 can be used to extract the τ_l needed to reproduce the experimental η_{EQE} . This technique produces an exact match of the shape and magnitude of the efficiency, including both the roll-up and roll-off. This is the first time in literature that a quantitative physical explanation has been attributed to the roll-up. Any error in this method are absorbed into τ_l. Extracted values of τ_l are shown in Figure 4.8. In order to justify these values, a simple drift model explanation can be used, quantified by

$$\tau_l = \frac{w}{E\mu(E)}. \tag{4.12}$$

Where μ is the mobility, obtained from Parshin et al. [220], w is the device width, and E is the electric field. This simple explanation for τ_l holds very well at low current density, corresponding to the efficiency roll-up, as well as the peak efficiency. Deviation from this model occurs as current density increases past 10^{-1} A/cm^2. However, in this regime, exciton and charge densities are becoming increasingly high, and the predicted values become increasingly non-physical. It is expected that in this regime, this simple model described in Equation 4.12, would break down.

4.6.5 Drift Model

With the transit time known, Equation 4.8 can be used to find η_{EF} , shown in Figure 4.8. The exciton formation efficiency remains relatively constant throughout the onset of roll-off and only falls when the efficiency approaches one quarter of its initial value. Using a different modeling approach, Giebink and Forrest [130] find that for a similar system, a larger portion of the roll-off is due to a loss of η_{EF} , likely due to a thicker emissive layer and differing transport layers than those used in this study. With the dependence of η_{EF} on current density established, the validity of the assumption of uniform η_{EF} during the fit of the normalized efficiency roll-off in Section 4.6.1 can

now be assessed. η_{EF} , seen in Figure 4.8, remains almost constant for the majority of the roll-off but deviates at high current density, suggesting that the high current density regime should not be fit with the quenching only model. However, the fit shown in Figure 4.5 is not limited by this restriction as there is excellent agreement between the model and experiment in the regime of near constant η_{EF} , with the only discrepancy in the fit coming at high current density where the model assumptions break down. Returning to fit the normalized efficiency in the regime of near constant η_{EF} , as defined by Figure 4.8, while holding τ and k_F constant, k_{TT} and k_{TP} are found to be $(4.5 \pm 0.4) \times 10^{-12}$ cm^3/s and $(2 \pm 3) \times 10^{-12}$ cm^3/s, respectively. This small variation of quenching parameters does not change the fit quality for the regime in question. Repeating the fitting process in this regime yields no significant differences in τ and k_F or the dependence of η_{EF} on current density.

4.7 Understanding Assumptions of Polaron Model

In the model described in this work, electrons and holes are summarized into a generalized polaron population with the dynamics described using Equation 4.3. To understand the impacts that this has on calculating the polaron injection rate and the exciton formation rate, the electrons and holes must be independently examined. The most complete dynamics picture related to the developed model would express individual electron and hole injection as well as individual transit times. This full picture can be written as:

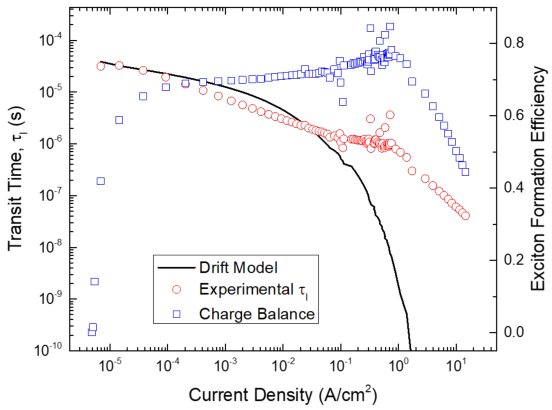

Figure 4.8: Transit time extracted from η_{EQE} measurements are shown as the red circles. Predictions using the drift model are calculated using Equation 4.12. The drift model assumes a uniform electric field. Good agreement between the experimental transit time and the drift model is found for a field distributed over 20 nm. η_{EF} is shown as a function of current density in blue squares.

$$\frac{dn_h}{dt} = -k_{\text{F}}\ n_e n_h - \frac{n_h}{\tau_{lh}} + \frac{J_h}{ew} \tag{4.13}$$

$$\frac{dn_e}{dt} = -k_{\text{F}}\ n_e n_h - \frac{n_e}{\tau_{le}} + \frac{J_e}{ew} \tag{4.14}$$

where and are the electron and hole population densities, n_e and n_h are the electron and hole transit times, respectively, J_h and J_e and are the single carrier injected currents. While more

accurate, Equation 4.13 and 4.14 pose several problems for replicating device behavior due to the inability to distinguish between carriers during device operation. This is further complicated by the inability to separately measure the single carrier injected currents and leak rates due to transit times. To better understand the approximations used in Equation 4.3, a detailed analysis of current injection is presented, followed by error analysis of the exciton formation term based on the composition of the polaron population.

4.7.1 Carrier Injection

Let J be the total current within our device. This must be maintained throughout our circuit assuming no charge buildup. Within the device, the total current can be written as $J = J_e + J_h$. Experimentally, J is the only measurable current as we are not able to distinguish between electron and hole or leaked currents. The current incident on either contact will be referred to as J_1 and J_2. These currents are summarized in Figure 4.9. In the case of no leakage current, there must be complete recombination in the emissive layer. Therefore all of the externally measured current from one side of the device contributes only to electron current and all current on the other side contributes only to hole current.

$$J_1 \rightarrow J_h = J_2 \rightarrow J_e \tag{4.15}$$

This maintains constant current throughout the external circuit. No charges are allowed to leave the emissive layer without recombining with the opposite charge species and constant current maintains that $J_e = J_h$. The injected polaron density is then:

$$\frac{J_e}{ew} + \frac{J_h}{ew} = \frac{J_1 + J_2}{ew} = \frac{2J}{ew} \tag{4.16}$$

This expression becomes more complicated when charge leakage is allowed. Let us assume that holes are the only leaking species. Let J_l be the current leaking through the emissive layer. On the hole side of the device, all current is hole current. However, on the electron side of the device, the measured current is a combination of the electrons injected and the leaked holes.

$$J_1 = J_h \tag{4.17}$$

$$J_2 = J_e + J_l \tag{4.18}$$

For current continuity, the current on either side of the device must be equal.

$$J = J_h = J_e + J_l \tag{4.19}$$

From this expression and the experimentally measured current, it is not possible to know the electron and hole currents independently without making some assumption about the leaked current. If both carriers are allowed to leak, there is a leakage term on the hole current side of Equation 4.18 as well. Without additional information about the proportion or magnitude of the leaked current, there is no exact expression for polaron injection in terms of J. Therefore, the approximation is used that the polaron injection and loss due to leakage can be written as:

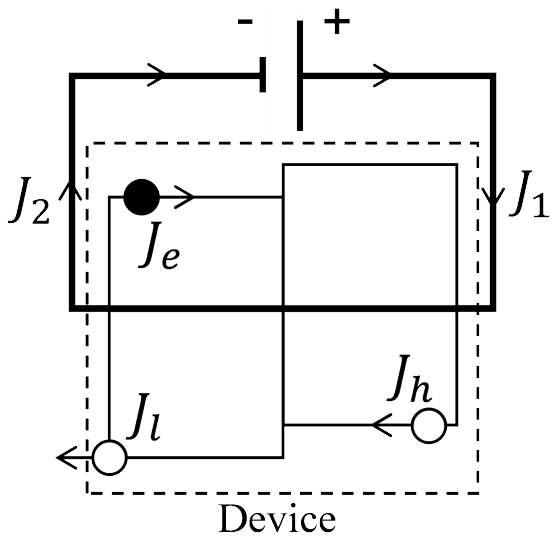

Figure 4.9: Current density formalism within the circuit. J_1 and J_2 are the currents measured on either side of the device. J_e and J_h are the electron and hole currents within the device and J_l is the unbalanced current, assumed to be only holes, that leaks out of the opposing contact.

$$G_{pol} - \frac{J_l}{ew} = \frac{2J - J_l}{ew} \tag{4.20}$$

This is the expression used in the final model, assuming the charge leakage can be written in terms of the total population and a transit time for leakage as $J_l/ew = n_{pol}/\tau_l$ and $G_{pol} = 2J/ew$. The approximation in Equation 4.19 is strong assuming is small relative to J_h and J_e.

4.7.2 Charge Imbalance

In the exciton formation term of Equation 4.3, the factor of two in the denominator assumes that charges are in equal proportion. More generally, Equations 4.14 and 4.13 can be used to evaluate the error in this term as the η_{EF} increases. Let the carrier ratio be defined as:

$$\alpha = \frac{n_h}{n_e + n_h} \tag{4.21}$$

This is different from the η_{EF} we have defined in the text as this is an actual ratio of carriers, rather than the exciton formation efficiency. Additionally, let $n + pol = n_e + n_h$ be the polaron population

density. With these definitions, the terms for polaron loss to exciton formation of Equations 4.14 and 4.13 can be summed as:

$$\left[\frac{dn_{pol}}{dt}\right]_{formation} = -2k_{F}\ n_{pol}^{2}\alpha(1-\alpha) \tag{4.22}$$

In the case of perfect balance, the expression $\alpha(1-\alpha) = 1/4$ and agrees with Equation 4.3. The variation in $\alpha(1-\alpha)$ as a function of α can be seen in Figure 4.10. With charge ratios up to 1:3, there is less than a 20% error in this expression. The high efficiency devices examined in this work are expected to operate in this regime, and the value of $\alpha(1-\alpha$ should not change the value of k_F significantly.

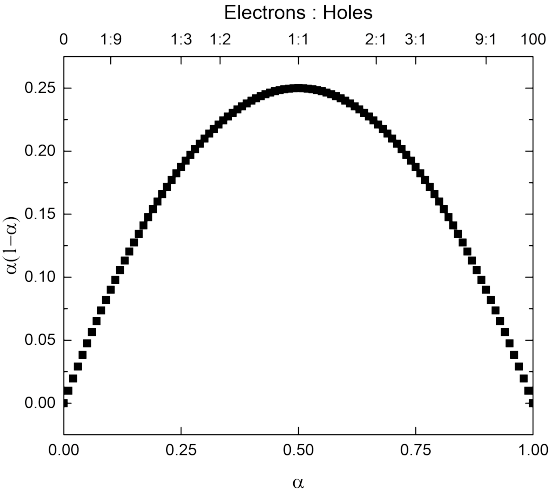

Figure 4.10: The quantity $\alpha(1-\alpha)$ is plotted as a function of the polaron composition, α and the electron to hole ratio.

4.8 Conclusion

A universal dynamics model has been successfully implemented that allows the fitting of the transient and steady-state EL behavior of OLEDs using $Ir(ppy)_3$ as an emitter. This model relies upon the previously studied parameters τ, k_{TT} , and k_{TP} as well as introducing polaron dynamics in the form of an exciton formation rate, k_F and polaron leakage time τ_l. This model has been used to deconstruct all features of the transient EL over three decades of decay. The fit parameters τ, k_{TT} , and k_{TP} have all been verified independently using PL studies in agreement with the proposed model. The steady-state efficiency has been fully characterized using quenching and charge leakage through the device. The behavior of the investigated devices suggests that charge leakage through the emissive layer dominates the roll-up in efficiency, while bimolecular quenching is responsible for the majority of the roll-off in efficiency.

This model has successfully been able to model all of the device physics present in the EL behavior. However, one of the initial goals of this project was to be able to quantify the bimolecular rate constants more effectively within a device. In this regard, the model is not useful as k_{TT} and k_{TP} are codependent and their relative values are still unknown.

In future chapters, the use of charge balance as an exciton formation efficiency, η_{EF} , will continue to be used in aiding the understanding of device behavior.

Chapter 5

Decoupling Degradation Mechanisms - Methodology and Experimental Design

This is a summary and extension of published works entitled *"Decoupling degradation in exciton formation and recombination during lifetime testing of organic light-emitting devices"*[153] as well as some error analysis from *"Isolating Degradation Mechanisms in Mixed Emissive Layer Organic Light-Emitting Devices"*[154].

As OLEDs become fully a fully commercialized technology, several challenges still exist that need to be overcome to realize full potential. Chief among these is the operational lifetime, which has been a key focus of recent studies.[93,162,192–194] Lifetime is typically characterized at constant current density, recording the luminance loss and voltage as a function of time. The lifetime is then reported as the time to reach some arbitrary fraction of the initial luminance. Unlike the steady-state efficiency, it is difficult to optimize a device lifetime by brute force. Due to the long lifetime of devices, even under accelerated aging, it takes a substantial amount of time to characterize devices and iteratively improve a design. This reality makes it essential to have a deeper insight into the processes that are limiting lifetime.

While this simple lifetime characterization is effective for device to device comparison, further insight into the mechanism is found wanting. Modeling techniques are used extensively for degradation characterization, using the mechanisms outlined in Chapter 3.8.1.[83,139,221] While these techniques

are able to reproduce the decay characteristics with a root in physical mechanisms, they suffer from over-parameterization and introduce parameters that cannot be experimentally confirmed. As discussed in Chapter 3.8.3, a variety of chemical, structural, and spectroscopic techniques are often employed to gain further insight into the physical processes.[93,172,192,193,222] These techniques can be insightful, but are difficult to apply on a large scale due to the additional processing time. Post-degradation analysis does not provide a temporal characterization of degradation without processing individual devices at several decay points, which can be extremely time consuming. Additionally, it may be helpful to categorize luminance loss into different luminance loss pathways, which few of these techniques are able to do. It would be beneficial to have a technique that is able to provide more information during the degradation, without increasing experimental time, as well as provide a way to decouple loss pathways. In this chapter, this goal is realized by introducing an optical pump to independently measure η_{PL} as a function of time. While previous works have measured PL during lifetime,[189,223,224] none have attempted to decouple the total loss into η_{PL} and η_{EF} losses. This chapter demonstrates a method for decoupling the device photoluminescence loss from the exciton formation losses during operational lifetime testing.

5.1 Luminance as Efficiency Loss

When OLEDs are degraded at constant current density, luminance loss is observed. As discussed in Chapter 3.3.2, quantum efficiency is the ratio of photons leaving the device per electron input. Therefore, at constant current density (or constant electron flux), luminance loss is actually an efficiency loss. Chapter 4 extensively discussed a revised formalism for understanding OLED efficiency. In particular, we will take advantage of the formalism of exciton formation efficiency. For decoupling luminance loss pathways, a categorical expression for η_{EQE} is desired, rather than the dynamics approach taken in Equation 4.7, therefore Equation 4.6 is modified to include a quenching term, yielding

$$\eta_{\text{EQE}} = \eta_{\text{PL}}\ \eta_{\text{OC}}\ \chi\eta_{\text{EF}}\ \eta_{\tau} \tag{5.1}$$

where η_{τ} is the fraction of excitons that relax via the natural exciton lifetime, τ. This term is current-density dependent and captures the quenching events discussed in Chapter 4. It is also important to note that during degradation, η_{EF} captures not only the previously discussed polaron loss due to leakage events, but also the formation of non-radiative recombination centers (NRRCs).[185,189]

The interpretation of η_{EF} as the exciton formation efficiency needs to be clarified to be the efficiency of exciton formation on the emissive molecule, but remains otherwise unchanged.

During degradation, to categorize efficiency loss, each term in Equation 5.1 could be considered to be time dependent. However, it is reasonable to assume that some of these terms are unchanged, or have minimal impact. The exciton radiative spin fraction, χ is a quantum mechanical property of the emissive molecule. Therefore, without changes in the emissive molecule, this term should remain constant. If emission from another state was observed spectrally, this would indicate a need to adapt Equation 5.1 for multiple emissive states, greatly complicating this process.

The out-coupling efficiency, η_{OC} , is a property dependent on the layer optical constants and thicknesses. Without significant changes in molecular composition and morphology, it is unlikely that η_{OC} should change. The most likely was to create these changes would be through crystallization. For these devices, no changes in morphology were seen in cross-polarized optical microscopy, a common technique for observing crystallization.[92] It is also important to note that η_{OC} depends on the emitter distribution within the device, and thus the recombination zone. If there is a shift in RZ, out-coupling is likely to change. It is difficult to assess recombination zone and unprecedented to measure as a function of degradation. However, this problem is minimized in thin emissive layers, so studies should attempt to focus on thinner EML devices to reduce error.

Lastly, η_{τ} is assumed to be constant during degradation. An approximation of the impacts of this term are discussed in Section 5.2.4

With the other terms assumed to be constant, η_{PL} and η_{EF} are the only time-dependent quantities, and the time-dependent version of Equation 5.1 can be written as

$$\frac{\eta_{EQE}\ (t)}{\eta_{EQE}\ ^{0}} = \frac{\eta_{PL}\ (t)}{\eta_{PL}\ ^{0}} \frac{\eta_{EF}\ (t)}{\eta_{EF}\ ^{0}} \tag{5.2}$$

where X^0 is the initial value of the parameter before degradation. Since $\eta_{EQE}\ (t)$ is the luminance loss as a function of time, an independent measurement of η_{PL} would allow a full decoupling of η_{EQE} into η_{PL} and η_{EF} . In other works, this separates η_{EQE} into the ability of excitons to form (η_{EF}) and the ability of excitons to radiate (η_{PL}).

5.2 Photoluminescence Characterization

In order to independently measure η_{PL} during degradation, intermittent optical excitation is done using a laser, as shown in Figure 5.1a. The laser active area is a 1mm diameter circular spot on the

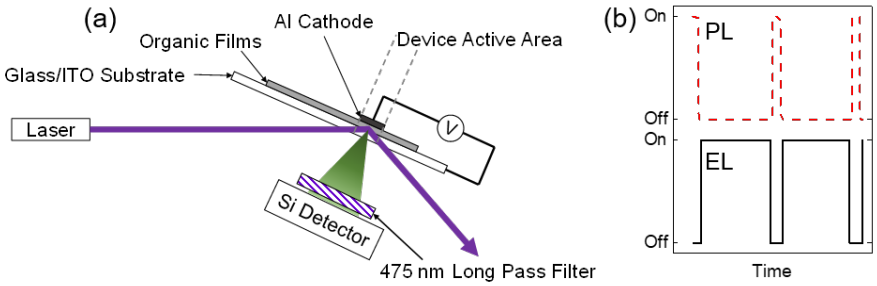

Figure 5.1: (a) Experimental configuration for the measurement of electro- (EL) and photoluminescence (PL) during OLED degradation. Laser excitation is incident on a subsection of the device area. The laser is aligned so that neither the incident nor reflected beam strikes the detector. Stray laser light is removed by a λ=475 nm dielectric long pass filter. (b) Excitation scheme. EL and PL signals are probed independently with no temporal overlap.

active device area. The photoluminescence loss observed from this measurement can be related to the photoluminescence efficiency loss by

$$\frac{\eta_{PL}(t)}{\eta_{PL}^0} = \frac{L_{PL}(t)}{L_{PL}^0}\frac{I^0}{I(t)}\frac{\alpha^0}{\alpha(t)} \tag{5.3}$$

where L_{PL} is the experimentally measured luminance, I is the pump intensity, and α is the film absorption. The pump intensity, I, can be measured and is observed to remain constant within error during the degradation. The absorption, α, has also been measured before and after degradation, and is found to be constant within error. However, the sensitivity of the absorption measurement may not reflect the sensitivity of the η_{PL} measurement. An alternative method to verifying the η_{PL} measurement is presented in Section 5.2.5.

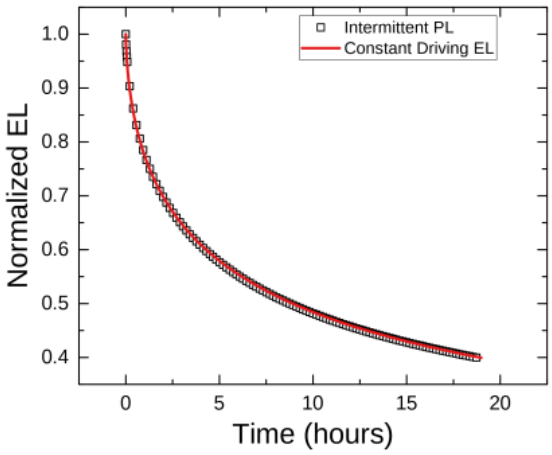

Figure 5.2: Lifetime obtained under a constant driving current is shown in red solid line. Lifetime under the same conditions but with PL measurement breaks is shown in open squares. Strong agreement is observed.

In traditional lifetime measurements, constant current density excitation is used. In order to measure η_{PL} as well, the current is paused every 10 minutes long enough to stabilize the laser and take a measurement, before the current is resumed. This takes on the order of 20 seconds, and is shown in Figure 5.1b. To make these measurements comparable with traditional lifetimes, time is reported as the elapsed time under electrical

current, with the laser breaks subtracted. This method has been shown to accurately match the traditional lifetime measurements, without additional degradation due to the PL measurement or relaxation from the breaks in current, as shown in Figure 5.2.

The accuracy of this measurement technique relies heavily on several testing considerations and assumptions. Important considerations of testing conditions and sources of error are discussed in the following sections.

5.2.1 Light Selection

Light sources for optical pumping are required to be powerful enough to pump the emitter sufficiently for measurement, stable enough to maintain output power for lifetimes over 100 hours, and long lived. Ideal candidates are lasers and high power lamps, though lamps often have a long warm up time, which is not ideal for the short on time needed for this experiment. Lamps do have the advantage that they can pump all of the device active area, getting a better sample of the behavior, though lasers can be expanded for the same effect.

During the optical pumping, it is important to only pump the emissive layer, and for the most direct measurement of η_{PL} , only the emitter molecule. To accomplish this, careful selection of wavelength must occur. Figure 5.3 shows the optical extinction coefficient for several materials. Ideally, the pump wavelength should be selected so that the emitter molecule has significant absorption, but the host does not. This is relatively easy for the green emitter, $\mathrm{Ir(ppy)_3}$ where a wide range of pumps would work between 375 and 500 nm. However, This becomes extremely difficult for blue emitters such as FIrpic, where hosts are more resonant with the emitter. In this case, the host may have to be pumped and exciton transfer from the host to the guest will be included in the measurement. Even with this, the transport layers would have to have higher triplet energies than the emitter.

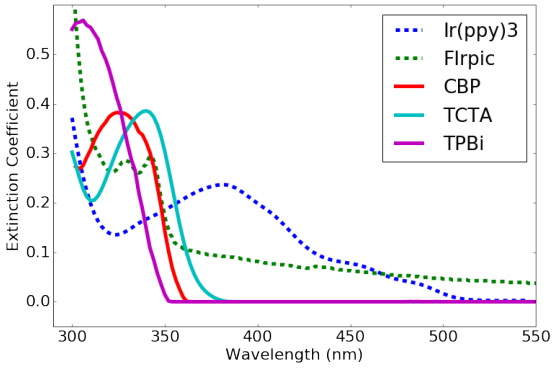

Figure 5.3: Extinction coefficients shown for the green emitter $\mathrm{Ir(ppy)_3}$ and blue emitter FIrpic as well as a few host materials.

Due to these limitations, lasers are ideal light sources for green emitters, since they are easily manipulated optically to pump multiple devices. Here, the limitations of available laser wavelengths are less important due to the wide pumping window. However, for blue emitters, a lamp may be a

more viable option as it would allow filtering or monochromation to be more selective of wavelength.

5.2.2 Absorption - Recombination Overlap

For the measurement of η_{PL} to accurately reflect the useful degradation of the emissive layer, it is important for the optical pump absorption to agree with the recombination zone within the device. To illustrate this, Figure 5.4 shows a device where there is disagreement between the absorption and the recombination zone. Assuming an exciton driven process, defect formation and degradation will focus around the recombination zone. However, the optical probe is weighted away from the electrically generated defects. This leads to a systematic underestimate of the actual η_{PL} degradation within the device.

To quantify this error for a particular device, a degradation and defect generation model must be employed in order to quantify the degradation profile within the device. Additionally, the absorption profile and recombination zone must be known (or estimated). The absorption profile can be calculated using a transfer matrix formalism.[225] The code used to calculate this is provided in Appendix F.2. The recombination zone can be measured using sensitizer molecules using the method outlined in Chapter 3.6. An excellent example of executing this analysis demonstrated by Bangsund et al. [154]

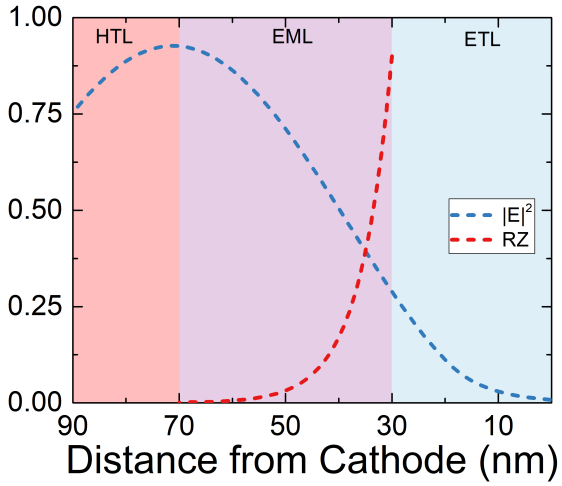

Figure 5.4: Exciton recombination zone (RZ) and pump intensity $|E|^2$ for a hypothetical thick EML device are shown. Figure produced by John Bangsund.

5.2.3 Contact Degradation

Exposure to UV light has been shown to enhance photodegradation of the organic/LiF/Al interface within devices.[200,222] This has been shown to be due to the dissociation and diffusion of positive ions from this interface, likely due to LiF. This becomes problematic in this measurement during the η_{PL} measurement, as

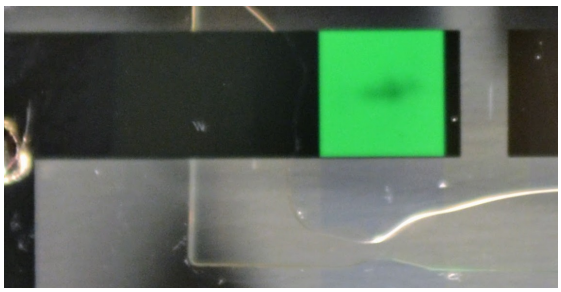

Figure 5.5: Dark spot formation on a device after exposure to a 405 nm laser.

illustrated in Figure 5.5. Here, the optical pump
has formed a dark spot on the active area of the device and accelerated degradation.

To minimize this behavior, the laser intensity incident on the device must be kept low. We have found that incident powers below 10 mW/cm^2 for a 405 nm laser do not exhibit dark spot formation. Devices can be inspected after lifetime testing to ensure that no visible degradation occurred. We have also observed that for longer wavelengths, the damage power threshold increases and higher power can be used.

5.2.4 Quenching Changes During Degradation

Equation 5.1 introduces a quenching term, η_τ, into η_{EQE} . This term captures bimolecular quenching losses which occur at high current and exciton densities. During lifetime measurements, the exciton density decreases as the efficiency reduces, which will change η_τ. To quantify this, the model presented in Chapter 4 can be used. Using this dynamics formalism, we can define η_τ as

$$\eta_\tau = \frac{1/\tau}{1/\tau + \frac{1}{2}k_{\text{TT}}\ n_{ex} + k_{\text{TP}}\ n_{pol}}. \tag{5.4}$$

To find η_τ at the end of degradation, the change in n_{ex}, n_{pol}, and τ must be known. The change in τ is known from η_{PL} . as discussed in Section 5.2.5. The exciton population, n_{ex}, is known from luminance as discussed in Chapter 4 and the temporal dependence follows the luminance loss assuming the radiative rate remains constant (which we assume). The polaron population likely increases to account for the decrease in our exciton density, but is difficult to quantify. Therefore, for this argument, we will assume it remains constant, though it will likely counteract some of the error that this method will estimate. With the temporal dependence of these quantities known, the time dependence of Equation 5.4 can be written as

$$\frac{\eta_\tau(t)}{\eta_\tau^0} = \frac{1/\tau}{1/\tau + \frac{1}{2}k_{\text{TT}}\ n_{ex} + k_{\text{TP}}\ n_{pol}} \frac{1/(R_{PL}(t)\tau) + \frac{1}{2}k_{\text{TT}}\ (R_{EL}n_{ex}) + k_{\text{TP}}\ n_{pol}}{1/(R_{PL}(t)\tau)} \tag{5.5}$$

where R_X is the degradation ratio of that term. Since degradation decoupling results are presented assuming $\eta_\tau(t) = C$, the presented out-coupling results can be corrected using $\eta_\tau^0/\eta_\tau(t)$ as a multiplicative correction factor, presented in Figure 5.6. In this figure, minimal correction is needed for low exciton and polaron populations. This only becomes important in regimes where bimolecular quenching are strong. Again, it is important to note that if changes in the polaron population are accounted for, this correction factor would be further reduced.

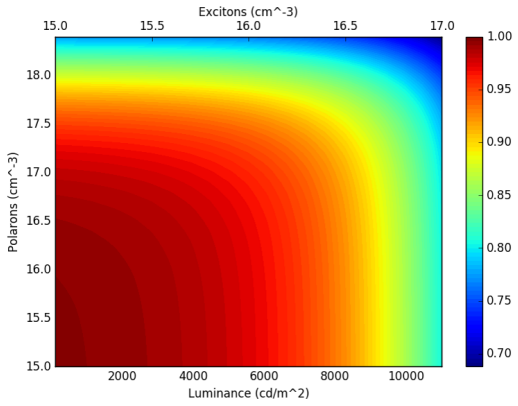

Figure 5.6: Multiplicative correction factor for exciton formation efficiency due to changes in quenching during lifetime. Shown as a function of polaron and exciton density as well as luminance, assuming a 10 nm emissive layer.

5.2.5 Exciton Lifetime Verification

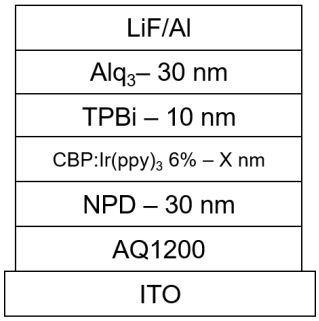

(a)

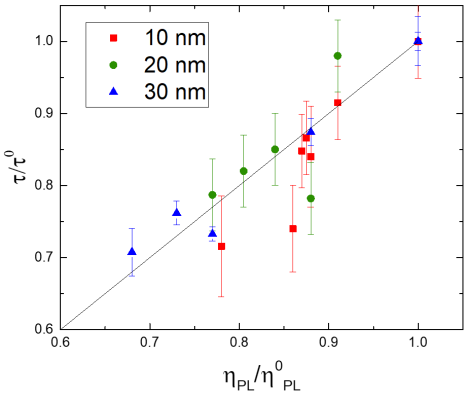

(b)

Figure 5.7: (a) Architecture of devices measured in (b) Exciton lifetime ratio extracted from transient PL measurements on degraded and undegraded devices as a function of PL degradation for several emissive layer thickness.

Alternative to the method for establishing the accuracy of the η_{PL} degradation presented in Equation 5.3, the exciton lifetime can be used. From photophysics, we have

$$\eta_{\mathrm{PL}} = \frac{k_r}{k_r + k_{nr}} \qquad \tau = \frac{1}{k_r + k_{nr}} \tag{5.6}$$

where k_r and k_{nr} are the radiative and non-radiative decay rates, respectively. From these equations, it is apparent that if k_r remains constant during the degradation,

$$\frac{\tau(t)}{\tau^0} = \frac{\eta_{\mathrm{PL}}\ (t)}{\eta_{\mathrm{PL}}\ ^0} \tag{5.7}$$

Therefore, if the exciton lifetime, τ is measured as a function of decay, it should have a 1-to-1 correlation with the observed PL loss if an accurate measure of η_{PL} is being conducted. In order to check this relationship, τ is measured from the transient photoluminescence decay at low pump intensity so that minimal triplet-triplet annihilation is observed. This is done on a 337 nm pulsed nitrogen laser, recorded with a fast photodiode connected to an oscilloscope. The result is shown in Figure 5.7b for the devices discussed in Chapter 6.1. The 1:1 relationship suggests that we are accurately measuring η_{PL} for this device. The large amount of scatter observed in the 10 nm EML results are believed to be due to the thin EML and small amount of material, producing low signal.

It is important to note that this confirmation of η_{PL} only demonstrates that no absorption or pump intensity deviations are causing error in the measurement. Since the transient photoluminescence and photoluminescence degradation are both pumped optically, both are subject to the recombination zone and absorption mismatch problem discussed in Section 5.2.2.

5.3 Experimental Implementation

5.3.1 Evolution of Experimental Approach

The conceptual idea of decoupling η_{EF} and η_{PL} during degradation was first investigated without specialized equipment. Devices were fabricated and aged to varying degrees in the same method as traditional lifetime measurements. After degradation, the device fluorescence was measured using a Photon Technologies International (PTI) fluorometer and compared to an undegraded device. In this way, the dependence of η_{PL} on time can be constructed, as shown in Figure 5.8. Though a proof of concept, this method suffers from experimental challenges. First off, experimental throughput is extremely low, since producing any η_{PL} curve requires separate aging of a device for every desired point. Even for the 5 point curves shown, this is extremely equipment heavy. Additionally, every point must be individually measured on the PTI, requiring substantial active lab time from the experimenter, as well as machine time. The second and more restricting problem with this technique is

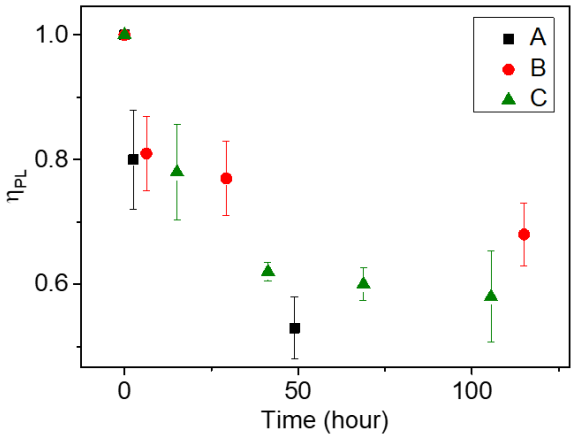

Figure 5.8: Initial Attempts at measuring η_{PL} during degradation using individual devices and fluorescence measurements.

the large error bars. As shown in Figure 5.8, with error bars of ±10%, it is impossible to differentiate between devices. These large error bars for any individual point are caused by differences in sample loading into the fluorimeter. Furthermore, this method has no way of eliminating sample-to-sample variation from the η_{PL} curve without reproduction of all experimental points, requiring dramatic increase in machine time. Because of this, only speculation as to the accuracy of the curvature and validity of any data point can be made. Comparison between devices, especially in the temporal behavior becomes impractical due to the experimental time and uncertainty.

These initial experimental techniques demonstrated the need for a new testing method. Ideally, this method would automatically measure η_{PL} on the same sample, dramatically reducing experimental time and throughput limitations. This automatic measurement can have the added benefit of reducing measurement error by holding the sample fixed throughout the decay and ensuring alignment. While sample-to-sample variation may still be an issue, it is no longer a problem in collecting a full dataset.

5.3.2 Development

In order to accomplish this automated measurement, the η_{PL} measurement needed to be conducted under computer control. A light source capable of producing a constant illumination source over the course of hundreds of hours was needed. A lamp source, such as the PTI was initially considered, but found to have lifetimes similar to the OLED lifetimes. The lamp would not be able to be turned on and off throughout the test since lamps require substantial warm up time to achieve steady-state. Instead, a laser was used since they can be rapidly turned on and off, eliminating any need for blocking the light source during EL measurement. To account for any fluctuations in laser power over time, the power can be measured as a function of time and corrected for if needed.

The first generation implementation of this setup is shown in Figure 5.9. This was a single channel apparatus with the laser and splitter shown in the Figure 5.9a on the left and the device and photodiode collection shown on the right. Laser power detection relied on the split signal into the photodiode. Home-built electronics, shown in Figure 5.9b, control the laser, current source and voltage measurements, and photodiode measurements. The laser was controlled by switching the interlock using an Arduino (red PCB). A constant current source was implemented, with the current being set using the potentiometer on the front of the box. This had to be set and measured manually and was only recorded in the software, not set. Photodiode signals were converted to voltages using the green PCB and recorded using the Arduino. The software, shown in Figure 5.9d recorded all

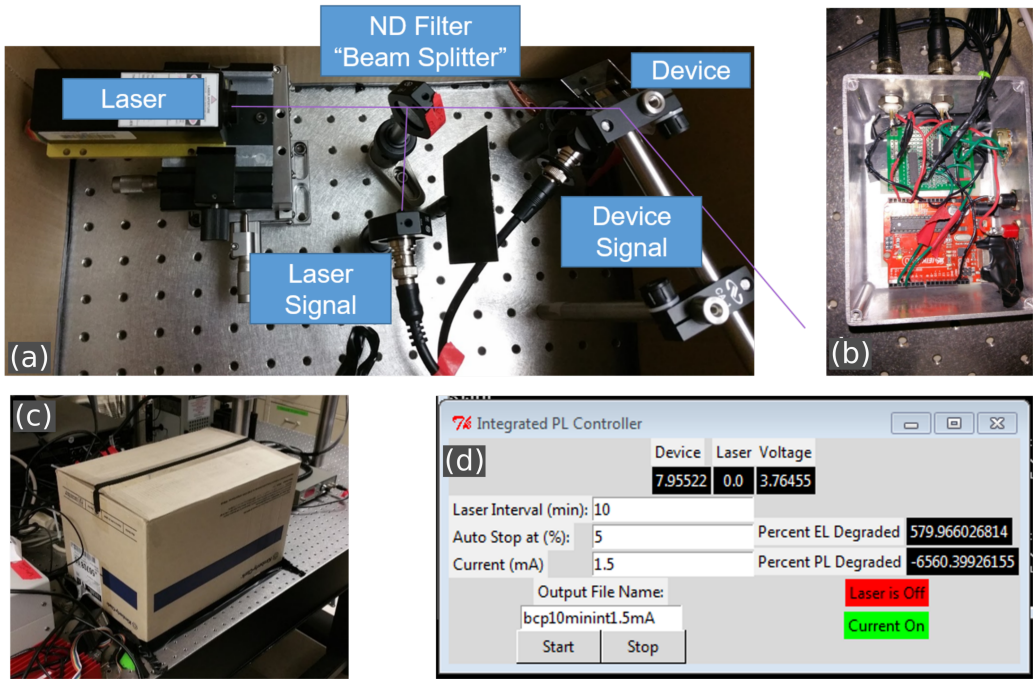

Figure 5.9: First generation lifetime box setup. (a) Box layout (b) Electronics (c) Dark enclosure (cardboard box) (d) Software interface

measurements and controlled the current, laser, and measurement timings. This was implemented in Python, using the Tk graphics library to create the GUI. At this initial stage, the software only had to interface with the Arduino, and did so using the Serial library. The Arduino was programmed to accept commands to turn on and off the laser and current, or report measurement values for voltage and the signals from either photodiode.

Soon after development, the limited resolution of the photodiode measurements, as well as the limitations of the manual current source were realized. In conventional measurements of lifetime, a Keithley 26XX source meter was used for sourcing current and measuring signals. This Keithley was rapidly integrated into the system to allow better measurements and more accurate current control. The laser was upgraded to realize brighter and more stable power, as well as programmatic control.

After this early development and hardware changes, little has changed about general workflow of this experiment. However, rather than individual boxes for each experiment, a single laser has been multiplexed to excite up to six different devices, dramatically cutting costs. Each experimental setup consisting of a single laser and multiple testing devices is termed a b̈ox;̈ with each device residing in a c̈ompartment.̈ A summary of all hardware and software connections and control is shown in Figure 5.10. There are two different hardware configurations shown, interfacing with different source-meters. In the top configuration, each compartment is controlled by an individual Keithley

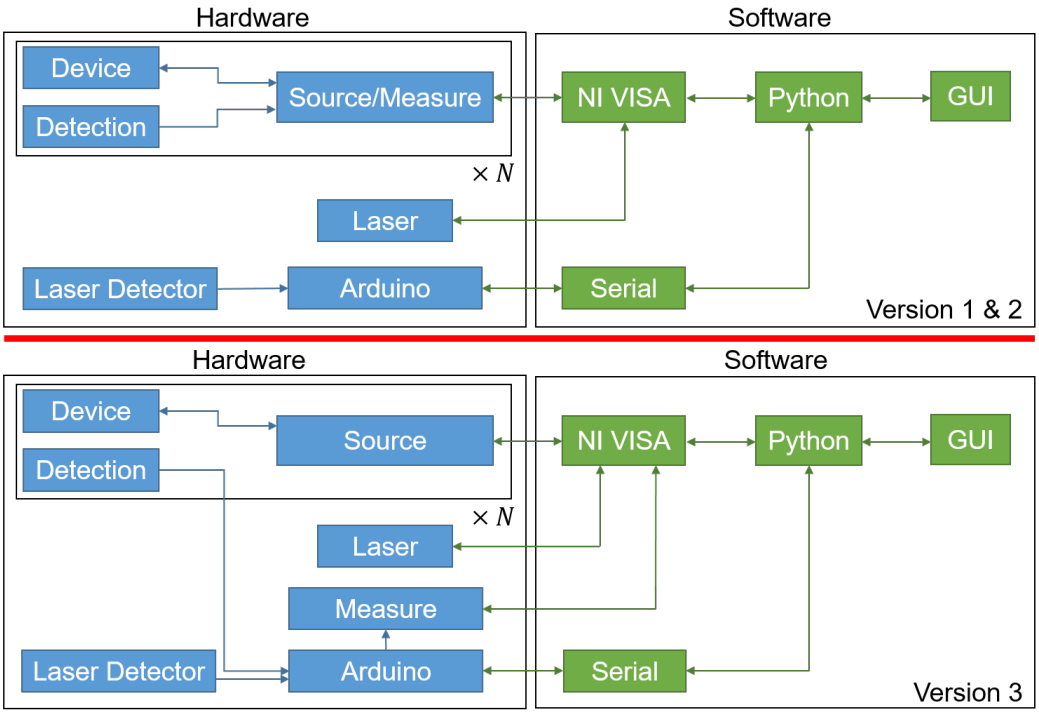

Figure 5.10: Box workflow summary. (Top) The operation of Boxes 1 and 2, (Bottom) Box 3.

source-meter. In the bottom configuration, to cut costs, a Keysight source-meter is used to supply current. The photodiodes in each box are measured by a single Keithley, switching between each compartment using an Arduino relay circuit. This allows a dramatic reduction in hardware and costs.

The next two sections go into detail regarding the implementation of of the hardware and software setups.

5.3.3 Hardware Setup

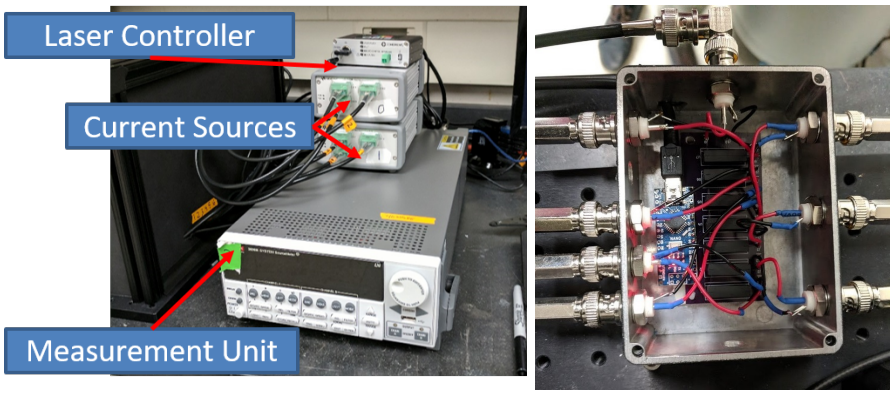

Figure 5.11: Source-Measure hardware and laser controller

Hardware for this setup requires control of current sources, voltage measurement, light source, as well as light measurements. Currently, there are four operational testing setups, termed "boxes", with varying hardware configurations. Several boxes are multiplexed to allow multiple measurements from the multiple compartments. Source units for providing current and voltage measurements have used either the Keithley 26xx or Keysight u2722a source meters.

The Keithley 26xx units are a two channel, low noise, high precision unit. The Keysight u2722a provides three channels with higher noise and lower precision at a lower price point per channel. Light sources for all boxes are conducted using Coherent OBIS lasers, with wavelengths of either 405 nm or 473 nm. Light measurements are conducted using the Keithley 26xx for all boxes, connected to a Hamamatsu S2281 photodiode. Figure 5.11a shows the electronic hardware setup for a box utilizing Keysights for source units and a Keithley for measurement. To reduce measurement units, the photodiodes in each compartment can be switched between using an Arduino relay system shown in Figure 5.11b. All of these pieces of hardware are compatible with the National Instrument VISA command library for control.

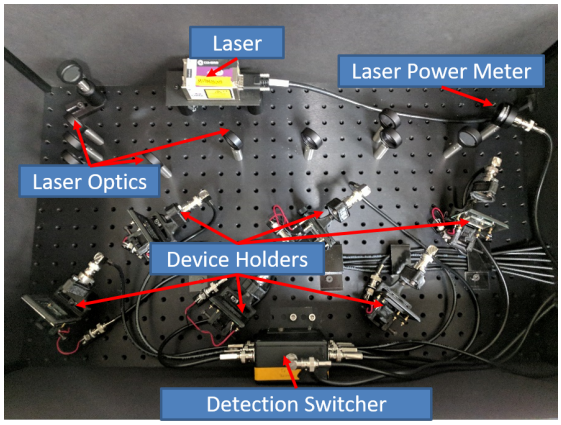

Figure 5.12: Device contacting, measurement, and optical hardware. Version 3 of the hardware is shown. Controlling hardware is shown in Fig. 5.11

Each device is held by a custom 3D printed vertical mount. The photodiode is wired into this mount with enough space for the laser to avoid the diode. A long pass filter is provided to minimize stray laser signal. The laser is optically split into six paths using beam splitters and neutral density filters are used where necessary to normalize laser power on each device.

5.3.4 Software Development

Software to control this measurements is implemented in Python and outlined in Appendix G. The code is able to control the hardware to run constant current, intermittent laser integrated PL measurements, optical degradation, as well as optical degradation with current break degradations. The frequency of laser breaks and laser power can be controlled on a whole box level. Laser emission can be turned on for alignment. The software is able to be configured to the number of channels available depending on the hardware. Each channel can be individually controlled for current, stop,

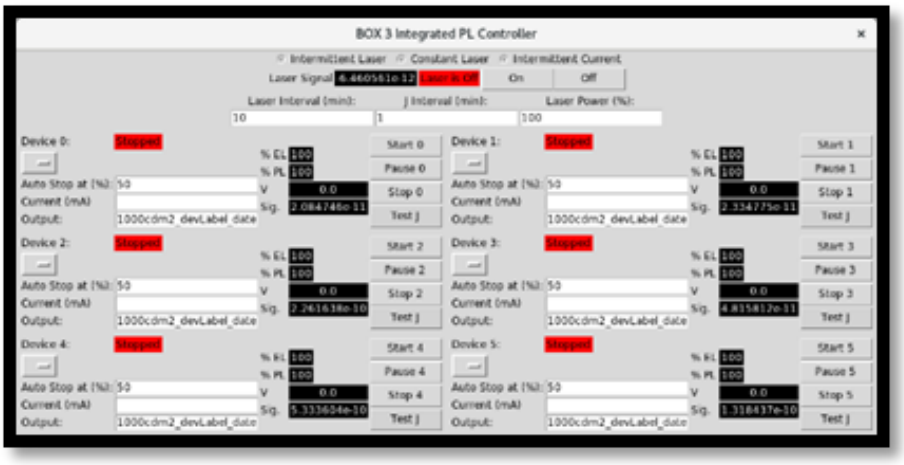

Figure 5.13: 6 channel software controller. Selection of test type, laser control for alignment, and global settings are accessible on the top of the interface. Individual channel settings are grouped on the bottom.

and labeling.

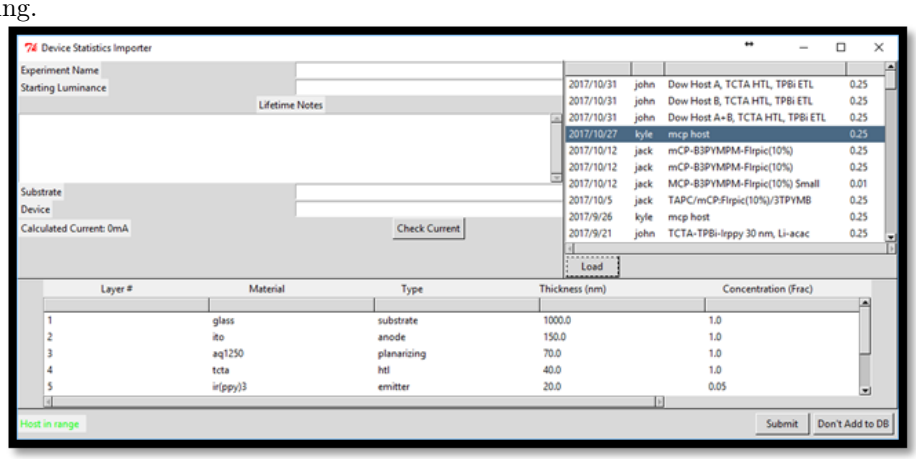

Figure 5.14: Test information for database import interface. The top left panel collects information about the specific device and lifetime. The right panel connects the device to a particular growth and architecture. The bottom panel confirms the architecture.

To organize collected data, a database for all lab data has been developed and is discussed in Chapter 9. Lifetimes integrate with this system when lifetimes are started, using the interface shown in Figure 5.14. Here, a lifetime test is connected to a particular growth, as well as the individual substrate and device pixel. Information about the lifetime is also connected. The lifetime operating current can be determined for a desired luminance by utilizing the current-voltage-luminance curve for the exact device within this interface. Additional notes and information are also able to be stored.

5.4 Conclusion

This chapter has outlined a system for decoupling degradation during operational lifetimes. Extensive care has been taken to outline the assumptions and assess error within the extracted parameters. Many of these assumptions need to be assessed for any device system to be tested to ensure accuracy. Applying this method to lifetime decoupling in device systems is the subject of Chapter 6.

The additional information offered by the decoupling technique described in Chapter 5 is directed at improving the screening of active materials and device architectures for the realization of long-lived OLEDs. Device degradation that is dominated by a loss in either η_{EF} or η_{PL} implies a dominant rate process and an opportunity for improvement of materials or architecture. In systems using a relatively stable emitter with demonstrated long optical and electrical lifetimes, such as $\mathrm{Ir(ppy)_3}$,[93] losses in the exciton formation efficiency are expected to represent the majority fraction of degradation. However, for novel molecules, limiting processes are largely unknown and would benefit from the separation of emitter and exciton formation efficiency loss. PL degradation could become increasingly important for blue-emitting species where the high exciton energies could contribute to material degradation.[93,155,226–229] This screening process would be dramatically improved if η_{EF} and η_{PL} can be mechanistically modeled. With additional datasets, modeling and understanding of degradation mechanisms can be improved and help to identify limiting processes. The model presented in Giebink et al. [83] could easily be adapted to separate losses that would be captured by η_{PL} and η_{EF} , and would provide further checks to this over-parameterized model.

Chapter 6

Decoupling Degradation Mechanisms - Application to OLEDs

Chapter 5 discussed a novel approach for decoupling lifetime. The studies in this chapter use this technique and exploit this additional information to better understand device behavior. This includes discussions of Hershey et al. [153] in Section 6.1, Bangsund et al. [154] in Section 6.2, as well as unpublished work in Section 6.3. The work presented in this chapter was done in collaboration with John Bangsund and Gang Qian. This chapter is organized into three sections, for these different works.

6.1 Ambipolar Host EML Thickness Dependence

6.1.1 Motivation and Experimental

Carbazole materials are archetypical hosts for phosphorescent devices, most common among them being 4,4'-Bis(N-carbazolyly)-1,1'-biphenyl (CBP).[61,126,202,230–234] These devices have a large range in device lifetime with architecture, and were a prime candidate for investigation with the decoupling method for isolating these lifetime sensitivities. Devices consisted of a 40-nm-thick hole-injection layer of Plexcore AQ1200 spun-cast on a glass substrate coated with a 150-nm-thick layer of indium-tin-oxide (ITO), followed by a 30-nm-thick hole-transport layer of N,N' -Bis(naphthalen-1-yl)-N,N' -bis(phenyl)-benzidine (NPD), and an EML of 4,4'-Bis(N-carbazolyl)-1,1'-biphenyl (CBP) doped at 6 vol. All devices were fabricated according to the processes outlined in Chapter 3.2. The structure shown in Figure 6.1a was used with EML thicknesses of X=10, 20, and 30 nm. The η_{EQE} for all three

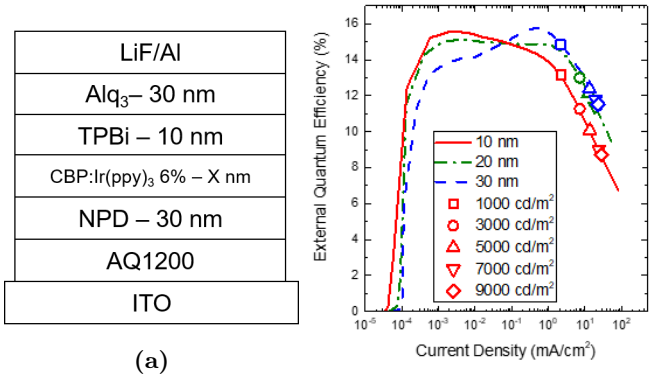

Figure 6.1: a. Device architecture, featuring EML thicknesses of X=10,20, and 30 nm. b. External Quantum Efficiency (η_{EQE}) for the three architectures. Operational points for lifetime are shown in symbols.

EML thicknesses, shown in Figure 6.1b, shows maximum efficiencies of 15.7%, 15.3%, and 15.7% for EML thicknesses of 10, 20, 30 nm, respectively. Though similar in peak value, as thicknesses increases, the peak η_{EQE} shifts to higher current. This is indicative of a shift in the charge dynamics and possible location of the recombination zone (RZ). Recombination zone has been previously linked with lifetime, with a longer lifetime expected for thicker RZ.[171,174–182] For a well balanced device, one would expect that expanding the EML would result in a wider RZ and thus longer lifetime.

6.1.2 Device Stability

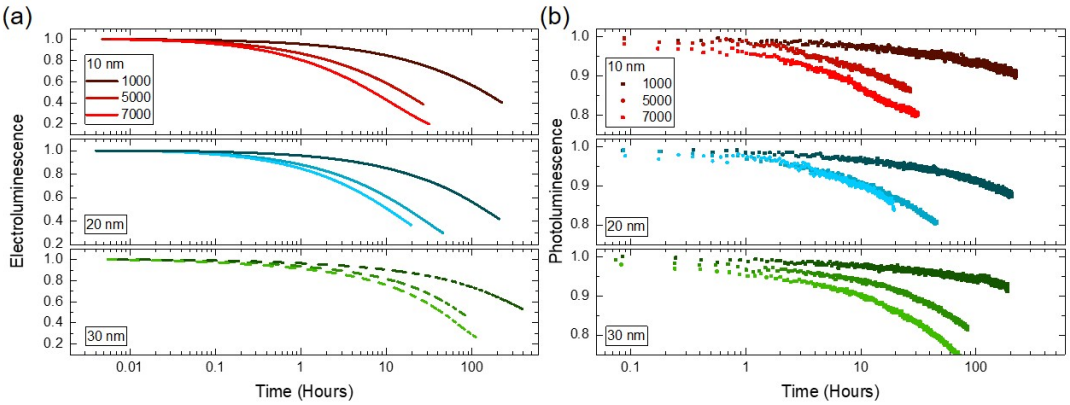

Figure 6.2: Device decay curves for multiple values of the initial luminance as a function of emissive layer thickness. Loss in (a) electroluminescence (EL) and (b) photoluminescence (PL) are shown and decrease monotonically with increasing luminance. For devices with a 10-nm-thick emissive layer, initial luminance values are 1000 cd/m^2, 5000 cd/m^2, and 7000 cd/m^2. For devices with a 20-nm- or 30-nm-thick emissive layer, initial luminance values are 1000 cd/m^2, 5000 cd/m^2, and 7100 cd/m^2.

Figure 6.2a shows the conventional EL lifetimes of these devices, and indeed the 30 nm EML shows a longer lifetime than the 10 and 20 nm. In Figure 6.2b, the intermittent η_{PL} measurements can be seen, discussed in Chapter 5, showing the advantage of this technique and the large amount

of additional data that is available. The operational conditions of each device is shown in Table 6.1. Similar currents are used across EML thicknesses, but voltage increases slightly with thickness, as might be expected. No birefringence was seen under cross polarization after degradation, and no new emission features were observed with degradation, verifying that η_{OC} and χ remain unchanged during degradation, as discussed in Chapter 5.

The lifetime decreases with luminance for all architectures. While a reduction in the EL lifetime is observed in Figures 6.2 and 6.3 in reducing device thickness from 30 nm to 20 nm, little difference is seen between devices having EML thicknesses of 20 nm and 10 nm. The degradation in the PL intensity does not appear to be a strong function of EML thickness. Indeed, comparing the EL and PL lifetimes with the extracted degradation in exciton formation shows that the EL decay is dominated by a loss in the efficiency of exciton formation with η_{EF} reaching 60% of its initial value by the time EL has reached 50%. A substantial component of this decay is likely due to non-radiative recombination center formation.[185,189] Over this same period, the PL intensity has only degraded by 10% of its initial value.

d_{EML} (nm)	L_0 (cd/m^2)	J (mA/cm^2)	V_0 (V)	t_{50} (hours)
10	1000	2.2	4.2	139.0
	3000	7.2	5.1	39.9
	5000	13.6	5.4	15.8
	7000	14.4	6.2	6.9
	9000	28.0	6.3	5.3
20	1000	2.2	5.4	141.1
	3000	7.2	6.0	33.1
	5000	12.4	7.2	17.2
	7100	19.2	7.3	10.0
	9000	24.0	7.5	8.0
30	1000	2.2	5.9	474
	5000	13.6	7.3	74.4
	7100	19.6	7.6	46
	8000	22.4	7.7	38.1

Table 6.1: Summary of device lifetimes. For each device, the starting luminance (L_0), current density (J), starting voltage (V_0) and time at which 50% of the initial luminance is reached (t_{50}) are reported.

The similarity in PL degradation observed across all EML thicknesses suggests that the exciton and polaron densities are similar between these devices,[83,139,140] and that they have similar exciton recombination zone widths. The accelerated degradation in the exciton formation efficiency (η_{EF}) observed for devices with EML thicknesses of 10 nm and 20 nm suggests that the recombination zone samples the EML/TPBi interface, which has been previously shown to cause degradation.[52,198] This change in recombination zone location is also suggested by the η_{EQE} behavior shifting peak

location, shown in Figure 6.1b To validate this suggestion, the position of the recombination zone was assessed in the devices with EML thickness of 20 and 30 nm devices using a quenching TPTBP sensitizer. The position of the recombination zone can be inferred by the corresponding reduction in device η_{EQE} due to quenching by TPTBP,[138] as discussed in Chapter 3.6. The sensitized 30-nm-thick EML devices showed no quenching, suggesting no recombination near the interface, while devices with a 20-nm-thick EML showed quenching only at the EML/TPBi interface, confirming the position of the recombination zone at that interface. Devices with a 10-nm-thick EML exhibited changing current-voltage behavior when sensitized with TPTBP, and thus PtTPTBP, an emissive sensitizer with a peak wavelength of 770 nm, was used in 2-nm-thick strips on either side of the EML at 0.5 vol. %. This configuration was able to match the current-voltage behavior of the control device while permitting the measurement of emission from PtTPTBP. For devices with a 10-nm-thick EML, strong emission from PtTPTBP is observed from the EML/TPBi interface and weak emission seen from the EML/NPD interface. These quenching experiments are shown in Figure 6.4. These results suggest that for devices with an EML thickness of 10 nm or 20 nm, the recombination zone samples the EML/TPBi interface, accelerating exciton formation loss. While detailed analysis of the relevant degradation mechanism is the subject of future work, previous work has suggested a role played by exciton-polaron interactions.[83,172,185,189,197]

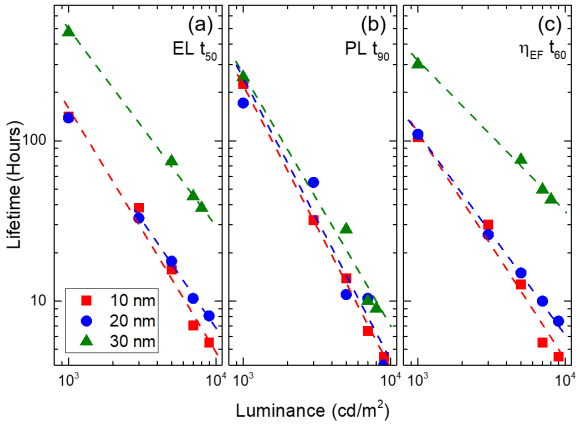

Figure 6.3: Extracted lifetimes for all 3 architectures as a function of luminance. (a) EL t_{50} (b) PL t_{90} and (c) η_{EF} t_{60}.

6.1.3 Conclusion

In summary, this work presents a method for decoupling optical and electrical losses during OLED operational decay by attributing the overall reduction in electroluminescence to a loss in η_{PL} or the exciton formation efficiency through η_{EF} . Model devices are shown as a function of luminance, with a loss in η_{EF} shown to be the limiting factor for the short-lived devices. By measuring the RZ, these devices are shown to be subject to interfacial degradation, only seen in narrow EML devices. Contrary to the expectation, the RZ is not found to expand with the EML thickness, but rather to shift within the device.

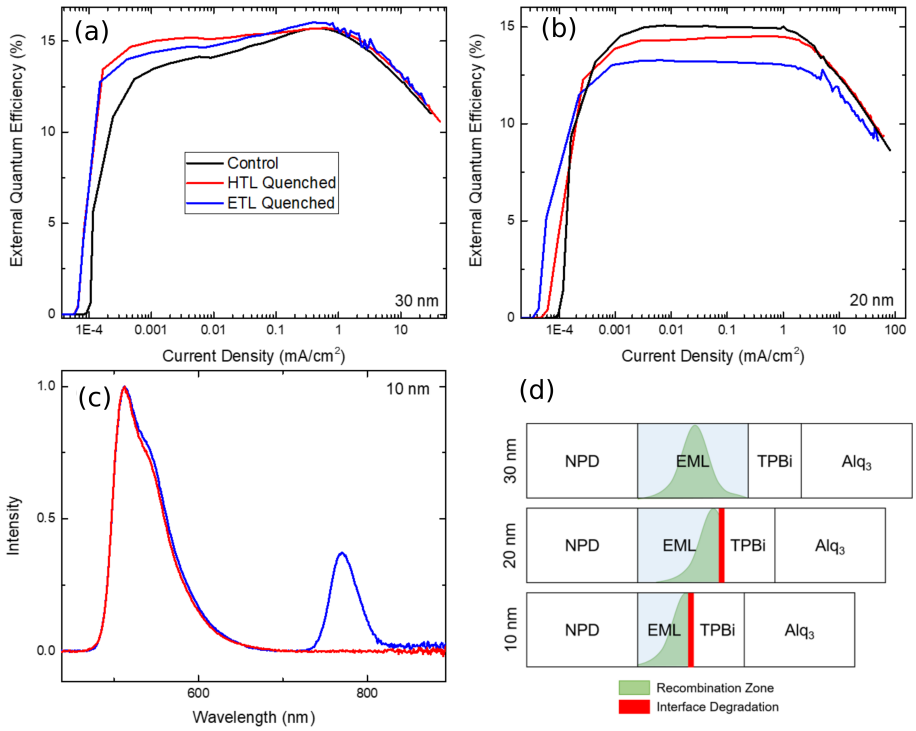

Figure 6.4: (a) η_{EQE} as a function of current denisty for TPTBP quenched 30 nm devices. No quenching is observed in the peak η_{EQE} . (b) η_{EQE} as a function of current density for TPTBP quenched 20 nm devices. Quenching is observed for the ETL side quencher, and minimally for the HTL side. (c) EL spectra for PtTPTBP quenched 10 nm EML devices. Emission from the sensitizer only at the ETL. (d) Summary of recombination zone measurements. The 30 nm device shows an RZ that is centered, while the 20 and 10 nm devices have an RZ peaked at the TPBi interface.

The behavior of η_{EF} and η_{PL} with thickness depends on the architecture system. In fact, the remaining sections of this chapter will offer alternative cases, showing differing behavior.

6.2 Mixed Host OLED Luminance Scaling

6.2.1 Motivation

As discussed in Section 6.1, RZ width has been extensively connected with lifetime, mediated by the exciton and polaron populations.[83,93,152,171–173,175,177,235] However, despite this observed trend with RZ thickness, the specific role of the RZ in degradation kinetics is still an active area of investigation. Using a mixed emissive layer (M-EML) architecture, the work described in this section seeks to provide a more concrete connection between the RZ and degradation within the same system.

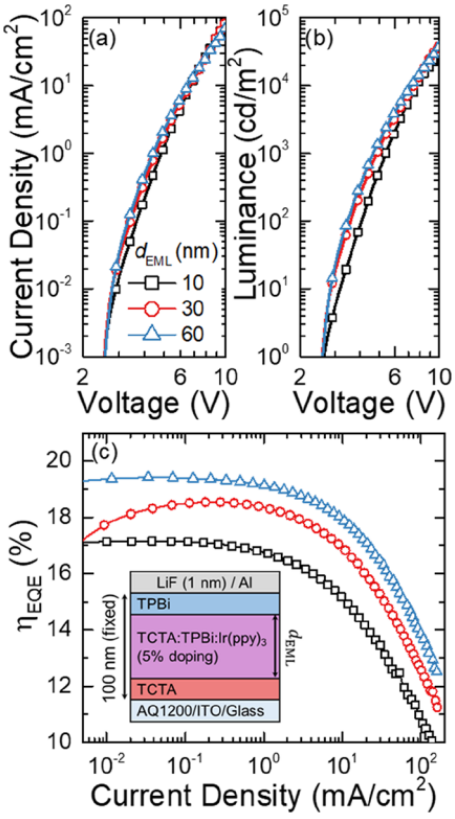

Figure 6.5: (a) Current Density and (b) Luminance as a function of Voltage. (c) η_{EQE} for all three EML thicknesses. Inset is M-EML device architecture.

6.2.2 Experimental

Devices consisted of a 60-nm-thick hole injection layer (HIL) of poly(thiophene-3-[2[(2-methoxyethoxy)ethoxy]-2,5-diyl)(AQ1200, Sigma Aldrich), a 4,4',4"-tris(N-carbazolyl) triphenylamine (TCTA, TCI America) hole-transport layer (HTL), a mixed-host emissive layer (M-EML) consisting of a 47.5 vol.% TCTA, 47.5 vol.% 2,2',2"(1,3,5-benzenetriyl) tris-(1-phenyl-1H-benzimidazole) (TPBi, Lumtec) and 5 vol.% of the green phosphorescent emitter, $Ir(ppy)_3$, a TPBi electron-transport layer (ETL), and a LiF (1 nm)/Al (100 nm) cathode. All layers were deposited according to the procedures outlined in Section 3.2. When varying the M-EML thickness (10 nm, 30 nm, 60 nm), the HTL and ETL thicknesses are varied equally to maintain a total device thickness of 100 nm. Device characteristics are shown in Figure 6.5, with the efficiency increasing slightly from 17% to 19% as the EML thickness increases from 10 to 60 nm.

This device architecture system, shown in the inset of Figure 6.5, was chosen because of its broad RZ, which spans the entire EML.[138] Because of this property, the M-EML thicknes, d_{EML} can be taken as a proxy for the RZ width, and the exciton density can be controlled by modifying the EML. The increase in RZ thickness is evidenced by the change in onset of the roll-off with increasing RZ

width, seen in Figure 6.5c.

To experimentally confirm the RZ breadth, the 60 nm EML architecture was investigated using PtTPTBP as a sensitizer, using the methodology outlined in Chapter 3.6. The exciton density is found to remain above 60% of the peak across the entire 60 nm M-EML at a current density of 10 mA/cm^2, shown in Figure 6.6. As current density increases from 0.1 mA/cm^2 to 10 mA/cm^2, the peak of the RZ migrates from the ETL side to the HTL side of the M-EML. These findings are consistent with other reports for similar device architectures,[138] and confirm that d_{EM} is a good proxy for RZ width. The 60 nm EML is the thickest investigated EML thickness and should be subject to the most variation in RZ intensity accross the EML. Therefore, thinner EML devices are also assumed to have a RZ spanning the EML.

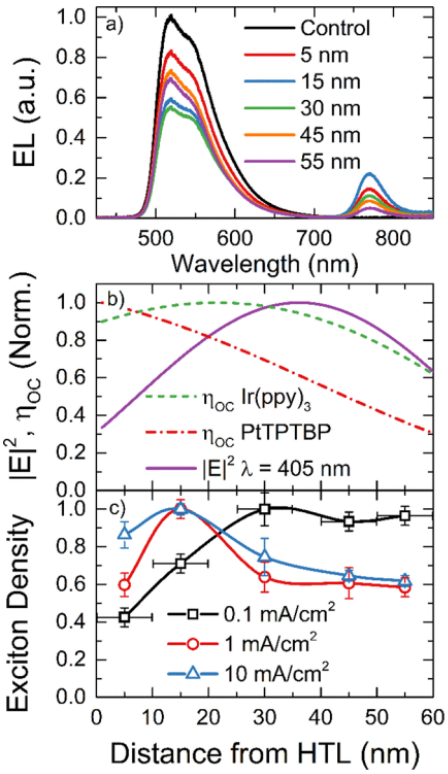

Figure 6.6: (a) Raw spectra of sensitized devices. (b) Out-coupling efficiency for Ir(ppy)$_3$ and PtTPTBP across the EML as well as electric field profile. (c) RZ as a function of current density. For all currents, the RZ is found to span the entire EML.

6.2.3 Device Stability

The degradation of these devices at a initial luminance of L_0=3,000 cd/m^2 is shown in Figure 6.7a. The EL lifetime increases by approximately a factor of 3 in increasing the thickness from 10 nm to 60 nm, and nearly all this enhancement can be attributed to a reduced rate of PL degradation, shown in Figure 6.7b. No trend with thickness is apparent in the η_{EF} decays, which are all within typical device-to-device variation. In contrast, the PL decays show a dramatic separation with thickness. We also note that a reduction in η_{EF} dominates the overall degradation rate in the 30 nm and 60 nm thick M-EML devices, but is comparable to PL losses in the 10 nm M-EML device. These results suggest that reduced degradation in emissive layer PL efficiency may be the primary reason for enhanced stability in M-EML architectures, as compared to with their single-host counterparts. Moreover, the combination of improved efficiency roll-off and PL lifetime with an increased RZ width, and thus decreased exciton density, provides further evidence of a link between bimolecular annihilation events and the degradation of PL efficiency.[235] Losses in η_{EF} , however, appear to be relatively

insensitive to exciton density.

To show that exciton density and PL loss are intimately related, the exciton density was matched between architectures by scaling the luminance to the EML thickness ratio. The 10, 30, and 60 nm EML devices were operated at initial luminances of 1,000, 3,000, and 6,000 cd/m^2, respectively. The results of this aging are shown in Figure 6.8. PL degradation is nearly identical for 10, 30, and 60 nm M-EML devices operated at luminances of 1,000, 3,000, and 6,000 cd/m^2, respectively. Exciton formation efficiency losses, in contrast, are rapidly accelerated as luminance is increased. At long times, the PL degradation slows slightly with increasing M-EML thickness, and this is attributed to large differences in exciton formation efficiency losses. The exciton density does not remain matched over the course of the entire test due to differences in η_{EF} losses, and consequently the formation rate for exciton quenchers is reduced at long times in thicker M-EML devices. This observation of matched PL losses under scaled luminance has been reproduced under a range of scaled luminances from 330 cd/m^2 to 15,000 cd/m^2, showing the same trend. Despite comparable exciton densities in the emissive layer, exciton formation efficiency losses differ substantially, and appear to scale with increased luminance and current density. Increased current density would result in a larger polaron density in the transport layers and could lead to an increase in the rate of defect formation mediated by unstable cationic or anionic molecules. Alternatively, the trend with luminance could be explained as an increase in interfacial photodegradation of the cathode or anode due to device electroluminescence.[200,236]

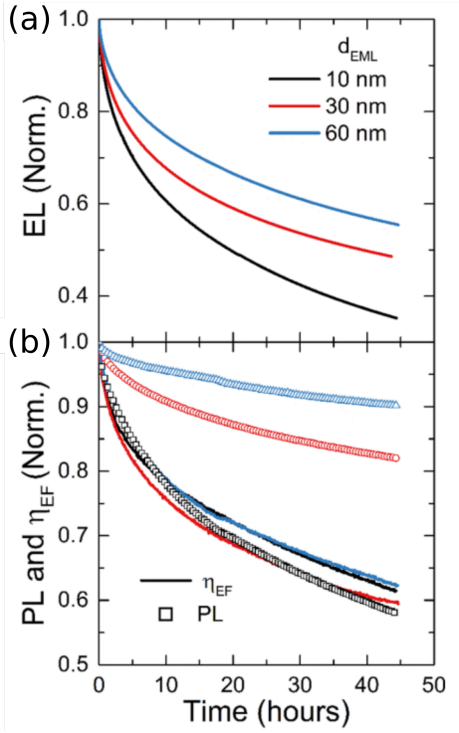

Figure 6.7: (a) EL lifetime at 3,000 cd/m^2 for EML thicknesses of 10,30,60 nm. (b) The corresponding η_{PL} and η_{EF} degradation.

An alternative approach to investigating this connection is to look at the scaling relationships with luminance and exciton density. OLED lifetime has been widely observed to follow a $1/L_0^n$ relationship,42 where L_0 is the initial luminance, and n is a device specific parameter typically between 1-2. For these devices, $n = 1.8 \pm 0.1$ for the t_{50} of EL and is independent of M-EML thickness. As shown in Figure 6.9a, the degradation in η_{PL} and η_{EF} for a 60 nm M-EML show similar acceleration behavior as a function of luminance, with $n = 1.8$ and $n = 1.75$, respectively. Comparable slopes are seen for 10 nm and 30 nm M-EML devices.

However, when scaled by $1/d_{EML}$, as displayed in Figure 6.9b, η_{EF} and η_{PL} show distinct scaling behavior. While PL t_{85} shows a slope of $n = 1.9 \pm 0.3$, almost identical to the slope under luminance acceleration, η_{EF} t_{85} shows a much shallower slope of $n = 0.5 \pm 0.2$ (decreasing to $n = 0.3 \pm 0.3$ at 10,000 cd/m^2). This raises several important implications. First, the identical slopes for PL provide further evidence that PL losses in this system are determined by the exciton density and the width of the RZ, and imply that there is a direct scaling law between RZ width and PL lifetime. While polaron density can play a role in PL degradation as well, it is unlikely that polaron density scales identically with both luminance and d_{EML}, implying that a single exciton driven or an exciton-exciton annihilation driven degradation mechanism is dominant in this system.

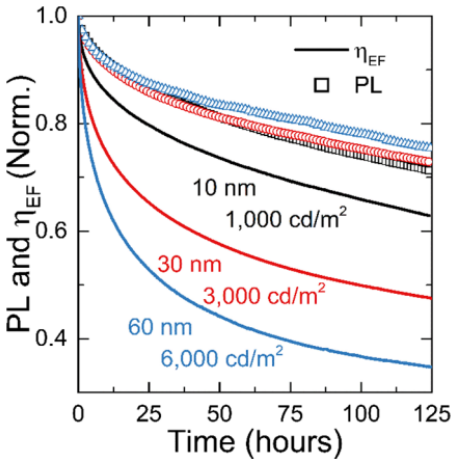

Figure 6.8: Lifetimes of devices with luminance scaled to match the EML thickness. PL collapses due to matched exciton density.

Second, the shallow dependence of η_{EF} t_{85} on RZ width (and hence exciton density) shown in Figure 6.9b suggests that excitons play a lesser role in η_{EF} degradation. Notably, the difference in scaling with L_0 and d_{EML} for η_{EF} t_{85} suggests that multiple degradation mechanisms comprise the total η_{EF} loss. Exciton formation loss is often attributed to the accumulation of non-radiative recombination centers in the emissive layer,[185,189] and has been linked to exciton-polaron interactions.[237] The shallow dependence on RZ width (and hence exciton density) shown in Figure 6.9b suggests that the d_{EML}-dependent increase in η_{EF} degradation to reflects the generation of non-radiative recombination centers by an exciton-mediated process, consistent with these reports. However, this mechanism alone cannot fully account for degradation in η_{EF} , as the slope against initial luminancescaling with L_0 is much steeper (Figure 6.9a). This contrasting behavior suggests that a second mechanism which is independent of emissive layer exciton density governs η_{EF} losses. This behavior is consistent with degradation mediated primarily by polarons or photodegradation of the cathode or anode interface, and may originate outside of the emissive layer.[200,236]

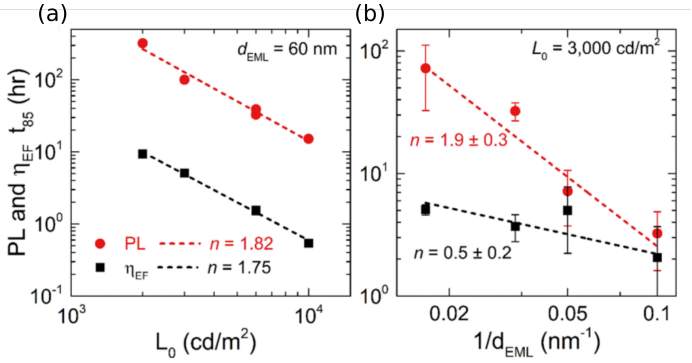

Figure 6.9: Scaling behavior of η_{PL} and η_{EF} as a function of (a) luminance and (b) exciton density.

These findings have implications for efforts in modeling OLED lifetime. Most modeling approaches assume that the same defect population responsible for exciton quenching was also responsible for non-radiative recombination of charge carriers. This immplies that the quenching population resides entirely in the emissive layer.[83,174] Defect populations external to the emissive layer have been considered, but only for the purposes of fitting voltage rise.[140] In all cases, the generation of defects is proposed to proceed via bimolecular quenching processes. While these treatments have yielded reasonable fits of the overall degradation behavior, they are unable to capture the behavior observed here. Exciton formation and PL degradation would be expected to trend together within these formalisms, whereas Figure 6.9 shows clearly distinct scaling behavior. Our results thus show that losses to η_{PL} and η_{EF} likely originate from kinetically distinct mechanisms. Moreover, the weak dependence of η_{EF} on exciton density indicates and that degradation defects external to the emissive layer may play an important role in luminance loss, and should be considered in future modeling attempts. Non-radiative recombination centers could have suitable energetics to serve as exciton quenchers, and vice versa. However, because losses in η_{EF} and η_{PL} show different dependences with initial luminance and M-EML thickness, the exciton quenchers formed in the EML are likely inefficient non-radiative recombination centers for charge carriers.

6.2.4 Conclusion

In conclusion, we find that broadening the RZ sharply reduces the rate of PL degradation, showing a similar scaling relationship as with initial luminance variation. This confirms that PL degradation is strongly dependent on exciton density and has minimal dependence on changes in the polaron density as driven by the RZ. However, losses in the exciton formation efficiency (η_{EF}) show a weaker dependence on RZ width, suggesting that η_{EF} losses are less sensitive to exciton density and may partly originate outside of the M-EML in this system. Notably, the different dependences of PL and exciton formation efficiency loss on RZ width provide clear evidence that kinetically distinct pathways drive OLED degradation, and that a single degradation mechanism cannot be assumed when attempting to model device lifetime. These results highlight the capability of decoupled measurements of η_{PL} and η_{EF} losses to yield useful diagnostic insight into the source of device instability and shed light on the kinetics of degradation and the nature of defects.

6.3 Application to Commercial Co-Host System

6.3.1 Motivation

In addition to my collaborator John Bangsund, I would also like to acknowledge contributions from from authors at The Dow Chemical Company, Dominea Rathwell, Peter Trefonas, Hong-Yeop Na, and Jeong-HwanJeon.

The previous two sections present two alternaitive machanisms for the dominant degradation pathway within devices, being interfacial and exciton density driven degradation. Both of these mechanisms are common explanations for device behavior in the literature. The rate of OLED degradation is widely regarded to depend strongly on the exciton density via exciton-exciton and exciton-polaron processes.[83,93,154,173,182,238] The width of the RZ determines the exciton density for a given luminance, and hence sets the rate of emissive layer degradation.[154,171,174,175] In other works, the absolute position of the RZ is shown to be significant, as proximity to a transport layer interface can exacerbate degradation,[52,153,239] or can influence exciton confinement and charge balance.[139,155] In studies showing interfacial degradation, the RZ is typically heavily pinned at the degrading interface. These two mechanisms are often view as seperate issues: for devices with pinned RZs, interfacial degradation is assumed dominant, but for well distributed RZs, broader is viewed as better.

This study presents a unique counter example, in which for commercial materials, both types of degradation are shown to be influential as a function of host material concentration. Using a co-host system, we find that lifetime can be significantly improved compared to single-host devices despite a reduction in RZ width. Most other works on mixed host emissive layers have employed exciplex-forming pairs which jointly show more balanced electron and hole mobilities than either host alone, leading to a broad RZ which spans the majority of the EML.[157,171,240,241] In this work, an ambipolar host, which features a broad RZ, and a wide energy gap host are used. Measurements of the RZ confirm that the mixed host decreases the RZ width and shifts the RZ away from the hole transport layer (HTL). The increased degradation rate due to a higher exciton density is offset by reduced degradation at the HTL/emissive layer (EML) interface, leading to an overall enhancement in device lifetime.

6.3.2 Experimental

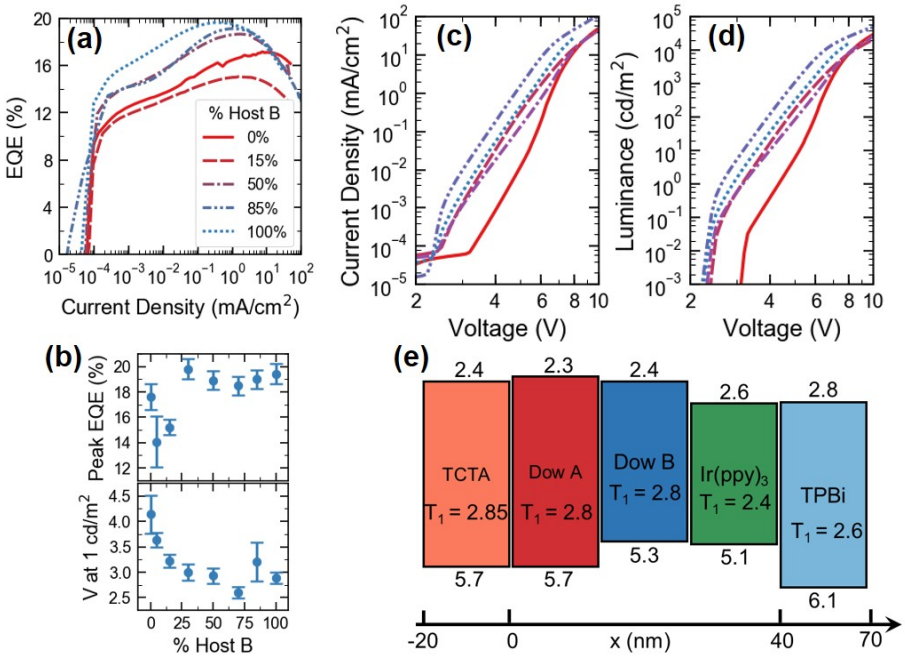

Figure 6.10: (a) η_{EQE} for selected host compositions. (b) Peak efficiency and turn on voltage as a function of host composition (% B). (c) and (d) show current density and luminance as a function of voltage. (e) Material energetics and layer thicknesses.

Two proprietary host materials, designated Host A and Host B, were provided by The Dow Chemical Company. In commercial devices, a mixture of these hosts was found to yield improved lifetimes up to =8.6 hrs at 15,000 cd/m^2 compared to 1.3 hrs and 4.2 hrs for Hosts A and B, respectively, where t_{90} is the time to degrade to 90% of the initial luminance. A hole-injection layer of poly(thiophene-3-[2[(2-methoxyethoxy)ethoxy]-2,5-diyl) (AQ1250) was spin-cast on the ITO anode, followed by a hole-transport layer (HTL) of 4,4',4"-tris(N-carbazolyl)triphenylamine (TCTA). The emissive layer (EML) consists of Host A, Host B, or a mixture of the two hosts, and a constant emitter doping concentration of 15 vol. % fac-tris(2-phenylpyridine)iridium(III) (Ir(ppy)$_3$). The Host A and Host B mixture was varied with compositions of 0%, 5%, 15%, 30%, 50%, 70%, 85%, and 100% Host B. An electron-transport layer (ETL) of tris-(1-phenyl-1H-benzimidazole) (TPBi) is deposited over the EML, followed by a LiF/Al cathode.

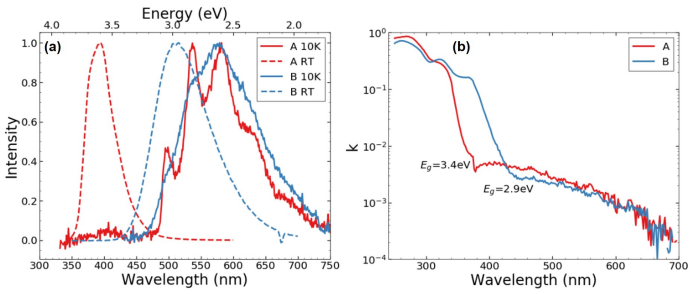

Figure 6.11: (a) Fluorescence and low temperature (10 K) Phosphorescence for both hosts. (b) Optical constant k for both hosts.

The external quantum efficiency with varying host composition is shown in Figure 6.10a-b, with

devices with less than 30% Host B showing a reduced efficiency and the remaining devices exhibiting efficiencies between 18% and 19%. The turn-on voltage to achieve 1 cd/m^2, shown in Figure 6.10c, is reduced by over one volt when increasing Host B concentration from 0 to 30%, then remains constant. This behavior is attributed to a change in the injection barrier for electrons into the EML.

Figure 6.10c shows molecular energy levels of interest for this work, with HOMO levels for Host A and Host B calculated from DFT, band gaps extracted from optical constants obtained by ellipsometry, and triplet energies obtained from low temperature phosphorescence. The measurement of triplet energies is further discussed in Appendix B. Host B is a material with a relatively narrow optical bandgap of 2.9 eV, a calculated HOMO of 5.3 eV, and a measured triplet energy of 2.6 eV. Host A as an optical gap of 3.4 eV, a calculate HOMO of 5.7 eV, and a measured triplet energy of 2.6 eV. Despite having a difference in energy gap and fluorescence energy, Host A and Host B have similar triplet energies as extracted from phosphorescence, shown in Figure 6.11. It is worth noting that the energy levels of Host B reside entirely within those of Host A, and Host A and B do not form an exciplex, as confirmed from measurements of PL on a mixed film and of electroluminescence of a simple bilayer device (ITO/Host A/Host B/LiF/Al), in contrast to the majority of reported co-host architectures.

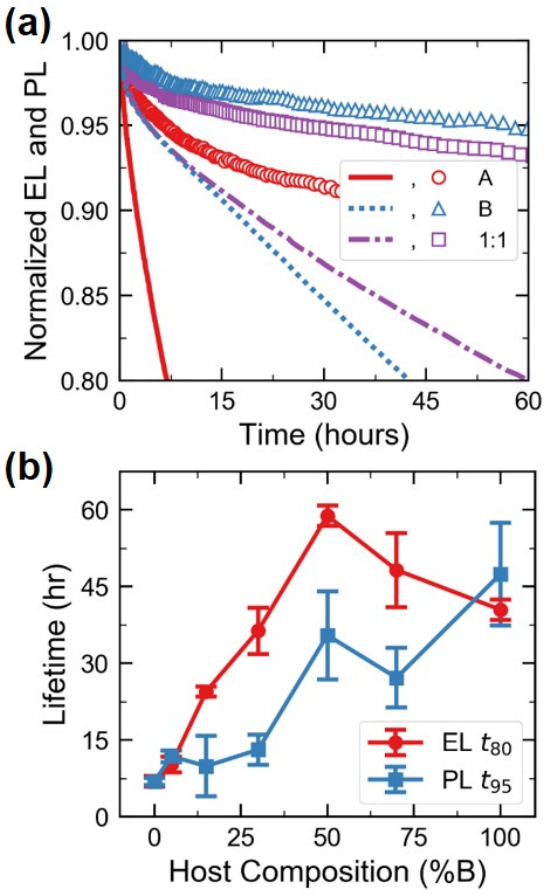

Figure 6.12: (a) Overal EL and PL loss for selected architectures. (b) Extracted lifetimes as a function of concentration.

6.3.3 Results

Figure 6.12 demonstrates that the mixed host architectures show the longest lifetimes. Host A has the shortest lifetime (hours), with lifetime rapidly increasing with the addition of small concentrations of Host B. A maximum lifetime is seen for 30% Host B in Host A, after which a steady decline in lifetime is seen as concentration is increased to pure Host B (hours). The simultaneous photoluminescence

(PL) lifetimes of these devices is reported in Figure 6.12. Interestingly, the PL stability increases monotonically as percentage of Host B increases. This inverse trend between the PL and EL lifetimes was not observed in the data of Sections 6.1 or 6.2and suggests that RZ width is maximized at pure Host B, but that maximizing RZ width does not optimize lifetime.

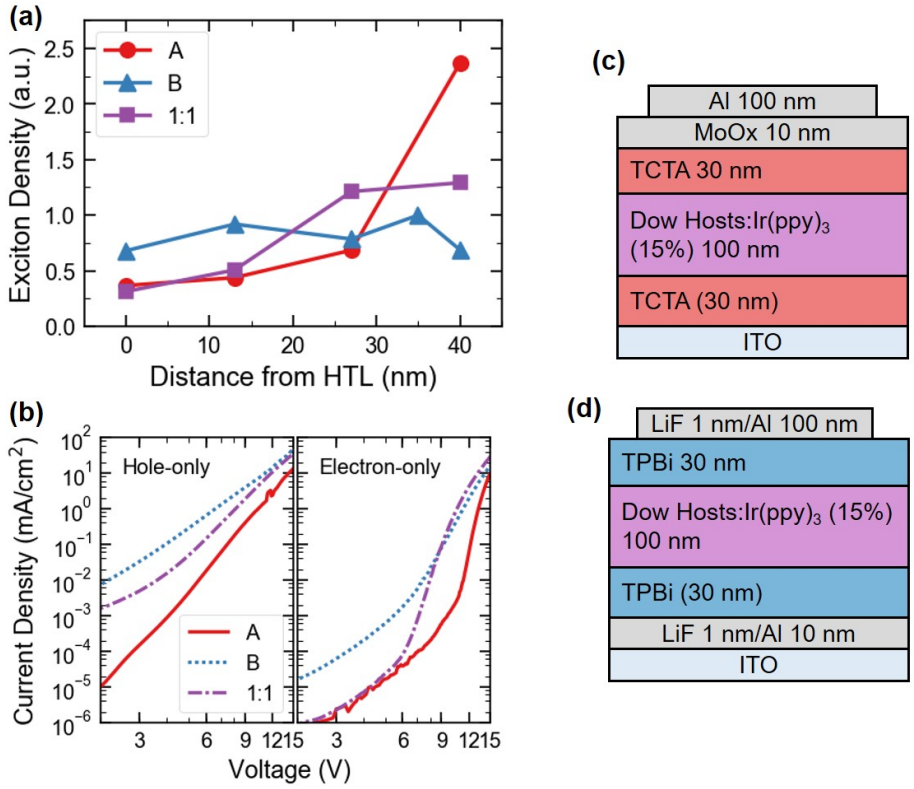

Figure 6.13: (a) Hole and electron only devices featuring hosts A and B, as well as a 1:1 mixture. The related architectures are shown in (c) and (d) for holes and electrons, respectively. (b) Measured RZs at 2 mA/cm^2.

In conventional mixed host architectures, hole- and electron-transporting hosts are blended to improve the balance of electron and hole mobilities, resulting in a broadened RZ and reduced exciton density.[138,171,178,242] To investigate how mixing Host A and Host B impacts charge transport, single-carrier devices were fabricated for emissive layers containing 0%, 50%, and 100% Host B. The current-voltage characteristics for HOD and EOD are shown in Figure 6.13a-b, along with the device architectures. For both holes and electrons, Host B is found to be a more conductive host than Host A. The 50% Host B mixture shows intermediate hole conductivity relative to pure materials. For electrons, at low voltage, the properties are similar to Host A, but transition to be Host B at high voltage. Thus, unlike conventional mixed EMLs where hole- and electron-transporting materials are blended to form a composite layer with overall improved charge transport, here Host B and the phosphorescent guest are likely responsible for both hole and electron transport. Thus, the addition

of Host A to Host B to form the mixture favorably adjusts the transport properties of the EML for increased operational lifetime. Given the differences in architecture between the HODs and EODs, the relative mobility of electrons and holes cannot be quantitatively assessed. How these charge transport and injection properties translate to the exciton spatial profiles is most straightforwardly addressed by direct measurement of RZ.

The RZs of devices with 0%, 50%, and 100% Host B were measured using a doped sensitizer approach, discussed in Chapter 3.6.[154] The area-normalized exciton population map resulting from this measurement for each architecture is shown in Figure 3c (EL spectra from which these profiles are extracted are included in the supporting information). Host A is shown to have the highest exciton density of all three architectures, peaked at the ETL interface. Host B has the widest RZ, with a nearly flat exciton density across the EML. The 50% Host B mixture shows an intermediate behavior with a narrower RZ than Host B that is also shifted away from the HTL/EML interface. This indicates that the EL lifetime improvement observed for the 50% mixture compared to pure Host B cannot be attributed to a reduction in exciton density, as is the case in most mixed host EML OLEDs.

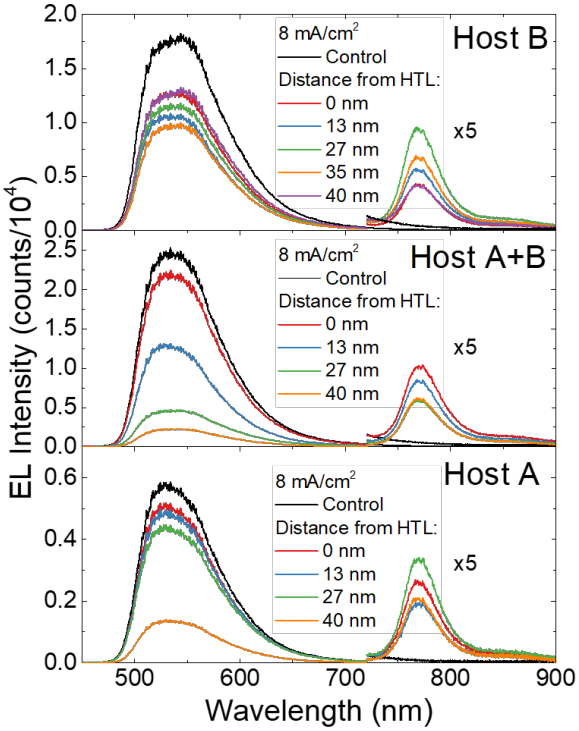

Figure 6.14: Raw spectral data for RZ measurements for hosts A, B and a 1:1 mixture

The photoluminescence degradation behavior shown in Figure 6.12b becomes more stable with increasing composition of Host B, following the measured increase in RZ width decreased exciton density. This is consistent with our previous studies on the dependence of PL on RZ width in mixed host architectures and expectations based on exciton-induced-degradation kinetics.[83,154] Considering device degradation by bimolecular processes, devices with high concentration of Host A might be expected to exhibit a shorter lifetime than those based on Host B. However, the total degradation, shown in Figure 6.12a shows a reduction in overall EL stability at concentrations above 30% Host B, indicating a competing mechanism that does not affect the PL stability. Host B has the highest exciton population at the HTL interface, suggesting there may be an interfacial degradation process at play, creating a shorter lifetime.[52,153] We hypothesize that as Host A is added to Host B, the RZ

is shifted away from the HTL interface, causing less interfacial degradation and increasing the total lifetime, despite reductions in PL lifetime as the RZ narrows. However, the benefits of added Host A fall off rapidly below 15% Host B as the injection barrier lowering provided by Host B are lost and significant narrowing of the RZ is observed.

To minimize differences in RZ width and normalize the effect of the HTL interface on degradation, devices were fabricated with EMLs of only 10 nm, with efficiencies shown in Figure 6.15. This thin emissive layer ensures that excitons are present throughout the entire EML and RZ is minimally different between the devices. For these devices, the ETL thickness was set to 50 nm to center the electric field profile of the λ=473 nm pump laser in the EML. The peak external quantum efficiency of these devices was found to be 14 $\pm$ 1% for all three architectures. The EL and PL lifetimes can be seen in Figure 6.16a and b, respectively. The 50% and 100% Host B are found to have the identical lifetimes for both EL and PL, = (22 $\pm$ 1) hr for EL, and = (16 $\pm$ 1) hr for PL.

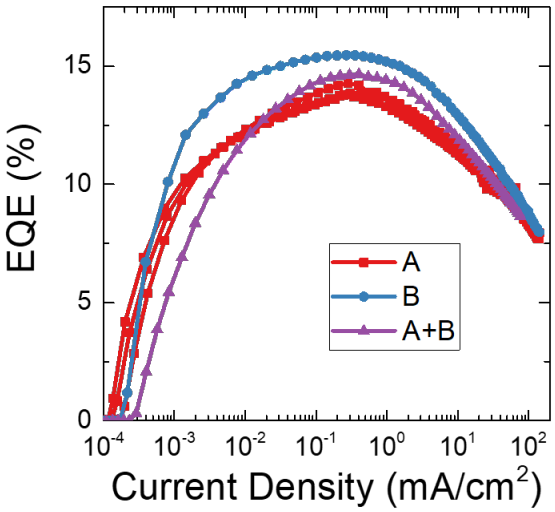

Figure 6.15: η_{EQE} for the 10 nm EML devices.

This identical behavior in both EL and PL degradation suggests that the kinetics and mechanism of degradation are the same for devices based on Host B and the 50:50 mixture. Host A shows a shorter lifetime in both EL and PL, likely due to its narrow RZ which is heavily peaked at the ETL interface (Figure 6.13c). Given this identical degradation behavior for a thin emissive layer, it is unlikely that the mixed host devices are longer lived due to enhanced morphological stability. Using a wide energy gap host along with an ambipolar host in this architecture has allowed tuning of the RZ away from the HTL interface. While successful in this device, it can be difficult to understand a priori how a wide energy gap material will shift the charge transport characteristics of the ambipolar host.

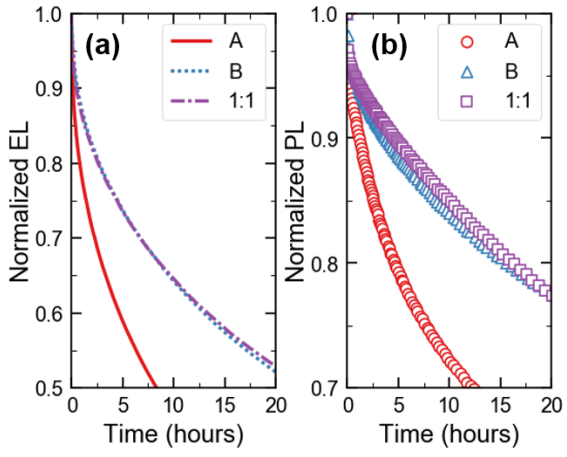

Figure 6.16: (a) EL and (b) PL lifetimes for the 10 nm EML devices.

This could make designing a co-host system around this type of material combination a challenge. However, when investigating material systems where transport properties are unknown, this type of interaction may be encountered. This system is also an important counterexample to the assumption that reducing charge transport is always detrimental to device behavior. In fact, device lifetime can be a much more subtle and intricate design system than the simple maximization of RZ width.

6.3.4 Conclusion

In this work, a unique co-host architecture is demonstrated using a wide energy gap host and an ambipolar host. Interestingly, despite a reduction in RZ width, an increase in device lifetime is observed. This increase in lifetime is demonstrated to be due to exciton formation at an unstable interface, known to accelerate degradation. This conclusion is contrary to the typical design rule that an increased RZ width is always beneficial to device lifetime. Rather, a balance of RZ width and position needs to be established, especially with regard to recombination at interfaces. This result provides an example of the blend of the two mechanisms demonstrated in Sections 6.1 and 6.2.

Chapter 7

Novel Blue Emitter Development

This chapter is a summary of work done in collaboration with Professor Thomas Hoye in the Departmeent of Chemistry at the University of Minnesota and his student Dr. Feng Xu who performed all chemical design and synthesis. This collaborative work is published in Xu et al. [226].

Despite extensive research and the transition of commercial red and green devices to phosphorescent materials, blue devices often utilize fluorescent emitters since phosphorescent emitters have a lower lifetime.[93] Because of the reduced efficiency, a larger blue fluorescent pixel is used than the corresponding red and green, in order to operate at a similar luminance point.[243] Though from an efficiency standpoint, a phosphorescent or TADF solution is the long term goal, there is still interest in developing high efficiency deep blue fluorescent emitters.[149,229,244–246] This is especially true if novel chemistry can be used, producing entirely new classes of molecules. Any new chemical understanding uncovered in fluorescent molecules may also be able to be transferred to phosphorescent molecules.

In this work, novel fluorescent emitter molecules were developed exhibiting deep blue emission. Three distinct chemical families are investigated, all of which rely on synthesis through a hexadehydro-Diels-Alder (HDDA) cycloisomerization reaction. The first set of these molecules focused around alkynyl substituted naphthalenes, work that was published in Xu et al. [226]. The second set features bis(arylethynyl) benzene derivatives.. The third presented set, though the first investigated, studies an arylethynyl fluorene.

7.1 Hexadehydro-Diels-Alder Reactions

The hexadehydro-Diels-Alder (HDDA) reaction is a method for producing aromatic compounds via cycloaddition. Specifically, HDDA uses an alkyne (unsaturated hydrocarbon containing a carbon-carbon triple bond) and a diyne (system containing two alkyne groups) in order to form a reactive benzyne. This benzene reacts with a trapping agent to form a substituted aromatic product.[247,248] Unlike conventional methods of preparation of benzenes, HDDA easily incorporates structural variations and substituents.[249–251] This makes HDDA a promising chemical method to produce conjugated, π-bond-rich molecules. As discussed in Chapter 2, conjugated molecules are of great interest as organic semiconductors.

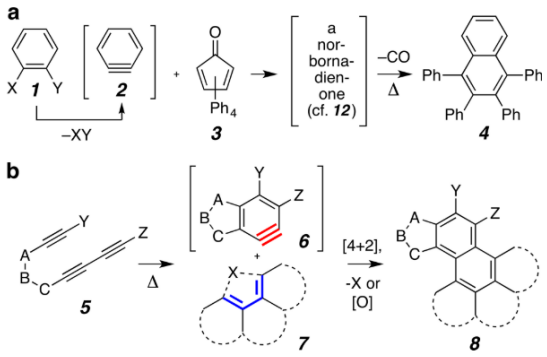

Figure 7.1: Preparation of benzenes through traditional Diels-Alder reaction (a) and an HDDA thermal cycloisomerization (b). HDDA provides easy incorporation of substitutes at the A,B,C, Y and Z cites, along with the reactant (**7**). Figure reproduced from Xu et al. [226]

A schematic illustrating the advantages of HDDA reactions is shown in Figure 7.1. Figure 7.1a shows a traditional method of production for naphthalene derivatives, starting from a benzenoid precursor (**1**). Removing the X and Y substituents from (**1**), **2** can then be reacted with tetraphenylcyclopentadienone (TPCP) (**3**) via a Diels-Alder reaction. After the thermal extrusion of carbon monoxide, naphthalene derivatives are formed (**4**). In this process, it is difficult to incorporate substituents into the final product. This is in contrast to the HDDA process shown in Figure 7.1b. Through HDDA thermal cycloisomerization of **5** into **6**, benzenes with complex substituents can be created. Then through trapping with dienes like **7**, more complicated conjugated products can be realized.

7.2 Naphthalene Derivatives

7.2.1 Synthesis

The first molecular system studied used the reaction pathway shown in Figure 7.2. Reactions between the tetraynes (**9**) and TPCP (**3**) via HDDA proceed through intermediates **11** and **12** before ejecting a carbon monoxide to form the fluorophores (**10**).[252–256] This HDDA cascade proceeded cleanly at 80 °C over the course of 12 hours and produced a yield of 82% following three recrystallizations of the naphthalene adduct **10**. An added advantage of using a tetrayne substrate is that the intermediate

benzene, here 11, and, consequently, the naphthalene formed following CO extrusion from 12, bears an arylethynyl substituent. The product **10a**, the first produced, showed strong emissive properties that were blue to the eye.

In light of these promising properties, the effect of the electronic character of the aryl substituents was probed. Two additional analogs in which the phenyl ring was modified by the presence of a pair of electron-donating (**10b**) as well as electron-withdrawing (**10c**) groups were prepared. These analogs were readily prepared by an entirely parallel and equally efficient sequence of reactions.

Upon realization of fluorescence in the solid state, solutions were prepared in THF, to investigate their optical properties. Absorption at 10^{-5}M and photoluminescence at 10^{-6}M are shown in Figure 7.3. A slight red shift in emission is seen for **10c** compared with **10a** and **10b**. The PL quantum yield of each compound is summarized in Table 7.1 Given the promising solution PL efficiencies, the emissive properties of all three compounds were investigated in thin films to explore their possible utility as emissive species in blue organic light-emitting diodes (OLEDs).

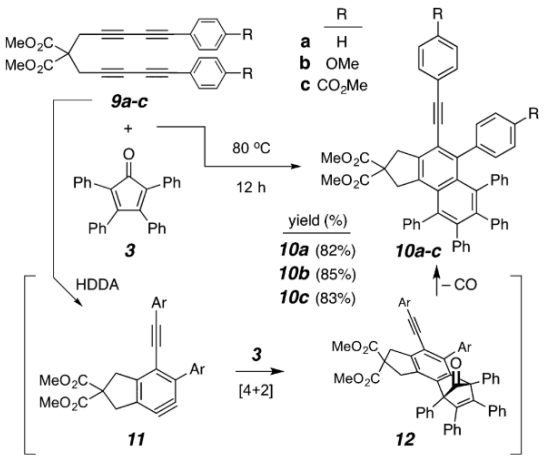

Figure 7.2: HDDA reactions between **9** and **3** proceed through **11** and **12**, resulting in the products (**10**). Figure reproduced from Xu et al. [226]

To probe thin film PL, each compound was examined both as a pure film (100%) as well as in a host-guest arrangement with the wide energy gap material 1,4-bis(triphenylsilyl)benzene (UGH2) serving as host. Thin films were deposited on cleaned quartz substrates by high vacuum thermal evaporation (10^{-7} Torr). Films composed of host and guest (UGH2 and **10**) in the ratios of 96:4, 80:20, and 0:100 (i.e., 4%, 20%, and 100% loading, respectively) were studied. The thin film PL spectra of the 20% samples of each of **10a-c** are shown in Figure 7.3a. The solution and film emission maxima (Figures 7.3 and 7.3b) are similar, suggesting that the excitonic state is unimolecular, without significant charge transfer states. The twisted nature of the five aryl substituents on the central naphthalene ring as well as the quasi-orthogonal orientation of the pair of malonate carbomethoxy groups may be responsible for preventing close association between molecules of **10** in films. These features can be seen in the single crystal X-ray crystallographic structure shown in Figure 7.3b.

The PL emission spectra of all three compounds showed a red shift of between **10** and 20 nm across the extreme concentrations of 4% vs 100% content of **10**. This could be a result of at least some degree of aggregation with increasing concentration in the film, a response to a change in bulk dielectric properties or to differing intermolecular restraints that change the geometry of the excited states. DFT calculations (M06-2X/6-31G(d)) of the optimized lowest energy conformer for each of **10a-c** showed both the twisted the ethynyl linker, quite similar to those features seen for the single crystal, shown in the SI of Xu et al. [226].

Emitter	η_{PL} (%)
10a	11.0 ± 2.6
10b	4.9 ± 1.3
10b	56 ± 8

Table 7.1: PL quantum yield (η_{PL})

7.2.2 Performance Optimization

OLEDs using each of **10a-c** as the emissive layer were constructed by high vacuum thermal evaporation. Devices (Figures 7.4a-c) were fabricated in accordance with our standard protocol. The device architecture consisted of a 30 nm-thick hole transport layer (HTL) of 4,4'- cyclohexylidenebis[N,N-bis(4-methylphenyl)benzenamine] (TAPC), a 20 nm-thick emissive layer of **10a**, **10b**,or **10c** doped into the wide energy gap host UGH2 at a concentration of 4, 20, or 100% of the emitter, and a 30 nm-thick electron transport layer of

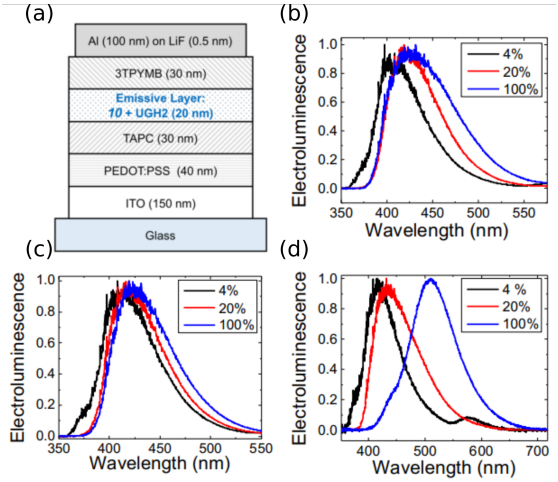

Figure 7.4: (a) OLED architecture. (b) EL spectra for **10a**. (c) EL spectra for **10b**. (d) EL spectra for **10c**. Figure reproduced from Xu et al. [226]

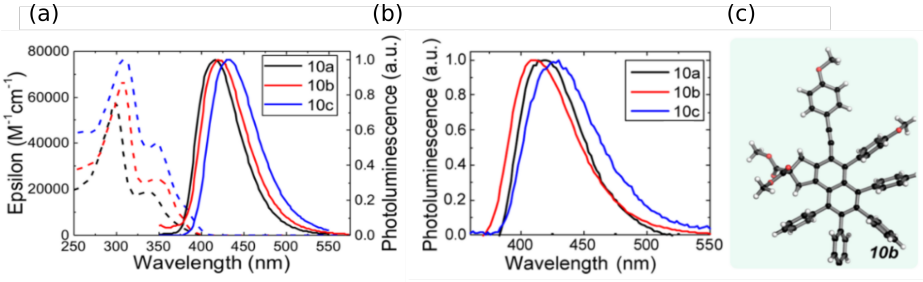

Figure 7.3: (a).Solution absorption (dashed lines) and emission (solid) pumped at 350 nm with concentrations of 10^{-5} M and 10^{-6} M, respectively, in THF. (b) Thin film PL from an 80/20 mixture of UGH2 and the emitter. (c) Single crystal X-ray structure of **10b** showing the relative orientation in the solid state of all aryl substituents with respect to the core naphthalene ring. Figure reproduced from Xu et al. [226]

tris(2,4,6-trimethyl-3-(pyridin-3-yl)phenyl)- borane (3TPYMB). All devices were capped with an electron- injecting cathode comprising a 0.5 nm-thick layer of LiF and a 100 nm-thick layer of Al. Electroluminescence (EL) intensity spectra collected for devices containing 20% loading are shown in Figure 7.4d. Data for devices containing a neat emissive layer of **10c** (Figure 7.4d) show a significant red shift compared to the PL spectrum. We speculate that this emission may originate from an interfacial exciplex in this particular device. Upon doping with the UGH2 host, this effect is eliminated for the devices containing the 20% and 4% films.

To evaluate spectral compatibility with display applications, the coordinate system describing the color gamut developed by the International Commission on Illumination (CIE) is used. Deep blue emission is required to reproduce fully the visible color spectrum for displays as well as to achieve true white colors. For application in television displays, desirable deep blue emission has CIE coordinates of x = 0.131, y = 0.04614a or x = 0.14, y = 0.08. The coordinates observed for the above devices based on **10a-c** are reported in Table 1 (and graphically in Figure 7.5). All but the last (100% **10c**) emit in the deep blue.

					CIE	
Emitter	Conc.	η_{EQE}	η_{PL}	V_{TO}	x	y
10a	4	1.4	93.3	3.6	0.18	0.10
	20	3.0	42.9	3.5	0.15	0.09
	100	1.6	34.8	3.3	0.15	0.13
10b	4	0.9	51.1	3.8	0.18	0.11
	20	1.9	46.2	3.5	0.15	0.08
	100	1.9	43.0	3.1	0.15	0.10
10c	4	0.7	73.9	4.6	0.18	0.14
	20	0.9	56.6	3.6	0.15	0.17
	100	0.4	30.2	3.1	0.23	0.43

Table 7.2: Summary of OLED device performance.

Current density-voltage and brightness-voltage characteristics were also measured for devices based on each emitter. From these measurements, the external quantum efficiency (η_{EQE}) was calculated. Device performance for all emitter species and concentrations are shown in Table 7.2. The highest performance device overall was found to be **10a** doped into UGH2 at 20% with an η_{EQE} of 3%. It is worth noting that for simple fluorescent emitters, a maximum theoretical efficiency of 5% is expected.[119,257] Peak η_{EQE} values for all three compounds are realized for devices having an emissive layer composition of 20% of **10**. This does not correlate directly with the PL efficiency η_{PL} , which increases monotonically with dilution, likely reflecting a role played by the emitter in charge transport. The wide energy gap of UGH2 (HOMO = 7.2 eV; LUMO = 2.8 eV)[258] forces charge transport to occur in part via the emissive guest molecule, especially for holes. This is supported by the observed increase in turn-on voltage (V_{TO}) with decreasing concentration. These

devices could likely be further optimized by using a charge transporting host and a lower guest concentration, capitalizing on the improved PL efficiency observed for more dilute films.

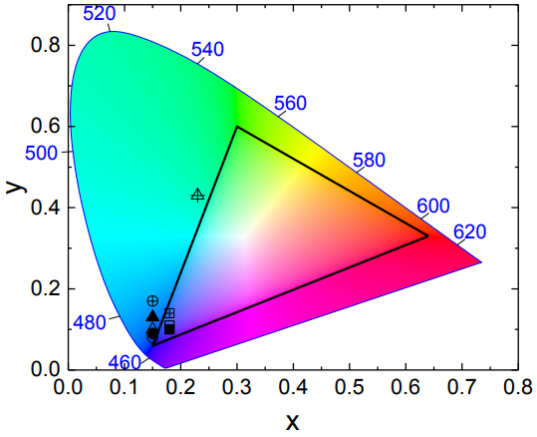

Figure 7.5: CIE coordinates of OLEDs. Circles, squares, and triangles are 4, 20 and 100%, respectively. Closed, open, and plus represent **10a**, **10b**, and **10c**, respectively. Figure reproduced from Xu et al. [226]

7.2.3 Electrical Lifetime

With reasonable device efficiencies, the primary motivation for fluorescent emitter development is to enhance lifetime. It is notable that following deposition of each of the naphthalenes **10a-c**, there was virtually no residue remaining in the heating crucible, suggesting little if any thermal degradation of these compounds. In fact, this point could be preliminarily established for samples of **10a-c** by observing (i) their sublimation in common laboratory apparatus with essentially no decomposition and (ii) their robust nature when held open in the air at a temperature of ≤300 °C, where they showed slight colorization but no sign of any significant decomposition. Finally, examination by differential scanning calorimetry again gave no indication of decomposition (exotherm) below 300 °C (for **10a** and **10b**) or 310 °C (for **10c**), and thermogravimetric analysis showed mass loss of greater than 5% only at temperatures >336-357 °C (see SI of Xu et al. [226]).

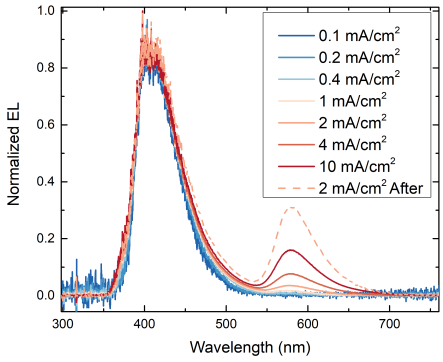

Figure 7.6: Spectral degradation of **10b** under applied current. Spectra were taken in the order of the legend.

Despite these positive signs of thermal stability, devices showed a significant spectral shift under applied current. Figure 7.6 shows the degradation of **10b** as a function of increasing current. As

the current increases above 1 mA/cm^2, an additional spectral feature at 575 nm is seen developing. The intensity of the feature increases with current density. This behavior is not reversible, and the intensity remains high even when returning to low current. Given the wide energy band of the host, it is unlikely that this is an exciplex with the host, though cannot be verified without knowing the energy levels of the guest. Additionally, since this is non-reversible, this is most likely a degradation state of the emitter.

With these positive indications from a molecular standpoint, lifetimes were investigated using NPD as an HTL and AlQ_3 as an ETL. These materials were used to show higher stability, along with a neat EML of **10c** to avoid the instability of UGH2. Unfortunately, the lifetimes shown in Figure 7.7 is very short at 4.7 hours, only operating at 7 cd/m^2. This is an unusable lifetime for device applications. Further optimization was not performed to improve lifetime.

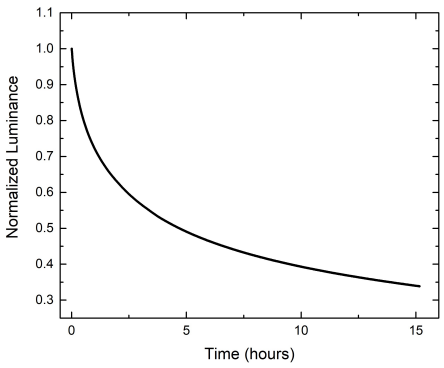

Figure 7.7: Lifetime of molecule **10c**.

7.2.4 Solution Molecular Aggregation

Surprisingly, the napthalene-based compounds also showed a behavior typical of aggregation-induced emission (AIE). Namely, as the strong solvent THF was exchanged for increasing amounts of the non-solvent water, the efficiency of blue emission grew (see SI). However, given the array of five orthogonal aryl substituents, one would not expect that two (or more) molecules of **10** would be able to reside close enough to show substantial excimeric behavior. Perhaps the planar (arylethynyl)- naphthalene portion of the molecule provides enough of a footprint for close association of molecular orbitals from two molecules. We do note that a topologically related compound, 1- methyl-1,2,3,4,5-pentaphenylsilole, also shows significantly enhanced emission when placed under aggregate-inducing conditions. This aggregation may be partially responsible for the shifting spectrum shown in Figure

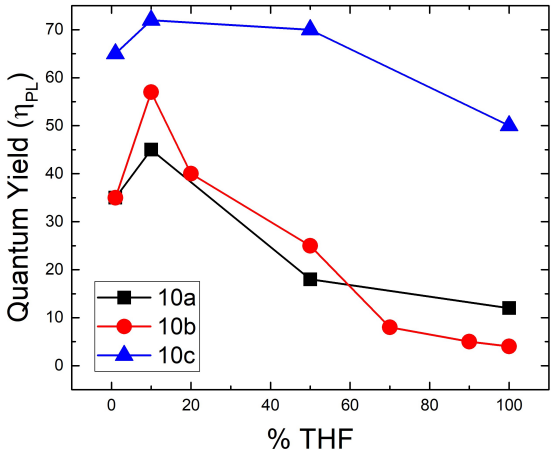

Figure 7.8: η_{PL} as a function of concentration THF in water. Figure reproduced from Xu et al. [226]

7.3 Bis(arylethynyl) benzene Derivatives

A second molecular series was investigated, consisting of 1,4-bis(arylethynyl) benzene derivatives. The synthesis for this series is depicted in Figure 7.9. An HDDA reaction occurs between **b1** and a concentration of **b2** in excess of 3:1, resulting in **b3**. With the further addition of another alkynyl group, the final products, **b4a** and **b4b** are formed.

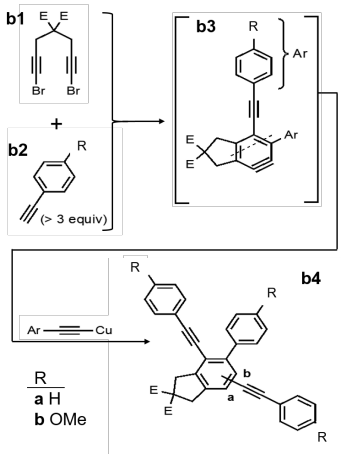

Figure 7.9: Synthesis pathway. Precursors **b1** and **b2** undergo a HDDA reaction to form **b3**, and with the addition of the additional alkynyl, forms the product **b4**. Substituent variants R are shown.

The solution absorption and photoluminescence spectra of these compounds is shown in Figure 7.10. The quantum yields of **b4a** and **b4b** were found to be $\eta_{\mathrm{PL}} = 75.7\%$ and $\eta_{\mathrm{PL}} = 81.2\%$, respectively. Despite the high quantum yield in comparison to the molecules discussed in Section 7.2, the emission spectra is found to be limiting to applications. Since the emission peak is below 400 nm for both materials, most emission is in the UV and would provide minimal visible output. This would result in an extremely low luminous power efficiency. These materials were not further pursued in devices, but may be of interest for UV led applications.

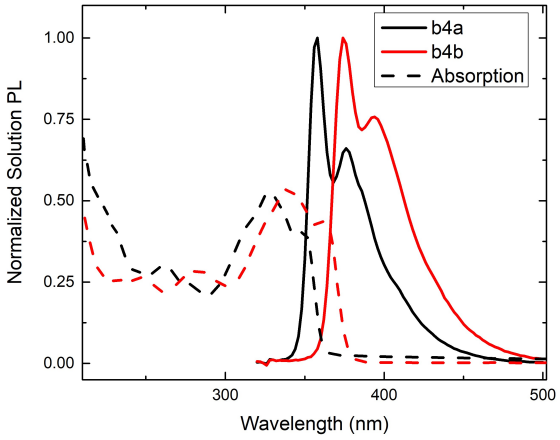

Figure 7.10: Photoluminescence spectra of compounds **b4a** and **b4b** shown in solid lines. Dashed lines show corresponding absorption spectra.

Molecule	λ_{peak} (nm)	η_{PL} (%)
OH (neat)	415	37
OMe (neat)	430	17
OMe (20% in UGH2)	400	30
COOMe (neat)	500	33

Table 7.3: Photoluminescence summary for the emitter molecules of Figure 7.11

7.4 Arylethynylfluorene

Molecules for this study were formed using the reaction shown in Figure 7.11. Three different R species were used, being OH, OMe, and COOMe. The photoluminescence peak wavelength and efficiency can be found in Table 7.3. Interestingly, in films and solution, the OMe molecule showed significant spectral changes based on the environment. This seems to indicate that there is a large interaction between molecules, most likely due to the large planar conjugated system. The OH molecule was expected to show similar behavior. The COOMe system showed greed emission, and was not further investigated.

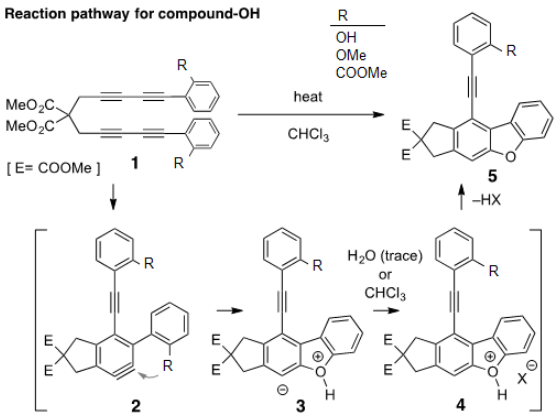

Figure 7.11: The thermal HDDA reaction of tetrayne (**1**) affords the arylethynyldibenzofuran (**5**). The reaction proceeds through three reactive intermediates: benzene (**2**), zwitterion (**3**), and oxonium ion (**4**). Credit to Xiao Xiao for reaction diagram.

In order to be useful, control over the emission wavelength needs to be obtained. Devices utilizing OMe were further investigated to try to optimize spectral purity and device efficiency. Four architectures were investigated, shown in Figure 7.12I with the corresponding spectra shown in Figure 7.12II. The spectral feature at 375 nm closely reflects the dilute solution spectra for this molecule. The feature at 675 nm is a degradation product that increases in intensity after testing at high current. It is unclear if this is a radiative degradation product or an exciplex formed with a degraded and undegraded molecule. For both A and C, a broad aggregate emission state is seen at 430 nm. Due to the lack of understanding of this emission state and wide variability in behavior, this molecular system was not deemed of further interest. The large planar conjugated state is thought to be the cause of this aggregate state emission, something which is avoided in the molecules discussed in Sections 7.2 and 7.3.

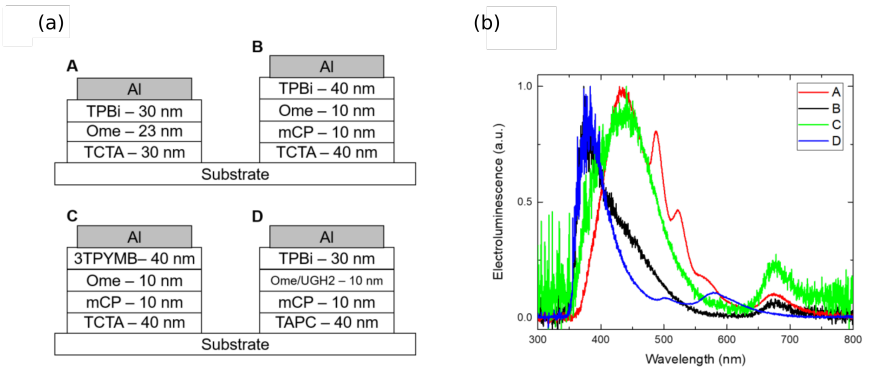

Figure 7.12: (a) Architectures used for EL spectra optimization. (b) El spectra for all devices reported at 2 mA/cm^2.

7.5 Conclusion

This chapter outlined progress on three families of emitter molecules for blue fluorescent OLEDs. Promising efficiency results were seen for the naphthalene derivatives, though the lifetime was found to be extremely short. Without a promising lifetime, further development was not pursued. A solution based molecular stability test was pursued in Section C.

The remaining two molecular families were eliminated from further investigation in the initial screening of photoluminescence. It is very important for OLED device design to have a reliable emission state that can be confined. This was found to be challenging due to molecular aggregation and charge-transfer states in Section 7.4. The molecules in Section 7.3 emitted in the UV and were of minimal interest for OLED devices.

For further development of these emitters, it would be useful to employ the decoupled degradation technique developed in Chapter 5. This would allow for isolation of the problems with device stability. This could also help to provide information about the differences between green and blue emitters, as well as fluorescent and phosphorescent emitters during degradation decoupling.

Chapter 8

Establishing Emissive Layer Host Design Rules for Stable OLEDs

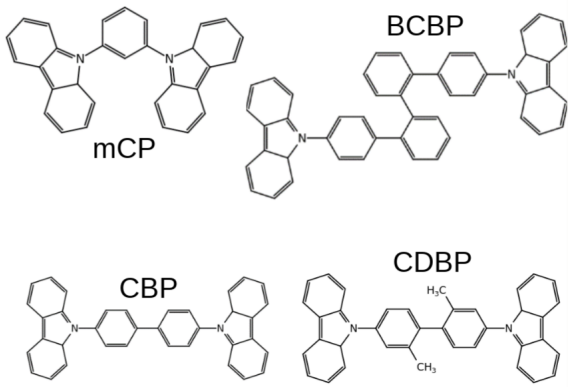

Figure 8.1: Host molecules used in this study.

Design rules for understanding the degradation behavior of OLED materials are not well understood. It can be difficult to isolate molecular property differences in devices, when changes in a molecule can affect many different device parameters, such as energy levels, mobilities, morphology, and the optical properties. It is therefore imperative to investigate closely related molecules and examine the affects on device performance. This provides the most isolation of device parameters and allows the most fundamental study of stability of the molecules. One of the most widely studies host molecule families is the carbazoles, with 4,4'-Bis(N-carbazolyl)-1,1'-biphenyl (CBP) and 1,3-Bis(N-carbazolyl)benzene (mCP) being extremely popular hosts for green and blue devices, respectively.[61,73,117,120,151,189,206,207,220,221,259–267] A series of closely related molecules is also readily available, including 2,2'-Bis(4-(carbazol-9-yl)phenyl)-biphenyl (BCBP) and 4,4'-Bis(9-carbazolyl)-2,2'-dimethylbiphenyl (CDBP). These molecules, all shown in Figure 8.1 provide a testing ground for investigating a molecular host family in a device system. This chapter seeks to compare the behavior of devices utilizing these hosts and understand their relative behavior from a molecular level.

8.1 Electrical Characterization

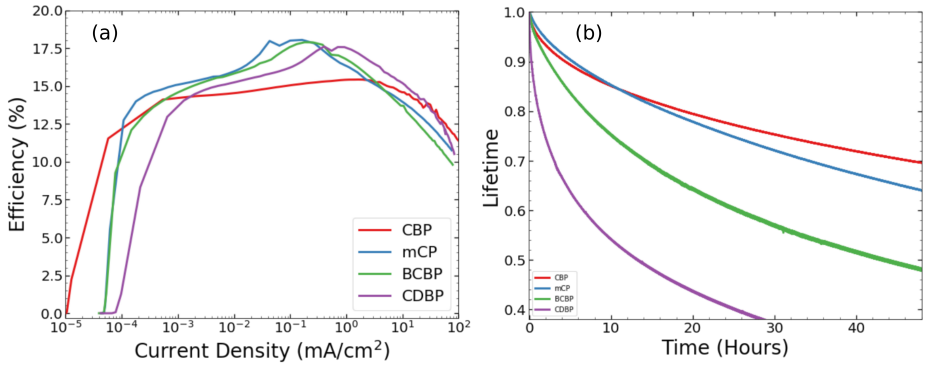

Figure 8.2: (a) η_{EQE} as a function of current density for devices based on each host. Similar peak efficiencies are observed. (b) Conventional EL lifetime for devices based on each host.

Devices were prepared consisting of an ITO patterned substrate followed by 40 nm of TCTA. The EML of all devices was 20 nm thick with the host doped with 5% $\mathrm{Ir(ppy)_3}$. A 40 nm thick TPBi ETL with an LiF/Al cathode finished off the devices.

The dependence of device η_{EQE} on current density is shown Figure 8.2a, as was similar between all devices. All devices showed a slow rise in efficiency, peaked between $10^{-1} - 10^{0}$ mA/cm^2. The electrical lifetimes were characterized for these devices at 1000 cd/m^2, and are shown in Figure 8.2b. Here, CBP shows the peak lifetime, though is comparable to mCP. BCBP shows a significant reduction in lifetime, with CDBP being the lowest performing device.

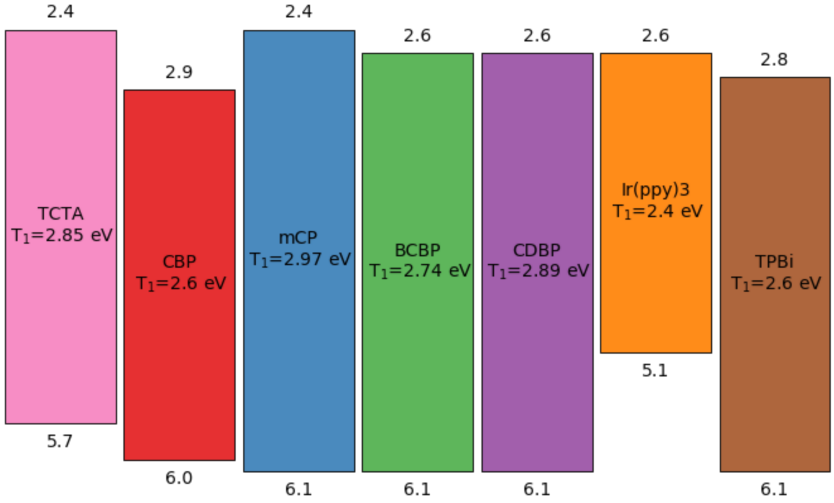

Figure 8.3: Energy levels for all materials used in devices. Triplet energies for the hosts are measured by low temperature phosphorescence, described in Appendix B. Remaining energy levels are obtained from the manufacturer.

Energy levels for all of these materials are shown in Figure 8.3. Triplet energies are extracted from low temperature phosphorescence, discussed in Appendix B.

From the EL lifetimes, there is no apparent trend with obvious device parameters, such as

efficiency or driving voltage, or with semiconductor properties such as energy levels or triplet energies. This lack of dependence can be seen in Figure 8.4. Without a clear explanation for this trend from the bulk and device properties, this suggests an explanation for device stability from a more fundamental level, possibly intrinsic to the molecule.

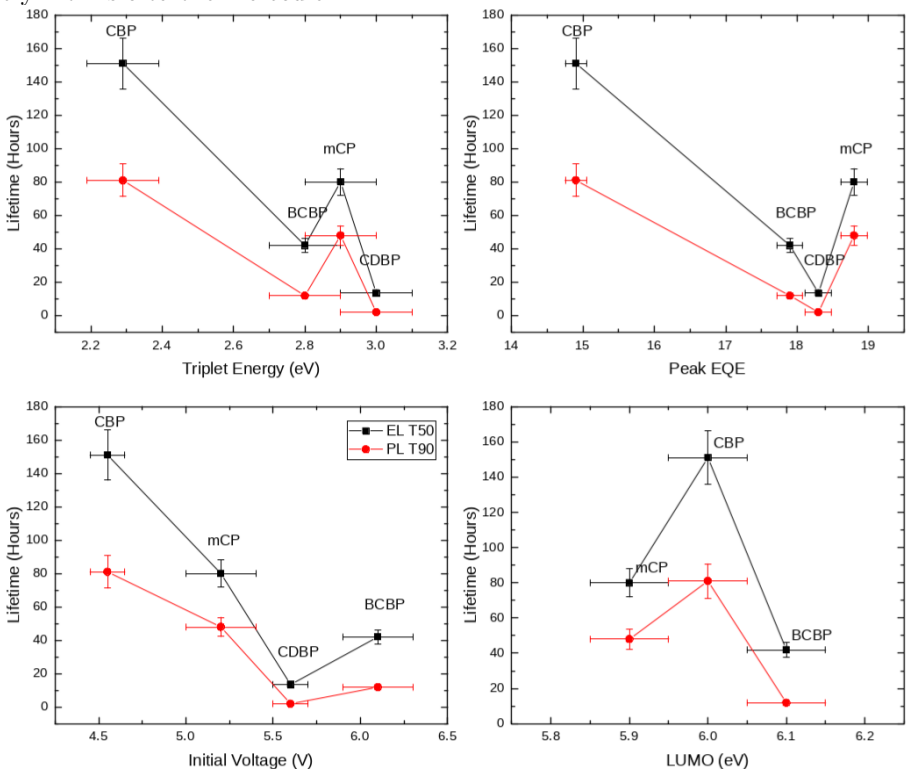

Figure 8.4: Extracted EL and PL lifetimes as a function of Triplet Energy (Top Left), Peak EQE (Top Right), Initial Driving Voltage (Bottom Left), and LUMO (Bottom Right). No universal trend is observed.

8.2 Optical Characterization

Without an explanation for the observed electrical behavior, the photostability of each host was investigated to remove carrier-driven degradation processes from the analysis. Section 8.2.1 describes the optical characterization of the various hosts and the development of the optical degradation technique, while Section 8.2.2 compares the data collected on each host.

8.2.1 Optical Design

In ultimately considering degradation under optical excitation, there are two pumping schemes to consider: pumping the host with transfer to the emitter, or pumping the emitter directly. These two schemes offer different dynamics with regard to the degradation behavior.

When pumping the host, host molecules are energetically stressed, potentially enabling bimolecular events that can lead to degradation. The transfer event of the exciton to the emitter molecule will have a rate, k_T that may be competitive with non-radiative decay on the host, k_{nr}. The efficiency of this transfer even can be expressed as

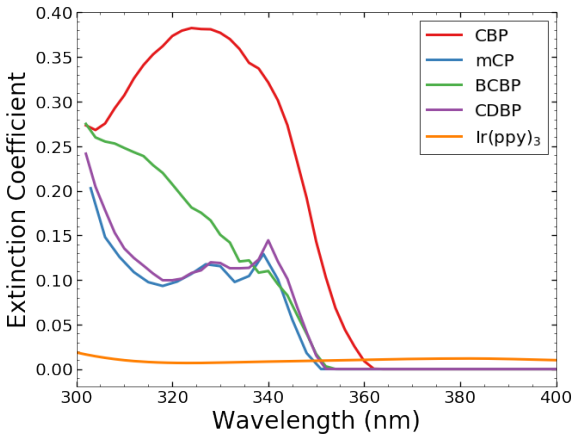

Figure 8.5: Extinction coefficients for each host and the emissive phosphor $Ir(ppy)_3$. The extinction coefficient for $Ir(ppy)_3$ is weighted by the 5% doping concentration to indicate relative absorption. All host materials show a turn-on in absorption between 340-350 nm.

$$\eta_T = \frac{k_T}{k_T + k_{nr}}. \tag{8.1}$$

When pumping the host during degradation, any loss in η_T during degradation will be convoluted with PL loss from the emitter, η_{PL} . In addition to the stress on the host, the energy transfer of the exciton from the host to the guest is exothermic, due to the lower triplet energy of the guest. This results in additional heat being released into the system, with the potential to accelerate degradation. Another issue is that the guest molecule can still absorb directly, so guest degradation may be convoluted into the interpretation of this data. It should be noted that based on the absorption strength weighted to molecular density, shown in Figure 8.5, $Ir(ppy)_3$ is still absorbing, though most absorption events below 350 nm will be on the host.

Alternatively, the guest may be pumped directly, by pumping above the absorption band edge of the host, which for these molecules is between 340-350 nm, as shown in Figure 8.5. This is a simpler measurement and provides a more direct measurement of the stability of excitons on the decaying guest molecule. Which technique is more representative of the behavior in devices could be debated depending on the exciton formation mechanism within the device, and if excitons are formed on the host during EL. Given the low HOMO level of $Ir(ppy)_3$ relative to the hosts, it is likely that $Ir(ppy)_3$ serves as a hole trap in devices and is responsible for some of the hole transport, and is unlikely that

excitons form exclusively on the host.

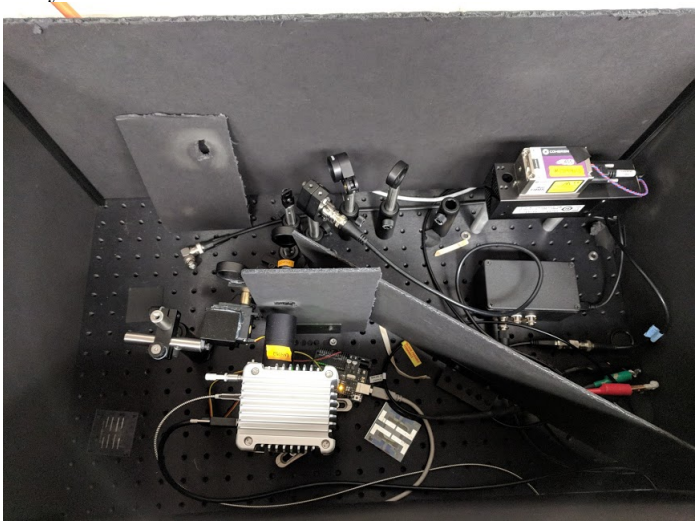

Figure 8.6: PL degradation setup. Silver box in the bottom is the white light source, and has attached lens tube containing collimation lenses. This is followed by a primitive cardboard iris, then a servo motor controlled mechanical shutter. This is followed by a wavelength filter, before reaching the sample mount in the top left, with collection diode at a 45° angle. The laser beam path follows the top of the box, with the laser on the top right.

To optically degrade devices, the setup shown in Figure 8.6 has been developed. This box features a 405 nm laser, as well as a white light source (LDLS, Energetiq) for pumping PL of devices, and can measure PL intensity of the device during degradation. The LDLS is a relatively flat spectral white light source, and can be filtered to provide pumping at various wavelength ranges. With the combination of these two light sources, both pumping regimes (host or guest) can be accessed within the same measurement.

Filtered pump spectra relevant to this study are shown in Figure 8.7. While there are a variety of pumping schemes available to this type of measurement, all data presented here uses either the 405 nm laser, or the 350 nm 40 nm FWHM filter, shown in Figure 8.7 in blue and green, respectively. The 350 nm and 405 nm pumps allow excitation of the host and guest, respectively. In addition to single wavelength degradation, the relative loss in η_T can be assessed by pumping with 350 nm light with a low duty cycle excitation from the 405 nm light to probe the guest directly. This is implemented

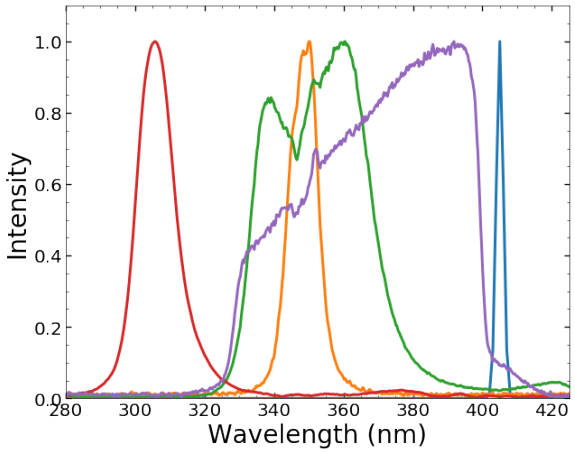

Figure 8.7: Available lamp spectra for photo degradation. Blue is the 405 nm laser, green is a 350 nm bandpass with 40 nm FWHM, yellow is a 350 nm bandpass with a 10 nm FWHM, purple is a 325 long pass in combination with a 400 nm shortpass, and red is a 300 nm bandpass with 10 nm FWHM.

by temporarily shuttering the LDLS lamp using a servo motor shutter. The 405 nm laser can be turned on and off with reliable power quickly, as previously shown in Chapter 5. Using this method, problems with the host energy transfer can be separated from the guest stability.

8.2.2 Photostability

For preliminary investigation into the optical stability of these hosts, the 350 nm lamp was used with an intermittent probe from the 405 nm laser. Films for this degradation consisted of the full device stack including cathode, but excluding the planarizing layer at the ITO (AQ1250) and excluding LiF at the cathode. LiF has been shown to dissociate under strong optical excitation.[222] The full stack with cathode was used because rapid degradation was seen even when encapsulated without the cathode, hinting at oxygen quenching of the film. At 350 nm, TCTA is being excited as well as the host, but shows much a bluer emission spectra, and is filtered from the collected signal by a 450 nm long pass filter on the detector.

Host stability can be seen in Figure 8.8 with the 350 nm and 405 nm signal shown in (a) and (b) respectively. This optical degradation shows the same trend with host as the electrical degradation, further evidencing that the stability in devices is due to the intrinsic stability of the host material, rather than an effect of the manufactured device. The signal at 405 nm also follows the same trend, but with much less degradation than the 350 nm pump. This suggests that the majority of the degradation seen is in η_T or in the host absorption.

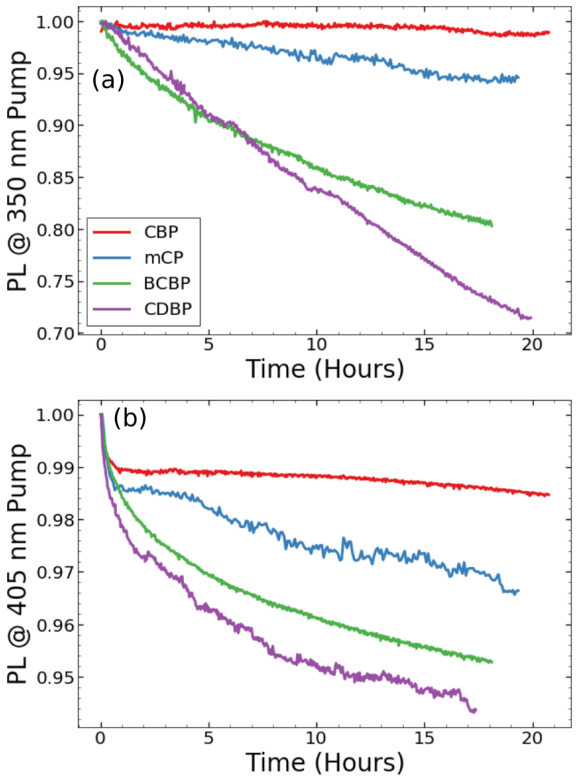

Figure 8.8: Photodegradation at 350 nm, with intermittent (10 s every 10 min) probe at 405 nm for all hosts.

With these results, it was hypothesized that the degradation in the 350 nm signal was due to loss in η_T and degradation of the host. The loss in 405 nm signal could be due to quenching of $Ir(ppy)_3$ by the degradation products of the host molecule. Under this assumption, if the host is not pumped, identical behavior between the four devices would be observed.

Therefore, the same devices were degraded under a 405 nm pump only, as shown in Figure 8.9. Contrary to the hypothesis, the behavior differed between hosts, rather than being identical. This is interesting because if the host is not being excited, this would suggest that simply the environment around the guest exciton on neighboring molecules is accelerating degradation. This could be due to a morphological effect, or a change in non-radiative pathways of the guest exciton.

Alternatively, it is possible that under high exciton density, bimolecular quenching is transferring excitons onto the host. Though these excitons would be short lived when compared to the guest excitons, they would be high energy and relax quickly, similar to bimolecular degradation mechanisms suggested for EL lifetimes.[83,154] This situation is difficult to avoid absolutely. While moving to lower emitter concentration to try to spatially separate the emitter and pumping at lower flux may increase the exciton spacing on average, high exciton density regions would still exist and it is plausible that the observed degradation is caused by these rare, but still active pathways. Additionally, if any sort of aggregation is observed with the emitter, and has been observed for some devices, then bimolecular quenching is always possible, regardless of doping concentration.[134]

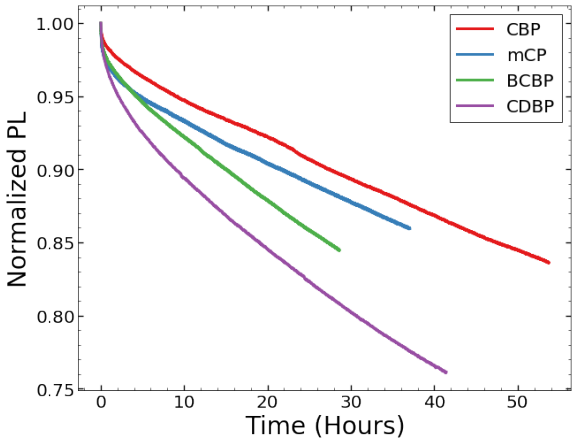

Figure 8.9: Photodegradation at 405 nm.

Despite these hesitations, if low doping concentration does show the same decay behavior, this would indicate host excitons. Devices were tested with 1% $Ir(ppy)_3$, shown in Figure 8.10. Interestingly, a difference is still observed, but CDBP shows higher stability than BCBP in this measurement. This is in contrast to the stability trend seen in all other degradations.

8.3 Ongoing Research

The working hypothesis for these devices is still that host excitons are being formed through bimolecular processes. To prove this hypothesis, it must be shown that guest excitons are still being excited. This could be done through an excited state absorption measurement.[268,269] Excitons on the host would have a separate signature than excitons on the guest. While emission is not seen from host excitons because they transfer to the guest, the host excitons would still have absorption. One problem with this technique is that the host exciton population would be very low when compared

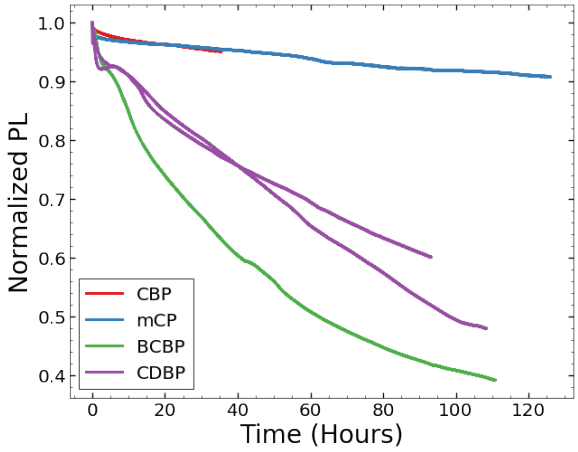

Figure 8.10: Photodegradation at 405 nm for architectures using 1% doping of $Ir(ppy)_3$ in the hosts. Higher stability is seen from CDBP compared to BCBP.

with the excited guest, and the host exciton absorption could be lost in the noise.

An alternative explanation for the observed behavior is morphological differences with regards to the $Ir(ppy)_3$ molecules. $Ir(ppy)_3$ has been previously shown to aggregate in dilute thin films.[134] If differences in the aggregation of $Ir(ppy)_3$ occur between the hosts, this could influence the degradation. To investigate this, η_{PL} is being investigated as a function of concentration and host to see if differences in aggregation are observed. For more aggregated $Ir(ppy)_3$, one would expect a lower η_{PL} , and possible a change in the relative η_{PL} with doping concentration between hosts due to a critical doping concentration to enable aggregation. Great care must be taken in the doping concentrations of these measurements to ensure that observed differences in η_{PL} are due to differences between the hosts, and not error in the doping concentration. If a difference in η_{PL} is observed, then TEM imaging will be used to see clusters of Iridium in the films. We expect that larger clusters would correspond to lower η_{PL} , and may correlate with the observed trend in lifetime.

Chapter 9

Data Management for Devices

9.1 Motivation

Within laboratory research, storage and organization of experimental data is a constant challenge. Any experiment can generate a large quantity of data in a variety of formats from various instruments. This data is typically delivered in unlabeled files, with only the name to convey all experimental information. Further details are left to a lab journal or formal write up, where researchers outline the experimental procedures and analyze results. Experimental details and data labeling in this manner is designed to help an active researcher with working knowledge of the experiments understand what has been done. However, as anyone who has worked in a lab can sympathize with, revisiting work, even your own, after the course of only a few months can often be incomplete, if not enigmatic. Given these challenges, researchers can often find themselves weighing the benefits of repeating experiments versus finding and attempting to comprehend previous results.

This frustration can be broken into two separate problem statements. First, experimental details and data are not intimately connected or collected by default when output from testing equipment. To find results, often experiments have to be searched for in a lab notebook, then cross referenced with electronic files. This relies on the searcher paging through notebooks, interpreting scribbled notes that were made, and hoping that whatever title was chosen for the days experiment to obviously identify what they are looking for. Then, assuming at best that this researcher provided a full filepath to experimental data on a computer that doesn't exist in your lab anymore, you have the task of searching through poorly labeled folders on a backup drive somewhere to find the data. As a researcher, it is nearly impossible to make this foolproof for later use, especially in an academic

setting, since these is no standardization of storage location or note taking applications. Corporate research facilities often use electronic lab notebooks and project archives to help have collected digital archives to mitigate this problem.

The second issue is the exclusion of critical information. In any experiment, there are numerous experimental parameters and details that need to be recorded. It can be easy to dismiss details as obvious or commit to memory for the purpose of analysis, then omitting this from the written information. However, when revisiting the experiment, these details are rarely obvious. An example out of this in our lab, is the planarizing layer in devices for lifetime testing. For large area patterned devices, we always use a planarizing layer, and for almost two years, that was always PEDOT-PSS. With this the case, it was considered almost a part of the substrate, and could be excluded from experimental details as it was implied. However, over time, we transitioned to using Plexcore AQ-1200, and then to AQ-1250 when AQ-1200 was discontinued. This easy and obvious case rapidly turned into a complex history, which could not have been predicted. The simple answer to this is to record every experimental parameter, but this is not logistically possible. Often it is even difficult to assess what is a constant and what will change.

While it can be easy to dismiss these issues as a problem for individual researchers, it is important to acknowledge that these are systematic issues and it should be a collective goal to minimize these issues. Every researcher attempts to provide clarity in this messy system, but the truth is that organizing and collecting data well using this system takes valuable time and effort that is hard to allocate and is not often appreciated until much later. Proposed methods for addressing these issues have to combat workflow inertia, and the resistance to change. Ideally, solutions will not interfere were current methods, and will make work easier in the active workflow as well as in archive searching.

Commercially, this issue of keeping track of experimental data is largely resolved. This is due to an ability to mandate research standards and organization required at this higher throughput scale. While the methods are not published, an example of commercial data management is shown from Merck & Company, Inc. in Figure 9.1. This figure references hundreds of efficiencies and lifetimes with extracted peak η_{EQE} characteristics and operating conditions.

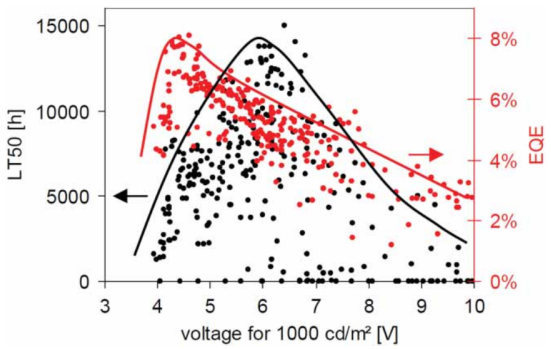

Figure 9.1: Dependence of η_{EQE} (red) and lifetime (black) on the driving voltage for various ETL configurations, sharing same HTL and EML. Reproduced from Böhm et al. [270].

Without data management, figures and conclusions like this would not be possible to make.

Within our lab, I have made an effort to address these issues using a relational database. This collects all data and connects with experimental details, and allows for easy search and manipulation of data in a standardized format. The details of implementation and usage examples are provided in this Chapter.

9.2 Overview

The first issue addressed above is the separation of experimental details from the actual collected data. This is almost universally resolved using relational databases. In a relational database, a series of records are stored with a list of attributes and values. Individual records can be looked at and all of the information is well organized. However, this system becomes increasingly valuable if records share a list of attributes, where the records can be searched based on the values of certain attributes.

Relational database systems are largely categorized into SQL and non-SQL systems. In SQL, all data is organized into tables, providing a relatively rigid structure. If values are not single valued, it is often necessary to create additional tables. Without going into further detail, non-SQL database systems are more ideal for laboratory data, as they have better support for list form values. With this in mind, I have developed this data collection system using MongoDB, a widely accepted non-SQL database. MongoDB supports interfacing directly as well as multiple other programming languages, including Python, the language I have utilized.

To facilitate this discussion, a few terms need to be defined. In the world of MongoDB, a "Document" is a single entry of data with many keys (attributes) and values, equivalent to a record in SQL. An example of this is:

```
{
        Name: Kyle Hershey,
        Occupation: Researcher,
        Lab: 421,
        Location: Minnesota
}
```

Here, several pieces of connected information are collected, creating a document. In this example, "Name" is a key, while "Kyle Hershey" is the associated value. Every document stored in MongoDB also has a unique ID, that can be used to reference it. Several Documents sharing the same type of information are organized into a "Collection". A Collection of Documents like the one above would

serve as a sort of directory of people. In MongoDB, not all Documents in a Collection are required to share the same list of keys. For example, other Documents may add a "Phone Number" or exclude the "Lab". However, Collections are intended to provide Documents with common information. A "Database" is a series of Collections that have related in formation and interact with each other. For example, a separate Collection in the same Database may store information about every lab.

```
{% Database
    {% Collection : People
        {% Document
            Name: Kyle Hershey,
            Occupation: Researcher,
            Lab: 421,
            Location: Minnesota
        }
        {% Document
            Name: Russell Holmes,
            Occupation: Professor,
            Location: Minnesota
        }
    }

    {% Collection : Labs
        {% Document
            Lab: 421,
            Function: OLED deposition,
            PI: Russell Holmes
        }
    }
}
```

This would then be able to be cross-referenced between the Collections for further information. If a value referencing another collection is not unique to a single document, the Document ID can be used.

9.3 Organization

As mentioned previously, databases require consistency of documents within the collection. This can be difficult to do effectively within a research environment where experimental design can change frequently. Within our lab, I have capitalized on the workflow of our experiments in order to organize

the collections. The four primary collections for daily workflow are **materials**, **architectures**, **growths**, and **lifetimes**. A full list of keys and datatype expectations can be found on the wiki page at `https://github.umn.edu/HolmesGroup/lifetimeTesting/wiki`, as well as in Appendix F.

At the most basic level, any film or device consists of a series of materials that are utilized for their physical properties. The **materials** collection seeks to keep track of all materials used in our lab and their various properties. Most notably, this includes energy levels, differing names, the CAS number, melting temperature and glass transition temperature (T_g). The other collections in the database utilize the material ID from this collection to uniquely identify materials for searchability and cross-referencing purposes.

The **architectures** collection captures the information required to describe what is grown. This includes the materialID (from the **materials** collection) and thickness for all substrate and deposited layers. Additionally, standard information like the EML thickness, doping concentration, and architecture type are stored for easy lookup.

For a planned experiment, once an architecture is decided upon, the experiment needs to be executed. An individual object in the **growth** collection consists of a single device architecture and the characterization data associated with the set. Characterization data includes all steady-state, standard characterization measurements, including spectrums, η_{EQE} , power efficiency, and current-voltage-luminance characteristics, among others. All data is stored for every device pixel, and is labeled by substrate and pixel number. Additional data about the experiment including the date, last chamber clean, grower name, and additional notes and reference tags is also collected.

Frequently in my work, in addition to steady state measurements, the operational lifetime is characterized. The **lifetimes** collection stores all information about lifetime measurements. This includes operating conditions, the associated **growth** and **architecture**, performance as a function of time, as well as any additional notes. Lifetimes are connected to the individual pixels from a **growth**.

This hierarchy creates lifetime objects which stems from a single growth, stemming from a single architecture. However, an architecture can be the base of multiple growths, which can each have multiple lifetimes.

Various spectral characterizations are stored in separate collections. These include photoluminescence, absorption, and excitation spectra, as well as optical constants. Each of these collections stores a layer structure, relevant illumination and testing conditions, tester name and date, as well as other test information.

9.4 Applications

Using this organizational framework for our data, I wanted to make sure all test information was recorded in this format to ensure utilization. In order to do this, I thought it was important to minimize the energy barrier for usage, and integrate usage of the database into the daily workflow. Since implementation, the database is now a critical part of data collection and analysis for OLED characterization in our lab, even offering new features that were not possible before. This section seeks to outline some of the key areas of use and capabilities of this database system.

9.4.1 Growth Characterization

After a growth is completed, spectral and current voltage characterization needs to be done. All of this data collection is done on a laboratory computer. Previously, generated datafiles would be transferred using a flash drive to the researcher's computer, where they would be organized and analyzed.

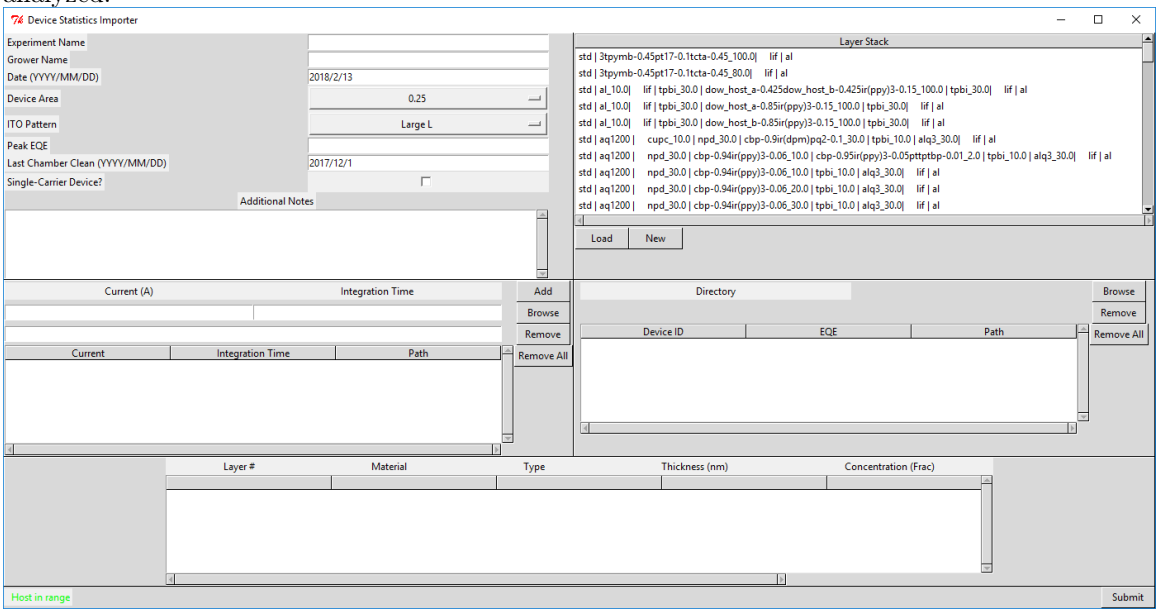

Figure 9.2: Graphical Interface for uploading test data into the database.

I developed a Graphical User Interface (GUI), shown in Figure 9.2, in order to collect all of the test information into the database. In the top left panel of Figure 9.2, basic test information can be entered. The top left allows selection of the architecture that was grown, or creation of a new architecture. Once loaded, the layer stack of the selected architecture will be displayed in the bottom panel of the interface. Spectral data can be input in the middle left panel, with current and integration time automatically extracted from the filename. Current-voltage characteristics can be selected using the middle right panel, with the substrate and device number extracted from the

filename.

Once completed, this form can be submitted and the information will be entered into the database. Before submission, the entered data is analyzed, and the η_{EQE} , luminance, power efficiency, as well as numerous other calculations are performed and stored along with the raw data. This reduces the workload of the researcher because they no longer have to do the analysis or transfer the files manually. Plotting the calculated data is the only task remaining for the user.

Two primary workflows have been developed for plotting and comparison of test data. For publication quality figures, our group historically has used Origin. To implement this, I developed another interface, shown in Figure 9.3. This interface allows easy selection of datasets either by growth or architecture. Once the data sets are selected, the desired plots are selected and the data is sent to origin where polished plots and worksheets are created.

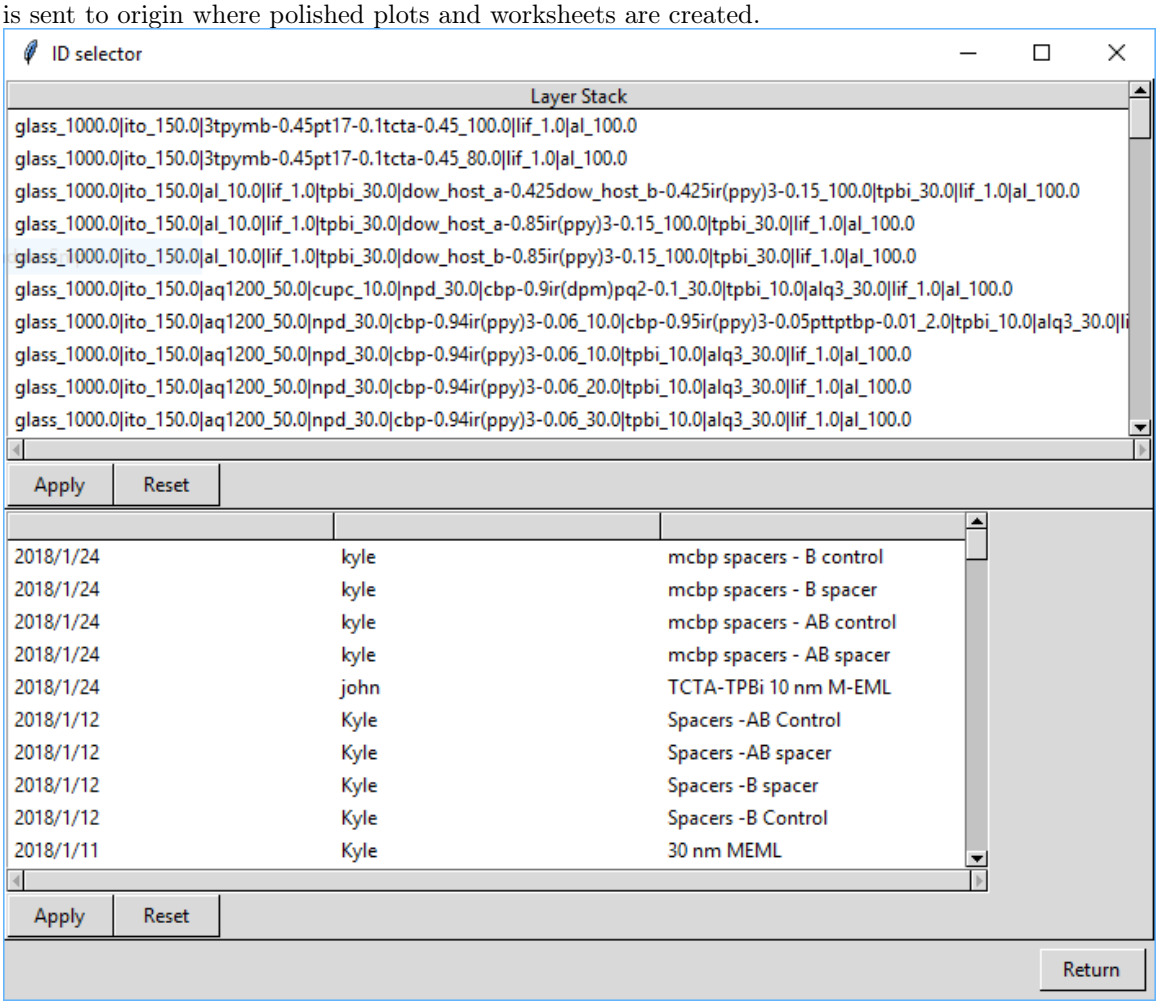

Figure 9.3: Graphical Interface for selecting data to send to Origin.

Within the database, representative IV scans can be identified by editing the **trust** key. The Origin plotter will not plot scans with a low trust factor, but will import the worksheet. This makes

it easy to compare datasets without having to first remove bad scans.

This GUI is useful as it fully replaces the previous behavior of manual file transfer and analysis, but adds on the ability of being able to easily access and compare any previous datasets. This selection process is efficient for standard characterization and processing, but is not very flexible when it comes to non-standard analysis or more intricate data selection.

Given the advanced sorting and organizational possibilities of the database, it is easy to select different data based off of criteria that the interface shown in Figure 9.3 does not allow. For example, what if we wanted to know to compare devices that used the material TCTA and had an EML thickness of 30 nm? This can be trivially done in python using the following command:

```
{
    selectedArchitectures=db.architectures.find({'eml_thickness':30, 'layers_list.
    material': 'tcta' })
}
```

With this ease of selecting data, a flexible plotting solution is needed to accommodate analysis or the resulting data. Primarily, we have settled on using Python in Jupyter Notebooks with Matplotlib for plotting. This allows for easy data selection, programmatic analysis, and plotting, all in a well organized notebook-like format.

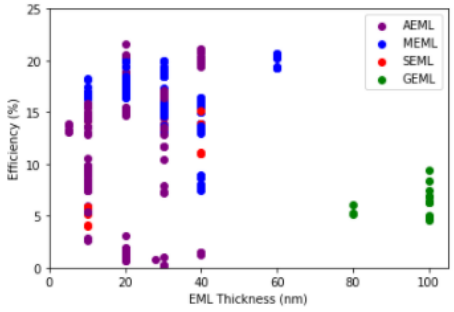

(a)

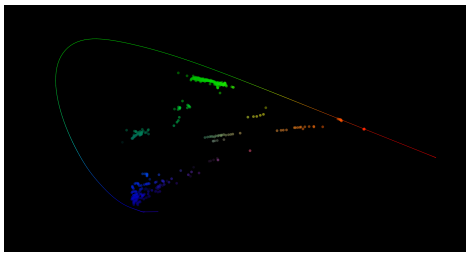

(b)

Figure 9.4: a. Peak EQE as a function of EML thickness b. CIE coordinates of every device collected during my thesis.

The first example, shown in Figure 9.4a, investigates the overall behavior of η_{EQE} as a function of the EML thickness for various device types. This was obtained using the following segment of code:

```
{
    growths=db.growths.find({,{'architectureID':1,'devices.peakEQE':1,'devices.trust
    ':1})
        colors={'MEML':'blue','AEML':'purple','SEML':'red','DEML':'orange','GEML':'
    green'}
        for growth in growths:
```

```
            arch=db.architectures.find_one({'_id':growth['architectureID']})
            nm=arch['eml_thickness']
            color=colors[arch['device_type']]
            for device in growth['devices']:
                if device['trust']>1:
                    plt.scatter(nm,device['peakEQE'],label=arch['device_type'],c=
    color)
    plt.legend()
    plt.show()
}
```

This search accesses a variety of information about almost 200 growths over the last 5 years. This plot consists of thousands of reference points, which are all easily organized due to the database.

It is also important to note that further analysis can be conducted after data selection, as well as plotting. A good example of this is shown in Figure 9.4b. This figure shows every device spectra that I have collected during this thesis, with CIE color coordinates calculated for every spectra.

These examples are not included for interest in the data itself, but for the ease of comparison and compilation. Without the database, organizing these datasets would be a nightmare of digging through lab notebooks and computer files, followed by a painful graphing process with dozens of files. The energy barrier of compiling this data would be enough to deter most researchers from even attempting to look for trends like this.

9.4.2 Lifetime Characterization

After devices are grown and characterized, they are immediately entered into the database. The lifetime testing setup capitalizes on this and connects the lifetime test data to the growth on startup. After hitting start on a lifetime test, the interface shown in Figure 9.5 must be filled out before the test will start. The test automatically populates the testing conditions, and the user is able to add additional information. The menu in the top left allows easy selection of a growth to connect to. If a luminance is entered here, the current can be calculated for operation based off of the IV scan for the exact device being tested. This eliminates a loading step of having to measure the luminance again with a luminance scope. Since this menu is part of the user experience of loading lifetimes, all lifetimes are seamlessly logged.

As the test is running, data is actively uploaded to the database, rather than waiting for the end of the test. A Jupyter notebook interface has been developed to plot all actively running tests. This allows remote monitoring of all running lifetime tests distributing between the four lifetime

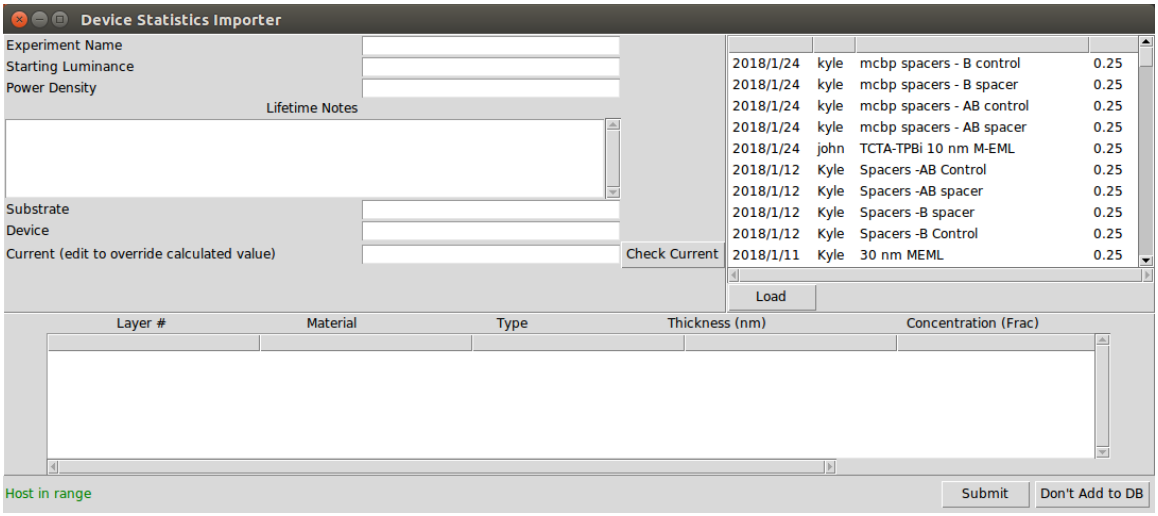

Figure 9.5: Graphical Interface for importing lifetime to database.

testing platforms in our labs. Upon test completion, the user gets an email alert that the test has completed, along with a graph of the lifetime results.

Similar to the growth collection capabilities, the lifetime collection allows unique filtering and analysis capabilities. A practical application example is from the work in Chapter 6.2. In this work, a relation is shown between the exciton density and the device lifetime. The exciton density can be manipulated using the EML thickness. In this system, the scaling function of lifetime as a function of luminance is known. Looking at all devices using a TCTA:TPBi MEML structure with 5% doping and scaling all lifetimes to 3000 cd/m^2, a relationship is seen between d_{EML} and the device lifetime, as shown in Figure 9.6. In fact, a scaling relation can be extracted, similar to the one shown for luminance. Prior to the completion of the dataset, we had hypothesized that this relationship existed. By utilizing these capabilities of the database, we were able to observe this relationship, further motivating the completion of a constant luminance dataset, which is shown in the final work.

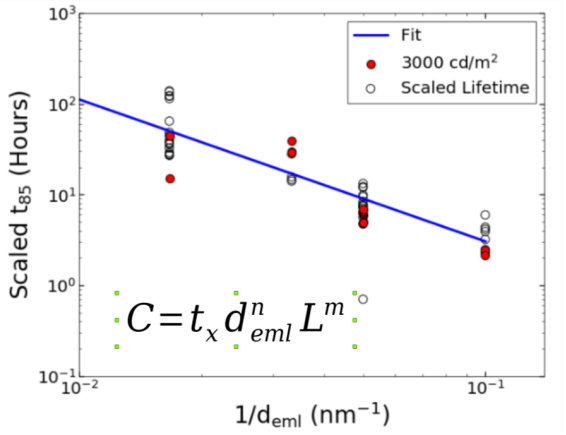

Figure 9.6: Device lifetime for a particular set of devices as a function of EML thickness. All lifetimes scaled to 3000 cd/m^2, with scaled lifetimes shown in red.

9.4.3 Materials Properties

The Growth and Lifetime collections offer a lot of features that are useful for device fabrication and characterization. The materials and spectral collections help in providing a well organized collection of materials characteristics. The simplest example of this would be a list of all known energy levels of materials, as shown in Figure 9.7. This dataset is actually much more rich than it first may appear. For a given material, multiple values can be stored, along with their literature reference. An accepted value can be identified as well.

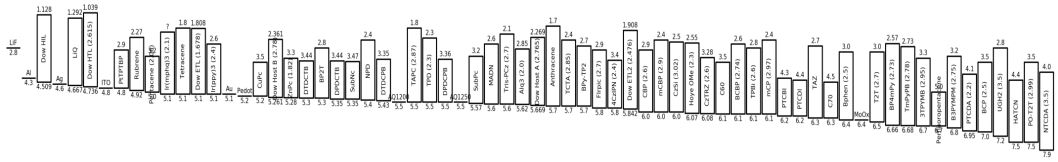

Figure 9.7: Energy levels of materials in database, sorted by HOMO value.

Spectral data can also be very important in material analysis. I have collected a large number of spectra recorded from the fluorimeter and UV-Vis, to populate the plSpectra, absSpectra, and excitaionSpectra collections. These collections can be easily search by material name and spectra type, using the Jupyter Notebook available at `http://holmes-carl.cems.umn.edu:8888/notebooks/databaseNotebooks/Spectra%20-%20Search%20.ipynb`. This notebook plots all spectra for the selected material, allowing variation and average features to be seen.

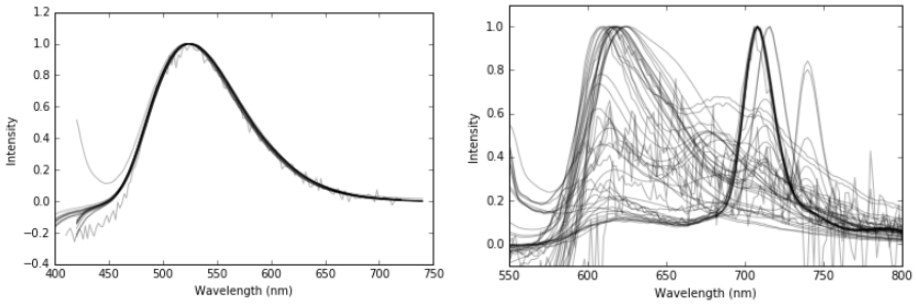

(a) **(b)**

Figure 9.8: (a) All collected spectra for Alq_3. (b) All collected spectra for SubPc.

Example output of this utility program can be seen in Figures 9.8a and 9.8b. For Alq_3 in Figure 9.8a, very consistent emission is seen, representing an efficient, well behaved emitter. However, Figure 9.8b shows the spectra for SubPc, a weak emitter that has been problematic in our group in that different batches and processing conditions can show varying spectral behavior. Two clear spectral features are shown as the most dominant, though they vary dramatically in intensity. Previous efforts to understand the changing spectra have relied on lab notebook notes and memory to understand differences between the spectra, and have been largely unsuccessful. Hopefully, with improved

recording of parameters using the database for future tests, a more complete understanding can be obtained.

Our group does a large amount of optical field modeling for layer stacks that relies upon optical constants obtained by the group. Standard procedure for management of these optical constants has been to share an excel document with obtained constants to new students, and selectively distribute new measurements as needed. This has resulted and every researcher having a differing set of constants and often various files with incomplete sets. Additionally, no experimental details are included, other than the results, making the history and validity of constants always being a problem.

With optical constants being included in the database, a central repository of constants has been developed, that can include all relevant test information for the curious researcher to use as needed. Developed by my colleague John S. Bangsund, a Transfer Matrix simulation package is now available to the group at `https://github.umn.edu/HolmesGroup/holmesPackage`. This package is capable of doing most Transfer Matrix calculations while fetching all necessary optical constants from the database. This eliminates any need for individual collections and makes any new data instantly available to the whole group.

9.4.4 Available Programs

In developing a workflow around using this database for data collection and analysis, John S. Bangsund and I have created several useful programs utilizing database features. These are available internally within the UMN at `http://holmes-carl.cems.umn.edu:8888/tree/databaseNotebooks`. A brief summary of useful programs is provided below.

- **Daily Analysis:** Allows selection of growth and plots all related IV, η_{EQE} , and lifetime plots. Serves as a template for analysis of a growth.
- **Database Query Examples:** A guide for building queries to find tests.
- **Energy Level Diagrams:** Constructs an energy level diagram that can be downloaded as an image. Energy levels are obtained from the materials collection. Diagrams can be constructed from a selected architecture, or from a custom list of materials.
- **EQEtrustAssess:** Allows selection of representative η_{EQE} scans for a growth.
- **lifetimeTrustAsses:** Sets the validity of lifetimes connected to a growth or architecture.

- **plotCurrentLifetimes:** Plots all actively running lifetimes in all boxes.
- **plotRecentLifetimes:** Plots lifetimes run recently. Date range is selectable.
- **Spectra - Search:** Advanced search tool for various spectral characterizations.
- **Tooling Factors:** Allows plotting of tracked tooling factors over time and as a function of deposition rate.
- **Importers (Folder):** Import functions for spectra into the database.

9.5 Future

The usage of a database system for organizing laboratory results for OLEDs have dramatically changed our workflow for the better. Data is easily and permanently logged in a format that is easily searchable and programmatically accessible. This has provided multiple capabilities that we did not previously have. Implementing this system to the point it is today has required significant investment of time and energy without generating immediate forward research progress. This has included thousands of lines of code and over 350 versions of the front-end software.

Thankfully, our team of OLED researchers has found this investment to be very useful and we have fully committed to using this system. All aspects of growth, materials analysis, lifetime and steady-state characterization are recorded and analyzed using this system. These analyses are standard procedures for our lab and invariant with time, providing consistent data compatible with a research database.

We have found that there are some experiments where the database system is not advantageous. For this system to be useful, a standard data structure is needed to provide easy searching and extraction of data. Often, for one time, novel experiments, there is minimal overlap with other tests. In these cases, logging experiments into the database does not fit the structure of other documents, and trying to force compliance into this system is not worth the effort. An example of this is optical degradation, where currently, no standard procedure has been developed. In these cases, it is difficult to identify important test parameters to record, and often results are not comparable even if they were recorded. In these cases, experimental methods need to develop sufficiently before logging into the database becomes useful. Moving forward for OLED research, it will be important to identify where this system can provide utility, and where it may not be worth the effort. Additionally, recognizing when new experiments have reached sufficient maturity to be worth archiving will require

active dialogue. However, given the value that this database archive has provided, I have confidence that it will continue to be used and expanded.

9.5.1 Machine Learning

Having a well populated dataset such as this also opens up the possibility for use of machine learning algorithms. Machine learning uses a large dataset to train an algorithm which in turn will predict outcomes of future data into either categorical or numerical output. With enough examples that have all input variables, the algorithm can predict many different behaviors. Due to the complexity of OLED design, and number of unknown variables, predicting η_{EQE} or lifetime from material information is unrealistic. However, less complex problems are solvable and can offer insight and utility into the manufacturing of devices. Here, I will outline three ventures into this space that I have conducted initial attempts to aid in research.

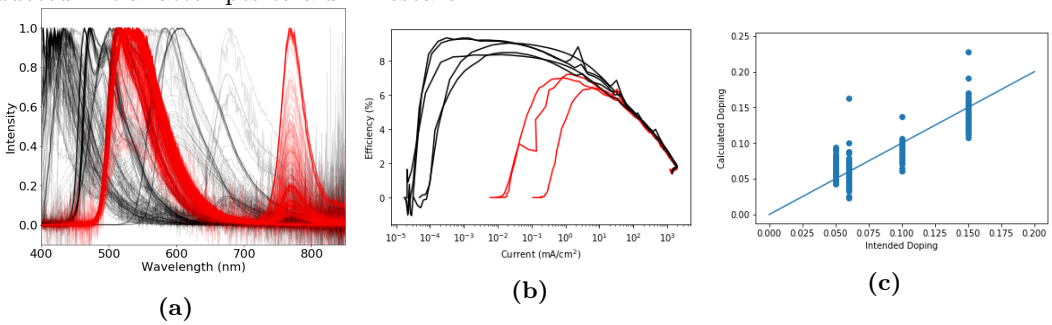

(a) **(b)** **(c)**

Figure 9.9: (a) Machine learning to spectrally identify $\mathrm{Ir(ppy)_3}$. Spectra shown in red are identified by the program as containing $\mathrm{Ir(ppy)_3}$. (b) Identifying and removing bad η_{EQE} scans. Spectra shown in red are identified as not representative and bad. (c) Predicting concentration base on spectra.

The first application is in predicting the emissive molecule from a PL spectra. Initial attempts at this involved identifying $\mathrm{Ir(ppy)_3}$ emission, shown in Figure 9.9a. In this figure, the $\mathrm{Ir(ppy)_3}$ feature is successfully identified, and depending on the algorithm training, can be taught to include or exclude the devices featuring the PtTPTBP sensitizer, whose emission is seen at 780 nm. While identifying the most recognizable emission feature from our lab is not very useful, this type of training could be useful for identifying unrecognized features. For example, if an impurity is seen in emission, it may be from a more exotic molecule. By having a trained algorithm to identify the emission, the researcher could be saved from having to look through spectra from every molecule. This identification could be done using a categorical algorithm. The implementation of a full identifier that can recognize all molecules has been hindered by the lack of spectral data for some molecules. The ability to predict output depends heavily on the size of the training set, so it is important to have a large number of example spectra. As more data is uploaded from the group, the resolution of this program will

improve.

The second example is to identify bad IV scans, shown in Figure 9.9b. This was an attempt to identify features of good η_{EQE} scans, using all devices in the database as a reference. However, this study found that given that all devices are not ideal, representative "good" behavior is not consistent between devices. Therefore, the ability to recognize characteristic behavior for all devices is variable. While the example in Figure 9.9a shows reasonable separation, there are other device sets that predict that all devices are bad. For better results, identified good and bad devices from the same architecture should be used. An interesting application of this would be to store trained algorithms for each architecture within the database, providing much better categorization. Then, when a new stack is grown for an existing architecture, the algorithm could identify scans immediately upon upload. Given the variety of devices we tend to grow, this would not be useful for most cases, but might be for benchmark devices.

The third application is an attempt to spectrally identify the $\mathrm{Ir(ppy)_3}$ concentration. This algorithm takes in the device spectra and predicts the $\mathrm{Ir(ppy)_3}$ concentration. Figure 9.9c compares the intended and predicted concentration, and surprisingly shows a reasonable correlation. The astute reader would note that the emission should also be a function of the emitter distance from the metal interface. However, further attempts at improving this algorithm are mostly limited by knowledge of the actual variation in the intended concentration. Since the reference value has a relatively large error bar, the accuracy of the training set is relatively low and limits the ability to resolve concentration differences.

These examples do not represent the full capabilities of machine learning, but offer some ideas as to useful information that it may provide. Given the amount of data that is being generated and input, it is important to think of applications for machine learning to help improve and provide feedback that will help the researcher. Abilities of this setup, especially with regards to spectra characterization, will greatly improve if a larger portion of the group begins to utilize the capabilities of the database.

9.5.2 Extension to Solar Cells

Given the success and utility of this database for OLEDs, an obvious extension in our group is the application to solar cells. Solar cells share much of the same data format to OLEDs: Materials are characterized in the same way, architectures and growths are conducted in the same manner with the same equipment, and characterization shares many similarities. Minimal modification of current

analysis and plotting scripts is needed to start collecting solar cell research data into a similar system.

Despite the advantages and currently developed code base, a solar cell research database has yet to be utilized within our group. This has largely been due to resistance to a change in workflow. Most data analysis within the solar cell research in our group is done within Matlab, with test data loaded from files. MongoDB does not have a Matlab driver, and for OLEDs, we have developed our scripts in Python. For established researchers, transitioning existing workflow and learning a new programming language is seen to outweigh the advantages of the database system. In order for the database to be utilized, new students will have to develop the analysis workflow to help establish this technique for solar cells.

9.5.3 Perovskite Film Growth

While vacuum-deposited solar cells share many similarities to OLEDs and the existing data, perovskites offer unique challenges to organization. For vacuum deposited OLEDs with reproducible growths, the discussed data structure allows for easy comparison against architectures, and growths should be relatively consistent. However perovskite growth is currently less reproducible and theoretical architecture may not translate to a consistent growth characteristics. In trying to extend this data structure to perovskite growths, less emphasis needs to be placed on the architecture, and more on the individual growth, due to reproducibility. This will require a different type of data structure, focused around the growth as a key construct. The beginnings of this organization and use for perovskite growth has been started. My colleague, Catherine Clark, has been using this database for recording her perovskite growth results for films from the perovskite vapor deposition system. As this expands into device fabrication, the structure of growth documents will need to be established.

All of these future applications will require development of new analysis functions and a shift away from programming in Matlab to a more functional programming language, such as Python. It is important that new students in the group realize the capabilities that this database provides and buy into the importance of its usage. With more group members actively using the database, the features and capabilities will greatly expand. If new students start using the features of this database, I think it will provide a valuable tool with capabilities not realized within more research groups.

Chapter 10

Future Research

10.1 Summary of This Work

This thesis has sought to increase the understanding of OLED device behavior from a fundamental physics standpoint. This has focused on three main topics, being device dynamics modeling, device lifetime decoupling, and attempting to develop molecular design rules. Rather than focusing on offering peak device performance, these studies have tried to present techniques for better understanding device behavior, allowing more informed optimization of peak devices. These research areas reflect the state of the field and limitations of further commercialization. The unique capabilities this previous research has developed within our group has enabled several potential future research directions.

In Chapter 4 an existing model for exciton dynamics within an OLED was extended to include polaron dynamics, allowing the fitting of transient and steady-state dynamics using the same fitting constants. This additionally allowed for the extraction of the charge balance factor, and quantification of these dynamics as the exciton formation efficiency. While attempts to utilize this improved dynamics model to quantify material differences have not been done extensively, the better understanding of polaron dynamics and exciton formation has triggered a different mindset for dissecting device behavior and analyzing results in both the steady-state, and lifetime.

In Chapters 5 and 6 an approach for decoupling lifetime into component efficiencies was developed. Taking the understanding of device operation developed in Chapter 4, intrinsic device degradation can be thought of as a combination of η_{PL} and η_{OC} loss over time. This has proven to be a very useful tool for understanding lifetime behavior. Chapter 6 talks about three studies where

this technique has provided valuable information, specifically in regard to the recombination zone width and position dependence. One limitation of this technique is that the degradation products are not known, only how it is affecting the device performance. This can make it difficult to attribute degradation problems to an individual molecule directly. However, this is still more information than just looking at the EL decay, so provides more information.

An understanding of design rules for OLED molecules was also considered. In Chapter 7, development of blue fluorescent emitters was considered along with device performance, while Chapter 8 took an alternative approach and investigated host material performance in device and optical degradation. In Chapter 7, devices were able to be fabricated with promising efficiency, but lifetimes were extremely unstable. Investigation of the mechanism for this degradation were not investigated at the time. Chapter 8 investigated EL lifetimes as well as the photostability to get a more fundamental look at degradation and try to attribute aspects of the EL lifetime to individual molecules.

In this chapter, potential future projects are discussed, mostly revolving around lifetime. Thermally Activated Delayed Fluorescence (TADF) molecules are a recent hot topic in OLEDs, and are a prime candidate for lifetime studies, and could benefit from investigation with our decoupling technique. During the lifetime decoupling of a device, accuracy of the measurement of η_{PL} relies on a constant η_{OC} . It is therefore important that the RZ of the device does not move during degradation, a claim that is largely uninvestigated, and could use further investigation. All of these topics are discussed in detail in this chapter.

10.2 TADF Lifetime Decoupling

Thermally Activated Delayed Fluorescence (TADF) is a promising OLED technology that has yet to see large commercial usage.[69–71,73,116] In TADF molecules, the energy difference between the singlet and triplet is similar to the thermal energy at room temperature. This allows triplet molecules to transfer back into the emissive singlet, providing an alternative method to achieve $\chi = 1$ without phosphorescence and the use of rare earth heavy metals. In addition to the potentially cheaper synthesis, TADF materials have been shown to improve exciton transport,[75] as well as a reduced efficiency roll-off[68,117] and promising preliminary lifetimes.[59,126] These features allow a potential alternative to Metal Ligan Charge Transfer (MLCT) molecules for commercial devices.[125]

With a large amount if interest, it is important to investigate device lifetimes. Promising initial results have shown operational $t_{90} > 200$ hours for a green emitter at 1000 cd/m^2.[126] This is not sufficient for commercial devices, but needs further development and optimization. With TADF

only being realized in the last half decade, this technology does not share the same long history of development of fluorescent and phosphorescent emitters.[94,95,103,109,202] Therefore, it does not share in the long history of brute-force optimization and understanding of limiting processes for lifetime through experience. Using the lifetime decoupling technique described in Chapter 5 could help to rapidly improved the understanding of TADF device operation.

One of the key parameters of a TADF emitter is the reverse intersystem crossing rate, k_{RISC}.[69,73,75,120,122] The population rate equations for singlets and triplets in a TADF system can be described as[75]

$$\frac{dn_S}{dt} = -n_S(k_{R,S} + k_{NR,S} + k_{ISC}) + n_T k_{RISC} + G \tag{10.1}$$

$$\frac{dn_T}{dt} = -n_T(k_{NR,T} + k_{RISC}) + n_S k_{ISC} \tag{10.2}$$

where n_S and n_T are the singlet and triplet densities, respectively, $k_{R,S}$ and $k_{NR,S}$ are the radiative and non-radiative singlet rates, $k_{NR,T}$ is the non-radiative triplet rate, k_{ISC} is the intersystem crossing rate, and G is the singlet generation rate. In this equation, excitons are freely allowed to transfer between the two states via k_{ISC} and k_{RISC}, but to observe significant delayed phosphorescence, k_{RISC} must be faster than $k_{NR,T}$ and k_{ISC} must be rapid. The transient photoluminescence of such a system is shown in Figure 10.1. Here, a prompt decay is seen on the order of nanoseconds corresponding to rapid decay of the generated singlet population via $k_{R,S}$. After the prompt component, the remaining excitons undergo ISC and are then limited by k_{RISC}, determining the rate of the delayed fluorescence component.

The efficiencies of prompt and delayed fluorescence can be written as

$$\eta_{PL,D} = \sum_{k=1}^{\infty} (\Phi_{ISC}\Phi_{RISC})^k \eta_{PL,P} \tag{10.3}$$

$$\eta_{PL,P} = \frac{k_{R,S}}{k_{R,S}+k_{NR,S}+k_{ISC}} \tag{10.4}$$

where Φ_{ISC} and Φ_{RISC} are the efficiencies of ISC and RISC in Equations 10.1 and 10.2, respectively.

During lifetime testing, it is not known what happens to PL degradation. It is possible that non-radiative rates change, as is the case for phosphorescent emitters, but is also possible that a change in k_{RISC} could occur. In phosphorescent emitters, k_{NR} is highly influenced by degradation in the surrounding environment.[153,154,271] However, a change in k_{RISC} would likely indicate a change in

the emitter molecule, or its configuration. These may have different implications on how to resolve the problem.

To measure k_{RISC} and k_{NR}, the transient PL would need to be measured. This has been done in Chapter 5 before and after degradation for phosphorescent emitters, trying to separate absorption losses from changes in k_{NR}. This same technique of measuring transients on degraded and undegraded devices could be used as an initial probe to see if any change in k_{RISC} is observed. If there is a change, transient PL should be incorporated into the degradation setup. This could replace the steady-state PL measurement, as the steady-state PL information can also be extracted from the transient.

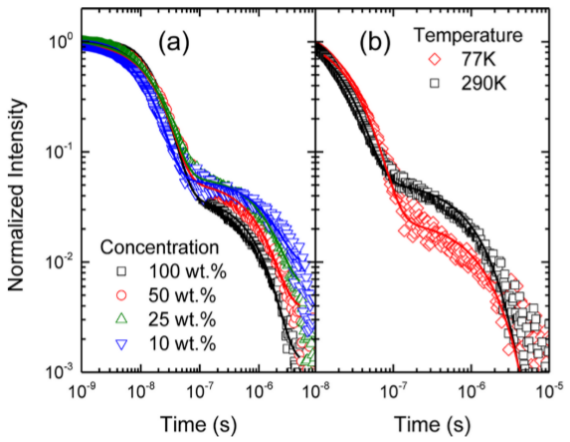

Figure 10.1: Transient PL lifetime of 4CzIPN, a TADF emitter, as a function of (a) Concentration in UGH2 and (b) Temperature. A short and long lifetime component are observed with lifetimes $\approx 1\ ns$ and $\approx 1\ \mu s$. Figure reproduced from Menke and Holmes [75].

The transient PL integration would require a pulsed laser source into the box, as well as integration of a fast photodiode and oscilloscope. Alternatively, an approach where multiple degradation points are investigated on different devices could be conducted. However, this technique utilizing different devices has been previously shown to show a large degree of sensitivity to optical alignment and device-to-device degradation. This could result in data with too much scatter to resolve the changes in rate constants.

Overall, probing TADF using a decoupled lifetime technique could result in rapid development of understanding of the degradation mechanisms. This could be of significant interest if a better understanding of k_{RISC} loss over time is developed. Such information would enable better device optimization, and may inform design rules for better molecular stability of TADF materials.

10.3 Recombination Zone Movement During Lifetime Testing

During device operation, modeling attempts and most device understanding of degradation relies on a fixed recombination zone profile.[83,93,152,221] Results from our research group on decoupled device degradation show that charge balance is degrading.[153,154,271] With changes in the charge balance, it is unlikely that the RZ is entirely constant. A changing recombination zone during degradation would result in a change in the out-coupling efficiency, η_{OC} , as a function of time. In simple EL

degradation, this could result in a misattribuation of degradation to physical degradation, which may just be an optical effect. During a decoupled lifetime measurement, a move in the RZ would change the degree of overlap between the EL RZ and the PL absorption, as discussed in Bangsund et al. [154]. Additionally, a change in RZ could result in a change in degradation mechanisms as a function of time, a prospect which is too daunting to have been considered in previous literature. To address these issues, it would be informative to track changes in the RZ during degradation.

Chapter 3.6 discussed measurement of the recombination zone in the steady-state undegraded case using a red sensitizer molecule. This technique used an out-coupling corrected relative peak intensity for a locally sensitized red emitter to indicate RZ presence. In a series of devices, the RZ can be mapped as a function of position of the red sensitizer.[153,154] One method of tracking the recombination zone during degradation is to use this same technique as a function of time. This would require spectral collection as a function of time, rather than the power measurement that is currently employed. However, some groups already collect spectral data during lifetime testing.[199,237,272] In fact, red sensitizers have already been used in lifetime testing devices for tracking exciton confinement to the emissive layer.[139]

Despite some precedent of similar techniques, great care has to be taken to ensure accuracy of this technique. First of all, degradation of the red sensitizer must be able to be controlled and isolated. Ideally, there would be no quenching of the red sensitizer, but it is likely that states that are able to quench the emission of $Ir(ppy)_3$ would be able to quench the sensitizer state. This makes it extremely difficult to separate movements of the RZ from degradation of the sensitizer. To control for this, one might create devices featuring extremely narrow and confined RZs where the RZ is not able to move. This would create a reference for how quickly the sensitizer degrades without allowing movement of the RZ. An additional problem is in assuring that the sensitizer is not influencing the lifetime it is probing. Since the red sensitizer is energetically nested within the emitter and host materials, it serves as a deep trap state, which are known to influence device performance. To counteract this, a low doping concentration would have to be used, and comparison to an undoped control would have to show no changes in the lifetime. While the testing of this concern is simple, developing a doping scheme that satisfies this condition could be challenging.

If these conditions are met, a significant improvement in degradation mechanics could be enabled. In our recent study, Bangsund et al. [271], competing mechanisms of bulk exciton density induced degradation and interfacial degradation were found to be influential. This was able to be optimized in devices that moved the RZ away from the interface of the HTL. In a system such as this, degradation could easily be a function of both mechanisms, the ratio of which may depend on the RZ position

during degradation. To be effectively modeled and understood, the RZ must be known throughout the degradation. In addition to the understanding of particular device systems, this technique would offer great insight in understanding the nature of η_{EF} degradation. In our previous studies,[153,154,271] degradation has been decoupled into a η_{PL} and η_{EF} components. However, exciton formation losses are not further understood in regards to which carrier is suffering a reduction, or where non-radiative recombination centers are forming. This technique would offer a further handle on understanding this behavior and what is happening to charges as fewer excitons are formed.

Bibliography

(1) Kenning, T. Engie and Heliatek launch 'world's largest' OPV system on French school roof | PV Tech., 2017.

(2) Soneira, R. M. Galaxy S7 and S7 Edge OLED Display Technology Shoot-Out., 2016.

(3) Soneira, R. M. The Flagship 2017 OLED Smartphones., 2017.

(4) Dimitrakopoulos, C. D.; Malenfant, P. R. L. *Adv. Mater.* **2002**, *14*, 99–117.

(5) P. Gaj, M. **2016**, 22.

(6) Peumans, P.; Yakimov, A.; Forrest, S. R. *Journal of Applied Physics* **2003**, *93*, 3693–3723.

(7) Park, J. S.; Chae, H.; Chung, H. K.; Lee, S. I. *Semiconductor Science and Technology* **2011**, *26*, DOI: 10.1088/0268-1242/26/3/034001.

(8) Gu, G.; Burrows, P. E.; Venkatesh, S.; Forrest, S. R.; Thompson, M. E. *Optics letters* **1997**, *22*, 172–174.

(9) Sugimoto, A.; Ochi, H.; Fujimura, S.; Yoshida, A.; Miyadera, T.; Tsuchida, M. *IEEE Journal of Selected Topics in Quantum Electronics* **2004**, *10*, 107–114.

(10) Cok, R. S. <Method of manufacturing an OLED device with a curved light emitting surface.pdf>., 2005.

(11) Han, C.-W.; Park, J.-S.; Choi, H.-S.; Kim, T.-S.; Shin, Y.-H.; Shin, H.-J.; Lim, M.-J.; Kim, B.-C.; Kim, H.-S.; Kim, B.-S.; Tak, Y.-H.; Oh, C.-H.; Cha, S.-Y.; Ahn, B.-C. *Journal of the Society for Information Display* **2014**, *22*, 552–563.

(12) Søndergaard, R. R.; Hösel, M.; Krebs, F. C. *Journal of Polymer Science, Part B: Polymer Physics* **2013**, *51*, 16–34.

(13) Hung, C.-H. *Manufacturing Process for OLED Integrated Substrate*; tech. rep.; U.S. Department of Energy, 2015.

(14) Tsujimura, T. In *OLED Displays: Fundamentals and Applications*; John Wiley & Sons, Inc.: Hoboken, New Jersey, 2012, pp 61–98.

(15) Fahlteich, J.; Steiner, C.; Top, M.; Wynands, D.; Wanski, T.; Mogck, S.; Kucukpinar, E.; Amberg-Schwab, S.; Boeffel, C.; Schiller, N.

(16) Manners, D. Taiwan's ITRI building OLED lighting line., 2016.

(17) Mertens, R. The EU aims to create a European-wide flexible OLED lighting pilot line | OLED-Info., 2016.

(18) Kalyani, N. T.; Swart, H.; Dhoble, S., *Principles and Applications of Organic Light Emitting Diodes (OLEDs) - N. Thejo Kalyani, Hendrik Swart, S. J. Dhoble - Google Books*; Elsevier: 2017.

(19) Morrison, G. LED LCD vs. OLED: TV display technologies compared., 2017.

(20) Rozario, H. Looking for Phones with OLED Displays? Here are Your Best Options., 2017.

(21) Morrison, G. Phone OLED vs TV OLED: What's the difference?, 2018.

(22) Statt, N. LG made an 18-inch display you can roll up like a newspaper - The Verge., 2016.

(23) Statista Worldwide TV market share in 2017 and 2018, by type., 2018.

(24) OLEDWorks New OLED lighting technology with high efficiency and high flexibility | Printed Electronics World.

(25) Evangeline, H. Opportunities and Challenges in OLED Lighting Market - LEDinside., 2018.

(26) Schlenker, C. W.; Barlier, V. S.; Chin, S. W.; Whited, M. T.; McAnally, R. E.; Forrest, S. R.; Thompson, M. E. *Chemistry of Materials* **2011**, *23*, 4132–4140.

(27) Sapkota, S. B.; Spies, A.; Zimmermann, B.; Dürr, I.; Würfel, U. *Solar Energy Materials and Solar Cells* **2014**, *130*, 144–150.

(28) Gregg, B. A. *The Journal of Physical Chemistry B* **2003**, *107*, 4688–4698.

(29) Fitzgerald Weaver, J. World's largest building integrated 'organic' solar power installation completed | Electrek., 2017.

(30) Wesoff, E. Belectric Goes After Building-Integrated PV With Organic Solar Cells | Greentech Media., 2014.

(31) InfinityPV infinityPV foil., 2018.

(32) Henion, A. Transparent solar technology represents 'wave of the future' | MSUToday | Michigan State University., 2017.

(33) Cuthbertson, A. Transparent Solar Panels Could Harvest Energy from Windows and Eventually Replace Fossil Fuels., 2017.

(34) Briseno, A. L.; Mannsfeld, S. C. B.; Ling, M. M.; Liu, S.; Tseng, R. J.; Reese, C.; Roberts, M. E.; Yang, Y.; Wudl, F.; Bao, Z. *Nature* **2006**, *444*, 913–917.

(35) Sirringhaus, H. *Advanced Materials* **2014**, *26*, 1319–1335.

(36) Yun, M.; Sharma, A.; Fuentes-Hernandez, C.; Hwang, D. K.; Dindar, A.; Singh, S.; Choi, S.; Kippelen, B. *ACS Applied Materials and Interfaces* **2014**, *6*, 1616–1622.

(37) Briseno, A. L.; Tseng, R. J.; Ling, M. M.; Falcao, E. H. L.; Yang, Y.; Wudl, F.; Bao, Z. *Advanced Materials* **2006**, *18*, 2320–2324.

(38) Pope, M.; Swenberg, C., *Electronic Processes in Organic Crystals and Polymers*, 2nd; Oxford University Press: 1999.

(39) No Title.

(40) Neamen, D. A., *Semiconductor Physics and Devices*, 2nd ed.; Irwin: 1992.

(41) Kittel, C., *Introduction to Solid State Physics*; Wiley: 2005.

(42) Wallis, R. F.; Balkanski, M., *Semiconductor Physics and Applications*; Oxford: 2000.

(43) Mark, P.; Helfrich, W. *Journal of Applied Physics* **1962**, *33*, 205.

(44) Kasap, S. O., *Principles of Electronic Materials and Devices*; McGraw Hill: 1997.

(45) Turro, N.; Scaiano, J.; Ramamurthy, V., *Modern Molecular Photochemistry of Organic Molecules*; University Science Books: 1991.

(46) Reineke, S.; Walzer, K.; Leo, K. *Physical Review B* **2007**, *75*, 125328.

(47) Hains, A. W.; Liang, Z.; Woodhouse, M. A.; Gregg, B. A. *Chemical Reviews* **2010**, *110*, 6689–6735.

(48) Gregg, B. A. *The Journal of Physical Chemistry B* **2003**, *107*, 4688–4698.

(49) Song, D.; Zhao, S.; Aziz, H. *Advanced Functional Materials* **2011**, *21*, 2311–2317.

(50) Park, J. P. J. *Journal of Lightwave Technology* **2010**, *28*, 2873–2880.

(51) Ryasnyanskiy, A.; Biaggio, I. *Physical Review B - Condensed Matter and Materials Physics* **2011**, *84*, 2–5.

(52) Wang, Q.; Aziz, H. *ACS Applied Materials and Interfaces* **2013**, *5*, 8733–8739.

(53) Erickson, N. C.; Holmes, R. J. *Advanced Functional Materials* **2014**, *24*, 6074–6080.

(54) Furno, M.; Meerheim, R.; Hofmann, S.; Lüssem, B.; Leo, K. *Physical Review B* **2012**, *85*, 115205.

(55) Baldo, M.; Holmes, R. J.; Forrest, S. *Physical Review B* **2002**, *66*, 35321.

(56) Mikhnenko, O. V., *Singlet and Triplet Excitons in Organic Semiconductors*.

(57) Zhang, Q.; Li, B.; Huang, S.; Nomura, H.; Tanaka, H.; Adachi, C. *Nature Photonics* **2014**, *8*, 1–7.

(58) Nakanotani, H.; Masui, K.; Nishide, J.; Shibata, T.; Adachi, C. *Scientific reports* **2013**, *3*, 2127.

(59) Méhes, G.; Goushi, K.; Potscavage, W. J.; Adachi, C. *Organic Electronics: physics, materials, applications* **2014**, *15*, 2027–2037.

(60) Menke, S. M.; Luhman, W. a.; Holmes, R. J. *Nature materials* **2013**, *12*, 152–7.

(61) Holmes, R. J.; Forrest, S.; Tung, Y.-J.; Kwong, R. C.; Brown, J. J.; Garon, S.; Thompson, M. E. *Applied Physics Letters* **2003**, *82*, 2422.

(62) Goushi, K.; Kwong, R.; Brown, J. J.; Sasabe, H.; Adachi, C. *Journal of Applied Physics* **2004**, *95*, 7798–7802.

(63) Volcker, A. *Chemical physics letters* **1989**, *159*, 103–108.

(64) Padhye, M. R.; McGlynn, S. P.; Kasha, M. *The Journal of Chemical Physics* **1956**, *24*, 588–594.

(65) Reineke, S.; Baldo, M. *Scientific Reports* **2014**, *4*, 3797.

(66) Chan, C.-Y.; Cui, L.-S.; Kim, J. U.; Nakanotani, H.; Adachi, C. *Advanced Functional Materials* **2018**, *1706023*, 1706023.

(67) Lee, S. Y.; Adachi, C.; Yasuda, T. **2016**, DOI: 10.1002/adma.201506391.

(68) Inoue, M.; Serevičius, T.; Nakanotani, H.; Yoshida, K.; Matsushima, T.; Juršenas, S.; Adachi, C. *Chemical Physics Letters* **2016**, *644*, 62–67.

(69) Zhang, Q.; Li, J.; Shizu, K.; Huang, S.; Hirata, S.; Miyazaki, H.; Adachi, C. **2012**, 0–3.

(70) Endo, A.; Ogasawara, M.; Takahashi, A.; Yokoyama, D.; Kato, Y.; Adachi, C. *Advanced materials (Deerfield Beach, Fla.)* **2009**, *21*, 4802–4806.

(71) Li, J.; Nakagawa, T.; Macdonald, J.; Zhang, Q.; Nomura, H.; Miyazaki, H.; Adachi, C. *Advanced Materials* **2013**, *25*, 3319–3323.

(72) Nasu, K.; Nakagawa, T.; Nomura, H.; Lin, C.-J.; Cheng, C.-H.; Tseng, M.-R.; Yasuda, T.; Adachi, C. *Chemical communications (Cambridge, England)* **2013**, *49*, 10385–7.

(73) Uoyama, H.; Goushi, K.; Shizu, K.; Nomura, H.; Adachi, C. *Nature* **2012**, *492*, 234–8.

(74) Mullenbach, T. K.; McGarry, K. A.; Luhman, W. A.; Douglas, C. J.; Holmes, R. J. *Advanced materials* **2013**, *25*, 3689–93.

(75) Menke, S. M.; Holmes, R. J. *The Journal of Physical Chemistry C* **2016**, *120*, 8502–8508.

(76) Luhman, W. A.; Holmes, R. J. *Advanced Functional Materials* **2011**, *21*, 764–771.

(77) Congreve, D. N.; Lee, J.; Thompson, N. J.; Hontz, E.; Yost, S. R.; Reusswig, P. D.; Bahlke, M. E.; Reineke, S.; Van Voorhis, T.; Baldo, M. A. *Science* **2013**, *340*, 334–337.

(78) Johnson, J. C.; Nozik, A. J.; Michl, J. **2012**, *XXX*, 6891–6936.

(79) Lee, J.; Jadhav, P.; Reusswig, P. D.; Yost, S. R.; Thompson, N. J.; Congreve, D. N.; Hontz, E.; Van Voorhis, T.; Baldo, M. A. *Accounts of Chemical Research* **2013**, *46*, 1300–1311.

(80) Shaheen, S. E.; Jabbour, G. E.; Morrell, M. M.; Kawabe, Y.; Kippelen, B.; Peyghambarian, N.; Nabor, M.-F.; Schlaf, R.; Mash, E. A.; Armstrong, N. R. *Journal of Applied Physics* **1998**, *84*, 2324.

(81) Fujii, A.; Ohmori, Y.; Morishima, C.; Yoshino, K. *Japanese Journal of Applied Physics* **1994**, *33*, L348–L350.

(82) Stampor, W.; Kalinowski, J.; Di Marco, P.; Fattori, V. *Applied Physics Letters* **1997**, *70*, 1935.

(83) Giebink, N. C.; D'Andrade, B. W.; Weaver, M. S.; MacKenzie, P. B.; Brown, J. J.; Thompson, M. E.; Forrest, S. *Journal of Applied Physics* **2008**, *103*, DOI: 10.1063/1.2884530.

(84) Hershey, K. W.; Holmes, R. J. *Journal of Applied Physics* **2016**, *120*, 195501.

(85) Tao, Y.; Yang, C.; Qin, J. *Chemical Society Reviews* **2011**, *40*, 2943.

(86) Shirota, Y.; Kageyama, H. *Chemical reviews* **2007**, *107*, 953–1010.

(87) Käfer, D.; Ruppel, L.; Witte, G.; Wöll, C. *Physical Review Letters* **2005**, *95*, 166602.

(88) Maldonis, J. J.; Hwang, J.; Voyles, P. M. *Computer Physics Communications* **2017**, *213*, 217–222.

(89) Maldonis, J. J.; Zhang, P.; Besser, M.; Kramer, M.; Voyles, P. M. *Microscopy and Microanalysis* **2015**, *21*, 1659–1660.

(90) Zhang, P.; Maldonis, J. J.; Liu, Z.; Schroers, J.; Voyles, P. M. *Submitted* **2017**, DOI: `arXiv:1710.04791v2`.

(91) Zhang, P.; Maldonis, J. J.; Besser, M. F.; Kramer, M. J.; Voyles, P. M. *Acta Materialia* **2016**, *109*, 103–114.

(92) Fielitz, T. R.; Holmes, R. J. *Crystal Growth and Design* **2016**, *16*, 4720–4726.

(93) Scholz, S.; Kondakov, D.; Lüssem, B.; Leo, K. *Chemical Reviews* **2015**, *115*, 8449–8503.

(94) Baldo, M.; Thompson, M. E.; Forrest, S. *Nature* **2000**, *403*, 750–3.

(95) Baldo, M.; O'Brien, D.; You, Y.; Shoustikov, A.; Sibley, S.; Thompson, M. E.; Forrest, S. *Nature* **1998**, *395*, 151–154.

(96) Furno, M.; Meerheim, R.; Thomschke, M.; Hofmann, S.; Lüssem, B.; Leo, K. *Proceedings of SPIE* **2010**, *7617*, ed. by Streubel, K. P.; Jeon, H.; Tu, L.-W.; Linder, N., 761716–761716–12.

(97) Lampert, M. A. *Reports on Progress in Physics* **2002**, *27*, 329–367.

(98) Forrest, S.; Bradley, D.; Thompson, M. E. *Advanced Materials* **2003**, *15*, 1043–1048.

(99) Smith, T.; Guild, J. *Transactions of the Optical Society* **1931**, *33*, 73–134.

(100) Wright, W. D. *Transactions of the Optical Society* **1929**, *30*, 141–164.

(101) Guild, J. *Philosophical Transactions of the Royal Society A: Mathematical, Physical and Engineering Sciences* **1932**, *230*, 149–187.

(102) Bohn, D. Google updates Pixel 2 XL with new 'saturated' color display option and other bug fixes - The Verge., 2017.

(103) Tang, C. W.; VanSlyke, S. *Applied Physics Letters* **1987**.

(104) Venkataraman, K., *The chemistry of synthetic dyes*; Elsevier, 2012: 1971.

(105) Schäfer, F. P.; Drexhage, K. H. *Topics in Applied Physics* **1977**.

(106) Dresner, J. *RCA REVIEW* **1969**.

(107) Williams, D. F.; Schadt, M. *Proceedings of the IEEE* **1970**, *58*, 476.

(108) Helfrich, W.; Schneider, W. G. *Physical Review Letters* **1965**, *14*, 229–231.

(109) Tang, C. W.; Vanslyke, S. a.; Chen, C. H. *Journal of Applied Physics* **1989**, *65*, 3610–3616.

(110) King, K. A.; Spellane, P. J.; Watts, R. J. *Journal of the American Chemical Society* **1985**, *107*, 1431–1432.

(111) Sprouse, S.; King, K. A.; Spellane, P. J.; Watts, R. J. *Journal of the American Chemical Society* **1984**, *106*, 6647–6653.

(112) Su, S. J.; Gonmori, E.; Sasabe, H.; Kido, J. *Advanced Materials* **2008**, *20*, 4189–4194.

(113) Erickson, N. C.; Holmes, R. J. *Applied Physics Letters* **2010**, *97*, 083308.

(114) Scholz, S.; Walzer, K.; Leo, K. *Advanced Functional Materials* **2008**, *18*, 2541–2547.

(115) Adachi, C.; Baldo, M. A.; Thompson, M. E.; Forrest, S. R. *Journal of Applied Physics* **2001**, *90*, 5048–5051.

(116) Zhang, Q.; Komino, T.; Huang, S.; Matsunami, S.; Goushi, K.; Adachi, C. *Advanced Functional Materials* **2012**, *22*, 2327–2336.

(117) Wang, H.; Meng, L.; Shen, X.; Wei, X.; Zheng, X.; Lv, X.; Yi, Y.; Wang, Y.; Wang, P. *Advanced Materials* **2015**, n/a–n/a.

(118) Liu, X.-K.; Chen, Z.; Zheng, C.-J.; Chen, M.; Liu, W.; Zhang, X.-H.; Lee, C.-S. *Advanced Materials* **2015**, n/a–n/a.

(119) Kim, K.-H.; Moon, C.-K.; Sun, J. W.; Sim, B.; Kim, J.-J. *Advanced Optical Materials* **2015**, n/a–n/a.

(120) Jankus, V.; Data, P.; Graves, D.; McGuinness, C.; Santos, J.; Bryce, M. R.; Dias, F. B.; Monkman, A. P. *Advanced Functional Materials* **2014**, n/a–n/a.

(121) Lavie-Cambot, A.; Cantuel, M.; Leydet, Y.; Jonusauskas, G.; Bassani, D. M.; McClenaghan, N. D. *Coordination Chemistry Reviews* **2008**, *252*, 2572–2584.

(122) Yersin, H.; Leitl, M. J.; Czerwieniec, R. **2014**, *9183*, 91830N.

(123) Hofbeck, T.; Monkowius, U.; Yersin, H. *Journal of the American Chemical Society* **2015**, *137*, 399–404.

(124) Linfoot, C. L.; Leitl, M. J.; Richardson, P.; Rausch, A. F.; Chepelin, O.; White, F. J.; Yersin, H.; Robertson, N. *Inorganic chemistry* **2014**, DOI: 10.1021/ic500889s.

(125) Reineke, S. *Nature Photonics* **2014**, *8*, 269–270.

(126) Cho, Y. J.; Yook, K. S.; Lee, J. Y. *Advanced Materials* **2014**, *26*, 4050–4055.

(127) Wehrmeister, S.; Jäger, L.; Wehlus, T.; Rausch, A. F.; Reusch, T. C. G.; Schmidt, T. D.; Brütting, W. *Physical Review Applied* **2015**, *3*, 1–10.

(128) Son, K. S.; Yahiro, M.; Imai, T.; Yoshizaki, H.; Nishide, J.; Sasabe, H.; Adachi, C. *Japanese Journal of Applied Physics* **2008**, *47*, 7363–7365.

(129) Murawski, C.; Leo, K.; Gather, M. C. *Advanced materials (Deerfield Beach, Fla.)* **2013**, *25*, 6801–27.

(130) Giebink, N. C.; Forrest, S. *Physical Review B* **2008**, *77*, 235215.

(131) Song, D.; Zhao, S.; Luo, Y.; Aziz, H. *Applied Physics Letters* **2010**, *97*, 243304.

(132) Xiang, C.; Fu, X.; Wei, W.; Liu, R.; Zhang, Y.; Balema, V.; Nelson, B.; So, F. *Advanced Functional Materials* **2016**, *26*, 1463–1469.

(133) Coehoorn, R.; Van Eersel, H.; Bobbert, P. A.; Janssen, R. A. J. *Advanced Functional Materials* **2015**, *25*, 2024–2037.

(134) Reineke, S.; Schwartz, G.; Walzer, K.; Falke, M.; Leo, K. *Applied Physics Letters* **2009**, *94*, 2007–2010.

(135) Mężyk, J.; Kalinowski, J.; Meinardi, F.; Tubino, R. *Applied Physics Letters* **2005**, *86*, 111916.

(136) Baldo, M.; Adachi, C.; Forrest, S. *Physical Review B* **2000**, *62*, 10967–10977.

(137) Köhler, a.; Bässler, H. *Materials Science and Engineering: R: Reports* **2009**, *66*, 71–109.

(138) Erickson, N. C.; Holmes, R. J. *Advanced Functional Materials* **2013**, *23*, 5190–5198.

(139) Coburn, C.; Forrest, S. *Physical Review Applied* **2017**, *7*, 041002.

(140) Lee, J.; Jeong, C.; Batagoda, T.; Coburn, C.; Thompson, M. E.; Forrest, S. *Nature Communications* **2017**, *8*, 15566.

(141) Holmes, R. J. *Nature Nanotechnology* **2007**, *2*, 7–8.

(142) Takenobu, T.; Bisri, S.; Takahashi, T.; Yahiro, M.; Adachi, C.; Iwasa, Y. *Physical Review Letters* **2008**, *100*, 066601.

(143) Samuel, I. D. W.; Namdas, E. B.; Turnbull, G. a. *Nature Photonics* **2009**, *3*, 546–549.

(144) Kasemann, D.; Brückner, R.; Fröb, H.; Leo, K. *Physical Review B* **2011**, *84*, 115208.

(145) Murawski, C.; Liehm, P.; Leo, K.; Gather, M. C. *Advanced Functional Materials* **2014**, *24*, 1117–1124.

(146) Soofi, H.; Saeidi, S. **2017**, 1–8.

(147) Chopra, N.; Swensen, J. S.; Polikarpov, E.; Cosimbescu, L.; So, F.; Padmaperuma, A. B. *Applied Physics Letters* **2010**, *97*, 95–98.

(148) Reineke, S.; Schwartz, G.; Walzer, K.; Leo, K. *Applied Physics Letters* **2007**, *91*, 1–4.

(149) Lee, J. I. J. Y. J.-I. J.; Lee, J. I. J. Y. J.-I. J.; Lee, J. I. J. Y. J.-I. J.; Chu, H. Y. *Applied Physics Letters* **2009**, *94*, 193305.

(150) Zang, F. X.; Sum, T. C.; Huan, a. C. H.; Li, T. L.; Li, W. L.; Zhu, F. *Applied Physics Letters* **2008**, *93*, 023309.

(151) Giebink, N. C.; Sun, Y.; Forrest, S. *Organic Electronics: physics, materials, applications* **2006**, *7*, 375–386.

(152) Giebink, N. C.; D'Andrade, B. W.; Weaver, M. S.; Brown, J. J.; Forrest, S. *Journal of Applied Physics* **2009**, *105*, 124514.

(153) Hershey, K. W.; Suddard-Bangsund, J.; Qian, G.; Holmes, R. J. *Applied Physics Letters* **2017**, *111*, 113301.

(154) Bangsund, J. S.; Hershey, K. W.; Holmes, R. J. *ACS Applied Materials & Interfaces* **2018**, acsami.7b16643.

(155) Coburn, C.; Lee, J.; Forrest, S. *Advanced Optical Materials* **2016**, *4*, 889–895.

(156) Reineke, S.; Lindner, F.; Huang, Q.; Schwartz, G.; Walzer, K.; Leo, K. *Physica Status Solidi (B) Basic Research* **2008**, *245*, 804–809.

(157) Erickson, N. C.; Holmes, R. J. *Journal of Applied Physics* **2011**, *110*, 084515.

(158) Féry, C.; Racine, B.; Vaufrey, D.; Doyeux, H.; Cinà, S. *Applied Physics Letters* **2005**, *87*, 213502.

(159) Giebink, N. *Optics InfoBase Conference Papers* **2017**, *Part F72-S*, 2017.

(160) Kolosov, D.; English, D. S.; Bulovic, V.; Barbara, P. F.; Forrest, S. R.; Thompson, M. E. *Journal of Applied Physics* **2001**, *90*, 3242–3247.

(161) Wang, W.; Lim, S. F.; Chua, S. J. *Journal of Applied Physics* **2002**, *91*, 5712–5715.

(162) Burrows, P. E.; Bulovic, V.; Forrest, S.; Sapochak, L. S.; McCarty, D. M.; Thompson, M. E. *Applied Physics Letters* **1994**, *65*, 2922–2924.

(163) Aziz, H.; Popovic, Z. D. *Chemistry of Materials* **2004**, *16*, 4522–4532.

(164) Popovic, Z. D.; Aziz, H. *IEEE Journal on Selected Topics in Quantum Electronics* **2002**, *8*, 362–371.

(165) Liew, Y.-f.; Aziz, H.; Hu, N.-x.; Chan, H. S.-o.; Xu, G.; Popovic, Z.; Liew, Y.-f.; Chan, H. S.-o. **2006**, *2650*, 1998–2001.

(166) Melpignano, P.; Baron-Toaldo, A.; Biondo, V.; Priante, S.; Zamboni, R.; Murgia, M.; Caria, S.; Gregoratti, L.; Barinov, A.; Kiskinova, M. *Applied Physics Letters* **2005**, *86*, 1–4.

(167) Liao, L. S.; He, J.; Zhou, X.; Lu, M.; Xiong, Z. H.; Deng, Z. B.; Hou, X. Y.; Lee, S. T. **2007**, *2386*, 1–6.

(168) Shin, H. J.; Song, H. J.; Lee, J.; Yoon, H. J.; Chung, J.; Lee, J. C. *Journal of Applied Physics* **2006**, *100*, 1–5.

(169) Scott, J. C.; Kaufman, J. H.; Brock, P. J.; DiPietro, R.; Salem, J.; Goitia, J. A. *Journal of Applied Physics* **1996**, *79*, 2745–2751.

(170) Cumpston, B. H. *Journal of Applied Physics* **1997**, *81*, 3716–3720.

(171) Chwang, A. B.; Kwong, R. C.; Brown, J. J. *Applied Physics Letters* **2002**, *80*, 725–727.

(172) Zhang, Y.; Aziz, H. *ACS Applied Materials and Interfaces* **2016**, *8*, 14088–14095.

(173) So, F.; Kondakov, D. *Advanced Materials* **2010**, *22*, 3762–3777.

(174) Zhang, Y.; Lee, J.; Forrest, S. *Nature Communications* **2014**, *5*, 1–7.

(175) Wu, Z.; Sun, N.; Zhu, L.; Sun, H.; Wang, J.; Yang, D.; Qiao, X.; Chen, J.; Alshehri, S. M.; Ahamad, T.; Ma, D. *ACS Applied Materials and Interfaces* **2016**, *8*, 3150–3159.

(176) Chin, B. D.; Suh, M. C.; Kim, M. H.; Lee, S. T.; Kim, H. D.; Chung, H. K. *Applied Physics Letters* **2005**, *86*, 1–3.

(177) Lee, J. Y. **2006**, 1103–1105.

(178) Han, T. H.; Kim, Y. H.; Kim, M. H.; Song, W.; Lee, T. W. *ACS Applied Materials and Interfaces* **2016**, *8*, 6152–6163.

(179) Lee, J. H.; Wu, C. I.; Liu, S. W.; Huang, C. A.; Chang, Y. *Applied Physics Letters* **2005**, *86*, 1–3.

(180) Brown, C. T.; Kondakov, D. *Journal of the Society for Information Display* **2004**, *12*, 323–327.

(181) Choong, V. E.; Shen, J.; Curless, J.; Shi, S.; Yang, J.; So, F. *Journal of Physics D: Applied Physics* **2000**, *33*, 760–763.

(182) Liu, S. W.; Huang, C. A.; Lee, J. H.; Yang, K. H.; Chen, C. C.; Chang, Y. *Thin Solid Films* **2004**, *453-454*, 312–315.

(183) Shen, Y.; Giebink, N. C. *Physical Review Applied* **2015**, *4*, 1–12.

(184) Aziz, H. *Science* **1999**, *283*, 1900–1902.

(185) Kondakov, D.; Sandifer, J. R.; Tang, C. W.; Young, R. H. *Journal of Applied Physics* **2003**, *93*, 1108–1119.

(186) Matsumura, M.; Ito, A.; Miyamae, Y. *Applied Physics Letters* **1999**, *75*, 1042–1044.

(187) Kondakov, D.; Nichols, W. F.; Lenhart, W. C. *SID Symposium Digest of Technical Papers* **2007**, *38*, 1494–1496.

(188) Kondakov, D. *Journal of Applied Physics* **2008**, *104*, DOI: 10.1063/1.3006890.

(189) Kondakov, D.; Lenhart, W. C.; Nichols, W. F. *Journal of Applied Physics* **2007**, *101*, 024512.

(190) Meerheim, R.; Walzer, K.; Pfeiffer, M.; Leo, K. *Applied Physics Letters* **2006**, *89*, 061111.

(191) Fry, C.; Racine, B.; Vaufrey, D.; Doyeux, H.; Cin, S. *Applied Physics Letters* **2005**, *87*, 1–3.

(192) Seifert, R.; Rabelo De Moraes, I.; Scholz, S.; Gather, M. C.; Lüssem, B.; Leo, K. *Organic Electronics: physics, materials, applications* **2013**, *14*, 115–123.

(193) Moraes, I. R. D.; Scholz, S.; Lüssem, B.; Leo, K. *Organic Electronics* **2011**, *12*, 341–347.

(194) De Moraes, I. R.; Scholz, S.; Lüssem, B.; Leo, K. *Applied Physics Letters* **2011**, *99*, 053302.

(195) Sivasubramaniam, V.; Brodkorb, F.; Hanning, S.; Loebl, H. P.; Elsbergen, V.; Boerner, H.; Scherf, U.; Kreyenschmidt, M. *Central European Journal of Chemistry* **2009**, *7*, 836–845.

(196) Peng, C.; Salehi, A.; Chen, Y.; Danz, M.; Liaptsis, G.; So, F. *ACS Applied Materials & Interfaces* **2017**, acsami.7b13537.

(197) Wang, Q.; Aziz, H. *Organic Electronics* **2015**, *26*, 464–470.

(198) Wang, Q.; Sun, B.; Aziz, H. *Advanced Functional Materials* **2014**, *24*, 2975–2985.

(199) Yu, H.; Zhang, Y.; Cho, Y. J.; Aziz, H. *ACS Applied Materials & Interfaces* **2017**, acsami.7b01432.

(200) Wang, Q.; Luo, Y.; Aziz, H. *Applied Physics Letters* **2010**, *97*, 1–4.

(201) Tsutsui, T.; Yang, M.-j.; Yahiro, M.; Nakamura, K.; Watanabe, T.; Tsuji, T.; Fukuda, Y.; Wakimoto, T.; Miyaguti, S. *Jpn. J. Appl. Phys. Part 2:* **1999**, *38*, L1502–L1504.

(202) O'Brien, D. F.; Baldo, M.; Thompson, M. E.; Forrest, S. *Applied Physics Letters* **1999**, *74*, 442.

(203) Kalinowski, J.; Stampor, W.; Mężyk, J.; Cocchi, M.; Virgili, D.; Fattori, V.; Di Marco, P. *Physical Review B* **2002**, *66*, 235321.

(204) Zhang, B.; Tan, G.; Lam, C. S.; Yao, B.; Ho, C. L.; Liu, L.; Xie, Z.; Wong, W. Y.; Ding, J.; Wang, L. *Advanced Materials* **2012**, *24*, 1873–1877.

(205) Tsuboi, T.; Murayama, H.; Penzkofer, A. *Thin Solid Films* **2006**, *499*, 306–312.

(206) Adachi, C.; Kwong, R.; Forrest, S. *Organic Electronics* **2001**, *2*, 37–43.

(207) Kawamura, Y.; Brooks, J.; Brown, J. J.; Sasabe, H.; Adachi, C. *Physical Review Letters* **2006**, *96*, 11–14.

(208) Kawamura, Y.; Goushi, K.; Brooks, J.; Brown, J. J.; Sasabe, H.; Adachi, C. *Applied Physics Letters* **2005**, *86*, 1–3.

(209) Rihani, A.; Hassine, L.; Fave, J.-L.; Bouchriha, H. *Organic Electronics* **2006**, *7*, 1–7.

(210) Hassine, L.; Bouchriha, H.; Roussel, J.; Fave, J. L. *Applied Physics Letters* **2001**, *78*, 1053–1055.

(211) Hassine, L.; Bouchriha, H.; Roussel, J.; Fave, J. L. *Journal of Applied Physics* **2002**, *91*, 5170–5175.

(212) Ruhstaller, B.; Beierlein, T.; Riel, H.; Karg, S.; Scott, J.; Riess, W. *IEEE Journal of Selected Topics in Quantum Electronics* **2003**, *9*, 723–731.

(213) Ruhstaller, B.; Carter, S. a.; Barth, S.; Riel, H.; Riess, W.; Scott, J. C. *Journal of Applied Physics* **2001**, *89*, 4575–4586.

(214) Pinner, D. J.; Friend, R. H.; Tessler, N. *Journal of Applied Physics* **1999**, *86*, 5116–5130.

(215) Blom, P. W. M.; De Jong, M. J. M.; Vleggaar, J. J. M. *Applied Physics Letters* **1996**, *68*, 3308–3310.

(216) Wei, B.; Furukawa, K.; Amagai, J.; Ichikawa, M.; Koyama, T.; Taniguchi, Y. *Semiconductor Science and Technology* **2004**, *19*, L56–L59.

(217) Liu, F.; Ruden, P. P.; Campbell, I. H.; Smith, D. L. *Applied Physics Letters* **2012**, *101*, 023501.

(218) Rothberg, L. J.; Lovinger, A. J. *Journal of Materials Research* **1996**, *11*, 3174–3187.

(219) Staroske, W.; Pfeiffer, M.; Leo, K.; Hoffmann, M. *Physical Review Letters* **2007**, *98*, 197402.

(220) Parshin, M. A.; Ollevier, J.; Van der Auweraer, M. In, ed. by Heremans, P. L.; Muccini, M.; Meulenkamp, E. A., 2006; Vol. 6192, 61922A.

(221) Ingram, G. L.; Zhao, Y.-B.; Lu, Z.-H. *Journal of Applied Physics* **2017**, *122*, DOI: 10.1063/1.5003011.

(222) Wang, Q.; Aziz, H. *Organic Electronics* **2011**, *12*, 1571–1575.

(223) Popovic, Z. D.; Aziz, H.; Hu, N. X.; Ioannidis, A.; Dos Anjos, P. N. M. *Journal of Applied Physics* **2001**, *89*, 4673–4675.

(224) Winter, S.; Reineke, S.; Walzer, K.; Leo, K. *Proceedings of SPIE* **2008**, *6999*, 69992N–69992N–8.

(225) Pettersson, L. A. A.; Roman, L. S.; Inganäs, O. *Journal of Applied Physics* **1999**, *86*, 487.

(226) Xu, F.; Hershey, K. W.; Holmes, R. J.; Hoye, T. R. *Journal of the American Chemical Society* **2016**, *138*, 12739–12742.

(227) Lee, J.; Chen, H.-F.; Batagoda, T.; Coburn, C.; Djurovich, P. I.; Thompson, M. E.; Forrest, S. *Nature Materials* **2015**, *15*, 92–98.

(228) Yi, S.; Kim, J. H.; Cho, Y. J.; Lee, J.; Choi, T. S.; Cho, D. W.; Pac, C.; Han, W. S.; Son, H. J.; Kang, S. O. *Inorganic Chemistry* **2016**, *55*, 3324–3331.

(229) Kim, S.-K.; Yang, B.; Ma, Y.; Lee, J.-H.; Park, J.-W. *Journal of Materials Chemistry* **2008**, *18*, 3376.

(230) Han, C.; Zhu, L.; Li, J.; Zhao, F.; Zhang, Z.; Xu, H.; Deng, Z.; Ma, D.; Yan, P. *Advanced Materials* **2014**, *26*, 7070–7077.

(231) Price, J. S.; Giebink, N. C. *Applied Physics Letters* **2015**, *106*, 263302.

(232) Adachi, C.; Kwong, R. C.; Djurovich, P.; Adamovich, V.; Baldo, M.; Thompson, M. E.; Forrest, S. *Applied Physics Letters* **2001**, *79*, 2082.

(233) Watanabe, S.; Ide, N.; Kido, J. *Japanese Journal of Applied Physics* **2007**, *46*, 1186–1188.

(234) Adamovich, V. I.; Cordero, S. R.; Djurovich, P. I.; Tamayo, A.; Thompson, M. E.; D'Andrade, B. W.; Forrest, S. *Organic Electronics* **2003**, *4*, 77–87.

(235) Schmidbauer, S.; Hohenleutner, A.; König, B. *Beilstein Journal of Organic Chemistry* **2013**, *9*, 2088–2096.

(236) Wang, Q.; Williams, G.; Aziz, H. *Organic Electronics: physics, materials, applications* **2012**, *13*, 2075–2082.

(237) Zhang, Y.; Aziz, H. *ACS Applied Materials and Interfaces* **2017**, *9*, 636–643.

(238) Schmidbauer, S.; Hohenleutner, A.; König, B. *Advanced Materials* **2013**, *25*, 2114–2129.

(239) Jeon, S. K.; Lee, J. Y. *Organic Electronics: physics, materials, applications* **2015**, *27*, 202–206.

(240) Kim, J.-M.; Lee, C.-H.; Kim, J.-J. *Applied Physics Letters* **2017**, *111*, 203301.

(241) Song, W.; Kim, T.; Lee, Y.; Lee, J. Y. *Organic Electronics* **2017**, DOI: 10.1016/j.orgel.2017.01.016.

(242) Kondakova, M. E.; Pawlik, T. D.; Young, R. H.; Giesen, D. J.; Kondakov, D.; Brown, C. T.; Deaton, J. C.; Lenhard, J. R.; Klubek, K. P. *Journal of Applied Physics* **2008**, *104*, 094501.

(243) Mertens, R. Samsung's KN55S9C sub-pixel design., 2013.

(244) Chi, Y.; Chou, P.-T. *Chemical Society Reviews* **2010**, *39*, 638–655.

(245) Zhu, M.; Yang, C. *Chemical Society reviews* **2013**, *42*, 4963–76.

(246) Lee, M.-T.; Liao, C.-H.; Tsai, C.-H.; Chen, C. H. *Advanced Materials* **2005**, *17*, 2493–2497.

(247) Hoye, T. R.; Baire, B.; Niu, D.; Willoughby, P. H.; Woods, B. P. *Nature* **2012**, *490*, 208–211.

(248) Yeoman, J. T. S.; Reisman, S. E. *Nature* **2012**, *490*, 179–180.

(249) Bradley, A. Z.; Johnson, R. P. *Journal of the American Chemical Society* **1997**, *119*, 9917–9918.

(250) Baire, B.; Niu, D.; Willoughby, P. H.; Woods, B. P.; Hoye, T. R. *Nature Protocols* **2013**, *8*, 501–508.

(251) Tadross, P. M.; Stoltz, B. M. *Chemical Reviews* **2012**, *112*, 3550–3577.

(252) Giguere, J. B.; Sariciftci, N. S.; Morin, J. F. *Journal of Materials Chemistry C* **2015**, *3*, 601–606.

(253) Cacioppa, G.; Carlotti, B.; Elisei, F.; Gentili, P. L.; Marrocchi, A.; Spalletti, A. *Physical Chemistry Chemical Physics* **2016**, *18*, 285–294.

(254) Pozo, I.; Cobas, A.; Peña, D.; Guitián, E.; Pérez, D. *Chemical Communications* **2016**, *52*, 5534–5537.

(255) Fieser, L. F. **1965**, *43*, 3–10.

(256) Wittig, G.; Knauss, E. *Chemische Berichte* **1958**, *91*, 895–907.

(257) Yang, C.; Vardeny, Z. V.; Köhler, a.; Wohlgenannt, M.; Al-Suti, M. K.; Khan, M. S. *Physical Review B - Condensed Matter and Materials Physics* **2004**, *70*, 1–4.

(258) Ren, X.; Li, J.; Holmes, R. J.; Djurovich, P. I.; Forrest, S. R.; Thompson, M. E. *Chemistry of Materials* **2004**, *16*, 4743–4747.

(259) Miyaguchi, S.; Katagi, K.; Ohata, H.; Kitago, Y.; Yoshioka, T.; Tsutsui, T. *Digest of Technical Papers - SID International Symposium* **2014**, *45*, 36–39.

(260) Choi, A. Y.; Yamaguchi, T.; Han, C. H. *Research on Chemical Intermediates* **2013**, *39*, 1571–1579.

(261) Bagnich, S. A.; Rudnick, A.; Schroegel, P.; Strohriegl, P.; Köhler, A. *Philosophical transactions. Series A, Mathematical, physical, and engineering sciences* **2015**, *373*, 20140446–.

(262) Goushi, K.; Kawamura, Y.; Sasabe, H.; Adachi, C. *Japanese Journal of Applied Physics, Part 2: Letters* **2004**, *43*, 0–3.

(263) Uratani, H.; Kubo, S.; Shizu, K.; Suzuki, F.; Fukushima, T.; Kaji, H. *Scientific Reports* **2016**, *6*, 39128.

(264) Notsuka, N.; Kabe, R.; Goushi, K.; Adachi, C. *Advanced Functional Materials* **2017**, *1703902*, 1703902.

(265) Kim, S.-y.; Kim, J.-j. *Organic Electronics* **2010**, *11*, 1010–1015.

(266) Chopra, N.; Lee, J.; Zheng, Y.; Eom, S.-H. S.; Xue, J.; So, F. *Applied Physics Letters* **2008**, *93*, 143307.

(267) Li, W.; Pan, Y.; Xiao, R.; Peng, Q.; Zhang, S.; Ma, D.; Li, F.; Shen, F.; Wang, Y.; Yang, B.; Ma, Y. *Advanced Functional Materials* **2014**, *24*, 1609–1614.

(268) Laming, R. I.; Poole, S. B.; Tarbox, E. J. **1988**, *13*, 1084–1086.

(269) Ichimura, K.; Kobayashi, T.; King, K. A.; Watts, R. J. *The Journal of Physical Chemistry* **1987**, *91*, 6104–6106.

(270) Böhm, E.; Anemian, R.; Büsing, a.; Fortte, R.; Heil, H.; Kaiser, J.; Kröber, J.; Leu, S.; Mujica-Fernaud, T.; Parham, a.; Pflumm, C.; Voges, F. *Journal of Information Display* **2011**, *12*, 141–144.

(271) Bangsund, J. S.; Hershey, K. W.; Rathwell, D.; Na, H.-N.; Jeon, J.-H.; Trefonas, P.; Holmes, R. J. **2018**.

(272) Zhang, Y.; Aziz, H. *Organic Electronics* **2016**, *30*, 76–82.

(273) Tokito, S.; Iijima, T.; Suzuri, Y.; Kita, H.; Tsuzuki, T.; Sato, F. *Applied Physics Letters* **2003**, *83*, 569–571.

(274) Zhang, Y.; Forrest, S. *Physical Review B - Condensed Matter and Materials Physics* **2011**, *84*, 1–4.

(275) Schueppel, R.; Uhrich, C.; Pfeiffer, M.; Leo, K.; Brier, E.; Reinold, E.; Baeuerle, P. *ChemPhysChem* **2007**, *8*, 1497–1503.

(276) Endo, A.; Suzuki, K.; Yoshihara, T.; Tobita, S.; Yahiro, M.; Adachi, C. *Chemical Physics Letters* **2008**, *460*, 155–157.

(277) Meerheim, R.; Furno, M.; Hofmann, S.; Lüssem, B.; Leo, K. *Applied Physics Letters* **2010**, *97*, 253305.

(278) Neyts, K. A. *Journal of the Optical Society of America A* **1998**, *15*, 962.

Appendices

Appendix A

List of Publications and Presentations

Journal Publications

- J Bangsund, **KW Hershey**, D Rathwell, HN Na, JH Jeon, P Trefonas, RJ Holmes. *Improved Stability in Organic Light-Emitting Devices by Mixing Ambipolar and Wide Energy Gap Hosts* In Preparation.
- J Bangsund, **KW Hershey**, RJ Holmes. *Origin of Lifetime Enhancement in Mixed Emissive Layer Organic Light-Emitting Devices* ACS Applied Materials and Interfaces. 2018.
- **KW Hershey**, J Suddard-Bangsund, G Qian, RJ Holmes. *Decoupling Degradation in Exciton Formation and Recombination During Lifetime Testing of Organic Light-Emitting Devices.* Applied Physics Letters. 2017.
- F Xu, **KW Hershey**, RH Holmes, TR Hoye. *Blue-Emitting Arylalkynyl Naphthalene Derivatives via a Hexadehydro-Diels-Alder Cascade Reaction* . Journal of the American Chemical Society. 2016.
- **KW Hershey**, RJ Holmes. *Unified Analysis of Transient and Steady-State Electrophosphorescence Using Exciton and Polaron Dynamics Modeling* . Journal of Applied Physics. 2016.
- **KW Hershey**, JP Cottingham. *Matierial Properties of Pipes of Reeds From the Southeast Asian Khaen* . Journal of the Acoustics Society of America. 2011.

Oral Presentations

- **KW Hershey**, RJ Holmes.*Decoupling Exciton Formation and Recombination Losses in Organic Light-Emitting Devices During Lifetime Testing*, Optical Society of America - Light, Energy and the Environment Congress. Boulder, CO. November 2017
- **KW Hershey**, RJ Holmes.*Decoupling Degradation Mechanisms During Lifetime Testing of Organic Light-Emitting Devices*, UMN IPrime. Minneapolis, MN. June 2017
- **KW Hershey**, RJ Holmes.*Modeling Exciton and Polaron Dynamics to Analyze OLED Behavior*, UMN IPrime. Minneapolis, MN. June 2016
- **KW Hershey**, RJ Holmes.*Modeling Exciton and Polaron Dynamics to Analyze OLED Behavior*, MRS Spring Conference. Phoenix, AZ. April 2016
- **KW Hershey**, JP Cottingham. *Material Properties of Pipes and Reeds from the Southeast Asian Khaen*, Acoustical Society of America National Meeting. Seattle, WA. May 2011

Poster Presentations

- **KW Hershey**, RJ Holmes.*Decoupling Degradation Mechanisms During Lifetime Testing of Organic Light-Emitting Devices*, UMN IPrime. Minneapolis, MN. June 2017
- **KW Hershey**, RJ Holmes.*Connecting Transient and Steady-State Dynamics in Organic Light Emitting Devices*, UMN IPrime. Minneapolis, MN. June 2016
- **KW Hershey**, RJ Holmes.*Transient Analysis of Organic Light-emitting Devices*, UMN IPrime. Minneapolis, MN. May 2015
- **KW Hershey**, JP Cottingham.*Material Properties of Pipes and Reeds from the Southeast Asian Khaen*, Sigma Pi Sigma Quadrennial Physics Congress. Orlando, FL. April 2012.

Appendix B

Measuring Triplet Energies

As discussed in Chapter 2.3, singlet excitons are typically responsible for molecular emission because the triplet state is quantum mechanically forbidden in the first order approximation.[45] Emission from the triplet state is allowed with the addition of spin-orbit coupling.[95] For applications including OLEDs, solar cells, and organic lasers, spectroscopic characterization of the triplet state is needed, often for molecules where the spin-orbit coupling is weak.[62,273–275]

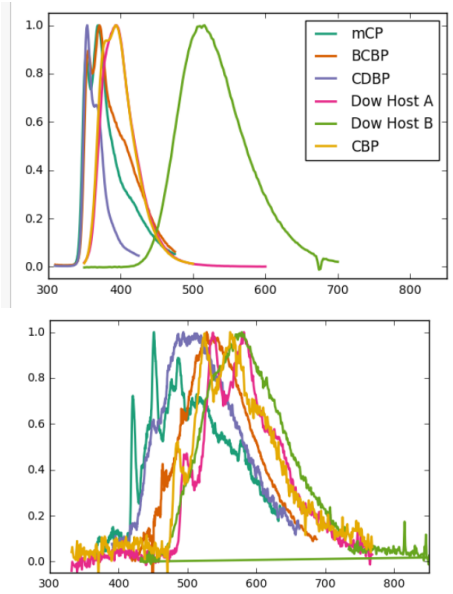

Figure B.1: Fluorescence (a) and Phosphorescence (b) spectra for several materials obtained from this system.

Most measurements of the triplet energy are conducted via optical pumping.[45,61,62,64] However, triplet populations are not generated optically in most materials.[45] In order for a triplet population to be established, k_{ISC} must be greater than 0. Additionally, the radiative rate, k_r must be at least competitive with k_{nr}. Since the triplet state is quantum mechanically disallowed without spin-orbit coupling, the radiative rate is typically low compared to the singlet, on the order of $10^6 s^{-1}$. At room temperature, k_{nr} is often seen be be $10^2 - 10^6 s^{-1}$.[65] In order to reduce k_{nr}, cryogenic temperatures are often employed, though room-temperature techniques do exist.[65]

In our lab, I have utilized Janis liquid helium cryogenic optical system to measure triplets. This takes the temperature to 10K and severely reduces k_{nr} Samples are prepared on Silicon to take

advantage of the strong thermal conductivity compared to glass. If the total emission is collected, the singlet still is far more emissive than the triplet. However, the difference in their lifetimes can be utilized to separate them. Using a pulsed nitrogen laser, the exciton population is excited. The singlet population decays quickly, within a few nanoseconds. However, the triplet lifetime at low temperatures is much longer. A triggered spectrometer can be used to measure the delayed phosphorescence, and thus measure the triplet emission only. I have done this with a Princeton Instruments Fergie spectrometer, with a delay of 5ms from the laser pulse. The setup for this can be seen in Figure B.2.

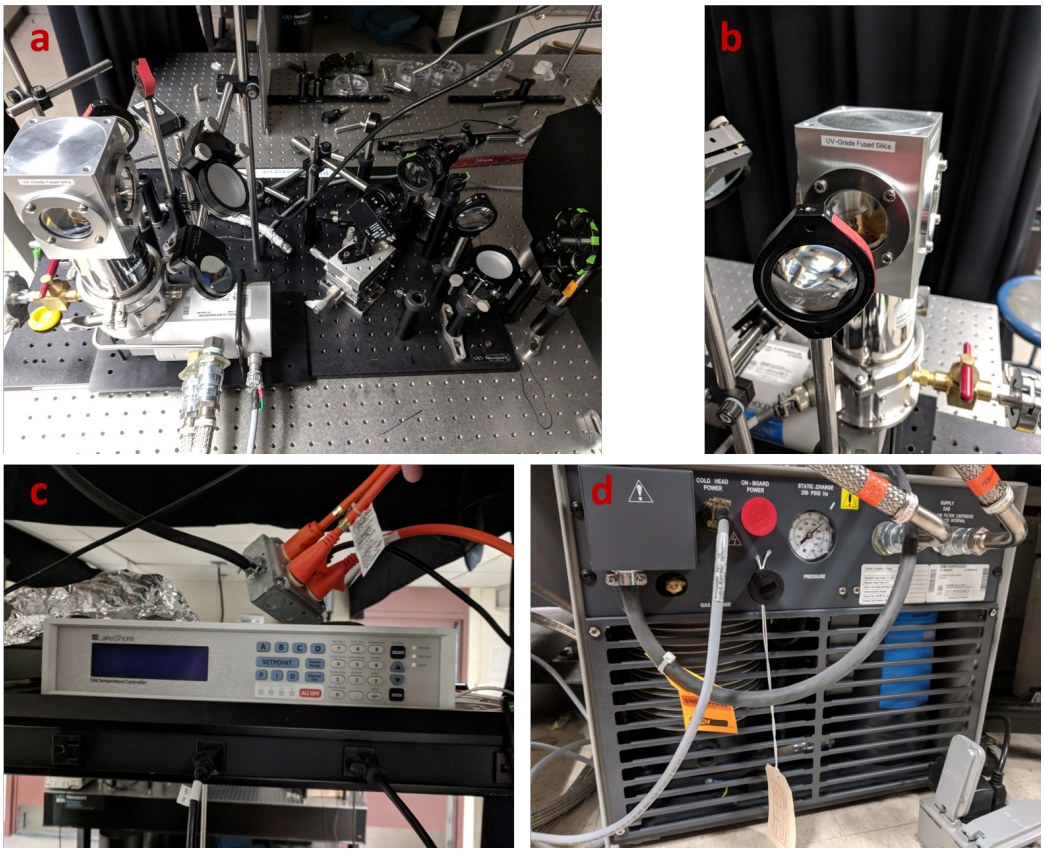

Figure B.2: Equipment used in this experiment. (a) Optics line for this setup. The flip mirror in the down position allows laser emission to travel to the two mirror system before entering the quartz window. (b) The emission window of the cryostat. A beam collimator is used to couple emission into the fiber of the Fergie spectrometer. (c) Temperature controller for the cryostat. (d) Helium compressor for the cryostat.

This system has been used to measure triplet spectra for a variety of materials, shown in Figure B.1. To extract triplet energies, the short wavelength turn on of the triplet spectra can be used. This is the highest energy, which seems counter intuitive, but the observed spectra is a decay from T_1 to vibrational states of the ground state, S_0. The triplet energy is defined as the difference between the lowest vibronic of T_1 to the lowest vibronic of S_0, which is the highest energy transition observed in the spectra. These spectra show different behavior for sharpness of the leading edge, but a 20% of

the maximum intensity is chosen as the threshold for defining the triplet energy.

Appendix C

Molecular Lifetime Screening

Design rules for stable emitters are not well developed, so it is possible that closely related molecules could have a significant change in stability. A rapid screening technique is needed to brute force optimize emitter molecules for lifetime since the stability cannot be predicted a priori. Ideally, this technique would probe the intrinsic stability of the emitter, rather than the stability of an OLED device, as device manufacturing requires optimization of its own. The most isolated molecular properties can be probed in solution, where molecules are not in contact with each other. Solution has the added advantage of easy processing, further enabling rapid screening.

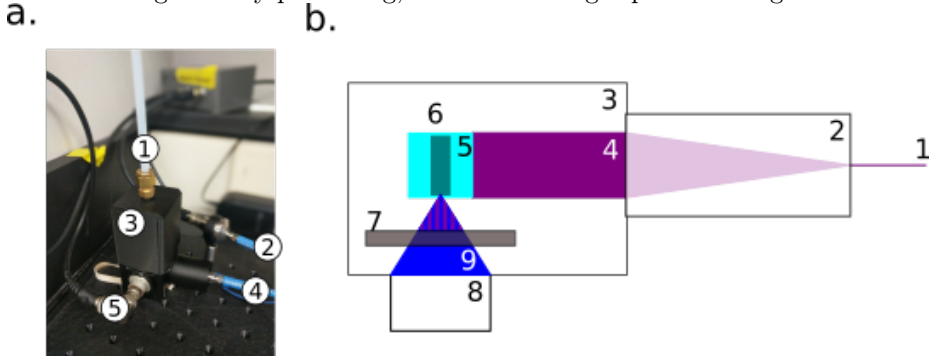

Figure C.1: (a) Solution degradation setup for molecular screening with 1. Nitrogen purge line 2. LED intensity measurement 3. Sample chamber 4. LED input 5. PL measurement. (b) Schematic of the sample chamber for solution degradation. 1. Fiber coupled incoming light. 2. Beam Collimator. 3. Dark enclosure with nitrogen purge. 4. Expanded beam covering sample. 5. Cuvette. 6. 3x10 mm solution well. 7. Long pass filter to remove scattered laser light. 8. Photodiode. 9. Light from sample.

To investigate molecular lifetime, the solution photoluminescence degradation apparatus shown in Figure C.1 was developed. This setup uses a 375 nm fiber coupled LED as a pump, powered by a Keithley 26XX source meter. When operated at the high luminance needed for a pump, UV LEDs suffer from low stability (interestingly, a related problem to the one we are trying to solve). In order to operate at a constant pump dose during the test and between samples, a feedback loop

is implemented using a split fiber. This fiber (blue in Figure C.1) has two cores, a large 1 mm diameter, as well as a 50 μm diameter. The small core is used for the feedback loop to the power supply, adjusting the optical power every 5 minutes during the lifetime. The large fiber is used to support the high light intensity needed to degrade the sample.

The sample is contained in the black box of Figure C.1, which supports a 1 cm by 1cm base dimensioned cuvette. During this measurement, it is important to evenly degrade the molecules in the solution. In an unstirred cuvette, it is likely that diffusion of molecules is slower than degradation, so it is important that the excitation condition is evenly applied. Several steps were implemented to ensure this was true in the testing configuration. Firstly, as the light passes through the sample, a Beer's law absorption profile creates a difference in the absorbed does between the incident and exiting plane. Dilute solutions used for this study typically have low absorption, but to minimize this effect, a short light path length is preferred. This is implemented by using a cuvette with inner dimensions of 10 mm by 3 mm, with the 3 mm to minimize the path length, as shown in Figure C.1. To minimize intensity differences across the face of the cuvette, an expanding beam collimator is used on fiber input. This takes the small area fiber input and collimates the beam over a diameter of $\approx$ 1 cm, spreading the beam across the full width of the cuvette. The beam likely has spatial non-uniformity, but exciting the full width of the cuvette was deemed adequate. Additionally, the cuvette is only filled partially, to ensure that all of the solution is in the beam.

The tested molecules require highly volatile solvents, so a screw top cuvette is used to minimize evaporation of the solvent. Emitters are frequently sensitive to oxygen quenching, increasing non-radiative relaxation processes.[94,275,276] To avoid this, in addition to the sealed cap with sample preparation in a nitrogen glovebox, the sample chamber is kept under a positive nitrogen pressure using a constant purge, shown as the white plastic line coming into the sample chamber in Figure C.1.

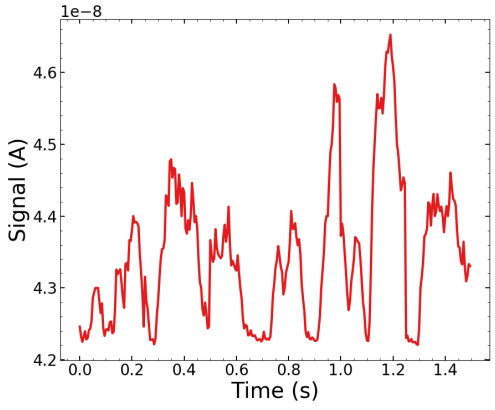

Figure C.2: Scatter in signal when stirring. Despite the noise, notice the constant baseline.

Initial tests using this setup showed loss in the photoluminescence that was reversible by physical agitation of the sample. This suggested that the molecule is precipitating out of the solution, though no precipitate was visible due to the dilute loading (10^{-6} M). Because of this, stirring needed to be added to the solution, and was done by adding a spherical stir ball and placing the apparatus on a

stir plate. However, the addition of the stir bar added significant noise to the measured PL signal, shown in Figure C.2. It was found that the movement of the stir bar caused significant scattering of the light and was impacting the measurement. In addressing this problem, points were taken every 5 ms to observe the scatter. It was found that a minimum signal was reliably achieved every 300 measurements. This is believed to be a period where the stir bar is out of the light path and not scattering light. To eliminate the noise, 300 points are taken at 5 ms intervals, and the minimum is taken as the solution signal.

This method has been developed and is able to produce reliable results on the same solution. Test results have started using FIr(pic) as an emitter. Molecular screening has yet to be done using this technique.

Appendix D

Single Carrier Device Modeling

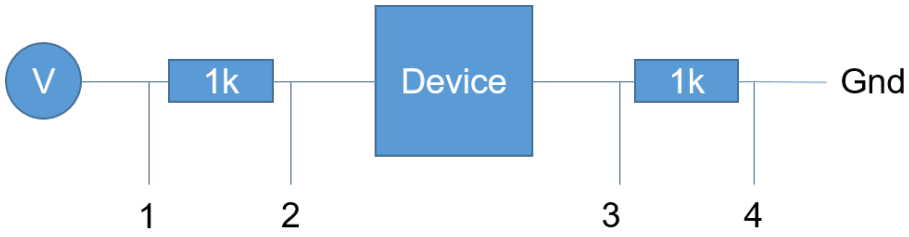

Figure D.1: Circuit used for measuring polaron density. Voltage readings are taken at 1-4 overs a 1MΩ termination.

When trying to understand device behavior, it is often important to investigate single carrier devices to understand one charge species at a time or isolate dynamic processes. An example of this is measurement of the triplet-polaron quenching rate constant, demonstrated in Chapter 4.5. Determination of the polaron density is often critical in order to quantify these results. This is often done by assuming the device is operating within the space charge limit, in which charges have overcome injection barrier limits and transport through the bulk of the material is the limiting process.[46,53] In the space-charge limit, current is most simply described using the Mott-Gurney Law, and can be modified to include various trap states to adapt to different semiconductor properties.[38] However, space-charge limited current is really only accurate for device behavior at high voltages for thick devices. Often, organic layer stacks of interest feature relatively thin layers, and voltages close to the injection limits. It can be difficult to identify when a device is operating in the space-charge limit.

In order to reduce some of the uncertainty associated with determining polaron density, a differential current measurement can be conducted. For a single carrier device, only one type of carrier is injected. As charge is being injected into the device and a steady-state polaron density is being

achieved, the current on the side of the device where charges are injected should be greater than on the other side. This can be seen in Figure D.1, where for a hole only device, the current over R_{12} should be greater than the current over R_{34}. All of these signals can be measured using an oscilloscope. Once steady-state is achieved, the currents should be equal. The polaron population injected into the device can be calculated using the following equation

$$N_{pol} = \int fracJ_{1-2} - J_{3-4}edt \tag{D.1}$$

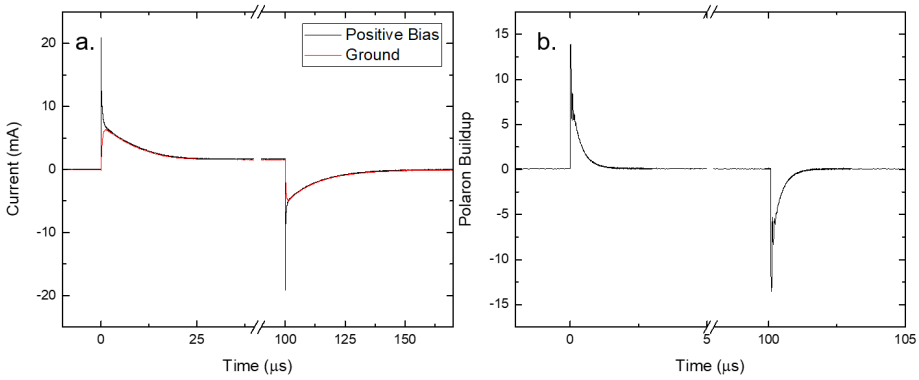

Figure D.2: Differential currents for a hole only device. Currents on either side of the device are shown in a. While the difference between them is shown in b.

where J is the current and 1-4 are labeled in Figure D.1. When voltage is removed from the device, the currents will diverge and the polaron density will be drained from the device. This is demonstrated in Figure D.2, with the currents on either side of the device and the differential current shown in D.2a and D.2b, respectively. Notice the positive differential when current is applied and polarons enter the device, and negative when they are removed.

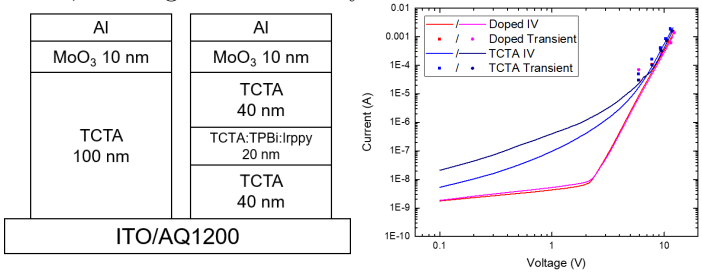

Figure D.3: a. Hole only device architectures. b. Current Voltage characteristics for the devices shown in a. Steady-state sweeps as well as current measured from the differential technique are shown.

While this technique is able to accurately tell the injected polaron population, the distribution of that population is still unknown. This technique does provide the advantage that with the total polaron population known, the current or voltage dependence of the population can be compared to different models to further validate the operational regime. Then, a model can be applied to show

the spatial dependence of charge.[38,43,97] This technique has the advantage that only the spatial dependence is needed, rather than having to estimate the total charge population, and is more accurate than previous methods relying on solely modeling.

Ideally the polaron population can be restricted to a small area of the device to minimize the extent of the spatial distribution. To achieve this, the devices shown in Figure D.3a were investigated. The region of interest is the mixed doped layer in the right hand device. This doped region should show a greater ability to facilitate trapped charge and show a larger polaron population. The current-voltage profile of these devices is shown in Figure D.3b where the doped devices show a stronger diode behavior. The currents obtained from the displacement current measurements show agreement with the steady state current.

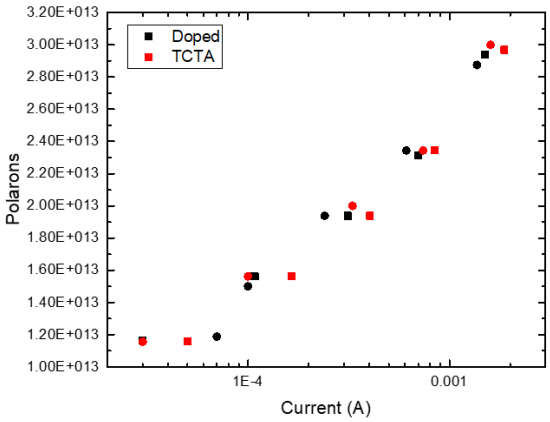

Figure D.4: Polaron population as a function of current for the devices in Figure D.3a

The polaron population as a function of current is shown for these devices in Figure D.4. Unfortunately, polaron populations for both devices are almost identical and the hypothesis of increased trapping in the doped region is not correct. This means that charges are not confined and there is likely a wide distribution of the polaron density. Despite these drawbacks, the polaron population is still obtained and can be compared to space-charge limited current models.

D.1 Future Work

This technique is useful for a variety of techniques where polaron population needs to be known precisely. One ready application of this technique is for triplet-polaron quenching measurements. As discussed in Chapter 4.5, measurement of k_{TP} relies on optically pumping a single carrier device under an applied current. To accurately determine the constant, the polaron density must be known precisely. The differential current technique would be useful for comparing different materials and their values of k_{TP} . Another application with similar motivations would be the optical degradation of single carrier devices.

Differential current analysis of single carrier devices provides a straight forward way of determining the polaron population within a single carrier device. While the spatial distribution of the polaron population may not be known, this can be easily modeled with the current dependence of

the polaron population available for validation of the model. Though so far unused in a relevant application, this technique allows more sophisticated comparison of devices when matched polaron population is important.

Appendix E

Modeling Out-Coupling

The out-coupling efficiency, η_{OC} is the efficiency of generated photons within an OLED device to exit the device in the forward viewing direction. Typically, η_{OC} is the limiting component of η_{EQE} , and ranges from 20-30%. It is therefore important to understand this quantity and it's dependence on the device geometry. It is not possible to physically measure this quantity, but extensive modeling has been done to calculate it's value.[54,96,277,278] This chapter will outline the theory that goes into modeling η_{OC} , then proceed into applications for using the model output.

E.1 Theory

Code used for implementation of this theory is provided in Appendix F.2 The implemented model is based off of the models developed in Furno et al. [96] and Neyts [278].

A dipole in a planar layer stack can radiate power in any direction. If we assume the in plane dimensions to be infinite, this system will be radiatively symmetric, and directions can be represented in terms of a unit normalized in-plane wave vector, u. The total power radiated by such a dipole can be expressed as

$$F = \int_0^\infty K(u)du. \tag{E.1}$$

Here, F is the total radiated power, and K is the power density per unit du. It should be noted that propagating waves are represented by $0 \leq u \leq 1$. However, $u > 1$ represent evanescent wave modes. In this model, there will be a critical value of $u = u_c$ that will allow light to escape into the substrate in the forward direction. This power fraction radiated into the substrate can be expressed

as

$$\eta_{\text{OC}} = \frac{\int_0^{u_c} K(u)du}{\int_0^{\infty} K(u)du}. \tag{E.2}$$

Different polarizations and orientations have different reflection conditions, so must be treated separately. An emitting dipole in a thin film layer stack can be considered as a superposition of a horizontal (h) dipole, oriented perpendicular to the planar system, and vertical (v) dipole, oriented within the plane. These different orientations can be summed as

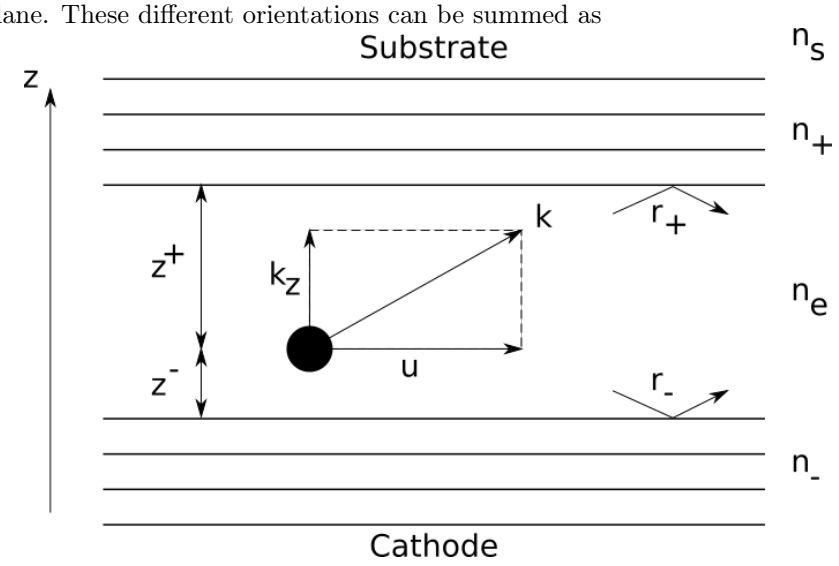

Figure E.1: Representation of model quantities. The positive z axis is shown, along with the wave vector, k, the normalized in-plane wave vector, u, and the out of plane wave vector, k_z. The positive and negative reflection directions, r_+ and r_-, respectively. n_e and n_s are the emitter and substrate indices of refraction, as well as the positive and negative layer stack indices. z_+ and z_- are the distances to the next interface of the emissive layer.

$$K = \frac{1}{3}K_{TM_v} + \frac{2}{3}(K_{TM_h} + K_{TE_h}. \tag{E.3}$$

Where TM represents the transverse magnetic modes and TE is the transverse electric modes. The power density for these different modes can calculated as

$$K_{TM_v} = \tfrac{3}{2}Re\left[\tfrac{u^3}{\sqrt{1-u^2}}\tfrac{(1+a_{TM}^+)(1+a_{TM}^-)}{1-a_{TM}}\right] \tag{E.4}$$

$$K_{TM_h} = \tfrac{3}{4}Re\left[\tfrac{u}{\sqrt{1-u^2}}\tfrac{(1-a_{TM}^+)(1-a_{TM}^-)}{1-a_{TM}}\right] \tag{E.5}$$

$$K_{TE_h} = \tfrac{3}{4}Re\left[u\sqrt{1-u^2}\tfrac{(1+a_{TE}^+)(1+a_{TE}^-)}{1-a_{TE}}\right] \tag{E.6}$$

Here Re is the real component of the enclosed quantity. Additionally, $a_{TM,TE}^{+,-}$ can be calculated

as

$$a^{+}_{TM,TE} = r^{+}_{TM,TE} exp(2jk_{z,e}z^{+}) \tag{E.7}$$

$$a^{-}_{TM,TE} = r^{-}_{TM,TE} exp(2jk_{z,e}z^{-}) \tag{E.8}$$

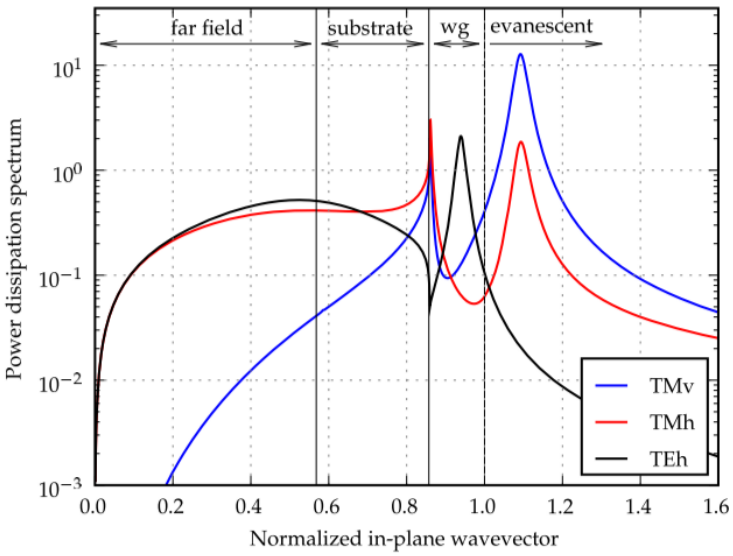

Figure E.2: Power Density as a function of u for all three polarizations and orientations. Image taken from Furno et al. [96].

Here, r is the reflection coefficient for waves traveling in the specified direction, with + oriented from the EML towards the cathode, $k_{z,e}$ is the out of plane component of the photon wave vector in the emitting material, and $j = \sqrt{-1}$. The distance of the dipole from interface is represented as $z^{+,-}$. These quantities can be seen schematically in Figure E.1. The reflection coefficients r can be calculated for arbitrary wave stacks using the transfer matrix model.[225] These power densities are used to calculate the total radiated power distribution, shown in Figure E.2. In this figure, the loss modes division of u is done using a simple Snell's law calculation. For coupling into the far field, $u < n_0(\lambda)/n_e(\lambda)$. For coupling into the substrate, $u < n_s(\lambda)/n_e(\lambda)$. If $u > 1$, this indicates an evanescent mode, with the large peak resulting from the cathode surface plasmon. The unaccounted for range in u is waveguided in the layer stack.

E.1.1 Far Field

The total radiated power density, $K(u, \lambda)$, is useful for calculating where losses occur within the layer stack. However, for far field transmission and the calculation of η_{OC} , a slight modification is needed.

For calculated out-coupled power, the power radiated into the substrate is calculated separately then the substrate transmission is calculated assuming an incoherent material. The component powers radiated into the substrate is calculated as

$$K'_{TM_v} = \frac{3}{8}\frac{u^2}{\sqrt{1-u^2}}\frac{\left|1+a^-_{TM}\right|^2}{|1-a_{TM}|^2}T^+_{TM} \tag{E.9}$$

$$K'_{TM_h} = \frac{3}{16}\sqrt{1-u^2}\frac{\left|1-a^-_{TM}\right|^2}{|1-a_{TM}|^2}T^+_{TM} \tag{E.10}$$

$$K'_{TE_h} = \frac{3}{16}\frac{1}{\sqrt{1-u^2}}\frac{\left|1+a^-_{TE}\right|^2}{|1-a_{TE}|^2}T^+_{TE} \tag{E.11}$$

and can be summed as before with

$$K' = \frac{1}{3}K'_{TM_v} + \frac{2}{3}(K'_{TM_h} + K'_{TE_h}. \tag{E.12}$$

The factors $T^+_{TM,TE}$ are

$$T^+_X = |t^+_X|^2\frac{n_s}{n_e}\frac{k_{z,s}}{k_{z,e}} \tag{E.13}$$

with $t^+_{TM,TE}$ being the transmission coefficient from transfer matrix calculations, n_s and n_e being the optical constants for the substrate and emissive layer respectively, and k_z is the out of plane wave vector component. The power radiated out of the substrate can then be calculated with

$$K_{out} = K'_{out}\frac{T_{s,o}}{1-R_{s,o}R_c} \tag{E.14}$$

The total out-coupled power can then be integrated using

$$U(\lambda) = \int_0^{u_{crit}(\lambda)} K_{out}(\lambda,u)du^2 \tag{E.15}$$

with the critical dipole orientation obtained from Snell's law by $u_{crit}(\lambda) = n_0(\lambda)/n_e(\lambda)$. Thus, the efficiency of generated photons can be calculated as

$$\eta_{\text{OC}} = \frac{U(\lambda)}{F(\lambda_)} \tag{E.16}$$

This can be thought of as an integration of the far field portion of Figure E.2 compared to the integration of the whole, with a modification for the transmission through the incoherent substrate.

These calculations allow direct calculation of η_{OC} for a single dipole location and emitter wave-

length. To be accurate for devices, a weighted average of these calculations must be done over the spectral features of the emitter, as well as weighting for the exciton distribution of the recombination zone within the device.

E.2 Applications

E.2.1 Gradient EML Recombination Profile Dependence

Out-coupling efficiency can be an important consideration when designing a high efficiency device. Even if operating at 100% internal quantum efficiency, a low η_{OC} can lead to poor device performance.[95] For extremely wide recombination zone profiles in devices, there can be a significant change in η_{OC} throughout the device, potentially negating the benefits of the wide recombination zone. A prime candidate for η_{OC} investigation is the gradient EML (GEML) device, since the RZ can potentially span the majority of the device thickness.[53]

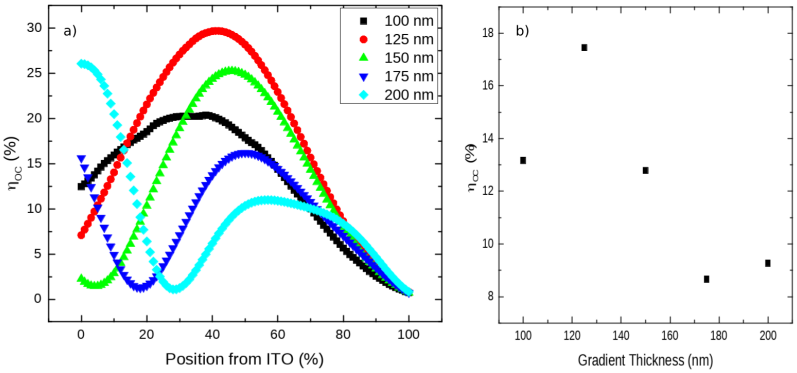

Figure E.3: (a) η_{OC} as a function of normalized device thickness. (b) The non weighted average of the left panel as a function of gradient thickness.

A GEML device consisting of TCTA as an HTL and BPhen as an ETL with 5% doping of $Ir(ppy)_3$ throughout was investigated. These device uses a 1:1 gradient profile, meaning that a ramp in the rate of TCTA from 4 to 0 Å/s and BPhen ramps from 0 to 4 Å/s in the same time period with the rate of $Ir(ppy)_3$ held constant. This results in a 50:50 blend of the HTL and ETL at the midpoint of the device. The spatial dependence of η_{OC} can be seen in Figure E.3a at $\lambda = 512$ nm.

Some common features of η_{OC} profiles should be discussed here. First off, notice that a near zero boundary condition is observed as the emission dipole nears the cathode interface at 100% on these profiles. This is a common feature of η_{OC} profiles in devices and is due to increased coupling to the surface plasmon mode of the cathode. In organic layer stacks, little change in the index of refraction is seen throughout the stack, and devices often behave similar to a single organic layer. Going through thick layer stacks, a cyclical peaking of η_{OC} is seen as can be seen in the 175 and 200

nm simulations. The periodicity of this cycling is a function of wavelength. Though difficult to see on this normalized axis, for green light, the first peak of this cycle is typically around 40 nm from the cathode. Most devices are on the order of 100 nm thick, and optimize around the first peak, resulting in ETL thicknesses around 30-40 nm, positioning the EML in this peak.

In Figure E.3b, the non-weighted average of η_{OC} as a function of gradient thickness is shown. To be representative of a device, the spatial η_{OC} should be weighted by the RZ profile, but since GEML devices show very broad RZs, this can be a good indicator of device behavior. It is of note that a significant roll-off in η_{OC} is seen with increasing gradient thickness. This is an important design rule, which we noted in Chapter 4, for increasing gradient thickness. Gradients offer a unique ability to distribute the exciton population throughout a device, and were predicted to improve roll-off behavior due to a reduction in bimolecular quenching. However, as shown by this calculation, the reduction in roll-off is in direct competition with a reduction in peak efficiency due to η_{OC} . This puts a limit on the amount exciton distribution that is useful for devices.

The spatial profile of the exciton density is also important in calculating of η_{OC} for a device. GEML devices have broad, featureless RZ profiles, which for the purposes of this modeling, we will assume are Gaussian.[53]. Figure E.4 captures dependence of average η_{OC} on the peak position and width of the recombination zone profile. Three center wavelengths for the RZ profile are shown as a function of the Gaussian width. The spatial dependence of η_{OC} is shown as the black curve in Figure E.3a. In Figure E.4, the RZ profiles centered at 25 and 50 take advantage of the broad peak in η_{OC} peaked at 35 nm, with the RZ centered at 50 nm showing a closer alignment and thus higher average η_{OC} at sharp RZ profiles near $\sigma = 0$. The RZ profile centered at 75 nm is too near the cathode and shows a significantly reduced efficiency. As the RZ profiles broaden, we approach the unweighted behavior, seen as $\lim_{\sigma\to\infty} \eta_{OC}\ (\sigma)$. Again, it is interesting to note that there is a limit in most devices at which broadening the RZ could be detrimental to device behavior due to a reduction in η_{OC} .

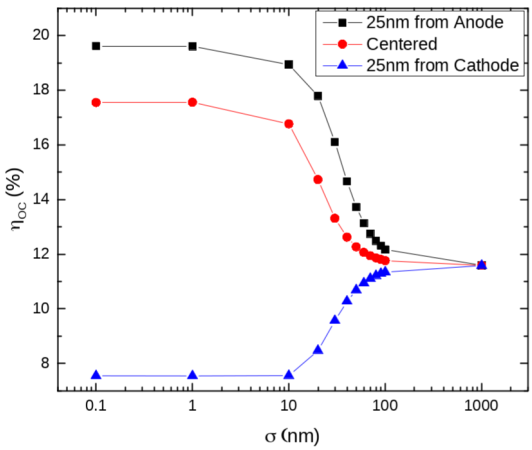

Figure E.4: Average η_{OC} for a 100 nm GEML device, weighted to Gaussian recombination zones centered at 25, 50, and 75 nm as a function of the Gaussian width.

E.2.2 Exciton Formation Efficiency Extraction

In Chapter 4, a method for extracting the exciton formation efficiency using a model for the transient and steady-state electrical regime was discussed. In Equation 4.7, η_{OC} is needed to normalize the resulting modeled behavior for the internal quantum efficiency η_{IQE}. Since a mean field approximation model is being used for this approach, only the average η_{OC} is needed. However, the recombination zone profile of this device is not known. Luckily, only a 10 nm EML is used, and there is minimal change in the η_{OC} as a function of thickness, resulting in reduced error.

E.2.3 Recombination Zone Measurement

The calculation of the spatial distribution of out-coupling has also been useful for extracting the RZ profile of devices.[154] One technique for measuring the recombination zone is to use an emissive sensitizer, that emits spectrally separated from the target emitter, as discussed in Chapter 3.6. In this case, we used PtTPTBP ($\lambda_{max} = 770nm$) as a sensitizer for $\mathrm{Ir(ppy)_3}$ ($\lambda_{max} = 512nm$), with spectra shown in Figure E.5a. The simulated η_{OC} , spectrally weighted for the emission of these two emitters is presented in Figure E.5b. Note the significantly different shape, a result of the significantly longer wavelength of PtTPTBP moving the peak in η_{OC} further from the cathode. For calculating the RZ shape, without accounting for η_{OC} , one would simply plot the intensity of the 770 nm peak as a function of emitter position. In Figure E.5a, we can see that this would result in a significant drop off in the RZ intensity as the ETL side interface is approached. However, from the calculation of η_{OC} , we see that the efficiency is going down in this region. The corrected RZ

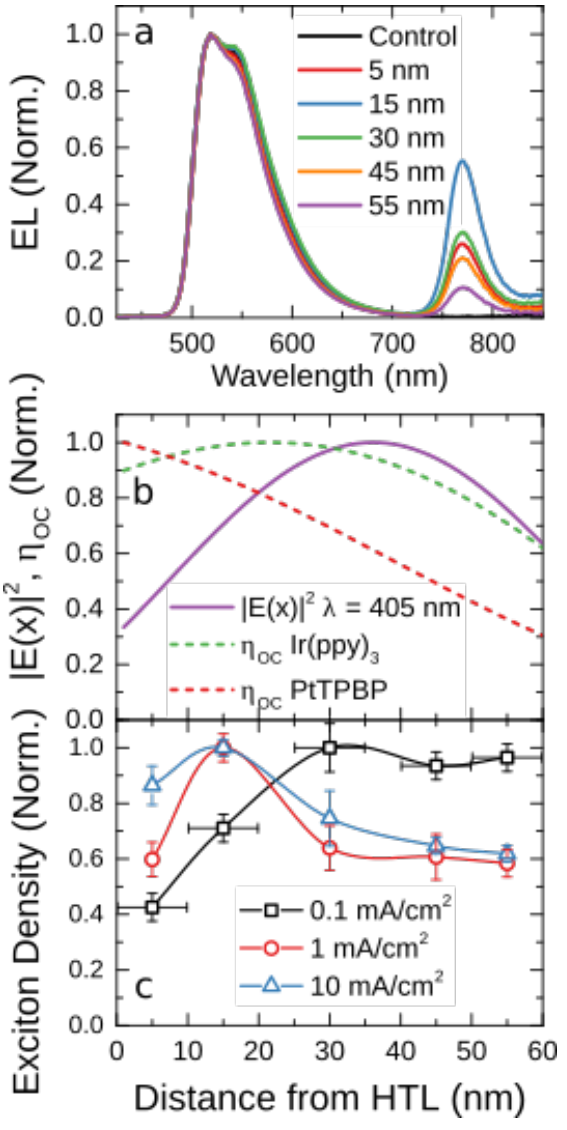

Figure E.5: (a) Raw electroluminescence spectra of devices with PtTPTBP sensitizer. (b) simulated electric field profile and out-coupling factors at 512 nm and 770 nm. (c) Out-coupling corrected RZ profile. Reproduced from Bangsund et al. [154].

profile is shown in Figure E.5c, and the actual shape can be seen, with a flat recombination zone profile in this region. This correction for η_{OC} is easy in this method of recombination zone measurement due to the clearly defined emitter position for PtTPTBP.

An alternative approach to measuring the recombination zone is in using a quenching sensitizer which does not emit light.[53] In this technique, a reduction in the $Ir(ppy)_3$ peak is observed, which corresponds to RZ intensity at that point in space. The remaining intensity is a function of both the RZ profile and η_{OC} . Since we are trying to measure the RZ, we cannot use it to correct the data. This causes a problem for trying to correct the quenching measurement data. This is somewhat minimized by still seeing emission from a majority of the EML, averaging out the loss, but still presents a problem.

E.2.4 PL Accuracy During Decoupled Lifetime Testing

When decoupling lifetime as discussed in Chapter 5, it is important that the EL and PL signals originate from the same position within the device. This can be assessed by comparing the electric field profile within the device with the measured RZ profile.[154] If these are perfectly overlapped, there is no need to consider η_{OC} , but that is likely not the absolute case. In a more general consideration, The electric field and RZ profiles must be considered for their overlap with the η_{OC} profile. Analysis of this error is assessed for a particular device system in the Supplementary Material for Bangsund et al. [154], but is found to be $< 5\%$ for wide recombination zone devices where strong overlap between these quantities is observed.

During lifetime, an additional out-coupling discrepancy is seen between the EL and PL measurement due to changes in the RZ position as a function of degradation. If charge transport is degrading, it is very likely that the RZ is moving as the device degrades, though is very difficult to characterize. If this occurs, the accuracy of the PL measurement changes as a function of degradation due to the overlap of the region probed during EL and PL changing. Again, investigation of a specific device is discussed in Bangsund et al. [154], and is found to increase in importance as the RZ narrows.

E.3 Conclusion

This section discussed the theory and application of an out-coupling efficiency (η_{OC}) model developed for use with our group. The careful consideration of η_{OC} is essential to any optical investigation of

devices due to the highly variant spatial dependence. This model has been used for calculations in the steady state behavior as well as lifetime applications. For lifetimes, broad recombination zones are found to minimize the influence of η_{OC} on the measurements.

Appendix F

Code

F.1 Transfer Matrix Model

The following is code to implement a transfer matrix model for calculating absorption and electric field profile within a thin film stack, as described by Pettersson.[225]

transfer.m

```
function transfer

global q
global d
global n

%%%%%%%%%%%%%%%%%%%%%%%%%%%%
%
% Model Setup
%
%%%%%%%%%%%%%%%%%%%%%%%%%%%%

% Layers. Must match names in lookup table
layers = {'SiO2' 'ITOsorizon' 'PEDOT' 'P3HTPCBMBlendDCB' 'Ca' 'Al'};



% layer thicknesses.  First value is unused
% but placeholder so indices match
d = [
    0
```

```
    110
    35
    220
    7
    200
    ];

% angle of incidence
phi_0 = 0;

%%%%%%%%%%%%%%%%%%%%%%%%%%%%%%%%%%%%%%%%%%%%%%%%%%%%
%
% Test Parameters
%
%%%%%%%%%%%%%%%%%%%%%%%%%%%%%%%%%%%%%%%%%%%%%%%%%%%%

% resolution in nm
res = 1;
%%% note: You should try to make this an even division of the layer
%%% thicknesses.  If not, the first output will always be at the left edge
%%% of the layer,sampling at each res step.  This could result in an uneven
%%% spacing between the last sample of j and the first of j+1.

% Wavelengths to test
waves = [400];


%%%%%%%%%%%%%%%%%%%%%%%%%%%%%%%%%%%%%%%%%%%%%%%%%%%%
%
% Generation
%
%%%%%%%%%%%%%%%%%%%%%%%%%%%%%%%%%%%%%%%%%%%%%%%%%%%%

%% Load in index of refraction for each material and each wavelength
ntable = zeros(size(layers,2),size(waves,2));
for index = 1:size(layers,2)
    ntable(index,:) = LoadRefrIndex(layers{index},waves);
end


```

```
% calculating array size for preallocation
numSteps=0;
x = [];
depth = 0;
for l = 1:length(d)-1
    numSteps=numSteps+(ceil(d(l+1)/res)-1)*res+1;
    steps = 0:res:(ceil(d(l+1)/res)-1)*res;
    x = [x (steps+depth)];
    depth = depth + d(l+1);
end
specs = zeros(numSteps,size(waves,2));

% hard work begins
for iter = 1:size(waves,2)
    lambda = waves(iter);
    n=ntable(:,iter);
    q = (n.^2-n(1)^2*(sin(phi_0))^2).^(1/2);
    % ! ! ! ! ! ! ! ! ! ! ! ! ! ! ! ! !
    % T_glass=abs(4*1*n(1)./(1+n(1)).^2);
    R_glass=abs((1-n(1))./(1+n(1))).^2;
    S=scattering(1,lambda);
    R=abs(S(2,1)/S(1,1))^2; %JAP Vol 86 p.487 Eq 9 Power Reflection from layers other
     than substrate
    T=abs(2/(1+n(1)))/sqrt(1-R_glass*R); %Transmission of field through glass
    substrate Griffiths Electrodynamics 9.85 + multiple reflection geometric series
    % ! ! ! ! ! ! ! ! ! ! ! ! ! ! ! ! !

    spec = [];


    for l = 1:length(d)-1
        steps = 0:res:(ceil(d(l+1)/res)-1)*res; % this is inefficient
        % x = [x (steps+depth)];
        spec = [spec pstm(steps,l,lambda)];
        % depth = depth + d(l+1);
    end

    % ! ! ! ! ! ! ! ! ! ! ! ! ! ! ! ! !
    spec = T * spec;
    % ! ! ! ! ! ! ! ! ! ! ! ! ! ! ! ! !

```

```
102     specs(:,iter)=spec;
103 end
104 
105 %%%%%%%%%%%%%%%%%%%%%%%%%%%%%
106 %
107 % Plotting
108 %
109 %%%%%%%%%%%%%%%%%%%%%%%%%%%%%
110 specs=(abs(specs)).^2;
111 plot(x,specs(:,1))
112 hold all
113 for iter = 2:size(waves,2)
114     plot(x,specs(:,iter))
115 end
116 title('PEDOT / P3HTPCBM Device')
117 xlabel('depth (nm)')
118 ylabel('|E|^2')
119 legend(strtrim(cellstr(num2str(waves'))'))
120 
121 % vertical lines for layers
122 axislimit1=axis;
123 for matindex=2:length(d)
124     line([sum(d(1:matindex)) sum(d(1:matindex))],[0 axislimit1(4)]);
125 end
126 
127 hold off
128 
129 
130 %%%%%%%%%%%%%%%%%%%%
```

```
143
144 % interface matrix
145 function [I] = interface(l,k) % indices match paper
146     global q
147     r_TE = (q(l+1)-q(k+1))/(q(l+1)+q(k+1));
148     t_TE = (2*q(l+1))/(q(l+1)+q(k+1));
149     % switch to these for TM transmission
150     % r_TM = (-n(k+1)^2*q(j+1)+n(j+1)^2*q(k+1))/(n(k+1)^2*q(j+1)+n(j+1)^2*q(k+1));
151     % t_TM = (2*n(j+1)*n(k+1)*q(j+1))/(n(k+1)^2*q(j+1)+n(j+1)^2*q(k+1));
152
153     I = 1/t_TE* [1 r_TE ; r_TE 1];
154
155 % scattering matrices
156 function [S_jp, S_jpp] = scattering(l,lambda)
157     global d
158     S_jp = eye(2);
159     for v = 1:(l-1)
160         S_jp = S_jp * interface(v-1,v) * layer(v,lambda);
161     end
162     S_jp= S_jp * interface(l-1,l);
163
164     S_jpp = eye(2);
165     for v = (l+1):(length(d)-1) %%
166         S_jpp = S_jpp * interface(v-1,v) * layer(v,lambda);
167     end
168     %S_jpp= S_jpp * interface(length(d)-2,length(d)-1); %%
169
170 % partial system transfer matrix.  E(x) for single layer
171 function [tm] = pstm(x,l,lambda)
172     global q
173     global d
174     [s_jp,s_jpp] = scattering(l,lambda);
175
176     xi = 2*pi/lambda * q(l+1);
177
178     tm = (s_jpp(1,1)*exp(-1i*xi*(d(l+1)-x))+s_jpp(2,1)*exp(1i*xi*(d(l+1)-x))) ./...
179         (s_jp(1,1)*s_jpp(1,1)*exp(-1i*xi*d(l+1))+s_jp(1,2)*s_jpp(2,1)*exp(1i*xi*d(l
    +1)));
180
181
182
```

```
function ntotal = LoadRefrIndex(name,wavelengths)
    %Data in IndRefr, Column names in IndRefr_names
    [IndRefr,IndRefr_names]=xlsread('Index_of_Refraction_library.xls');

    % Load index of refraction data in spread sheet, will crash if misspelled
    % file_wavelengths=IndRefr(:,strmatch('Wavelength',IndRefr_names));
    file_wavelengths=IndRefr(:,strncmp('Wavelength',IndRefr_names,10));
    % n=IndRefr(:,strmatch(strcat(name,'_n'),IndRefr_names));
    n=IndRefr(:,strncmp(strcat(name,'_n'),IndRefr_names,length(name)+2));
    % k=IndRefr(:,strmatch(strcat(name,'_k'),IndRefr_names));
    k=IndRefr(:,strncmp(strcat(name,'_k'),IndRefr_names,length(name)+2));

    % Interpolate/Extrapolate data linearly to desired wavelengths
    n_interp=interp1(file_wavelengths, n, wavelengths, 'linear', 'extrap');
    k_interp=interp1(file_wavelengths, k, wavelengths, 'linear', 'extrap');

    %Return interpolated complex index of refraction data
    ntotal = n_interp+1i*k_interp;
```

F.2 Out-Coupling (Power Dissipation)

The following model implements an out-coupling calculation by calculating the power dissipation as a function of the normalized in-plane wavevector, u. This is an implementation of the method outlined by Furno *et al.*.[54,96]

PowerDissipationModel.m

```

function [] = PowerDissipationModel
%TE=s
%TM=p
clear

%%%%%%%%%%%%%%%%%%%%%%%%%%%%%%%%%%%%%%%%%%%%%%%%%%%%%%%%%%%%%%%%%%%%%%%%%%%%
% ------------------------------------------------------------------------%%
% Model Parameters                                                        %%
% ------------------------------------------------------------------------%%
%%%%%%%%%%%%%%%%%%%%%%%%%%%%%%%%%%%%%%%%%%%%%%%%%%%%%%%%%%%%%%%%%%%%%%%%%%%%


% Layers. Must match names in lookup table
```

```
materials = {'SiO2' 'ITOsorizon' 'TCTA' 'Bphen' 'Irppy' 'Al' 'Air'};

% Wavelengths to test
waves = 1E-9*510; % freespace wavelengths

%% start u initiation and nreftable fetching
%#########################################################################################
% Dipole inplane wave vectors                                                            %#
u_range = cat(2,0:.005:.999,1.001:.005:pi/2);                                            %#
                                                                                         %#
% Load in index of refraction for each material and each wavelength                      %#
nreftable = zeros(size(materials,2),size(waves,2));                                      %#
for index = 1:size(materials,2)                                                          %#
    nreftable(index,:) = LoadRefrIndex(materials{index},waves*1E9);                      %#
end                                                                                      %#
%#########################################################################################
%% end u initiation and nreftable fetching

% Save u
% u_r = u_range';
% save('u.txt','u_r','-ascii')

%construct layer matrix
ntable(1,:) = nreftable(1,:); % glass
ntable(2,:) = nreftable(2,:); % ITO
ntable(3,:) = nreftable(3,:); % neat TCTA
ntable(4,:) = (nreftable(3,:)+nreftable(4,:))/2; % MEML
ntable(5,:) = nreftable(4,:); % neat bphen
ntable(6,:) = nreftable(6,:); % Al
ntable(7,:) = nreftable(7,:); % air

% layer thicknesses.
d(1) = 0; % Sio2
d(2) = 150; % ito
d(3)=20; %tcta
d(4)=60; %MEML
d(5)=20; %bphen
d(6) = 100; % Al
d(7) = 0; % air
d = d * 1E-9; % convert to nm

```

```
for thick_iter=1:60
% Emitter Matrix
% [layer    location_p(nm)    weight]
emitters = [
    4 thick_iter 1
];
emitters(:,2)=emitters(:,2)*1E-9;

%% Start main work loop
%#########################################################################################
% ------------------------------------------------------------------------------------%#
% Generation                                                                          %#
% ------------------------------------------------------------------------------------%#
%%%%%%%%%%%%%%%%%%%%%%%%%%%%%%%%%%%%%%%%%%%%%%%%%%%%%%%%%%%%%%%%%%%%%%%%%%%%%%%%%%%%%
                                                                                      %#
% initialize power array                                                              %#
K_TMv = zeros(size(u_range));                                                         %#
K_TMh = zeros(size(u_range));                                                         %#
K_TEh = zeros(size(u_range));                                                         %#
K_TMvp = zeros(size(u_range));                                                        %#
K_TMhp = zeros(size(u_range));                                                        %#
K_TEhp = zeros(size(u_range));                                                        %#
                                                                                      %#
% hard work begins                                                                    %#
for wavelength_iter = 1:size(waves,2)                                                 %#
    for wavenumber_iter = 1:size(u_range,2)                                           %#
        u = u_range(wavenumber_iter);                                                 %#
                                                                                      %#
                                                                                      %#
        lambda = waves(wavelength_iter); % free space lambda                          %#
        n=ntable(:,wavelength_iter);                                                  %#
                                                                                      %#
        K_TMv(wavenumber_iter)=0;                                                     %#
        K_TMh(wavenumber_iter)=0;                                                     %#
        K_TEh(wavenumber_iter)=0;                                                     %#
        K_TMvp(wavenumber_iter)=0;                                                    %#
        K_TMhp(wavenumber_iter)=0;                                                    %#
        K_TEhp(wavenumber_iter)=0;                                                    %#
                                                                                      %#
        for emitter = 1:size(emitters,1)                                              %#
            q= (n.^2-((n(emitters(emitter,1)).*u)).^2).^(1/2);                        %#
```

```
97                                                                  %#
98          % reflection coefficiencts                               %#
99          [r_TMp,t_TMp,~]= reflection_neg(emitters(emitter,1),lambda,0,n,d,q);     %
    #
100         [r_TMn,~,~]  = reflection_pos(emitters(emitter,1),lambda,0,n,d,q);       %
    #
101         [r_TEp,t_TEp,~] = reflection_neg(emitters(emitter,1),lambda,1,n,d,q);    %
    #
102         [r_TEn,~,~] = reflection_pos(emitters(emitter,1),lambda,1,n,d,q);        %
    #
103                                                                 %#
104         k=2*pi*n(emitters(emitter,1))/lambda;                    %#
105         z_p = emitters(emitter,2);                               %#
106         z_n = d(emitters(emitter,1))-z_p;                        %#
107         a_TMp = r_TMp*exp(2*1j*k*sqrt(1-u.^2).*z_p); % Furno A4      %#
108         a_TMn = r_TMn*exp(2*1j*k*sqrt(1-u.^2).*z_n); % Furno A5      %#
109         a_TEp = r_TEp*exp(2*1j*k*sqrt(1-u.^2).*z_p); % Furno A4      %#
110         a_TEn = r_TEn*exp(2*1j*k*sqrt(1-u.^2).*z_n); % Furno A5      %#
111                                                                 %#
112         % Radiated Power Density                                 %#
113         K_TMv(wavenumber_iter) = K_TMv(wavenumber_iter) + emitters(emitter,3)
    .*3/4*real(u.^2./sqrt(1-u.^2).*(1+a_TMp).*(1+a_TMn)./(1-a_TMp.*a_TMn)); % Furno
    A1          %#
114         K_TMh(wavenumber_iter) = K_TMh(wavenumber_iter) + emitters(emitter,3)
    .*3/8*real(sqrt(1-u.^2).*(1-a_TMp).*(1-a_TMn)./(1-a_TMp.*a_TMn)); % Furno A2
              %#
115         K_TEh(wavenumber_iter) = K_TEh(wavenumber_iter) + emitters(emitter,3)
    .*3/8*real(1./sqrt(1-u.^2).*(1+a_TEp).*(1+a_TEn)./(1-a_TEp.*a_TEn)); % Furno A3
              %#
116                                                                 %#
117         % Transmission of the top half-stack                     %#
118         T_TMp = abs(t_TMp).^2*(n(1)/n(emitters(emitter,1)))*sqrt((1-(u*n(emitters
    (emitter,1))/n(1))^2)/(1-u^2)); % Furno A12
119         T_TEp = abs(t_TEp).^2*(n(1)/n(emitters(emitter,1)))*sqrt((1-(u*n(emitters
    (emitter,1))/n(1))^2)/(1-u^2)); % Furno A13
120                                                                 %#
121         % Power radiated into the substrate                      %#
122         K_TMvp(wavenumber_iter) = K_TMvp(wavenumber_iter) + emitters(emitter,3)
    .*3/8*(u.^2./sqrt(1-u.^2).*(abs(1+a_TMn)).^2./(abs(1-a_TMp.*a_TMn)).^2)*T_TMp; %
    Furno A8    %#
123         K_TMhp(wavenumber_iter) = K_TMhp(wavenumber_iter) + emitters(emitter,3)
```

```
    .*3/16*(sqrt(1-u.^2).*(abs(1-a_TMn)).^2./(abs(1-a_TMp.*a_TMn)).^2)*T_TMp; % Furno
     A9          %#
124             K_TEhp(wavenumber_iter) = K_TEhp(wavenumber_iter) + emitters(emitter,3)
    .*3/16*(1./sqrt(1-u.^2).*(abs(1+a_TEn)).^2./(abs(1-a_TEp.*a_TEn)).^2)*T_TEp; %
    Furno A10      %#
125                                                                          %#
126         end % emitter                                                    %#
127     end % wavenumber                                                     %#
128 end % wavelength                                                         %#
129                                                                          %#
130 K = (1/3*(abs(K_TMv)+2*abs(K_TMh)+2*abs(K_TEh))); % Furno A6            %#
131 K = K./sum(emitters(:,3));                                              %#
132                                                                          %#
133                                                                          %#
134 % Transmission out of the substrate to air                              %#
135 n_g = ntable(1,1);                                                      %#
136 n_a =  1;                                                               %#
137 u_g = u_range*ntable(emitters(1),1)/ntable(1,1);                        %#
138 cos_g = sqrt(1-u_g.^2);                                                 %#
139 cog_a = sqrt(1-(n_g./n_a.*u_g).^2);                                     %#
140 Rs = ((n_g.*cos_g-n_a.*cog_a)./(n_g.*cos_g+n_a.*cog_a)).^2;             %#
141 T_s = 1-Rs;                                                            %#
142 Rp = ((n_g.*cog_a-n_a.*cos_g)./(n_g.*cog_a+n_a.*cos_g)).^2;             %#
143 T_p = 1 - Rp;                                                          %#
144 % This calculation assumes a lossless interface                        %#
145                                                                          %#
146 % Outcoupled Power                                                     %#
147 n = ntable(:,1);                                                        %#
148 Rc_s=zeros(1,size(u_range,2));                                          %#
149 Rc_p=zeros(1,size(u_range,2));                                          %#
150 for u_iter = 1:size(u_range,2)                                          %#
151     q= (n.^2-((n(1,1).*u_range(u_iter))).^2).^(1/2);                    %#
152     Rc_s(u_iter) = abs(reflection_neg(1,waves(1),1,ntable(:,1),d,q))^2; %#
153     Rc_p(u_iter) = abs(reflection_neg(1,waves(1),0,ntable(:,1),d,q))^2; %#
154 end                                                                     %#
155 K_outTMv = K_TMvp.*T_p./(1-Rp.*Rc_p); % Furno A14                       %#
156 K_outTMh = K_TMhp.*T_p./(1-Rp.*Rc_p); % Furno A14                       %#
157 K_outTEh = K_TEhp.*T_s./(1-Rs.*Rc_s); % Furno A14                       %#
158                                                                         %#
159 K_out = (1/3*(abs(K_outTMv)+2*abs(K_outTMh)+2*abs(K_outTEh)));          %#
160 K_out=K_out./sum(emitters(:,3));                                        %#
```

```
                                                                          %#
% Power Dissipation Spectra                                               %#
y=u_range.*K;                                                             %#
y_out=u_range.*K_out;                                                     %#
                                                                          %#
% critical angle from snells law                                         %#
u_crit = 1/real(ntable(emitters(emitter,1),1));                           %#
index=find(u_range<u_crit,1,'last')+1;                                    %#
out = trapz(u_range(1:index),y_out(1:index)); % Furno A15                 %#
tot = trapz(u_range,y); % Furno A7                                        %#
                                                                          %#
eta(thick_iter)=out/tot;                                                  %#
                                                                          %#
% Power vs Angle                                                          %#
% sin_theta = u_range(1:113)/u_range(113);                                  %#
% theta = asind(sin_theta);                                               %#
% cos_theta = cosd(theta);                                                %#
% P_out = (1/ntable(emitters(1),1)).^2.*cos_theta/pi.*K_out(1:113); % Furno A18
                                                                          %#
                                                                          %#
%##########################################################################
%% End main work loop

% End Control Loops
end

%%%%%%%%%%%%%%%%%%%%%%%%%%%%%%%%%%%%%%%%%%%%%%%%%%%%%%%%%%%%%%%%%%%%%%%%%%%
% ------------------------------------------------------------------------%%
% Plotting                                                                %%
% ------------------------------------------------------------------------%%
%%%%%%%%%%%%%%%%%%%%%%%%%%%%%%%%%%%%%%%%%%%%%%%%%%%%%%%%%%%%%%%%%%%%%%%%%%%


% Power Spectrum vs u
% semilogy(u_range,y)
% xlabel('u')
% ylabel('K*u')

% Power Intensity vs Angle (requires uncommenting of angle code)
% plot(theta,P_out);

```

```
202
203
204 %%%%
```

```
243         % TM light
244         r = (n(k)^2*q(l)-n(l)^2*q(k))./(n(k)^2*q(l)+n(l)^2*q(k)); % pettersson 3a
245         t = (2*n(l)*n(k)*q(l))./(n(k)^2*q(l)+n(l)^2*q(k)); % pettersson 3b
246
247     end
248
249     I = 1/t .* [1 r ; r 1]; % pettersson 1
250     % checks for singular matrix.  If so, a small term is added to the diagonal,
251     % a common method of dealing with singular matrices.
252     % This adds in potential error, but
253     % makes the system solvable and stable.  Will fail if NaN is passed
254     %if ( cond(I) > 1E8)
255     %   I = I+eye(2)*1E-5;
256     %end
257
258 % reflection coefficient Positive Direction ------------------------------
259 % ------------------------------------------------------------------------
260 %Uses the Interface and layer matrices, but in the appropriate directions.
261 function [r,t,D] = reflection_pos(active_layer,lambda,orientation,n,d,q)
262
263     S_jpp = eye(2);
264     for v = (active_layer):(length(d)-2)
265         S_jpp = S_jpp * interface(v,v+1,orientation,n,d,q) * layer(v+1,lambda,n,d,q);
        % pettersson 13
266     end
267     S_jpp = S_jpp * interface(length(d)-1,length(d)-0,orientation,n,d,q);
268     r = S_jpp(2,1)/S_jpp(1,1); % pettersson 9
269     t = 1/S_jpp(1,1); % Pettersson 15
270
271     D=det(S_jpp);
272
273 % reflection coefficient Negative Direction ------------------------------
274 % ------------------------------------------------------------------------
275 function [r,t,D] = reflection_neg(active_layer,lambda,orientation,n,d,q)
276     S_jp = eye(2);
277     % for v = (active_layer):-1:3
278     for v = (active_layer):-1:3 % Treat glass as semiinfinite
279         S_jp = S_jp * interface(v,v-1,orientation,n,d,q) * layer(v-1,lambda,n,d,q); %
        pettersson 13
280     end
281     S_jp = S_jp * interface(2,1,orientation,n,d,q);
```

```
282     r = S_jp(2,1)/S_jp(1,1); % pettersson 9
283     t = 1/S_jp(1,1); % Pettersson 15
284
285     D=det(S_jp);
286     %t=D*t;
287
288 % Index fetching from files ---------------------------------------------------
289 % -----------------------------------------------------------------------------
290 function ntotal = LoadRefrIndex(name,wavelengths)
291     %Data in IndRefr, Column names in IndRefr_names
292     [IndRefr,IndRefr_names]=xlsread('Index_of_Refraction_library.xls');
293
294     % Load index of refraction data in spread sheet, will crash if misspelled
295     file_wavelengths = IndRefr(:,strncmp('Wavelength',IndRefr_names,10));
296     n = IndRefr(:,strncmp(strcat(name,'_n'),IndRefr_names,length(name)+2));
297     k = IndRefr(:,strncmp(strcat(name,'_k'),IndRefr_names,length(name)+2));
298
299     % Interpolate/Extrapolate data linearly to desired wavelengths
300     n_interp = interp1(file_wavelengths, n, wavelengths, 'linear', 'extrap');
301     k_interp = interp1(file_wavelengths, k, wavelengths, 'linear', 'extrap');
302
303     %Return interpolated complex index of refraction data
304     ntotal = n_interp+1i*k_interp;
```

F.3 Database Keys

F.3.1 materials

- commonName : string (all lowercase)
- formattedName : string (as you would like it displayed)
- chemicalName : string (long chemical name)
- allNames : list of all possible names
- LUMO_list : [[LUMO (eV) , source (string)],...]
- HOMO_list : [[HOMO (eV) , source (string)],...]
- E_T_list : [[E_T (eV) , source (string)],...]
- LUMO : float (eV) (preferred value)
- HOMO : float (eV) (preferred value)
- E_T : float (eV) (preferred value)
- CAS : integer (no dashes)
- molecularWeight : float (amu)
- Tg : float (Celcius)
- meltingTemp : float (Celcius)
- L_D : float (nm)
- L_D_list : [[L_D (nm) , source (string)],...]
- tau : float (ns)
- tau_list : [[tau (ns) , source (string)],...]

F.3.2 architectures

- layers_list - [layer,...]
  - 'layer':int(layernum),

  - 'material':string,
  - 'materialID' : _id(material),
  - 'type':string,
  - 'thickness':float,
  - 'concentration':float<1
- eml_thickness-float
- doping_concentration-float<1
- device_type - string(SEML/DEML/MEML/AEML/GEML)

F.3.3 growths

- experiment_label - string
- grower_name - string
- growth_date - datetime.datetime
- peak_eqe - float(%)
- device_area - float(cm^2)
- ito_pattern - string
- last_chamber_clean - datetime.datetime
- architectureID - _id(architecture)
- notes - string
- tags - [string,...]
- spectrums - [spectrum,...]
  - current_density - float (A/cm^2),
  - integration_time - float (s),
  - waves - [float,...] (nm),
  - intensity - [float,...]

- devices - [stat,...]
  - filename - string,
  - devID - string,
  - substrate - int,
  - device - int,
  - area - float,
  - V_raw - [float,...],
  - I_dev_raw - [float,...] (A),
  - I_photo_raw - [float,...] (A),
  - V - [float,...] (V),
  - I_photo - [float,...] (A),
  - J - [float,...] (mA/cm^2),
  - P_opt - [float,...] (W),
  - EQE - [float,...] (%),
  - peakEQE - float (%),
  - lumens - [float,...] (lm),
  - cdm2 - [float,...] (cd/m^2),
  - P_eff - [float,...] (lm/W),

F.3.4 lifetimes

General Info

- experiment_label - string
- test_date - datetime.datetime
- growthID - _id(growth)
- architectureID - _id(architecture)
- notes - string
- tags -[string,...]

- device - int
- substrate - int

Test Info

- background - float(A)
- box - int
- compartment - int
- current - float(A)
- luminance - int(cd/m2)
- powerDensity - int(mW/cm2) // Power density of light source for optical and L+J tests
- break_interval - float(min) //break time for laser or current
- test_type - str([IL/CL/IC]+'-'+[var_testDrop])
- pump_wavelength - float(nm) // Wavelength of PL pump
- pump_type - str // obis laser, led, etc.

Test Data

- ELdatetime - [datetime,...]
- ELonTime - [float,...]
- voltage - [float,...]
- initial_voltage=float
- ELdevSignal = [float,...]
- ELnormDevSignal - [float,...]
- ELtrust - int (0,1,2) //2 is most trusted
- PLtrust - int (0,1,2) //2 is most trusted
- PLdatetime - [datetime,...]
- PLonTime - [float,...]

- PLdevSignal = [float,...]
- PLelDecSignal = [float,...] //el decay at the pl points
- PLlaserSignal = [float,...]
- PLnormSignal - [float,...] //normalized to laser signal then peak norm
- EQEdegPoint - [float,...] //the degradation point for each EQE
- EQEcurrent - [[float,...],...]
- EQEvoltage - [[float,...],...]
- EQEel - [[float,...],...]
- EQErelativeEQE - [[float,...],...]

Test specific data Single-Carrier + Photodegradation For this test, "voltage" is measured with no applied light, and "PLdevSignal" is measured with no applied current.

- VoltageWithLight - [float,...] // Voltage measured while light is applied to device
- PLWithCurrent - [float,...] // PL measured while current is applied to device

lifetimes

- ELt50 - (float(hours),float(hours)) // exp,fit
- ELt75 - (float(hours),float(hours)) // exp,fit
- ELt90 - (float(hours),float(hours)) // exp,fit
- PLt95 - (float(hours),float(hours)) // exp,fit
- PLt90 - (float(hours),float(hours)) // exp,fit
- PLt85 - (float(hours),string(fit/experiment))
- PLt80 - (float(hours),string(fit/experiment))

F.3.5 absSpectra

- tester: string (all lowercase)
- notes: string
- label: string
- waves: wavelengths in nm (float)
- abs: absorbance (float) - same length as waves
- date: datetime
- type: solution or film (string)
- composition: [layer,...]
- layer : dict
  - 'layer':int(layernum),
  - 'material':string,
  - 'materialID' : _id(material),
  - 'thickness':float,
  - 'concentration':float<1

F.3.6 excSpectra

- tester: string (all lowercase)
- notes: string
- label: string
- inslits: slit opening in mm (float)
- outslits: slit opening in mm (float)
- pump : pump wavelength in nm
- waves: wavelengths in nm (float)
- rawBackground: background scan [float,...] - same length as waves

- rawPL: pl scan [float,...] - same length as waves
- pl: background corrected PL [float,...] - same length as waves
- date: datetime
- type: solution or film (string)
- composition: [layer,...]
- layer : dict
  - 'layer':int(layernum),
  - 'material':string,
  - 'materialID' : _id(material),
  - 'thickness':float,
  - 'concentration':float<1

F.3.7 opticalConstants

- substrate - string [glass/quartz/Si]
- acquisitionDate - datetime
- acquiredBy - name (string)
- label - string
- wavelengths = [float,...]
  - n - [float,...]
  - k - [float,...]
- composition: [layer,...]
- layer : dict
  - 'layer':int(layernum),
  - 'material':string,
  - 'materialID' : _id(material),
  - 'thickness':float,
  - 'concentration':float<1

F.3.8 plSpectra

- tester: string (all lowercase)
- notes: string
- label: string
- inslits: slit opening in mm (float)
- outslits: slit opening in mm (float)
- pump : pump wavelength in nm
- waves: wavelengths in nm (float)
- rawBackground: background scan [float,...] - same length as waves
- rawPL: pl scan [float,...] - same length as waves
- pl: background corrected PL [float,...] - same length as waves
- date: datetime
- type: solution or film (string)
- tempK: temperature in Kelvin
- emission_type: string [fluorescence delayed phosphorescence]
- composition: [layer,...]
- layer : dict
  - 'layer':int(layernum),
  - 'material':string,
  - 'materialID' : _id(material),
  - 'thickness':float,
  - 'concentration':float<1

Appendix G

Lifetime Box Code

The following code outlines our implementation of lifetime setup and can be found on the Holmes Group Github page at `https://github.umn.edu/HolmesGroup/lifetimeTesting`. To implement all boxes, code is organized into separate files. *box.py* contains all general functions shared between all hardware implementations and is the main driver for lifetime. Different hardware configurations require different commands in order to control the hardware. These hardware specific implementation details are located in *keithleyBox.py*, *keithleyBox2.py*, and *keysightBox.py*. To facilitate hardware rearrangement, configuration files, such as *box1.json* coordinate hardware. Finally, each piece of hardware is uniquely named in Linux using udev rules, outlined in *85-lifetime.rules*.

Appendix H

Chemical Structures

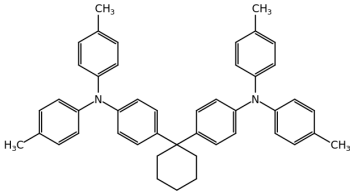

TAPC

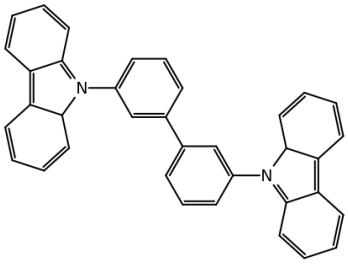

mCBP

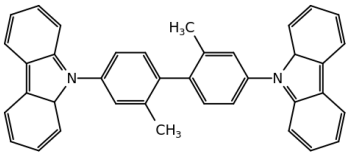

CDBP

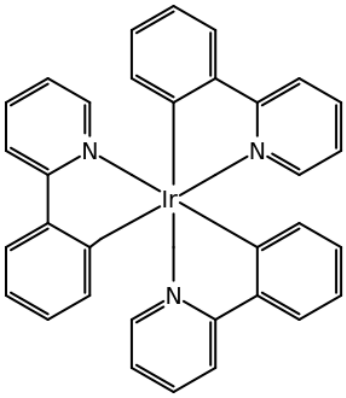

Ir(ppy)3

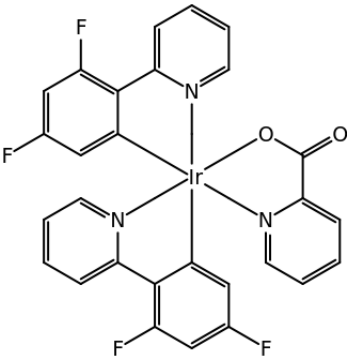

FIrpic

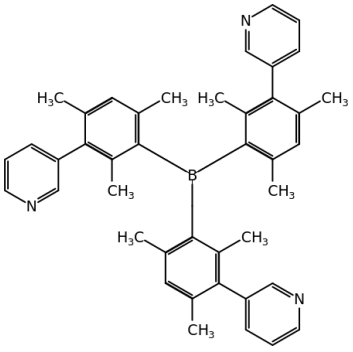

3TPYMB

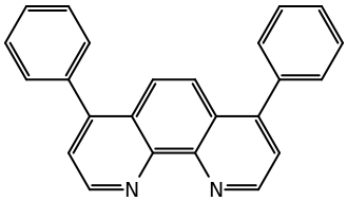

Bphen

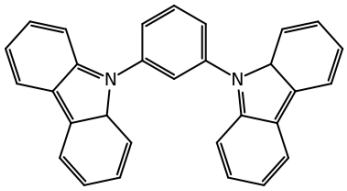

mCP

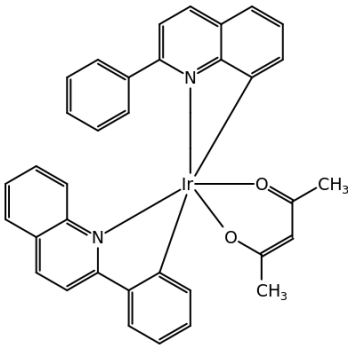

PQIr

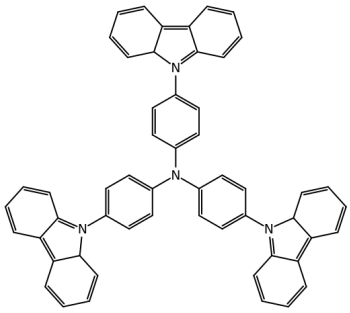

TCTA

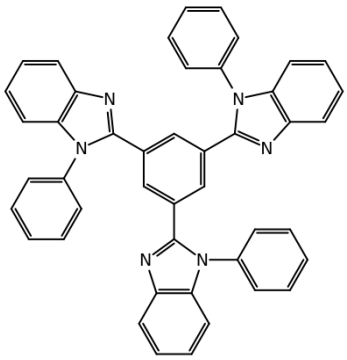

TPBi

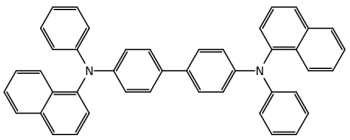

NPD

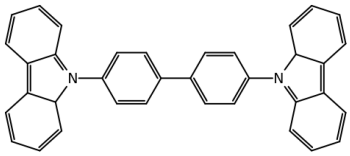

CBP

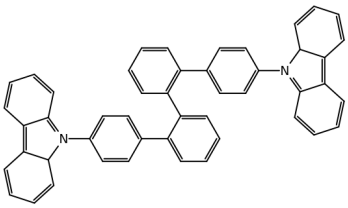

BCBP

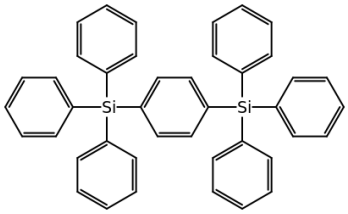

UGH2

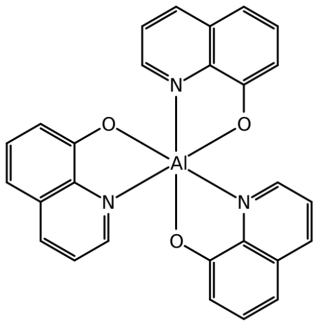

Alq3

Appendix I

Material Properties

Common Name	**Chemical Name**	**Other Names**	**HOMO**	**LUMO**	E_T	**CAS**	T_{melt}	**M.W.**	τ
3TPYMB	b'Tris(2,4,6-triMethyl-3-(pyridin-3-yl)phenyl)borane'		6.7	3.3		929203021		599.61	
4CzIPN	b'(4s,6s)-2,4,5,6-tetra(9H-carbazol-9-yl)isophthalonitrile'		5.8	3.4		1416881521		788.893	48
Ag	b'Silver'	silver ag	4.6	4.6		7440224	962.0	107.868	
Air									
Al	b'Aluminum'			4.3		7429905	660.0	26.981	
Alq3	b'Tris(8-hydroxyquinoline)aluminum'	Tris(8-hydroxyquinolinato)aluminum Aluminum oxinate Aluminum 8-hydroxyquinolinate 8-Hydroxyquinoline aluminum salt	5.62	2.85		2085338		459.43	
Anthracene	b'Anthracene'		5.7	1.7		120127		178.23	
AQ1200	b"			5.5					
AQ1250				5.5					
Au	b'Gold'	gold au	5.1	5.1		7440575	1064.0	196.97	

Common Name	**Chemical Name**	**Other Names**	**HOMO**	**LUMO**	E_T	**CAS**	T_{melt}	**M.W.**	τ
B3PYMPM	b'bis-4,6-(3,5-di-3-pyridylphenyl)-2-methylpyrimidine'		6.8	3.3		925425963		554.64	
BCBP	b"2,2'-Bis(4-(carbazol-9-yl)phenyl)-biphenyl"		6.1	2.6		858131701		636.78	
BCP	b'Bathocuproine'		6.5 7.0	1.6 3.5		4733395		360.45	
BP2T	b'5,5u-[Di(1,1u-biphenyl)-4-yl]-2,2u-bithiophene'		5.3	2.8		175850289		470.658	
BP4mPy	b'3,5,3A,5A-tetra(m-pyrid-3-yl)phenyl[1,1A]-biphenyl'	3,5,3',5'-tetra(m-pyrid-3-yl)phenyl[1,1']biphenyl	6.66	2.57		1009033946	191	766.93	
Bphen	b'Bathophenanthroline'	4,7-Diphenyl-1,10-phenanthroline	6.4	3.0		1662017		332.4	
BPy-TP2	b' 2,7-Bis(2,20-bipyridine-5-yl)triphenylene'		5.7	2.7		1394813581		536.624	
c-TiO2									
C60	b'Fullerene'	fullerene	6.1	3.7		99685968		720.64	

Common Name	**Chemical Name**	**Other Names**	**HOMO**	**LUMO**	E_T	**CAS**	T_{melt}	**M.W.**	τ
				3.5					
C70	b'[5,6]-Fullerene'	fullerene C60	6.3			115383227		840.75	
CBP	b'4,4-Bis(N-carbazolyl)-1,1-biphenyl'		6.1 6.0	1.9 2.9		58328317		484.59	0.7
CDBP	b"4,4'-Bis(9-carbazolyl)-2,2'-dimethylbiphenyl"					120260017		512.64	
ClAlPc	b'Aluminum phthalocyanine chloride'					14154428		574.96	
CuPc	b'Copper(II) phthalocyanine'		4.8 5.2	2.6 3.5		147148		576.07	
CzSi	b'9-(4-tert-butylphenyl)-3,6-bis(triphenylsilyl)-9H-carbazole'		6.0	2.5		898546822		816.19	

Common Name	**Chemical Name**	**Other Names**	**HOMO**	**LUMO**	E_T	**CAS**	T_{melt}	**M.W.**	τ
CzTRZ	b'9-[4-(4,6-diphenyl-1,3,5-triazin-2-yl)phenyl]-9H-carbazole'		6.08	3.28		nan		nan	
Dow ETL			5.1	1.808					
Dow ETL2			5.842	1.908					
Dow HIL			4.509	1.128					
Dow Host A			5.669	2.269 1.223					
Dow Host B			5.261	2.361 1.872					
Dow HTL			4.736	1.039					
DPDCPB	b'2-[7-(4-Diphenylaminophenyl)-2,1,3-benzothiadiazol-4-yl]methylenepropanedinitrile'		5.5	3.36		1393343606		455.53	
DPDCTB	b"		5.35	3.44					

Common Name	**Chemical Name**	**Other Names**	**HOMO**	**LUMO**	E_T	**CAS**	T_{melt}	**M.W.**	τ
DTDCPB	b'2-[(7-4-[N,N-Bis(4-methylphenyl)amino]phenyl-2,1,3-benzothiadiazol-4-yl)methylene]propanedinitrile'		5.43	3.35		1393343582		483.59	
DTDCTB	b'2-[7-(5-N,N-Ditolylaminothiophen-2-yl)-2,1,3-benzothiadiazol-4-yl]methylenemalononitrile'		5.3	3.44		1335150098		489.61	
FIrpic	b'Bis[2-(4,6-difluorophenyl)pyridinato-C2,N](picolinato)iridium(III)'		5.8	2.9		376367930		694.66	
Glass	b'Silicon Dioxide'								
H2Pc	b'29H,31H-Phthalocyanine'					574936		514.54	
HATCN	b'1,4,5,8,9,11-Hexaazatriphenylenehexacarbonitrile'		9.5 7.5	5.5 4.4		105598274		384.27	
Hoye CoOMe									
Hoye Nap CoOMe									
Hoye Nap NPh2									

Common Name	**Chemical Name**	**Other Names**	**HOMO**	**LUMO**	E_T	**CAS**	T_{melt}	**M.W.**	τ
Hoye Nap OMe									
Hoye Nap H									
Hoye OH									
Hoye OMe									
Hoye Triben-H									
Hoye Triben OMe									
Hoye OMe	b"		6.07	2.55					
Ir(dpm)PQ2	b'Bis(2-phenylquinoline)(2,2,6,6-tetramethylheptane-3,5-dionate)iridium(III)'					713079039		783.98	
Ir(mphq)3	b'Tris[2-phenyl-4-methylquinoline)]iridium(III)'					1433853907		847.04	
Ir(ppy)3	b'Tris[2-phenylpyridinato-C2,N]iridium(III)'		5.1	2.6		94928866		654.78	1000.0
ITO	b'Indium Tin Oxide'					50926119			
Li(acac)									
LiF	b'Lithium Fluoride'			2.8		7789244		25.94	
LiQ	b'8-Quinolinolato lithium (Liq)'		4.667	1.292		25387933		151.09	

Common Name	**Chemical Name**	**Other Names**	**HOMO**	**LUMO**	E_T	**CAS**	T_{melt}	**M.W.**	τ
MADN	b'2-Methyl-9,10-bis(naphthalen-2-yl)anthracene'		5.6	2.6		804560007		444.57	
MAI									
mCBP	b"3,3'-Bis(N-carbazolyl)-1,1'-biphenyl"		6.0	2.4		342638544		484.589	16
mCP	b'1,3-Bis(N-carbazolyl)benzene'		6.1 5.9	2.4		550378784	187.0	408.49	
MgPc	b'Magnesium phthalocyanine'					1661036		536.83	
MoOx	b'Molybdenum(VI) oxide'					1313275		143.94	
NPD	b'N,N-Di(1-naphthyl)-N,N-diphenyl-(1,1-biphenyl)-4,4-diamine'		5.3 5.4 5.4	2.3 1.52 2.4		123847858	280.0	588.74	3.5

Common Name	**Chemical Name**	**Other Names**	**HOMO**	**LUMO**	E_T	**CAS**	T_{melt}	**M.W.**	τ
NTCDA	b'1,4,5,8-Naphthalenetetracarboxylic dianhydride'		7.9	4.0		81301		268.18	
NTU1	b'2-[7-(4-ethyl-4H-thieno[3,2-b]indol-2-yl)benzo[c][1,2,5]thiadiazol-4-yl]-methylenemalononitrile'								
NTU2	b'2-[7-(8-ethyl-8Hthieno[2,3-b]indol-2-yl)benzo[c][1,2,5]thiadiazol-4-yl]-methylenemalononitrile'								
P3HT	b'Poly(3-hexylthiophene-2,5-diyl)'					156074985			
PbPc	b'Lead(II) phthalocyanine'					15187163		719.72	
Pedot	b'Poly(3,4-ethylenedioxythiophene)-poly(styrenesulfonate)'								

Common Name	**Chemical Name**	**Other Names**	**HOMO**	**LUMO**	E_T	**CAS**	T_{melt}	**M.W.**	τ
Pentacene	b'Pentacene'		5.2 4.85 5.0	3.0 2.8 3.2		135488	300.0	278.35	
Perfluoropentacene	b'perfluoropentacene'		6.7	5.0		646533882		530.22	
PO-T2T	b'2,4,6-Tris[3-(diphenylphosphinyl)phenyl]-1,3,5-triazine'		6.83 7.5	2.83 3.5		1646906264	287	909.8	
PPT	b'2,8-Bis(diphenylphosphoryl)dibenzo[b,d]thiophene'					1019842999		584.6	
PQIr	b'(2,4-Pentanedionato)bis[2-(2-quinolinyl)phenyl]iridium(III)'					337526951		699.82	
Pt17									
PTCBI	b'3,4,9,10-Perylenetetracarboxylic Bisbenzimidazole '		6.2	4.3		79534911		536.54	
PTCDA	b'Perylene-3,4,9,10-tetracarboxylic dianhydride'		6.95	4.1		128698		392.32	3.2

Common Name	**Chemical Name**	**Other Names**	**HOMO**	**LUMO**	E_T	**CAS**	T_{melt}	**M.W.**	τ
PTCDI	b'N,N-Dioctyl-3,4,9,10-perylenedicarboximide'	PTCDI-C8	6.2	6.2		78151583		614.77	
PtOEP	b'Platinum octaethylporphyrin'					31248392		727.84	
PtTPTBP	b'Platinum(II) tetraphenyltetrabenzoporphyrin'	[6,13,20,27-Tetraphenyl-29H,31H-tetrabenzoporphinato(2-)-κ2N29,N31]platinum Pt(II) meso-Tetraphenyl Tetrabenzoporphine platinum tetraphenyl-tetrabenzoporphine PtTPBP	4.8	2.9		166174056		1008.0	
Quartz									
Rubrene	b'5,6,11,12-Tetraphenylnaphthacene'		4.85 5.3	3.15 2.7		517511		532.67	9.1

Common Name	**Chemical Name**	**Other Names**	**HOMO**	**LUMO**	E_T	**CAS**	T_{melt}	**M.W.**	τ
			4.47 4.45 4.51 4.83 4.85 4.92	1.88 1.88 1.95 2.18 2.2 2.27					
SnI22									
SnNcCl2	b'Tin(IV) 2,3-naphthalocyanine dichloride'					26857614		902.37	
SubNc	b'Boron sub-2,3-naphthalocyanine chloride'	SubNc-Cl	5.35 5.5	3.47 3.5		142710563		580.83	
SubPc	b'Boron subphthalocyanine chloride'	SubPc-Cl	5.6 5.57	3.2 3.6		36530060	375.0	430.66	0.5
T2T	b'2,4,6-tris(biphenyl-3-yl)-1,3,5-triazine'		6.5	3.0		1201800830		537.652	

Common Name	**Chemical Name**	**Other Names**	**HOMO**	**LUMO**	E_T	**CAS**	T_{melt}	**M.W.**	τ
TAPC	b'4,4-Cyclohexylidenebis[N,N-bis(4-methylphenyl)benzenamine]'		5.5	1.8		58473782		626.87	
TAZ	b'3-(Biphenyl-4-yl)-5-(4-tert-butylphenyl)-4-phenyl-4H-1,2,4-triazole'		6.3	2.7		150405699		429.56	
TCTA	b'Tris(4-carbazoyl-9-ylphenyl)amine'		5.7	2.4		139092787		740.89	
Tetracene	b'Benz[b]anthracene'		5.1	1.8		92240		228.29	
TmPyPB	b'1,3,5-Tri(m-pyrid-3-ylphenyl)benzene'		6.63 6.68	2.54 2.73		921205030	181	537.65	
TPBi	b'2,2,2"-(1,3,5-Benzinetriyl)-tris(1-phenyl-1-H-benzimidazole)'		6.1	2.8		192198859		654.76	
TPD	b'N,N-Bis(3-methylphenyl)-N,N-diphenylbenzidine'		5.5	2.3		65181784		516.67	

Common Name	**Chemical Name**	**Other Names**	**HOMO**	**LUMO**	E_T	**CAS**	T_{melt}	**M.W.**	τ
Tris-PCz	b'9,9,9-triphenyl-9H,9H,9H-3,3:6,3-tercarbazole'	9,9'-Diphenyl-6-(9-phenyl-9H-carbazol-3-yl)-9H,9'H-3,3'-bicarbazole	5.6	2.1		1141757836		725.88	
UGH2	b'p-Bis(triphenylsilyl)benzene;Benzene,1,4-bis(triphenylsilyl)-;1,4-Phenylenebis[triphenylsilane;1,4-Phenylenebis(triphenylsilane)'		7.2	2.8		18856081	345.0	594.89	
ZnPc	b'Zinc phthalocyanine'		5.28	3.3		14320048		577.91	